Radionuclide alteration behaviour in engineered subsurface environments

A thesis submitted to the University of Manchester for the degree of

Doctor of Philosophy

in the Faculty of Science and Engineering

2021

Alana E. McNulty

School of Natural Sciences

Department of Earth and Environmental Sciences

Blank page

Table of Contents

Blank page

List of Figures

Blank page

List of Tables

List of Abbreviations

ALARA	As Low As Reasonably Achievable
CLESA	Calder Landfill Extension Segregated Area
DECC	Department of Energy and Climate Change
EDS/EDX	Energy Dispersive X-ray Spectroscopy
EXAFS	Extended X-Ray Absorption Fine Structure
GDF	Geological Disposal Facility
GRR	Guidance on Release from Radioactive Substances Regulation
HLW	High Level Waste
ICP-MS	Inductively Coupled Plasma Mass Spectrometry
ILW	Intermediate Level Waste
ITFA	Iterative Transformation Factor Analysis
KIT	Karlsruhe Institute of Technology
LCF	Linear Combination Fitting
LLW	Low Level Waste
LLWR	Low Level Waste Repository
NDA	Nuclear Decommissioning Authority
SEM	Scanning Electron Microscopy
SRS	Savannah River Site
US DOE	United States Department of Energy
VLLW	Very Low Level Waste
WHO	World Health Organisation
XANES	X-ray Absorption Near Edge Structure
XAS	X-Ray Absorption Spectroscopy
XMCD	X-ray Magnetic Circular Dichroism
XRD	X-Ray Diffraction
XRF	X-Ray Fluorescence

Blank page

Thesis Abstract

Nuclear activities over the last 75 years, both in the UK and globally, have resulted in a legacy of contaminated land and structures at nuclear sites. Over the next 100 years, many of these sites will progress through various stages of decommissioning, producing significant volumes of radioactive waste that will require careful management. These wastes will largely comprise concrete, contaminated land, as well as steelwork including concrete reinforcing bar (rebar) and pipelines. One emerging option in the UK to manage the large volumes of radioactive waste produced during decommissioning is in-situ disposal, where low-level radioactively contaminated land and subsurface structures may be safely left in place under the assumption that sites meet strict regulatory requirements. Many radionuclides are likely to be present in these radioactive waste disposal scenarios, including uranium (U), a chemotoxic as well as radiotoxic element. As such, it is important to develop an understanding of these radionuclide interactions with engineered components and their alteration products to underpin any future site environmental safety cases that may include in-situ disposal as an optimised solution for radioactive waste management.

In this thesis, the transport and speciation of U in a number of engineered subsurface systems was investigated. Field lysimeter experiments were chosen to explore these systems as they offered a unique opportunity to research U behaviour in environmentally relevant conditions that were representative of the subsurface at nuclear sites. A multi-technique approach was utilised to analyse and build a picture of the altered lysimeter samples post-field emplacement including X-ray absorption spectroscopy techniques, inductively coupled plasma mass spectrometry and environmental scanning electron microscopy. In the first study, the fate of U(V)-incorporated in magnetite, a common zero-valent iron corrosion product, was explored using a field lysimeter set up. The results showed limited to no transport of U away from the originally emplaced U(V)-magnetite source horizons and retention of U(V) incorporated into the structure of the iron (oxyhydr)oxide despite oxidation of both U and the magnetite itself over 12 months. The second study explored the fate of U in U-contaminated sediment and concrete subsurface lysimeter systems. Here, U speciation was found to be the defining factor in the extent of transport within the systems, with greater U migration in the system without concrete, where uranyl speciation dominated. In contrast, the formation of insoluble uranate phases in the systems containing concrete resulted in significantly reduced U transport over 13 months. These studies provide much needed insight into the transport and speciation of U in field scale engineered subsurface environments and contaminated land scenarios.

Declaration

The author of this thesis declares that no portion of the work referred to in this thesis has been submitted in support of an application for another degree or qualification of this or any other university or institute of learning.

Copyright Statement

i. The author of this thesis (including any appendices and/or schedules to this thesis) owns certain copyright or related rights in it (the "Copyright") and she has given The University of Manchester certain rights to use such Copyright, including for administrative purposes.

ii. Copies of this thesis, either in full or in extracts and whether in hard or electronic copy, may be made **only** in accordance with the Copyright Designs and Patents Act 1988 (as amended) and regulations issued under it or, where appropriate, in accordance with licensing agreements which the University has from time to time. This page must form part of any such copies made.

iii. The ownership of certain Copyright, patents, designs, trademarks and other intellectual property (the "Intellectual Property") and any reproductions of copyright works in the thesis, for example graphs and tables ("Reproductions"), which may be described in this thesis, may not be owned by the author and may be owned by third parties. Such Intellectual Property and Reproductions cannot and must not be made available for use without the prior written permission of the owner(s) of the relevant Intellectual Property and/or Reproductions.

iv. Further information on the conditions under which disclosure, publication and commercialisation of this thesis, the Copyright and any Intellectual Property and/or Reproductions described in it may take place is available in the University IP Policy (see http://documents.manchester.ac.uk/DocuInfo.aspx?DocID=487), in any relevant Thesis restriction declarations deposited in the University Library, The University Library's regulations (see http://www.manchester.ac.uk/library/aboutus/regulations) and in The University's policy on Presentation of Theses.

Blank page

Acknowledgements

Closer to home, I'd like to thank my Blackburn girls, you gave me the opportunity to escape the bubble a few weekends a year and Covid Facetime catch ups were a real boost!

To my family, thank you for always being there when I needed you and providing many laughs, and often too much red wine, during a particularly crazy few years for us all. Thanks mum (and Nicole!), dad, Lewis and Elliott. A massive thanks also here to the incredible teams at RBH ICU and Rakehead Neurorehabilitation Centre who got my mum through the worst year ever – I am so grateful for everything you all did.

Last, but most certainly not least, Tim, you've kept me sane (mostly) and provided me with an incredible amount of love and support over the last few years and especially in the last few months of writing, where juggling a job and writing a thesis may arguably have been more arduous for you than for me. You're awesome!

I definitely could not have completed this PhD without the support of all the people above, so, plenty of hard work, a fair dose of stress, a global pandemic, and one broken finger later, I thank you all from the bottom of my heart for getting me through it…you're all legends!

About the Author

The Author graduated from The University of Manchester with an undergraduate master's degree in Chemistry (MChem) in July 2016. The author then completed a graduate internship with Peer Support at The University Manchester, simultaneously joining the Royal Naval Reserve as a Training Officer. Sorely missing science and research, Alana joined the Geomicrobiology group to conduct the work reported in this thesis at The University of Manchester in September 2017 under the supervision of Professor Katherine Morris.

Blank page

Chapter 1   Project Relevance and Thesis Structure

This chapter details the project context and rationale for the thesis and includes an overview of the thesis structure including collaborator contributions to papers.

1.1 Project relevance

Nuclear activities and accidents over the last 75+ years have left behind a significant legacy of radioactively contaminated land that must be managed and disposed of. Globally, 10% of nuclear licenced sites including Sellafield, UK and Savannah River Site, USA, each have over 1,000,000 m^3 of contaminated land, comprising a variety of radionuclides (OECD, 2014). Concrete, often with steel reinforcement (rebar) is widely used on nuclear sites as both a primary building material and as backfill for disposal sites. Iron (oxyhydr)oxides such as magnetite are also likely to be present in the subsurface either from engineering metal, from corrosion of steel or rebar, or as naturally occurring iron (oxyhydr)oxides in sediments. Characterising and understanding the long-term behaviour of priority radionuclides such as uranium in contact with these materials in subsurface environments is key to successful decommissioning and developing routes to site end states. One potential option which is emerging for the disposal of contaminated land and structures is in-situ disposal, where parts of a facility or contaminated land will left in place and classed as disposed if certain requirements are met (SEPA et al., 2018). Current Nuclear Decommissioning Authority (NDA) strategy aims to develop this idea to enable "beneficial reuse" of excavated building materials such as using demolished buildings as backfill and void filler (NDA, 2016). Leaving materials in place will not only minimise waste disposal off-site, but is also likely to significantly reduce decommissioning costs as well as having potential environmental benefits through reduction in CO_2 emissions as a result of transportation of materials. A current example, the Winfrith site, located close to the Dorset coast, is due to complete physical decommissioning by 2021 and in the decommissioning process, the site managers are actively exploring opportunities to leave contaminated materials in-situ (NDA, 2016b). This project concerns uranium behaviour in contaminated land environments in the context of in-situ disposal and focuses on the surface reactions of uranium interacting with concrete and magnetite. The findings have implications for understanding the speciation and transport of uranium in subsurface environments and inform the discussions regarding the feasibility of in-situ disposal at nuclear sites.

1.2 Research objectives and approach

The aims of this research were to investigate the alteration of uranium, a key radionuclide contaminant, in the subsurface under environmental conditions, with a specific focus on speciation and transport in disposal scenarios. Interactions of uranium with the iron

(oxyhydr)oxide phase, magnetite, and concrete were studied in year-long outdoor field lysimeter experiments to gauge an understanding of speciation and compositional changes during environmental alteration. Previous research into the incorporation of U(V) into magnetite was built upon here, expanding upon the relevant literature (Pidchenko et al., 2017; Roberts et al., 2017) to investigate samples at the field scale under environmental conditions. Sellafield-representative concrete (supplied by industry) and sediment were also used in the investigation of subsurface uranium interactions with cementitious materials to increase understanding of how these materials influence the environmental behaviour of uranium. This builds on a wide array of scientific literature studying cementitious interactions with uranium (Gaona et al., 2012; Golovich et al., 2011; Harfouche et al., 2006; Macé et al., 2013; Moroni and Glasser, 1995; Sutton et al., 2003; Tits et al., 2015, 2011; Wieland et al., 2010; Zhang and Wang, 2017; Zhao et al., 2000).

The following research questions were highlighted based on gaps in current scientific knowledge:

- How does environmental exposure alter the speciation of U(V) when incorporated into magnetite?
- What is the impact of environmental alteration at the cement/subsurface interface on uranium mobility and speciation?

The project took a multidisciplinary approach and used a range of geochemical and spectroscopic techniques to analyse altered field lysimeter samples with sediment and concrete representative of the Sellafield and Savannah River nuclear sites. Techniques used to determine uranium speciation and behaviour included X-ray absorption spectroscopy (XAS), X-ray diffraction (XRD), X-ray fluorescence spectroscopy (XRF), inductively coupled plasma – mass spectrometry (ICP-MS), environmental scanning electron microscopy (ESEM), sequential extractions and acid digestions.

1.3 Thesis structure

This thesis is structured in a journal format and comprises this context and relevance chapter (Chapter 1), a discussion of the relevant literature (Chapter 2), details on experimental methodology (Chapter 3) and two research papers that have been prepared for publication. A summary chapter is also included drawing together conclusions from this research.

Chapter 2 covers a review of the literature and scientific knowledge relevant to this research including an overview of the geochemistry that underpins the work in this project and two contaminated land case studies of Sellafield, UK and Savannah River Site, USA, in addition to the environmental behaviour of U in contaminated land scenarios.

Chapter 3 provides details on experimental research methods and analytical techniques used in this project.

Chapter 4 presents the results of a novel field lysimeter experiment, investigating the environmental stability of U(V)-incorporated into magnetite combining a range of geochemical and synchrotron techniques to determine movement and/or alteration of U(V) in the system. The chapter is presented as a lead author manuscript and is to be submitted for publication in the journal, ACS Earth and Space Chemistry.

Contributions: *McNulty* was the principal author, and led all post-lysimeter lab work and data collection; *Powell* was involved in lysimeter design and concept development; *Bower* helped in the preparation and dismantling of the lysimeter experiment; *Fallon* assisted in experimental work (preparation and dismantling of lysimeter experiment, sediment digests, resin embedding, XRF, XAS)*;* *Peruski* assisted with lysimeter construction and effluent sample collection; *Coker* helped with XMCD data collection and analyses; *Warnicke* provided technical assistance (micro-focus XRF); *Abrahamsen-Mills* provided insight from an industry perspective; *Roberts* prepared the U-doped magnetite samples for the lysimeter experiment. *Morris*, *Shaw* and *Law* were involved in experimental design and assisted with conceptual development and extensive manuscript review.

Chapter 5 details an experimental investigation into three in situ disposal scenarios and the results of a year-long field lysimeter experiment. Using uranium sources mixed with sediment and concrete representative of Sellafield, UK, the work focusses on the behaviour and coordination environment of uranium in these systems and the effects of a high pH environment. The chapter is presented as a lead author manuscript and is to be submitted for publication in the journal, Environmental Science and Technology.

Contributions: *McNulty* was the principal author and was responsible for experimental design, led laboratory work and collected most of the data. *Powell* was involved in lysimeter design and concept development; *Bower* assisted in the lysimeter sectioning; *Peruski* assisted with lysimeter construction and effluent sample collection; *Rothe* and *Vitova* provided HR-XANES technical assistance; *Abrahamsen-Mills* provided modelling guidance; *Morris*, *Shaw* and *Law* were involved in experimental design and assisted with conceptual development and extensive manuscript review.

Chapter 6 provides a summary of key project findings and suggestions for future work in this area.

Blank page

Chapter 2 Literature Review

This literature review will present a brief summary of the nuclear fuel cycle and the resultant global legacy of contaminated land and facilities that exist as a result of nuclear fuel cycle operations over the last 75+ years. Relevant scientific literature will be reviewed to provide an overview of key uranium geochemistry, with a particular focus on the interactions of uranium with iron (oxyhydr)oxides and concrete phases. Case studies of contaminated land at Sellafield, UK and Savannah River Site, USA, are also included and discussed in the context of the thesis.

2.1 An Introduction to the Nuclear Fuel Cycle

In World War II, a nuclear arms race to produce plutonium for atomic weapons led to major global nuclear science development which continued throughout the Cold War. It was not until after the end of World War II that attention turned to harnessing atomic energy for civilian purposes, namely power generation, but also for use in the medical sector. The rapid growth and development of the nuclear industry, particularly with regards to weapons production, meant that many site facilities were not constructed with longevity or disposal in mind, sometimes resulting in leaks and now significantly ageing structures and facilities. The rush to produce nuclear materials in reactors also resulted in a huge amount of radioactive waste that was originally poorly contained and disposed of, with significant quantities of radioactively contaminated land arising as a result. Increasingly, there is a shift in focus towards the decommissioning and clean-up of nuclear sites around the world, with management of decommissioning wastes including contaminated land and structures, arising from legacy nuclear activity, being a key priority. The nuclear fuel cycle encompasses a range of industrial processes (Figure 2.1), from the mining and preparation of uranium to be used in reactors as fuel, to the management and disposal of radioactive wastes.
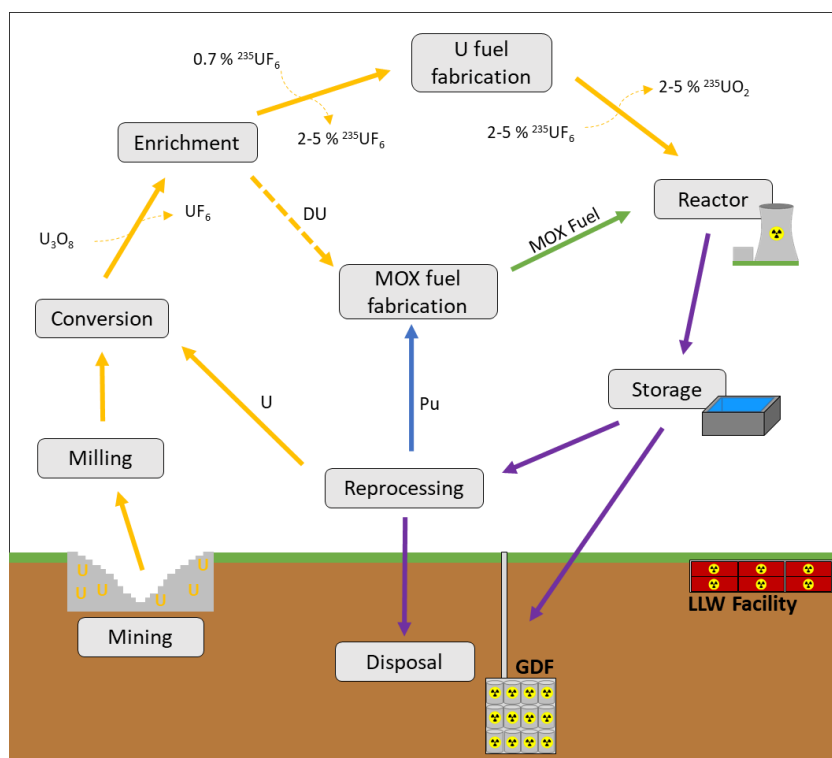
Figure 2.1: The nuclear fuel cycle, from mining to disposal. Adapted from Wilson, (1996).

Uranium is naturally present in the subsurface at levels of between 2-4 ppm, though in some regions the uranium concentration is high enough that it is economically viable enough to be

mined for the production of fuel, with Kazakhstan, Canada and Australia being the three largest producers, globally (NEA/IAEA, 2021). Currently, uranium is mined primarily via an in-situ leaching process, where slightly alkali or acidic leaching water is pumped through the subsurface to dissolve uranium from the enriched zone in the subsurface, which is then milled to produce uranium oxide concentrate, consisting mainly of U_3O_8, known as 'yellowcake' (Linsley, 2012). A by-product of the milling process is the production of uranium mill tailings, comprising crushed rock waste which retains high levels of radioactivity. These tailings are collected and generally stored or disposed at mine sites in slurry ponds or piles (IAEA, 2004). After milling, yellowcake is then shipped to the country of fuel fabrication and refined further to remove impurities and to convert U to uranium dioxide, UO_2 for further processing. As only 0.7 % of naturally occurring U is fissile [235]U (Wilson, 1996), the purified uranium must be enriched to 2.5-5 % [235]U to render it suitable for use in a reactor. At this stage, UO_2 is converted to uranium hexafluoride, UF_6, before enrichment. During enrichment, the UF_6 is separated by gas centrifugation, exploiting the 1% mass difference between the 235 and 238 isotopes of uranium (World Nuclear Association, 2020); here both enriched (>3.5 % [235]U) and depleted (<0.7 % [235]U) uranium are produced. The depleted uranium can be utilised in mixed-oxide (MOX) fuel, as fuel for fast breeder reactors (Simnad, 2003), or can be used in munitions (MoD, 2013), though some depleted uranium is also classed as waste (NDA and BEIS, 2019a). The enriched UF_6 (2.5 – 5 % [235]U) is re-converted to UO_2 to be formed into ceramic fuel pellets to be inserted into fuel rods during fuel fabrication. Those fuel rods are then deployed in the nuclear reactor core. Here, energy released from the controlled continuous fission of nuclear fuel in the reactor core in the form of heat is harnessed to generate electricity.

$$^{1}_{0}n + {}^{235}_{92}U \rightarrow {}^{236}_{92}U \rightarrow {}^{96}_{39}Y + {}^{137}_{53}I + 3\,{}^{1}_{0}n \qquad\qquad \text{(Eq. 2.1)}$$
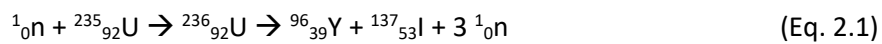
Fission is controlled through the use of neutron moderators which slow the release of neutrons so the probability of fission is higher, and control rods, which can absorb neutrons and slow or stop the reaction if required. These neutrons are absorbed via neutron capture by fissile atomic nuclei such as [235]U, leading to nuclear fission, producing large amounts of energy, additional neutrons and two or more fission products (De Sanctis et al., 2016a). An example can be seen in Equation 2.1. The release of further neutrons during fission initiates the controlled chain reaction which ultimately leads to the production of energy in the form of heat. Dependant on the reactor type (Table 2.1), gas or water coolants are circulated through the reactor to transfer heat from the core which is converted to electricity via steam generation which drives turbines to generate power. The specific fuel, coolant and moderators used vary with reactor design, with a wide range of reactors currently in operation. Table 2.1 provides details on the moderator and coolants used

in some of the more widely used reactors. The UK currently has 15 operational reactors for commercial electricity generation; 14 advanced gas reactors (AGRs), and one pressurised water reactor (PWR) at Sizewell B (IAEA, 2017). The two AGRs at EDF's Hunterston B site are set to cease operation and enter into decommissioning soon, whilst the legacy fleet of 26 Magnox reactors in the UK are currently in various stages of decommissioning.

Table 2.1: Popular reactor designs and the corresponding moderator and coolant used (Murray, 2000).

Reactor Design	Moderator	Coolant
Magnox	Graphite	CO_2
Pressurised water reactor (PWR)	Light water	Light water
Boiling water reactor (BWR)	Light water	Light water
Advanced-gas cooled reactor (AGR)	Graphite	CO_2
CANDU	Heavy water	Heavy water
RBMK	Graphite	Light water

Eventually, the fuel in a reactor can no longer sustain an efficient nuclear reaction as a result of ^{235}U depletion and the build-up of fission products. At this point, the fuel is classified as 'spent'. Spent fuel from power reactors typically comprises around 3% high activity waste, 1% plutonium generated from the neutron capture of ^{238}U and subsequent beta emission, and 96% uranium (De Sanctis et al., 2016b) and is intensely radioactive so must be carefully managed. Initially, the spent fuel is transferred and stored in cooling ponds, where water is used to both absorb radiation and cool the spent fuel, enabling the shorter-lived fission products to decay and reducing the radiological risk before the fuel is reprocessed or put into interim storage before disposal. Reprocessing is a means of recycling uranium and plutonium by separating them from other radionuclides and recovering any fissile material to reduce the waste arisings. In the UK, the PUREX method was exploited for the extraction of uranium and plutonium and involves the dissolution of the spent fuel in nitric acid and tri-butyl phosphate (TBP) followed by solvent extraction to yield uranium and plutonium. The extracted uranium can then be enriched and re-used as reactor fuel, or mixed with plutonium to create a MOX fuel, also for use in commercial reactors (IAEA, 2008). Spent fuel and wastes arising throughout the process are then disposed of depending upon the classification of waste. The combination of interim storage, cooling, reprocessing and disposal processes in the nuclear fuel cycle are often referred to as the 'back-end' of nuclear, but this also encompasses the decommissioning of nuclear facilities and sites which will itself produce high volumes of radioactive waste that requires management. The decommissioning of nuclear sites and the implications of the waste generated will be discussed further in later sections.

2.1.1 Radioactive Waste

A legacy of radioactive wastes have been produced as by-products of nuclear fuel cycle activities spanning the last 75+ years. These wastes encompass a range of materials, from operational wastes largely consisting of spent fuel, ion exchange resins and aqueous wastes from reprocessing and effluent treatment, to decommissioning wastes including contaminated land, structures, building materials and pipework (NDA and BEIS, 2019b). The development of management and disposal strategies for the wide array of wastes generated is crucial in ensuring the safety of the general public over the timescales relevant to radioactive waste. To aid with determining the best route for disposal, the International Atomic Energy Agency (IAEA) has classified radioactive waste into categories that are defined by the level of radioactivity and heat that the waste produces (IAEA, 2009). For the UK, the primary waste categories are very low level waste (VLLW), low level waste (LLW), intermediate level waste (ILW), and high level waste (HLW) and their categorisation criteria are given below in Table 2.2.

Table 2.2: Categories of waste classification and their criteria and disposal route in the UK (NDA and BEIS, 2019b)

Waste Category	Criteria	Typical Disposal Route
Very Low Level Waste (VLLW)	High volume: $< 4 \times 10^6$ Bq per tonne of total activity	Specified landfill
	Low volume: $< 4 \times 10^5$ Bq of total activity per 0.1 m³, or single items containing $< 4 \times 10^4$ Bq total activity	Municipal, commercial or industrial landfill
Low Level Waste (LLW)	$< 4 \times 10^9$ Bq per tonne of alpha $< 12 \times 10^9$ Bq per tonne of beta/gamma	LLWR (Drigg, Cumbria) Dounreay
Intermediate Level Waste (ILW)	Activity levels exceeding that of LLW, but does not generate significant heat	Cement encapsulation, then disposal in a GDF
High Level Waste (HLW)	Activity levels exceeding that of LLW and also generates heat	Vitrified into glass, then disposal in a GDF

For higher activity wastes, disposal in a geological disposal facility (GDF) is the preferred route both in England and Wales, and internationally (DECC, 2014; NDA, 2013). These facilities are intended to house both ILW and heat-generating HLW (ONR and Environment Agency, 2017). A small fraction of LLW containing some long-lived radioisotopes at significant concentrations may also require geological disposal (NDA and BEIS, 2019b). The GDF, which will be built between 200 m and 1000 m below surface in a suitable host rock (DECC, 2014), will utilise a multi-barrier system, where a range of both natural and engineered barriers will restrict the transport of radionuclides into the geosphere (RWM, 2016). The multi-barrier approach consists firstly of packaging waste into engineered containers. For ILW, encapsulation in cement is the preferred route, whilst for HLW, the waste must be vitrified into a borosilicate glass waste form which is

capable of withstanding the heat arising from the radioactivity (Nexia Solutions, 2007). The encapsulated or vitrified waste is then packaged into steel containers before transport to the GDF, where the containers will be backfilled using cements or other buffer materials such as bentonite clay (NDA, 2014a), which form the intermediary between the packages and the host rock. Currently, the UK is in the process of securing a site for a GDF, with the recent formation of two working groups in Copeland and Allerdale, in Cumbria, providing a step forward in the siting process (RWM, 2021).
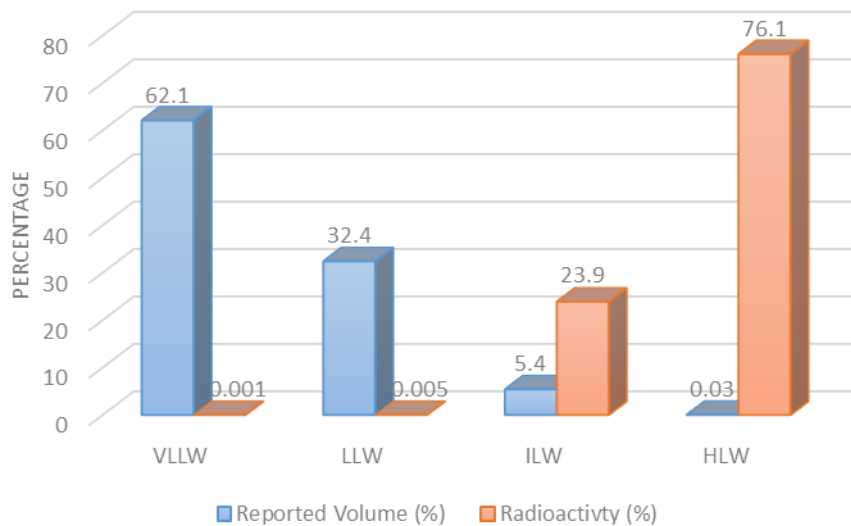
Figure 2.2: Comparison of UK waste inventory volumes and radioactivity by waste category (data sourced from NDA and BEIS, 2019b).

For lower activity wastes in the UK (VLLW and LLW), disposal in near-surface facilities such as the Low Level Waste Repository (LLWR) in Cumbria (DECC, 2016), or through alternative routes which for very low level wastes can include landfill (DECC, 2016; NDA and BEIS, 2019b), is typical. Though VLLW and LLW account for less than 0.01% of the total radioactivity present in UK wastes, they represent almost 95% of the volume (Figure 2.2) (NDA and BEIS, 2019b). The vast majority of the volume of VLLW and LLW reported is attributed to decommissioning and site clearance activities at Sellafield, with waste materials including concrete rubble (~90% of VLLW) and contaminated metals, which will be discussed in more detail in the next section.

As part of the NDA's integrated waste management strategy, they have implemented the waste management hierarchy (Figure 2.3), set out in the EU Waste Framework Directive (2008/98/EC),

into all areas of radioactive waste management in the UK and is applied to all wastes produced by the NDA estate (NDA, 2019).
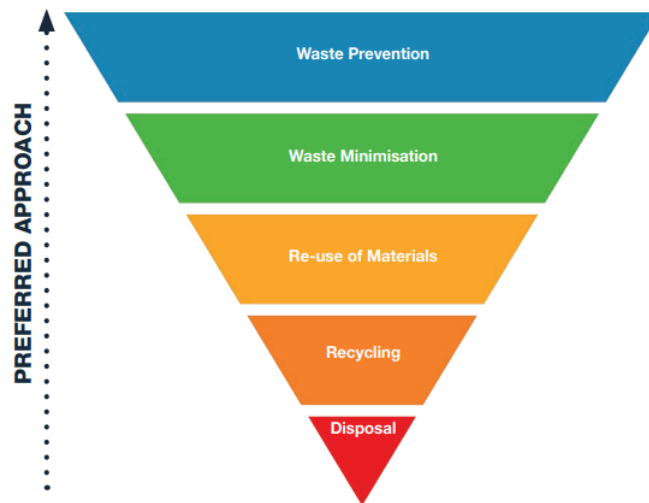
Figure 2.3: The waste management hierarchy applied to NDA assessments of radioactive waste (NDA, 2019)

Here, the hierarchy aims to promote the prevention of waste generation altogether, with beneficial re-use and recycling of materials preferred over disposal. Particularly for LLW, the application of the waste hierarchy is key to minimising the volumes of waste sent to the LLWR. This has been put into practice already through the National Waste Programme which has enabled the diversion of wastes traditionally sent to LLWR through treatment and alternative disposal methods (NDA and BEIS, 2019b).

2.2 The global legacy of radioactive contaminated land

Globally, nuclear activities including a range of permitted and accidental discharges of radionuclides to the subsurface over the last 75+ years have led to a legacy of contaminated land, groundwater, and subsurface structures at nuclear sites. Nuclear accidents including the Windscale fire (1957), Three Mile Island (1979), Chernobyl (1986) and most recently at the Fukushima Daiichi Nuclear Power Plant (2011) have contributed to significant releases of radionuclides into the environment (UNSCEAR, 2020, 1993, 1988). After the Fukushima accident, it was estimated that 10-20% of the total radionuclide releases were deposited over land, with dispersal of ^{137}Cs and ^{131}I up to 200 km away from the plant (Yoshida and Takahashi, 2012). Some of this contaminated land was remediated through removal of the topsoil which was collected and bagged (Evrard et al., 2019) (Figure 2.4) and has generated a total estimated 14 million m^3 of radioactive waste that is due to be disposed of in an interim storage facility (IAEA, 2019).

Figure 2.4: Contaminated topsoil collected from the areas surrounding the Fukushima Daiichi nuclear power plant and awaiting disposal (image taken from Evrard et al., 2019).

Uranium ore mining activities (Mihalík et al., 2011; Wang et al., 2014), nuclear weapons testing (Prăvălie, 2014) and the permitted discharge of radioactive effluents at nuclear sites have also led to the widespread release of radioactivity, globally. Notably, atmospheric testing of nuclear weapons from 1945 onwards contributed the largest effective dose to the global population from man-made radiation sources largely as a result of the release of ^{14}C, ^{137}Cs and ^{90}Sr (UNSCEAR, 1993), though local concentrations of radioactivity where weapons testing occurred are also a significant problem (Prăvălie, 2014). The radionuclides released from these, as well as those released in accidents and through authorised discharges of effluents from nuclear sites, typically accumulate in the oceans and can be deposited on land, where uptake into soils and plants is possible (UNSCEAR, 2020). At the Sellafield nuclear licenced site in the UK, authorised discharges of aqueous waste to the environment are permitted under environmental regulations and include levels of up to 2000 kg U/year (Environment Agency, 2020). Despite this, discharge levels are often significantly below the authorised limits, with 260 kg U reported as discharged in 2019 (Sellafield Ltd, 2020a).

Accidental releases of radionuclides at nuclear sites, mostly from leaks to the subsurface or historical disposal practices, have also led to the contamination of land and structures. At the Hanford US Department of Energy (DOE) site, Washington, significant releases of radioactivity to the environment have occurred including through the historical deposition of liquid waste in ponds and trenches on the site (Peterson et al., 2008; Um et al., 2007). These uranium-containing wastes leached into the surrounding areas resulting in significant contamination of the groundwater, with a reported 650,000 m^3 of contaminated groundwater above the drinking water standard (Peterson et al., 2008). Work on these contaminant plumes has shown uranium is

present in groundwater as mobile uranyl carbonate complexes and persists despite the removal of the original contaminant sources in the 1990s (Maher et al., 2013; Peterson et al., 2008). Leaks from storage tanks on the site are also an ongoing challenge, where 67 of Hanford's 149 single-shelled tanks containing liquid radioactive wastes generated during plutonium production, have been suspected of, or known to have leaked to the subsurface, with an estimated 4.5 million L of waste released (Triplett et al., 2013). Notably, a historic overflow from one tank (BX-102), contributed to the release of 7000 kg of uranium to the subsurface (Catalano et al., 2004; Um et al., 2010). ^{99}Tc is also a problem on the site, with one of the most significant leaks from tank T-106 in the 1970s having released ~1400 GBq of ^{99}Tc (Triplett et al., 2013). Other large DOE sites such as the Savannah River Site, South Carolina, also have significant levels of contamination as a result of legacy operations leading to contaminated soils, surface water and groundwater (Savannah River Site, 2020a). At the Sellafield site in the UK, historical practices and aging facilities have also resulted in radioactive contamination of land, groundwater and structures on-site. Typically, contamination is concentrated around the Separations Area on site, where reprocessing and storage of spent fuel occurs (Sellafield Ltd, 2020a). One of the most significant accidental releases of radioactivity to the subsurface is associated with leaks from the Magnox Swarf Storage Silo (MSSS) (Kuras et al., 2016), a legacy facility that has been used to store irradiated Magnox fuel cladding (swarf) and other wastes underwater since the 1960s. This along with legacy disposal practices, including disposal of low-level radioactive wastes to trenches and the subsurface, have resulted in plumes of radioactivity in the subsurface extending out towards the Irish Sea (Sellafield Ltd., 2016). Indeed, the estimated total volume of contaminated land on site at Sellafield is ~6,000,000 m^3, largely consisting of high volume VLLW, whilst the volume of contaminated foundations and subsurface structures is ~235,000 m^3, mostly classified as high-volume VLLW, but with some areas of LLW and ILW (NDA and BEIS, 2019c). Other accidental releases of radionuclides at nuclear sites have been well documented and indicate radionuclide contamination is significant at some nuclear sites, globally (IAEA, 1996; Riley and Zachara, 1992; US NRC, 2018).

This on-site contamination of land also extends to the structures radioactivity comes into contact with and is contained within, with contamination of reactor vessels, reprocessing facilities, cooling ponds, storage facilities, made ground beneath sites and various equipment prevalent across nuclear sites. As the focus of many sites starts to move towards decommissioning, this complex mix of contaminated materials must be fully understood and characterised to enable safe and efficient dismantling and decommissioning.

2.3 Nuclear Site Decommissioning

The decommissioning of nuclear sites, which occurs when a site reaches the end of its useful life, is a complex and lengthy process and involves a wide range of activities to ultimately enable de-designation and reuse of the land. The fully decommissioned and remediated state of any nuclear site in the UK is known as the 'site end state' (Figure 2.5) which can vary between sites.
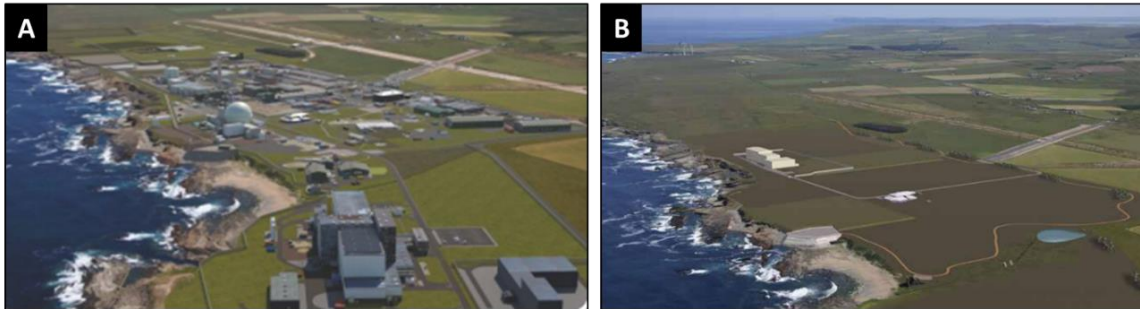
Figure 2.5: Artist's impression of the Dounreay site, Scotland as it is now (A) and in its site end state (B) (Dounreay, 2021)

Decommissioning activities encompass the defueling of reactors, decontamination of site facilities, dismantling of structures and the demolition of buildings on site as well as any remediation of remaining ground or groundwater contamination and landscaping work (Figure 2.6) (NDA, 2021). Combined, these processes are estimated to take around 100 years in total, with the current predicted date for end of decommissioning for the Magnox reactors in the UK set for 2125 (NDA, 2021).
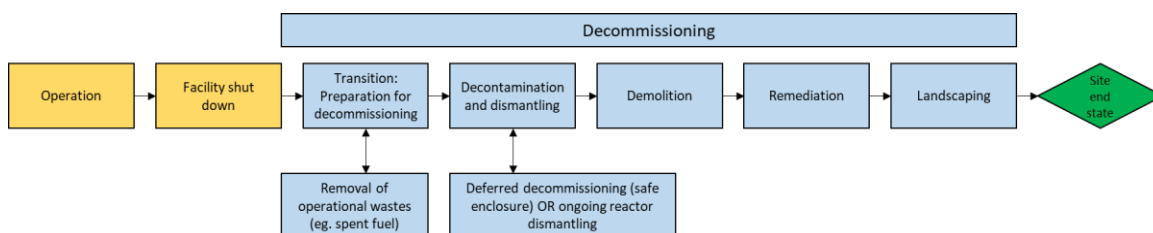
Figure 2.6: Diagram outlining the high-level decommissioning processes involved prior to reaching a site end state (adapted from NDA, 2014b).

The decommissioning of nuclear sites and the various structures within is expected to produce high volumes of radioactive wastes that need to be managed safely and ultimately disposed of (NDA and BEIS, 2019b). Similar to spent nuclear fuel, wastes categorised as higher activity will be treated, packaged and sent to interim storage before final disposal in a GDF. Typically, defueling of reactors occurs soon after the reactor shutdown and the transfer of this HLW off site generally corresponds to a reduction of 99% of the radioactivity associated with a site (NDA, 2014b).

However, a much larger volume of VLLW and LLW is expected to be produced as a result of decommissioning activities. In the latest radioactive waste inventory, the NDA predicted the total future volumes of LLW and VLLW that are due to arise up to the end of all decommissioning activities to be 1,450,000 m^3 and 2,830,000 m^3, respectively (NDA and BEIS, 2019b). For the latter, approximately 98% is related to the volume of VLLW waste that will be produced as a result of decommissioning work at the Sellafield site. With finite storage capacity at facilities such as LLWR in Cumbria, alternative disposal strategies and routes for this waste must be considered.

In the UK, the legacy Magnox fleet of reactors are currently all in the decommissioning stage, with defueling at the most recently operational site, Wylfa, now complete (Magnox Ltd et al., 2019). Recently, there has been a marked change in the strategy used to decommission the Magnox reactor sites in the UK. Previously, and developed over 30 years ago, a deferred reactor decommissioning strategy for all Magnox reactors was in place; where sites would be placed in an interim state 'Care and Maintenance' for ~85 years before final reactor decommissioning (NDA, 2014b). This strategy was at odds with the decommissioning of similar graphite reactors in France, where the regulatory authority promotes accelerated decommissioning of sites (Wealer et al., 2019). Recently, and building on experience from deferred decommissioning at the Bradwell site, the NDA has moved towards optimising site end states with a focus on amending regulatory frameworks that will allow for risk-informed and proportionate solutions for nuclear sites (NDA, 2021). This will involve considering site specific decommissioning strategies, where decommissioning will largely take place as quickly as possible, thereby potentially reducing the overall timeframes for site clearance. For the Magnox reactors, Trawsfynydd has been chosen as the 'lead and learn' site for ongoing reactor decommissioning, largely due to its degrading structure. For other sites, individual strategies will be considered and in some cases, deferred decommissioning will remain the preferred route (NDA, 2021). Recently, it was also announced that EDF's current fleet of AGR stations will also transfer to the NDA upon completion of defueling (BEIS, 2021), and, with several sites due to stop generation over the next few years, the change in strategy will also likely be reflected in the decommissioning plans for these sites too. This change in NDA decommissioning strategy came with the publication of the Guidance on Requirements for Release from Radioactive Substances Regulation (GRR) (SEPA, Environment Agency and Natural Resources Wales, 2018) by the environment agencies, which outlines how sites can be released from regulation through various radioactive waste management approaches. One such approach to optimising the site end states is 'in-situ disposal' which will be discussed in further detail in the next section.

2.3.1 In-situ disposal

The concept of in-situ disposal potentially provides a pathway for radioactive waste that has the potential to drastically reduce the costs of disposal, whilst also having environmentally beneficial effects in the form of reduced CO_2 emissions from the transportation of waste to more traditional permanent disposal sites. '*In-situ* disposal' in the context of decommissioning nuclear sites can be defined as the permitted and permanent emplacement of radioactive waste on a nuclear site with the intention of no further work or remediation, however monitoring may take place in this situation for reassurance or technical purposes (Office for Nuclear Regulation et al., 2016). This is in contrast to ex-situ disposal, where wastes would be subject to "dig and dump" practices with inferred movement of wastes to a bespoke facility, such as the LLWR. It is also different to in-situ decay storage; an interim disposal solution for ILW, used as a strategy for decommissioning structures including pressure vessels and reactor vessels. These structures are left in place until site clearance towards the end of the decommissioning process, allowing for the decay of radioactivity (ONR and Environment Agency, 2017). In some cases, shorter-lived radionuclides including ^{137}Cs and ^{90}Sr will have decayed to background levels and, as such, will vastly reduce the radiological hazard associated with the site. Despite this, there have been historical cases of, and studies into, the permanent on-site disposal of such vessels (IAEA, 1999).

In the UK, in-situ disposal is a principal detailed in the recently published GRR, which provides guidance on how best for sites to manage and optimise wastes arising from decommissioning activities at nuclear facilities and attain release from regulations (SEPA, Environment Agency and Natural Resources Wales, 2018). Here, the GRR outlines a range of generic scenarios where in-situ disposal might be appropriate, with certain conditions also in place, where sites will be required to produce a site-wide environmental safety case and recognise how much radioactivity will remain onsite on completion of all radioactive practices. This includes any previous authorised disposals and any residual contamination from site processes, ensuring the risk of leaving radioactivity on site and thus, any potential exposure to ionising radiation from the general public remains as low as reasonably achievable (ALARA) (SEPA, Environment Agency and Natural Resources Wales, 2018). These potential pathways for in-situ disposal on sites are illustrated in Figure 2.7 and include the following:

- leaving contaminated land (a) or waste (b) in situ, with (c) or without engineered barriers
- leaving contaminated structures in situ (d) (e.g. subsurface pond or other buried structure)
- re-use and disposal of (un)contaminated materials for filling an existing structure that may or not be contaminated itself (d)

- re-use and disposal of (un)contaminated materials for void filling (e)
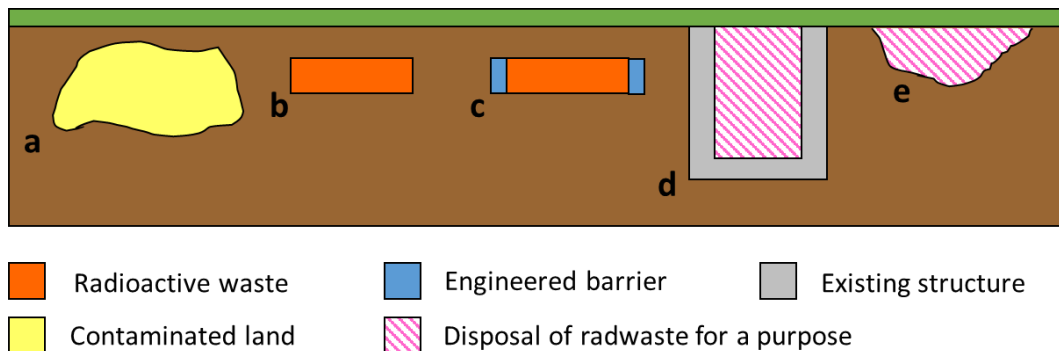
Figure 2.7: Illustration of in situ disposal options for radioactive waste on a nuclear site. Alphanumeric labels relate to text above (adapted from SEPA et al. (2018))

By emplacing wastes on site and leaving contaminated structures in situ, in-situ disposal also aligns with the waste management hierarchy (Figure 2.3) by avoiding disposal of contaminated land and materials at facilities with finite capacity, such as the LLWR. Re-use of out of scope or low-level contaminated materials such as concrete rubble from demolition ensures a reduction in the volume of waste disposed of off-site, whilst also helping nuclear sites to reduce the cost of void or structure filling by having to use alternative materials. Unlike LLW disposal such as that at LLWR, in-situ disposal also eliminates the need to solidify waste into containment packages and the waste can instead all be handled on site, reducing potential exposure to radiation for waste management personnel (IAEA, 1997). This also extends to legacy contaminated land, which, if radioactivity levels are low enough, may be left in-situ without disturbance or, engineered barriers could also be used to permanently cover these areas. Enhancement of sites used for in-situ disposal is also an option to further protect the surrounding environment and limit the exposure of radionuclides whereby secondary containment could protect the waste from flooding, severe weather and other natural or anthropogenic intrusion. Layers of natural materials including rock, soil, sand and clay can also be used as surface covering (IAEA, 1999). Eventually, sites that dispose of waste in this way will be released from Radioactive Substances Regulation, leaving the sites eligible for unrestricted use (SEPA, Environment Agency and Natural Resources Wales, 2018).

In-situ disposal in the UK is a new waste management strategy, with some Magnox sites having already started to implement this approach. In particular, the site end state for Winfrith was very recently revised to allow below-ground structures from the two reactor sites to be left in place (NDA, 2021). Similarly, at Trawsfynydd, the in-situ disposal of lightly contaminated subsurface pond structures and reactor bioshields has been proposed in the revised site end state assumptions and includes the reuse of concrete from on-site demolition activities to fill

subsurface voids (NDA, 2021). To progress with these works, site licence companies will need to produce fully underpinned site-wide environmental safety cases with justification for waste management plans if in-situ disposal is to be successfully implemented (SEPA, Environment Agency and Natural Resources Wales, 2018). To do this, the interactions between radionuclides, contaminated land, structures and any other materials that radionuclides may encounter in the subsurface need to be properly understood and predicted. At the same time as the technical understanding is developed, there is also a need to build on experiences from 'lead and learn' sites such as Winfrith and Trawsfynydd to inform strategy, whilst also engaging with relevant stakeholders. The next section of this chapter will review radionuclide interactions with contaminated land, and relevant engineered and natural subsurface components with a focus on literature relevant to the work produced as part of this thesis.

2.4 Contaminated land geochemistry

In this section, the geochemistry of uranium, the radionuclide of interest in this thesis, iron (oxyhydr)oxides and cementitious materials will be reviewed within the context of the work undertaken.

2.4.1 Uranium geochemistry

Uranium is typically the most substantial radionuclide by mass in many contaminated land scenarios and in low level radioactive wastes. ^{238}U is the most abundant isotope of uranium with a half-life of 4.5 x 10^9 years (Craft et al., 2004). This very long half-life means uranium will persist in the environment for extensive timescales and, considering its toxicity, highlights the importance of understanding the long-term mobility and behaviour of uranium in subsurface environments.

The transport of uranium in the environment is typically controlled by its oxidation state and speciation. Generally, the U(IV) and U(VI) oxidation states are prevalent in natural environments, with recent work also suggesting U(V) is stable in environmental systems (Pidchenko et al., 2017; Roberts et al., 2017; Vettese et al., 2020). For U(VI), the uranyl ion (UO_2^{2+}), dominates in oxic, circumneutral conditions, dependent on the presence of carbonate (Newsome et al., 2014). The uranyl ion, which is characterised by two linear formally triply-bonded axial oxygen atoms at a distance of ~1.82 Å (Catalano and Brown, 2004), is highly soluble and therefore contributes to the mobility of uranium in the environment. In solution above pH ~4, the hydrolysis of the uranyl moiety leads to uranyl hydroxide complexes which compete with ligands in solution (Figure 2.8), including carbonate and silicate (Maher et al., 2013). Alternatively, uranate species can also form

under environmental conditions, with the formation of solubility limiting U(VI) metal uranates (eg. $CaUO_4$) reported at high pH (Bots et al., 2014; Ding et al., 2016; Macé et al., 2013) and is characterised by an elongation in the U-O axial bond length relative to uranyl species (King, 2002). Octahedrally coordinated U(V) uranates have also been shown to form upon incorporation into iron (oxyhydr)oxides (Ilton et al., 2012; Kerisit et al., 2016; Roberts et al., 2017).

In reducing environments, typically U(IV) dominates, generally as uraninite (UO_2), which is sparingly soluble (Ilton et al., 2010) and so transport of uranium is limited under these conditions (Choppin et al., 2002), though the formation of mobile U(IV) colloids has been reported (Kaminski et al., 2005; Neill et al., 2019; Wang et al., 2013; Zänker and Hennig, 2014).
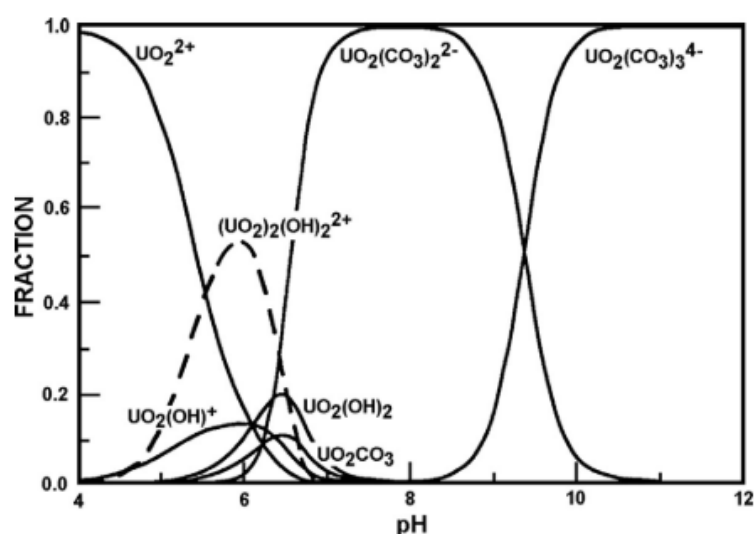
Figure 2.8: Aqueous uranium speciation in oxic, atmospheric CO_2 conditions across a range of pH values (Choppin et al., 2002).

In sediments, the transport of U(VI) at circumneutral pH can be limited through biogenic reduction to U(IV) (Anderson et al., 2003; Law et al., 2011; Lovley et al., 1991; Newsome et al., 2014; Wilkins et al., 2006), sorption to organic matter (Cumberland et al., 2016), clays (Akçay, 1998; Catalano and Brown, 2005; Maher et al., 2013; Tournassat et al., 2018) and to iron- (Bargar et al., 2000; Crawford et al., 2017; Hsi and Langmuir, 1985; Sherman et al., 2008; Um et al., 2008) and manganese oxide minerals (Wang et al., 2013). The solubility of uranium in the subsurface can also be controlled by the precipitation of solid phases or formation of secondary alteration products including uranyl oxide hydrates such as schoepite and metaschoepite (Finch and Ewing, 1992; Maher et al., 2013). Metaschoepite, which can form via the oxidation of uraninite, UO_2, present at many nuclear sites, (Finch and Ewing, 1992; Wronkiewicz et al., 1996) can be altered over time, forming common uranyl oxides such as schoepite and, in the presence of Ca, becquerelite, and later forming more stable uranyl silicates and phosphates (Maher et al., 2013;

Sowder et al., 2001). In addition to the weathering or corrosion of particulate UO_2, elevated uranium concentrations in solution have also been shown to induce the precipitation of mineral phases such as schoepite (Allen et al., 1996; Duff et al., 2002; Giammar and Hering, 2001), with the formation of these precipitates typically controlling the solubility of uranium (Gorman-Lewis et al., 2008). In uranium-Cu(II) contaminated sediments beneath now dry waste process ponds at the Hanford site, USA, Catalano et al. (2006) investigated the speciation of uranium with depth. They found uranium was coprecipitated with calcite in near surface sediments as a result of neutralisation of the ponds, in the vadose zone, the migration of U, Cu and P from wastes enabled the precipitation of metatorbernite ($Cu(UO_2PO_4)_2.8H_2O$), whilst at greater depth, uranium was found to be sorbed to phyllosilicates (Catalano et al., 2006). In a different area of the site however, the U(VI) uranyl silicate sodium boltwoodite ($Na(UO_2)(SiO_3OH).1.5H_2O$), part of the uranophane group of minerals, was formed.

In the context of the long-term stability of uranium in subsurface environments, the behaviour of uranium at natural reactor sites, such as that in Oklo, Gabon, has been studied in depth as it provides insight into uranium migration in sediments and groundwater over long timescales. In the case of the Oklo natural reactors, Bangombé (11 m depth) and Okelobondo (450 m depth), analogues for shallow subsurface and geological disposal, respectively, the uranium deposits went critical 2 billion years ago (Gurban et al., 2003). In both cases, the local subsurface geology controls the mobility of uranium, where the estimated maximum migration of uranium (axial plume lengths) are 0.25 km and 1.3 km for Bangombé and Okelobondo, respectively (Jove Colon et al., 2001). For Bangombé, sorption of uranium to aluminosilicates and iron minerals has been reported, with pore water chemistry controlled by $Fe^{2+}/Fe(OH)_3$ equilibria, protecting the uraninite in the deposits from oxidative dissolution (Ayora et al., 1998).

The immobilisation of uranium through adsorption to subsurface components or precipitation are extremely sensitive to the presence of carbonate (Um et al., 2007; Zhou and Gu, 2005) which has been shown to drastically reduce the uptake of uranium to many subsurface minerals across a range of pH values. This is as a result of the formation of highly mobile, stable uranyl carbonate complexes such as $UO_2(CO_3)_3^{4-}$ and $UO_2(CO_3)_2^{2-}$ (Bernhard et al., 2001), thereby contributing to the transport of uranium in the subsurface (Figure 2.8) (Clark et al., 1995). Elevated carbonate concentrations can also lead to enhanced dissolution of precipitated uranyl minerals including uranyl (oxyhydr)oxides, that typically control the solubility of uranium in natural environments (Stanley and Wilkin, 2019). The presence of calcium in carbonate-containing systems has also been shown to negatively influence sorption (Bernhard et al., 2001; Zheng et al., 2003). Zheng et al (2003) looked at soils from two different nuclear sites and found that uranium sorption to components was typically highly pH dependent, with maximum sorption occurring in the near-

neutral pH range for soils low in carbonate. In contrast, the formation of the $Ca_2UO_2(CO_3)_3$ complex was shown to hinder U(VI) sorption in the soil profile with a higher calcium carbonate content, particularly at weakly alkaline pH values, with sorption at more acidic pH values shown to be similar in both soils irrespective of carbonate content. Indeed, a study of uranium-contaminated alkaline Hanford sediments found that the presence of Ca^{2+} and carbonate promoted the desorption of uranium (Catalano et al., 2006).

As previously alluded to, pH has a marked effect on the speciation of uranium in environmental systems (Crawford et al., 2017). Above pH 9, U(VI) adsorption to mineral surfaces has been shown to decrease as a result of the formation of stable anionic uranyl carbonate complexes, which do not adsorb to mineral surfaces to the same extent as cationic species at lower pH (Kaplan et al., 1998). In the same study above pH 10.3 however, U(VI) co-precipitated with a calcium carbonate phase was predicted to have formed. Allen et al. (1996) investigated the effects of pH at ambient temperature on the structures of U(VI) precipitates in oversaturated solutions using EXAFS. At pH 7, a schoepite-like phase was precipitated from solution, however when the pH was increased to 11, the structure changed significantly and was attributed to the formation of a poorly soluble hydrated uranate, such as $Na_2U_2O_7$. This was characterised by an elongation in the U-O axial bond length from 1.80 Å at pH 7, to 1.86 Å in the pH 11 sample, and a simultaneous reduction in the average equatorial bond lengths. Solubility studies of the same oversaturated uranate phase at high pH and under a range of carbonate concentrations showed that $Na_2U_2O_7$ is the solubility limiting phase (Altmaier et al., 2017; Sutton et al., 1999) and that U(VI) solubility decreases over time attributed to increased crystallinity of the uranate phase (Yamamura et al., 1998). In Ca-rich and elevated pH systems, such as those expected in cementitious environments, calcium uranates are predicted to be the solubility limiting phases (Bots et al., 2014; Moroni and Glasser, 1995; Smith et al., 2015; Sutton et al., 1999; Tits et al., 2011, 2008; Tits and Wieland, 2018) and will be discussed in more detail in a later section (2.4.5).

Typically, U(V) has been considered unstable and readily disproportionates to U(IV) and U(VI) under ambient environmental conditions (Heal and Thomas, 1949). More recently, it has been shown to be an important intermediate in both microbiological (Renshaw et al., 2005; Vettese et al., 2020) and photochemical (Cowie et al., 2019) reduction of U(VI), and has also been shown to be stabilised on the surface of magnetite nanoparticles (Pan et al., 2020) in anoxic conditions. Indeed, a body of literature is developing that highlights U(V) as an environmentally relevant oxidation state of uranium by stabilisation through incorporation into iron (oxyhydr)oxide minerals including goethite and magnetite (Kerisit et al., 2016; Pidchenko et al., 2017; Roberts et al., 2017). In these systems, U(V) is the dominant oxidation state, stabilised in a distorted and uranate-like coordination through substitution with octahedrally coordinated Fe(III). One-

electron reduction of U(VI) by Fe^{2+} in solution at circumneutral pH (Collins and Rosso, 2017) and the biogenic one-electron reduction of U(VI) to U(V) using *Geobacter sulfurreducens* (Jones et al., 2015; Renshaw et al., 2005) and *Shewanella oneidensis* (Vettese et al., 2020) have also shown U(V) to be an environmentally relevant intermediate over weeks to months. Clearly the stabilisation of U(V) into iron (oxyhydr)oxide minerals has apparent implications for the environmental fate of uranium and will be discussed in further detail in the next section (2.4.2).

2.4.2 Iron (oxyhydr)oxide geochemistry

Iron (oxyhydr)oxides, containing Fe and O or OH, are ubiquitous at nuclear sites, occurring naturally in soils and sediments, in engineered forms and as corrosion products. In the environment, iron (oxyhydr)oxides are the most abundant of the metal oxides present in sediments (Schwertmann and Taylor, 1989) and are formed through the alteration or weathering of igneous and metamorphic rocks and other mineral phases, thereby releasing Fe(II) and Fe(III) ions into solution. The formation of a range of different iron (oxyhydr)oxides is then dependent on the environmental conditions, where weathering can contribute to the continual transformation in natural environments by dissolution of $Fe(II)_{(aq)}$ and subsequent oxidative re-precipitation (Cornell and Schwertmann, 2003a). In oxic conditions, the $Fe(III)_{(aq)}$ ion dominates at low pH (pH < 3), with spontaneous hydrolysis at pH values above this to form secondary Fe (oxyhydr)oxides (Bigham et al., 2002). In contrast, $Fe(II)_{(aq)}$ is oxidised to Fe(III) in circumneutral pH conditions, typical of the oxic near-subsurface. Under anoxic conditions, however, dissolved Fe(II) dominates and is strongly dependent on both pH and redox chemistry, forming a range of Fe(II) and mixed Fe(II)/(III) phases (Langmuir, 1997). The pH dependence of iron (oxyhydr)oxide speciation in aqueous conditions is considered to sum to a total and can be expressed as a mole fraction (Figure 2.9). Fe(III) (ferric iron) species dominate over a wider pH range than Fe(II) (ferrous iron) species, with Fe(II) becoming more relevant at higher pH (pH > 8), typical of subsurface alkaline altered zones surrounding buried concrete structures.
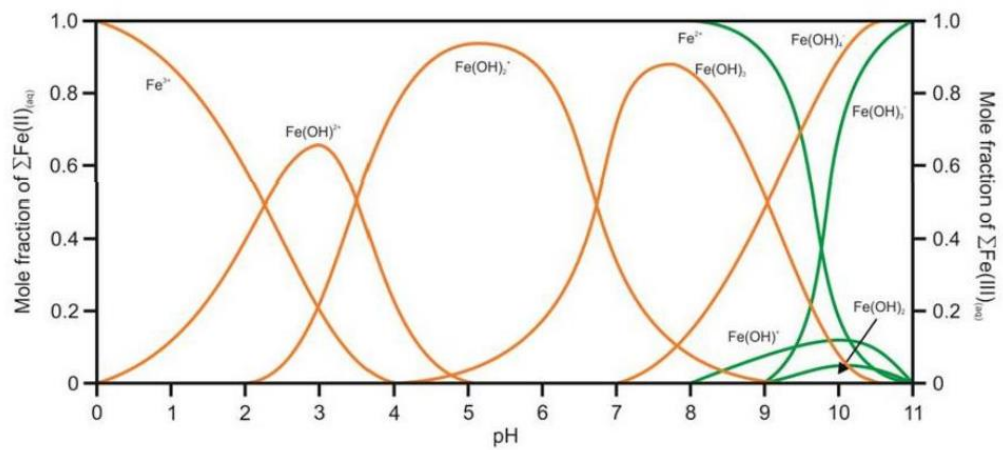
Figure 2.9: Aqueous Fe(II) (green) and Fe(III) (orange) speciation of pure water at 25 °C across a range of pH values (adapted from Langmuir (1997) and sourced from (Roberts, 2017)).

Iron(III) (oxyhydr)oxides are generally very stable, with low solubility at circumneutral pH, due to the formation of strong inner sphere complexes, typically with OH^- ligands; however minerals containing Fe(II) are generally more unstable, where aerobic conditions, such as those that might be expected in near surface oxic sediments, can promote the oxidation of structural Fe(II) to Fe(III) thereby weakening the structure through charge imbalance (Bigham et al., 2002; Schwertmann, 1991) and promoting the re-precipitation of Fe(III) minerals.

Iron (oxyhydr)oxides are also relevant in engineered environments, particularly at nuclear sites where a large array of pipelines, steel structures and structural steel reinforcing bar used in concrete (rebar) are widely used. Steel, containing zero valent iron is subject to electrochemical corrosion when exposed to environmental conditions (Crossland, 2011). In the presence of both oxygen and water, iron will corrode over time to form a range of different iron (oxyhydr)oxides. Iron corrodes via a series of anodic and cathodic reactions at the zero valent iron surface. These reactions are summarised in Equations 2.2-2.4, below. At the anode, Fe^0 is oxidised to Fe^{2+}, releasing electrons that migrate to the cathode region, where oxygen is subsequently reduced OH^-.

$$Fe \rightarrow Fe^{2+} + 2\ e^- \qquad\qquad (Eq.\ 2.2)$$

$$O_2 + 4H^+ + 4e^- \rightarrow 2H_2O \qquad\qquad (Eq.\ 2.3)$$

$$O_2 + 2H_2O + 4\ e^- \rightarrow 4\ OH^- \qquad\qquad (Eq.\ 2.4)$$
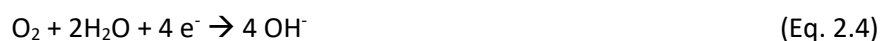
Oxidation of the Fe^{2+} to Fe^{3+} in solution followed by the subsequent reaction of Fe^{3+} with hydroxide produced at the cathode generates hydrated ferric oxide ($Fe_2O_3.xH_2O$) ("rust") (Deacon and Hudson, 2012) over time, but other products including ferrous and ferric hydroxide are also formed through reaction of Fe^{2+} and Fe^{3+} respectively with hydroxide ions. In conditions with

limited concentrations of dissolved oxygen, oxidation of Fe^{2+} to Fe^{3+} is limited and so formation of Fe(II)- and Fe(II)/Fe(III) containing minerals including lepidocrocite (γ-FeO(OH)), magnetite ($Fe(II)Fe(III)_2O_4$) and green rust ($[Fe(II)_3Fe(III)(OH)_8]^+[Cl,nH_2O]^-$) is common (Cornell and Schwertmann, 2003b; Dodge et al., 2002; Lagha et al., 2007; McGill et al., 1976).

Buried pipelines and in-situ steel structures at nuclear sites may have radionuclide contamination associated with them or, land and groundwater surrounding those structures may be contaminated with radionuclides (Environment Agency and Natural Resources Wales, 2010). As such, understanding the interactions between a range of radionuclides and iron (oxyhydr)oxides formed during the corrosion of steel structures on sites is important in underpinning site safety cases and decommissioning strategies where these structures may potentially be left in situ. Furthermore, naturally occurring iron (oxyhydr)oxides are also present in the soils and sediments at nuclear sites and so where land is contaminated with radionuclides, these interactions need to be understood.

2.4.2.1 Magnetite

Magnetite is an environmentally relevant iron (oxyhydr)oxide with the formula Fe_3O_4 and is the focus of the work described in Chapter 4 of this thesis because of its importance in engineered and natural environments. Under anaerobic, alkaline conditions, magnetite can precipitate from Fe(II) and Fe(III) in solution (Petcharoen and Sirivat, 2012) by the equations described below (Equations 2.5-2.7).

$$Fe^{2+} + 2OH^- \rightarrow Fe(OH)_2 \qquad\qquad\qquad \text{(Eq. 2.5)}$$

$$Fe^{3+} + 3OH^- \rightarrow Fe(OH)_3 \qquad\qquad\qquad \text{(Eq. 2.6)}$$

$$Fe(OH)_2 + 2Fe(OH)_3 \rightarrow Fe_3O_4 + 4H_2O \qquad\qquad\qquad \text{(Eq. 2.7)}$$
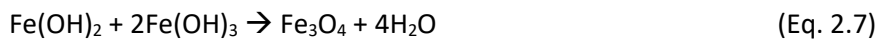
Magnetite can also be formed through the oxidation of green rust or $Fe(OH)_2$ (Cornell and Schwertmann, 2003c), the interaction of ferrihydrite with Fe^{2+} (Cornell and Schwertmann, 2003c; Marshall et al., 2015) or through high temperature reduction of Fe(III) (oxyhydr)oxides. In engineered scenarios, magnetite is a key product from the corrosion of steel under anoxic conditions (Dodge et al., 2002; Duro et al., 2014; Lagha et al., 2007) which is particularly relevant to geological disposal of radioactive waste, where steel storage canisters will be used to encapsulate waste, or in the near-surface or in-situ disposal of buried steel structures at nuclear sites.

Magnetite is a mixed-valence Fe(II) and Fe(III) bearing iron (oxyhydr)oxide with an inverse spinel structure and a face centred cubic unit cell (Cornell and Schwertmann, 2003d). To account for the

mixed valency, the formula can be written as $Fe(III)[Fe(II),Fe(III)]O_4$, where the oxygen atoms are arranged in a cubic close packed structure along the [111] plane and iron occupies the interstitial tetrahedral and octahedral sites (Figure 2.10) (Cornell and Schwertmann, 2003d). Here, the Fe(III) occupies tetrahedral sites, and the square brackets denote octahedral sites, where the remainder of Fe(III) and the Fe(II) reside (Fleet, 1981). The oxygen framework is flexible and so can expand to accommodate a range of other cations that can fully or partially substitute for structural Fe(II) or Fe(III) (Cornell and Schwertmann, 2003d). Due to the similarity in size, transition metal cations including Mn(II), Zn(II), Ti(IV), Co(II) and Ni(II) have been reported to readily substitute for Fe(II) and Fe(III) in magnetite (Bliem et al., 2015; Pearce et al., 2006), with changes in the unit cell dimensions as a result.
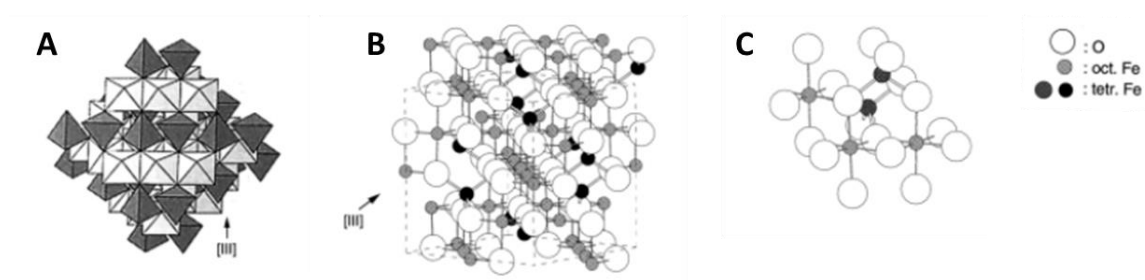
Figure 2.10: Diagrams depicting the structure of magnetite taken from Cornell and Schwertmann (2003d). (A) Tetrahedral and octahedral polyhedral model; (B) Ball-and-stick model with the unit cell highlighted; (C) Local octahedral and tetrahedral structure (ball-and-stick model).

In oxic, subsurface environments at ambient temperature, magnetite particles have been shown to oxidise to maghemite (γ-Fe_2O_3) (He and Traina, 2007; Swaddle and Oltmann, 1980; Taylor and Schwertmann, 1974) via the outward migration of Fe(II), which oxidises to Fe(III), forming a rind of maghemite on the surface (Gorski and Scherer, 2010; Sidhu et al., 1977). Magnetite particle size has been shown to have an effect on the oxidation rate, with the oxidation of finer-grained magnetite, such as the nanoparticulate magnetite used in this thesis, occurring at a higher rate (Swaddle and Oltmann, 1980). Though the exact mechanism of magnetite oxidation is not defined, Sidhu et al. (1977) demonstrated the decrease in Fe^{2+} concentration from the centre to the surface of oxidised particles was suggestive of Fe migration, rather than oxygen diffusion into the structure, which is unlikely due to the large crystal radius (1.40 Å). Additionally, goethite has also been seen to be an oxidation product of magnetite via the formation of a maghemite intermediate (Blesa and Matijević, 1989; He and Traina, 2007; Kiyama, 1974; Marshall et al., 2014b). Here oxidation proceeds through the dissolution of maghemite to form ferric hydroxo complexes which hydrolyse to form goethite (Blesa and Matijević, 1989; He and Traina, 2007; Kiyama, 1974).

Magnetite has also been widely reported to interact with uranium and other radionuclides and this is discussed in the next section.

2.4.3 Radionuclide interactions with iron (oxyhydr)oxides

Radionuclide interactions with iron (oxyhydr)oxides are well documented in the literature with adsorption, precipitation and incorporation of radionuclides reported. Understanding these interactions is of the utmost importance in developing strategies for disposal of radioactively contaminated land and structures, where the presence of iron (oxyhydr)oxides can impact on the mobility of radionuclides. Here, sorption and incorporation of radionuclides will be discussed in the context of this work.

2.4.3.1 Adsorption

Adsorption describes the uptake of ions or molecules from solution by solid mineral surfaces, such as iron (oxyhydr)oxide phases, to create inner sphere or outer sphere complexes on the surface (Figure 2.11) (Stumm and Morgan, 1995). Outer sphere complexes arise from weak electrostatic interactions between the solute and the mineral surface, where waters of hydration present between the surface and the solute limit the binding capacity. Conversely, for many iron (oxyhydr)oxide phases in solution, hydroxyl functional groups present on the surface act as electron donors (denoted by the arrows in Figure 2.11) that can form complexes with metal ions such as radionuclides; these complexes are known as 'inner-sphere'. For radionuclides present in solution, inner-sphere adsorption to iron mineral surfaces present in subsurface sediments and in engineered structures can therefore be a means to control the transport of contaminants and sequester them from solution. As such iron (oxyhydr)oxides have been implemented in a range of applications in the nuclear industry, including for effluent treatment (Winstanley et al., 2019).
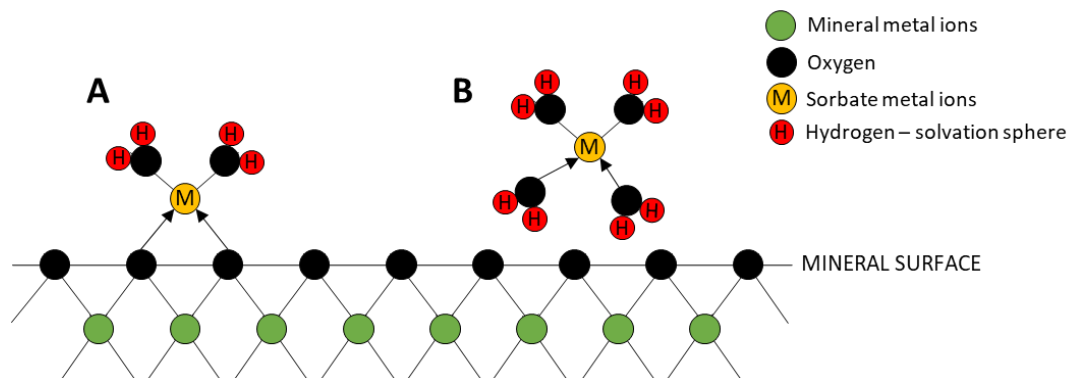
Figure 2.11: Schematic representing (A) inner sphere adsorption complexes and (B) outer sphere adsorption complexes. Arrows indicate covalent bonds. Adapted from Roberts (2017).

Typically, uptake of radionuclides to iron (oxyhydr)oxide surfaces in this way is highly pH and solution composition specific. As solution pH changes, so too does the mineral phase surface charge. When the pH rises, surface hydroxyl groups (S-OH) deprotonate and the surface becomes negatively charged (S-O⁻), thereby increasing sorption of cations to the surface (Dzombak and Morel, 1990). In contrast, for iron (oxyhydr)oxides, at low pH, protonation of the hydroxyl groups can occur, forming $S-OH_2^+$ (Musić and Ristić, 1988). The pH at which surface hydroxyl groups protonate or deprotonate is known as the point of zero charge (pH_{pzc}) and this is typically at circumneutral to slightly alkaline pH values for many iron (oxyhydr)oxides (Cornell and Schwertmann, 2003e).

Adsorption of a range of radionuclides including uranium, neptunium and plutonium to iron (oxyhydr)oxides have been widely reported in the literature (Bots et al., 2019, 2016; Li and Kaplan, 2012; Roberts et al., 2019; Tochiyama et al., 1995). For uranium, adsorption of U(VI) uranyl in solution to iron (oxyhydr)oxides typically results in the formation of inner sphere, bidentate complexes (Boland et al., 2011; Hsi and Langmuir, 1985; Moyes et al., 2000; Waite et al., 1994), with sharp adsorption edges usually across only one or two pH units (Cornell and Schwertmann, 2003f). The presence of carbonate in solution has been shown to limit the sorption of uranium to iron oxides through the formation of highly soluble uranyl carbonate complexes (Duff and Amrhein, 1996; Hsi and Langmuir, 1985; Waite et al., 1994; Wazne et al., 2003), though the formation of inner sphere iron(oxyhydr)oxide-U(VI)-carbonato ternary complexes, where the U(VI) was simultaneously bound to both carbonate and the iron oxide surface, have been reported (Bargar et al., 2000; Rossberg et al., 2009; Sherman et al., 2008; Winstanley et al., 2019). For ferrihydrite, Waite et al. (1994) found that sorption of U(VI) was highly pH dependant, with the formation of an edge-sharing bidentate surface complex at acidic pH, and a ternary carbonate complex at higher pH. Later work by Wazne et al. (2003) came to similar conclusions, with carbonate shown to limit the adsorption of uranium at higher pH. In contrast, with low carbonate concentration, complete removal of U(VI) from solution as a result of the adsorption of UO_2^{2+} to the ferrihydrite surface at pH > 7 was shown (Wazne et al., 2003). For goethite, similar adsorption trends have been seen with strong adsorption of uranyl to the surface in the absence of carbonate reported, particularly above pH 5 (Hsi and Langmuir, 1985). Here, the formation of inner sphere uranyl complexes are also reported, with modelling work showing the formation of UO_2OH^+ monodentate complexes and $(UO_2)_3(OH)_5^+$ monodentate, bidentate or tridentate uranium complexes in carbonate free scenarios. Later modelling work showed similar results, with adsorption of UO_2OH^+ and UO_2^{2+} to the surface of goethite forming monodentate and bidendate complexes, respectively (Missana et al., 2003b). Sherman et al. (2008) proposed that the dominant mechanism for uranyl sorption to goethite was through the formation of bidentate corner sharing complexes, and suggested that the U-Fe peak, previously attributed to corner-

sharing complexes with iron(oxyhydr)oxides in EXAFS analyses, was instead attributed to multiple scattering.

Magnetite is well reported to rapidly remove uranium from solution through a range of surface-mediated reactions. U(VI) is widely reported to be reduced to U(IV) at the magnetite surface and early work showed that this reduction was preceded by the sorption of U(VI) to the magnetite surface forming complexes $>FeO-UO_2^+$ and $>FeO-UO_2(OH)_2^-$ (El Aamrani et al., 1999). The formation of these surface complexes was fast but much slower under anoxic conditions (El Aamrani et al., 1999) and this observation was confirmed by Scott et al. (2005) who used X-ray photoelectron spectroscopy (XPS) to show rapid adsorption of UO_2^{2+} to the magnetite surface. They reported that the gradual reduction to U(IV) on the surface was as a result of direct electron transfer with Fe(II) (Scott et al., 2005). Building on this, later work by Latta et al. (2012) found that the sorption of U to magnetite was highly dependent on stoichiometry. Sorption of U(VI) to the surface was preferred in more oxidised magnetites where the Fe(II)/Fe(III) ratio was <0.38. In contrast, for partially oxidised and stoichiometric magnetites, reduction of U(VI) to U(IV) uraninite was favoured, coupled to the oxidation of Fe(II) (Latta et al., 2012). Sorption of U(VI) to magnetite has also been shown to be pH dependant, with higher sorption at circumneutral pH than in acidic conditions (pH 5) reported and precipitation of U(IV) phases favoured under more acidic, anoxic conditions (Missana et al., 2003c).
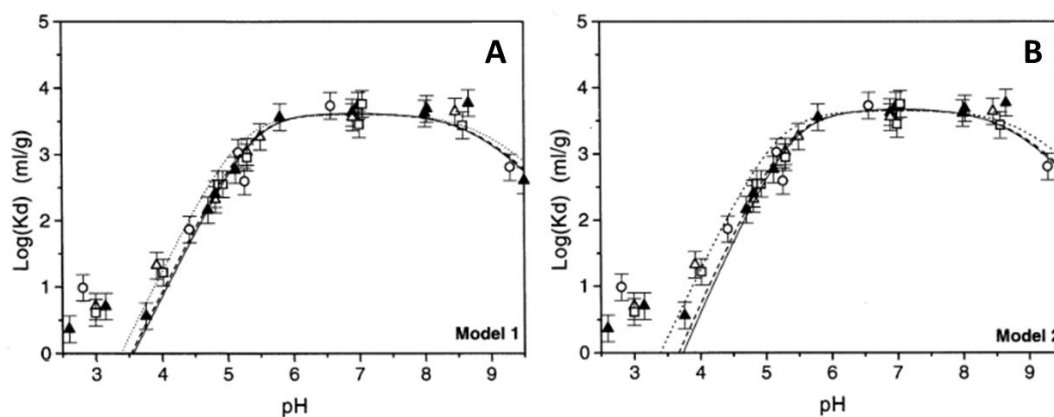
Figure 2.12: Comparison of experimental sorption of U to magnetite in different ionic strength solutions (symbols) with models of monodentate (A) and bidentate (B) complex formation in different ionic strength solutions (solid or dashed lines) across a range of pH values (taken from Missana et al., 2003a).

Sorption pH dependence was also investigated in a separate study where sorption in CO_2- and O_2-free conditions was explored and compared to models (Missana et al., 2003a). It was found that at pH 3.5, sorption to the magnetite surface was 0% and increased to ~90% at pH 6 before decreasing slightly above pH 9 (Figure 2.12). Modelling this sorption behaviour assuming formation of monodentate or bidentate complexes (Figure 2.12 A and B, respectively), resulted

in a very good fit with the experimental data, with the sorption behaviour found to be independent of ionic strength signalling the formation of inner sphere complexes.

2.4.3.2 Incorporation

Iron (oxyhydr)oxides have been widely reported as able to incorporate a range of radionuclides, including uranium, into their structures; essentially immobilising any contaminants (Boglaienko et al., 2020; Boland et al., 2014, 2011; Bots et al., 2016; Ilton et al., 2012; Marshall et al., 2015; Marshall et al., 2014a, 2014b; McBriarty et al., 2017; Nico et al., 2009; Pearce et al., 2020; Pidchenko et al., 2017; Roberts et al., 2017; Stewart et al., 2009). This has huge implications for nuclear sites where the presence of iron (oxyhdr)oxides could limit the migration of radionuclides in the subsurface as a result.

Uranium can become incorporated into iron (oxyhydr)oxide structures through co-precipitation or as a result of mineral transformations (Marshall et al., 2015; Nico et al., 2009; Roberts et al., 2017; Stewart et al., 2009). Kerisit et al. (2011) used atomistic simulations of uranium incorporation into a range of iron (oxyhydr)oxides to determine the uranium oxidation state and coordination when incorporated. For each calculation, charge imbalances are created when U(IV), U(V) and U(VI) substitute for Fe(III) or are incorporated into unoccupied sites. To account for the charge imbalance, charge compensation schemes were also created as a part of the simulations. For goethite, U was found to substitute for Fe(III) in octahedral coordination in either the U(V) or U(VI) oxidation state, with little distortion to the lattice. In contrast, simulations where U(IV) was substituted into octahedral vacancies contributed to distinct lattice distortion (Kerisit et al., 2011). Later work using similar computational methods confirmed that U(V) was the dominant incorporated oxidation state in goethite under reducing conditions, where it was substituted for Fe(III) in an octahedral uranate coordination (Kerisit et al., 2016). Laboratory studies of U incorporation into goethite have also taken place with confirmation that the likely oxidation state of incorporated uranium into goethite is U(V) (Massey et al., 2014), consistent with computational work. Most recently, Doornbusch et al. (2015), who studied uranyl fate during the formation of goethite in oxic conditions, evidenced the formation of a very short U-O bond (1.82 Å) that they did not attribute to uranyl given no evidence was seen in the XANES (Doornbusch et al., 2015). Similar U-O bond lengths have been seen in other work with uranium incorporation into goethite, but have been attributed to adsorbed uranyl on the goethite surface (Nico et al., 2009). In the Doornbusch study however, they presented this shorter U-O bond as necessary for uranium to be incorporated into goethite to reduce the size of the U polyhedron, thereby reducing the crystal strain caused by the larger atomic radius of uranium comparative to Fe(III). Indeed, the atomic radii of Fe(III) and U(VI) or U(V) in octahedral coordination are 0.645, 0.73 and 0.76 Å, respectively (Shannon, 1976).

Uranium incorporation into hematite has also been widely researched. Marshall et al. (2014a) showed that U(VI) could become incorporated into hematite following the adsorption of uranium onto ferrihydrite and subsequent crystallisation to hematite. X-ray absorption spectroscopy (XAS) analysis indicated that U(VI) replaced Fe(III) in a distorted octahedral site with lengthening of the U(VI)-O axial bonds from 1.81 to 1.87 Å and the retention of some uranyl character. The U-O equatorial bonds shortened as a result of incorporation, with an average U-O bond distance of 2.06 Å also reported, matching that of previous atomistic simulations (Kerisit et al., 2011). This work is in contrast with a previous study that suggested the loss of the uranyl U-O bonds altogether, with U(VI) incorporation into hematite in a uranate coordination (Duff et al., 2002). This difference was later attributed to an unrealistically low U-O coordination, suggesting the EXAFS were only partially resolved in the Duff et al. (2002) study (Kerisit et al., 2011). Similarly Ilton et al. (2012) also reported loss of uranyl bonds on incorporation and attributed uranyl present in the samples to adsorbed phases (Ilton et al., 2012). More recent *ab initio* molecular dynamics (AIMD) simulations for uranium incorporation into hematite have reported the co-existence of adsorbed U(VI) uranyl species and U(VI) in a uranyl-like coordination, substituting for structural Fe(III) (McBriarty et al., 2018).

For magnetite, atomistic simulations revealed both U(V) and U(VI) were housed within the octahedral site, though the tetrahedral site was also considered (Kerisit et al., 2011). The simulation data for U(V) and U(VI) incorporation showed good agreement of the U(V/VI)-O bond lengths with previous experimental EXAFS work (Nico et al., 2009), however the simulations also revealed that the experimental U-Fe distances in the work of Nico et al. (2009) (2.89 Å), which were very similar to the distances of Fe-Fe in pure magnetite, were unrealistic and more likely attributed to U-C interactions. Similar to work with uranium incorporated into goethite (Doornbusch et al., 2015), Kerisit et al. (2011) showed that the U-Fe bond distance relative to the Fe-Fe distance in magnetite increases as a result of incorporation, something that is reported in later work and attributed to the larger size of uranium compared with the Fe that it is substituted for (Roberts et al., 2017). The differences between simulated and experimental work here, highlight the need for further work to understand the mechanisms by which uranium becomes incorporated.

Recently, more work has focused on specifically determining the uranium oxidation states present within incorporated magnetite. A new high-resolution X-ray absorption spectroscopy technique (discussed further in Chapter 3), which measures absorption at the U M_4 edge, has allowed for better determination of the oxidation states in samples including U-containing magnetite (Pidchenko et al., 2017; Roberts et al., 2017). In these studies, uranium incorporated magnetite was synthesised through co-precipitation of uranium solutions with Fe(II) and Fe(III)

solutions with the addition of either NaOH (Pidchenko et al., 2017) or NH$_4$OH (Roberts et al., 2017) to stimulate precipitation of the magnetite nanoparticles. In both studies, iterative transformation factor analysis (ITFA) was used to determine the contributions of different uranium oxidation states in samples of the synthesised nanoparticles and U(V) was identified to be the main incorporated component in both. Pidchenko et al. (2017) found that the proportion of U(V) present in the samples was dependent on the uranium concentration, with samples containing 1000 ppm U found to have the highest proportion of U(V) (81%). They proposed a mechanism for uranium incorporation whereby U(V) becomes incorporated in a symmetrical octahedral coordination during the formation of the magnetite nanoparticles. U(VI) also adsorbs to the surface but is reduced to U(IV) (Pidchenko et al., 2017). Roberts et al. (2017) saw similar uranate coordination environments in their work, with slight differences in the proportion of U(V) observed with a change in Fe(II)/Fe(III) ratio. Roberts et al. suggested that incorporation of U(V) proceeded via two stages, with adsorption of U(VI) to the surface of the magnetite and reduction to U(V) at the surface via one-electron transfer. The second step, similar to the mechanism proposed by Pidchenko et al. involves the incorporation of U(V) into the Fe octahedral site during rapid crystal growth. They suggested that the incorporation of U(V) prevented its disproportionation to U(IV) and U(VI) under reducing conditions which has clear implications for the stability of U(V) in anoxic environmental systems (Roberts et al., 2017).

A number of studies have looked at the impact of oxidation on the stability of the incorporated uranium into magnetite. Earlier work by Nico et al. (2009) reported that incorporated samples exposed to 5 days of oxidation were subject to only minor changes in coordination, indicated by EXAFS, with the suggestion of some oxidative dissolution of magnetite evident from reduced coordination numbers in the U-Fe shells. These minor changes however, were within error and no change to the U-O bond lengths were observed, suggesting the oxidation state of the U was preserved during oxidation. They attributed the lack of structural O changes to U(VI) being the overriding uranium speciation, however they did not discount the presence of U(V). Pidchenko et al. (2017) oxidised samples under ambient conditions over much longer timescales (142 days) and used M$_4$-edge HERFD-XANES to observe retention of U(V) upon oxidation attributed to incorporation in addition to oxidation of sorbed U(IV) to U(VI) uranyl. Earlier work that explored the oxidative dissolution of uranium incorporated into magnetite also showed that a significant fraction of U was recalcitrant to oxidation after 14 days, with the dissolution of a small portion of U (6-21%) into solution (Marshall et al., 2015).

These studies highlight the stability of incorporated U within iron (oxyhydr)oxide systems relevant to engineered environments in the nuclear industry. Recent work has highlighted the stability of U(V) in incorporated systems, with recalcitrance to oxidation and leaching also observed

(Marshall et al., 2015; Pidchenko et al., 2017). These studies provide a unique perspective on uranium in the environment, however longer oxidation studies under field conditions would provide a more representative insight into the behaviour of incorporated uranium in the subsurface.

2.4.4 Cementitious materials geochemistry

Cementitious materials and concrete are the most widely used building material globally, with a range of concrete structures present at nuclear sites including engineered made ground, reactor halls, cooling towers and supporting buildings and infrastructure all mainly constructed from concrete. In addition, cements are widely used in the nuclear industry as a direct means of immobilising or encapsulating waste, or included as a barrier layer due to its high pH, which promotes the precipitation, co-precipitation or incorporation of many radionuclides, and high sorption capacity, effectively immobilising radionuclide contaminants. Here, cement chemistry will be discussed briefly before review of relevant literature of uranium behaviour in cementitious environments.

2.4.4.1 Concrete chemistry

Ordinary Portland Cement (OPC) is the main component of any cement and was first introduced after a period of decline in concrete and cement use after the fall of the Roman Empire (Kurdowski, 2014). OPC is generated through the crushing of limestone, clays and other materials which are then fed into a rotary cement kiln. The mix is heated to around 1500 °C and this drives off certain impurities and components leaving clinker, the raw cement material, in the form of small balls. These are crushed to yield a fine cement powder which is then used as the binding agent in the formation of concrete when combined with water, sand and aggregate materials (Portland Cement Association, 2017). Portland cement is often partially substituted with pulverised fly ash (PFA) or ground-granulated blast furnace slag (GGBS) to slightly alter the properties. CaO (lime) is one of the largest components of cement clinker by volume and is introduced to cement by the calcination of $CaCO_3$ (Valverde and Medina, 2015) which decarbonates at 680 °C. SiO_2, also present in significant quantities, is introduced in the form of aluminosilicates from shales and clays which combine with CaO during clinker formation to yield alite and belite, the bulk mineral components of Portland cement clinker. Iron oxides present in clinker also arise from shale and clays, the compositions of which are dependent on the redox conditions of the shales and clays involved. The final main component of clinker are aluminium oxides, which arise from heating clays and substances such as bauxite (Hewlett and Lea, 1998).

The addition of water to cement clinker starts the hydration process, whereby the cement forms a paste which hardens over time. When setting, the humidity must be at least 95% to ensure full

58

hydration and the paste continues to harden beneath water, giving rise to the name 'hydraulic cements' (Hewlett and Lea, 1998). This hardening principally arises from the reactions of di- and tri-calcium silicates (belite and alite, respectively) with water and initially, the rate of hydration is controlled by the dissolution rate of these clinker phases and calcium sulphate. Beyond this, the rate of nucleation and hydrate phase crystal growth dominate. Past a certain point, hydration is controlled by the diffusion of water and other ions into the cement pore spaces as cement precipitates most readily at the interface between the water and cement clinker (Hewlett and Lea, 1998). Upon contact with water, the dissolution of ions from cement clinker into the water occurs followed by rapid formation of hydrate phases. K^+, Na^+ and SO_4^{2-} ions are present due to the rapid dissolution of alkali sulphates as well as Ca^{2+}. Alite dissolves to form calcium silicate hydrate (CSH) precipitates ($xCaO.SiO_2.yH_2O$) within minutes, controlled by the Ca/Si ratio, which is between 0.7 and 1.7 (Pointeau et al., 2001). This ratio is lower in CSH phases than in alite, leading to an increase of Ca^{2+} and OH^- concentration in the solution phase, precipitating crystalline $Ca(OH)_2$ (Portlandite). Calcium aluminates also dissolve and react with calcium and sulphate ions in solution to form Ettringite, a hydrous calcium aluminate sulphate mineral, which precipitates at the surface. The original cement clinker composition is a major factor in the proportion of hydrate phases in hydrated cement, which generally consists of the following phases by weight: CSH phases (40-50%), Portlandite $Ca(OH)_2$ (20-25%), calcium aluminates, Ettringite and ferric phases (10-20%), pore solution (10-20%) and up to 5% of other minor components (Berner, 1992).

CSH phases are characterised by a layered tobermorite-like amorphous structure consisting of layers of Ca-O sheets with the oxygen atoms all bonded to silica arranged in a 'dreierketten' formation (Figure 2.13). This formation describes the bonding of silica dimers to bridging silica tetrahedra on both sides of the Ca-O sheets (Tits and Wieland, 2018). The structure has a net negative charge due to silanediol groups ($>Si-OH_2$) on the bridging silica tetrahedra, where increasing pH results in the deprotonation of these groups. Ca^{2+} is also present in the Ca-O sheet interlayers which act to neutralise the negative charges from the silanediol groups, but can also be substituted for other cations (Gaona et al., 2012). The high surface area of CSH (~148 m^2/g (Tits et al., 2006; Thomas et al., 1999)), net negative surface charge and presence of Ca^{2+} in the interlayer therefore provides a platform for the sorption or substitution of cations, including radionuclides.
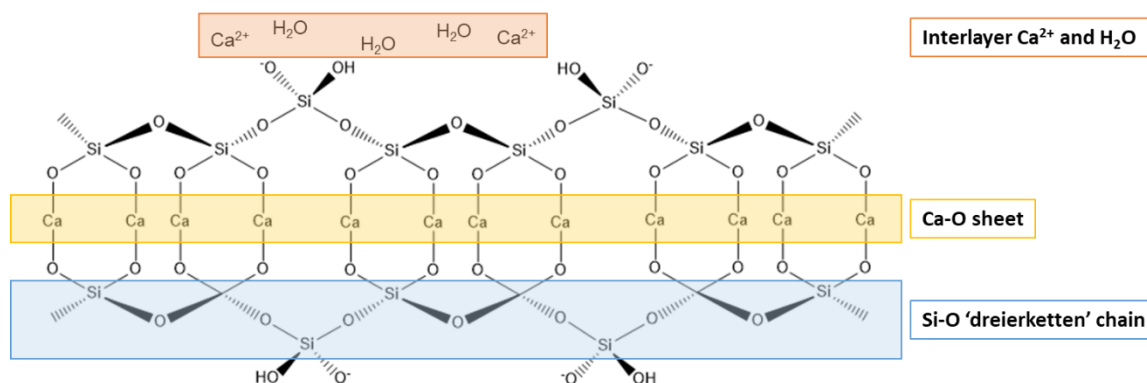
Figure 2.13: Structure of CSH with the silica dreierketten structure, Ca-O sheets and interlayer Ca^{2+} highlighted (adapted from Wu and Ye, 2016).

As hardened cements come into contact with water, a high pH leachate is produced that varies in both composition and alkalinity with the age of the cement. With younger cements, the leachate is dominated by Na and K ions and a pH of ~13.5 is typical. In aged cements, the pH typically decreases to ~12.5 with the solution saturated with respect to $Ca(OH)_2$. As cements continue to age, the dissolution of CSH phases leads to a reduction in the leachate pH over time (Tits and Wieland, 2018). As discussed previously in this chapter, the pH of a solution can have a drastic impact on uranium speciation and so the high pH leachate produced from cementitious materials will likely affect the speciation of radionuclides such as uranium and will be discussed in the next section.

2.4.5 Radionuclide interactions with cementitious materials

The high specific surface area of cement components such as CSH, and the high pH leachate produced when cementitious materials contact with water provide the perfect environment for the immobilisation of radionuclide contaminants (Tits and Wieland, 2018) and as such, cements have been widely utilised in the nuclear industry for the encapsulation of waste (Corkhill and Hyatt, 2018; Koťátková et al., 2017; Ojovan et al., 2019). Additionally, cementitious materials are widely used in the nuclear industry as a building material in the construction of active- and non-active areas on sites; for example in the building of spent fuel ponds or the use of concrete to provide radiation shielding for reactor vessels, in addition to use as a general construction material. The widespread use of cementitious materials at nuclear sites has implications for the decommissioning industry, where large volumes of concrete waste are expected to be produced during the dismantling and demolition of structures (NDA and BEIS, 2019b). Alternative waste management routes for these wastes such as in-situ disposal, described earlier in this chapter, bring with them a need to understand the interactions of radionuclides with cements to ensure

the safety of the general public and the environment over timescales relevant to the decay of many radionuclides.

Radionuclide interactions with cements and their components have been widely studied in the literature, with a range of reported retention mechanisms including sorption, incorporation and precipitation (Evans, 2008). Typically, studies have focussed on the interactions of radionuclides including ^{238}U, ^{90}Sr, ^{137}Cs, Cm and ^{237}Np with CSH phases, as these have been shown to be the primary sink for radionuclides in cementitious materials (Atkins and Glasser, 1992; Baston et al., 2012; Macé et al., 2013; Wieland et al., 2010), with comparison of actinide sorption to fresh and degraded cements providing very similar results to that of actinide sorption to CSH (Macé et al., 2013; Stumpf et al., 2004; Wieland et al., 2010).

Mechanisms of interaction with cementitious materials can vary between radionuclides. For example, a study reacting Cs and Sr with a core section of pond wall from the Hunterston A site in the UK showed that Sr was sorbed to the cement as a partially hydrated species (Bower et al., 2016). This was consistent with previous work examining uptake of strontium to both hardened cement paste and CSH samples (Wieland et al., 2008), where CSH was found to be the uptake-controlling phase. Meanwhile, Cs was shown to preferentially associate with the aggregate present in the concrete instead. Interestingly, the same study found that radiostrontium was in fact bound to TiO_2 present in the paint coating the surface of the concrete core (Bower et al., 2016), which has clear implications for decommissioning of these structures, where removal of the paint could be sufficient to remove a significant amount of radioactivity prior to demolition or in-situ disposal.

Interactions of trivalent radionuclides including Nd(III), Eu(III) and Cm(III) with CSH have also been studied. For Eu(III), uptake onto CSH was rapid, with 90% of Eu(III) in solution removed within 15 minutes (Schlegel et al., 2004), consistent with a previous study where strong retention (>99%) of Eu(III) onto CSH was also observed (Pointeau et al., 2001). Here, EXAFS analyses indicated the possible precipitation of a Eu(III) phase, with the authors also describing substitution of Eu(III) for Ca^{2+} in the CSH interlayer (Schlegel et al., 2004). Similarly, Cm(III) was also found to substitute for Ca^{2+} in both the Ca sheets and the CSH interlayer (Stumpf et al., 2004) but was also reported to become incorporated into the CSH structure, indicated by low coordination of H_2O molecules (Tits et al., 2003). Incorporation into CSH was also reported for Nd(III), where the same study showed preferential accumulation of Nd in rims around CSH interlayers and observed changes in the coordination environment of Nd over time (Mandaliev et al., 2009). Reduction of radionuclides at the cement surface has also been reported; neptunium, for example, is seen to sorb to the surface of cements as Np(V) followed by reduction to Np(IV) (Sylwester et al., 1999), whilst later XAS

investigation of Np(IV) found that it became incorporated into the interlayer of CSH, however this process was dependent on the Ca:Si ratio of the CSH phases (Gaona et al., 2011).

For uranium in particular, an extensive body of work has focussed on mechanisms of uptake to cementitious materials with surface complexation mechanisms widely studied. Sutton et al. (2003) studied uranium interactions with ordinary Portland cement grout and found that U(VI) sorption to the grout proceeded by formation of a hydroxide bridge between silanol groups on the surface of the grout and uranyl hydroxide ions present in solution. The study found that sorption to the grout occurred at high pH despite both the uranyl hydroxide ions in solution and the grout surface being anionic. Here, the formation of inner sphere complexes also suggests that uranium is less susceptible to desorption and, over time, has been shown to lead to the precipitation of uranyl minerals (Sutton et al., 2003). This work is consistent with a number of other studies, where EXAFS has been used to show that uranyl is bonded to cement mineral surfaces via inner sphere complexation (Sylwester et al., 1999; Wieland et al., 2010; Zhao et al., 2000). A recent density functional theory study also supported this, with uranyl sorption in the interlayer modelled and compared to EXAFS data which suggested uranyl sorption to Si-O tetrahedra in the CSH interlayer (Kremleva et al., 2020). Work using luminescence line-narrowing spectroscopy to explore the interactions of U(VI) with CSH phases and hardened cement paste have also shown that uranyl uptake by CSH phases can occur via sorption to surface silanol sites (Tits et al., 2015, 2011). Partitioning of uranium to cements in this way has been reported to be high and rapid, with higher distribution ratios reported in cements or CSH phases with pH values between 10.5 -12.5, rather than in highly alkaline solutions above pH 13 as a result of changes in U(VI) aqueous speciation (Gaona et al., 2012; Tits et al., 2008). Interestingly, an in-diffusion study was carried out to determine the level of U(VI) penetration in a sample of hardened cement paste (Wieland et al., 2010). This study, which provides a good analogue for processes that may occur in in-situ cementitious environments, showed that U(VI) preferentially accumulated around Ca-rich areas, largely consisting of CSH phases, but also diffused into the cement to a depth of 10 μm over 9 months (Wieland et al., 2010). This has implications for the behaviour of uranium over time, which may become further immobilised by slow diffusion into cements or become incorporated as a result of cement phase recrystallisation processes. For the sorbed species in this study, sorption of U(VI) at low concentrations to Si on the surface, or sorption in the interlayer was proposed with coordination environments similar to the uranyl silicates, uranophane $(Ca(UO_2)2SiO_3(OH)_2.5(H_2O))$ and soddyite $((UO_2)_2SiO_4 \cdot 2H_2O)$ observed (Wieland et al., 2010).

In addition to the formation of surface complexes however, the precipitation of mineral phases and the formation of incorporated uranium have also been reported (Tits et al., 2015, 2011). Here, the incorporated species becomes more dominant over time and is attributed to U(VI)

incorporation into the interlayer during recrystallisation of CSH (Tits et al., 2015, 2011). This is consistent with X-ray diffraction (XRD) studies of U(VI) interactions with CSH, where a change in the diffraction pattern of CSH was attributed to the formation of the mineral haiweeite ($Ca[UO_2]_2Si_5O_{12}(OH)_2].3H_2O$), a calcium-uranyl-silicate-hydrate-phase, which became more crystalline over time suggesting potential incorporation of the U(VI) into the CSH structure (Yorkshire et al., 2018).

Solubility studies on mineral phases have also been performed to determine the long term stability of uranium in cementitious systems and a range of different solid phases have been shown to form. Typically, at high pH, U(VI) solubility is predicted to be low (Yamamura et al., 1998). An early study investigating uranium uptake onto hydrothermally altered concrete found that sorption to the solid was enhanced at lower U concentrations. They also suggested the uptake of uranium to the concrete was potentially controlled by the formation of oligomeric clusters or a precipitate indicated by U-U backscatterers in the EXAFS spectra (Zhao et al., 2000). Brownsword et al. (1990) determined the solubility of uranium in cement-equilibrated pore waters was equal to or lower than the solubility of both calcium and sodium uranates, however later work has also suggested uranyl silicate minerals are significant in the immobilisation of uranium within concrete (Moroni and Glasser, 1995). Other work suggested that the solubility limiting phase instead corresponds to a becquerelite-type solid, however thermodynamic modelling in the same study also predicted the formation of calcium uranate phases (Felipe-Sotelo et al., 2017). Harfouche et al. (2006) compared the coordination environment of uranium in CSH sorption samples to the structural parameters for uranophane, with a split equatorial shell, Si neighbouring atoms at short and long distances, corresponding to bidentate and monodentate coordination of uranyl to SiO_4 tetrahedra, respectively, and U-Ca backscatterers and similar coordination was also reported in later sorption studies (Macé et al., 2013; Wieland et al., 2010). Pointeau et al. (2004), highlighted the difficulties in reproducibility of results in the literature for U(VI) sorption to cementitious materials, which is clear from the vast differences in speciation reported above. This is largely due to the complex chemistry and composition of cement or the experimental aqueous solution coupled with differences in experimental protocols and conditions.

Of particular interest to this work is the formation of poorly soluble calcium uranates, which has been found to be the solubility limiting phase in several studies (Harfouche et al., 2006; Macé et al., 2013; Tits et al., 2008), where the concentrations of Si and Ca were also shown to impact on the solubility of U(VI). Here, increasing Ca concentration leads to a decrease in the solubility limit as a result of increased competition with Ca for sorption sites. Sorption isotherm experiments have largely reported linear sorption of U(VI) to cementitious materials up to a point (Harfouche

et al., 2006; Pointeau et al., 2004; Wieland et al., 2003), with some slight differences in the uptake dependent on the Ca:Si ratio, however at high U(VI) concentrations, precipitation of calcium uranate phases is seen instead (Wieland et al., 2003). Clearly, uranium loading has some impact on the speciation of uranium in cementitious environments. Macé et al. (2013) looked at U(VI) speciation across a range of concentrations and found that U(VI) was primarily sorbed to CSH as a $UO_2(OH)_4^{2-}$ species across a range of U(VI) concentrations. This is consistent with an earlier study that used PHREEQC calculations to show a number of potential U(VI) species present in cement solutions at different pH, where at pH 10-12, $UO_2(OH)_3^-$ was found to be the dominant species with $UO_2(OH)_2$ and $UO_2(OH)_4^{2-}$ also present in this range (Pointeau et al., 2004). Despite this, at high U(VI) loadings, precipitation of a calcium uranate phase was instead seen (Macé et al., 2013) and also reported in a previous study under similar conditions (Wieland et al., 2010). Here, the calcium uranate phase was characterised by a U-O axial component at 1.94 Å, four Ca atoms at a distance of 3.69 Å and a U-U shell at a distance of 3.85 Å in the EXAFS, which was roughly consistent with a later study that observed the formation of stable uranate-like colloids at high pH (pH > 13) in an anaerobic system (Bots et al., 2014). Interestingly, the formation of uranate phases in these systems is accompanied by a corresponding elongation of the U-O axial bond, relative to uranyl speciation, consistent with expected values for uranates such as clarkeite (Catalano and Brown, 2004; King, 2002). Bots et al. also observed a distorted octahedral coordination around uranium, where a split equatorial U-O shell was observed as opposed to just one U-O bond length, which was attributed to variable hydration of the clarkeite-like phase formed and explained previously by Catalano and Brown (2004) who suggested the hydration of such phases caused multiple uranium crystallographic positions. Critically here, calcium uranates are typically highly insoluble and so the precipitation of such phases in cementitious environments is likely to lead to long-term immobilisation, however more work is needed in this area to understand the extent of immobilisation in oxic, subsurface systems relevant to disposal.

2.5 Contamination at nuclear sites: Case Studies

2.5.1 Sellafield, UK

Sellafield is a nuclear licenced site located in Cumbria, U.K., and covering six square kilometres on the northwest coast of England, with the Lake District National Park to the east and the Irish Sea to the west (Figure 2.14). The site started out as a Royal Ordnance Factory during the Second World War producing trinitrotoluene (Cruickshank, 2012), and was chosen for its remote location. Shortly after the war, the site was acquired for the production of plutonium for nuclear weapons and consequently, the Windscale Piles were built; air-cooled, graphite moderated reactors. A

range of facilities were also built to support this, including the first generation reprocessing plant. The first commercial nuclear reactor, an advanced gas-cooled reactor, was later developed on the same site at Calder Hall.
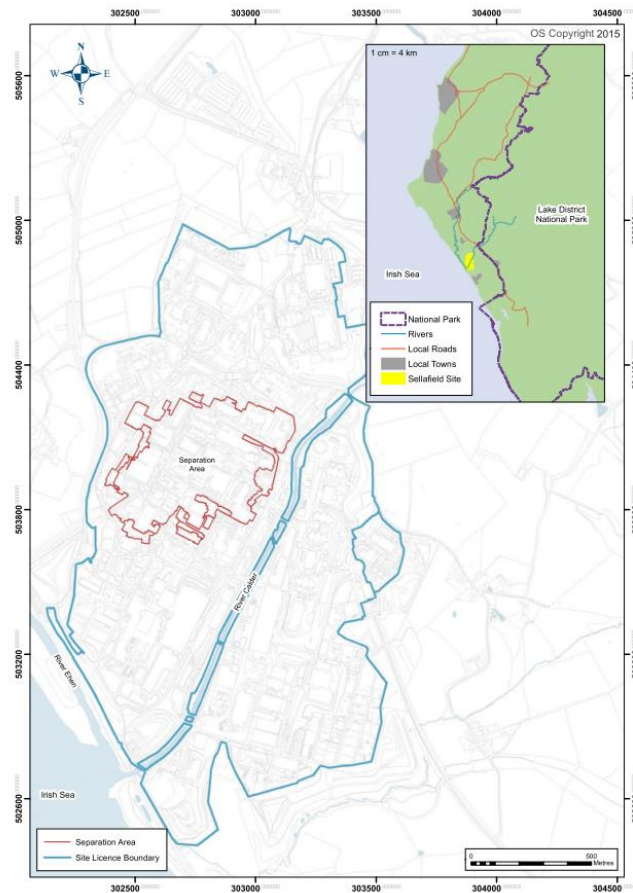
Figure 2.14: Sellafield site and geographical location (Marshall et al., 2015)

The Sellafield site has therefore been host to a vast array of activities from the running of military and civil nuclear reactors, to the reprocessing and storage of spent nuclear fuel. Now the site's focus has turned to decommissioning with Sellafield Ltd, the company responsible for the running of the site, becoming a wholly-owned subsidiary of the Nuclear Decommissioning Authority (NDA) in 2016. Sellafield's strategy now encompasses four main 'value streams' which are retrieval of nuclear sludge, waste and fuel stored in silos and legacy ponds, remediation of site facilities, storage of special nuclear materials and spent nuclear fuel management (Sellafield Ltd, 2020b). Due to the complexity and history of the Sellafield site, decommissioning presents several challenges. These include the density of infrastructure on site as well as extensive groundwater and land contamination from both nuclear and non-nuclear activities, deteriorating infrastructure and significant quantities of corroding radioactive material housed in legacy plants (NDA, 2016b). The legacy facilities associated with the early years of reactor operation including the Pile Fuel Storage Pond (PFSP), the pile fuel cladding silo and the facilities built to deal with the Magnox spent fuel including the First Generation Magnox Storage Pond (FGMSP) and the Magnox Swarf

Storage Silo (MSSS), can be found in the Separations Area of the Sellafield site (highlighted in red in Figure 2.14), where the majority of the radioactive legacy is focussed. These facilities pose the greatest radiological hazard on site and as such, current NDA strategy is focussed on their safe and timely decommissioning (NDA, 2021).

For example, the Magnox Swarf Storage Silo (MSSS) facility is known to have leaked radioactive liquor below ground for several years in the 1970s/80s at a maximum rate of 3 m^3/day, introducing a significant source of contamination (Kuras et al., 2016). Though the exact composition of this leak is unknown, Sellafield has a range of known co-contaminants present in the ground and groundwater. Known alpha-emitters include ^{238}U, ^{239}Pu, ^{240}Pu and ^{241}Am, whilst ^{90}Sr, ^{137}Cs, ^{241}Pu and ^{99}Tc are amongst the known beta emitters (Sellafield Ltd., 2016). To track the movements and concentrations of these radionuclides on- and off-site, Sellafield Ltd conducts a vast array of environmental monitoring including the monitoring of onsite groundwater using a network of wells, airborne radioactivity, local seafood and agricultural produce and the monitoring of sediments from local estuaries and harbours. Monitoring of radionuclides present in the groundwater on site through wells enables quantification of radionuclide movements and identification of any new leaks or spills to the subsurface. Figure 2.15 shows the total alpha and beta concentrations from monitoring wells in 2019 (Sellafield Ltd, 2020a). In several areas of the site, largely contained within the separations area, the concentration of both alpha and beta emitters are above the World Health Organisation (WHO) drinking limits (Sellafield Ltd, 2020a). For total beta concentrations in particular, the highest concentrations in groundwaters are associated with legacy waste storage facilities including the Highly Active Liquor Tanks and the Solid Waste Storage Facility, where over 99% of the total radioactivity released to the subsurface at Sellafield is believed to have originated (Sellafield Ltd., 2016). For total alpha, the concentrations in the majority of wells were below the limit of detection (LOD) and ^{238}U and ^{234}U were the dominant radionuclides, where concentrations could be measured.
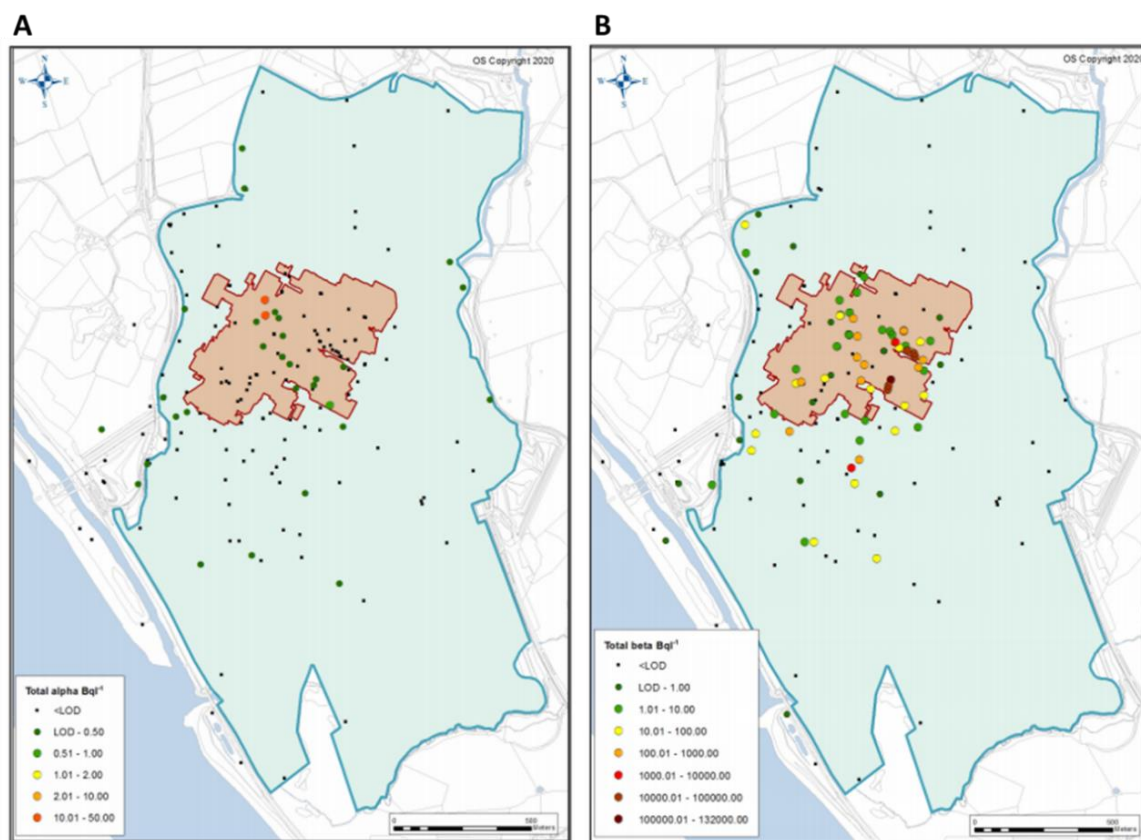
Figure 2.15: Average total (A) alpha and (B) beta concentrations from environmental monitoring of the Sellafield site (site boundary highlighted in blue) in 2019. The Separations Area is highlighted in red. NB: WHO drinking water limits for total alpha = 0.50 Bq L^{-1} and total beta = 1.00 Bq L^{-1} (Sellafield Ltd, 2020a).

The annual monitoring data for the Sellafield site, which must be completed to fulfil site licence requirements, can provide a picture of the migration behaviour of different radionuclides over time. Comparison of the monitoring data over the latest five year reporting period (2015-2019) shows that radionuclide activity concentrations both on-site and at the perimeter are broadly consistent over time (Sellafield Ltd, 2020a). This is consistent with relatively low migration away from the point source of contamination for many radionuclides, signifying natural attenuation processes taking place in the subsurface. Data show in particular that uranium and other alpha emitters are not distributed as widely around the site as key beta emitters (^{99}Tc, ^{90}Sr), suggesting more significant retention of these radionuclides in the subsurface. Consequently, these data can provide a qualitative assessment of the likely locations of contaminated land and structures on site, informing future decommissioning work.

Historically, before modern environmental regulations, some VLLW/LLW comprising contaminated soil from excavation and construction was disposed in "pits" and "trenches" on the Sellafield site, with some contamination of the ground and surrounding areas likely to have occurred (DECC, 2015). The unlined Calder Landfill and South Landfill, both of which no longer

receive wastes, are two examples of such historical on-site disposal in at Sellafield (DECC, 2015; Environment Agency, 2002). Currently operational is the Calder Landfill Extension Segregation Area (CLESA) VLLW/LLW facility. This facility is a basal lined Environmental Permitting Regulations (EPR) authorised landfill for the disposal of VLLW and low activity LLW and provides an alternative disposal route for low-level wastes to the LLWR (AECOM, 2017). CLESA accepts wastes such as soils and concrete and, in the latest UK Radioactive Waste and Material Inventory, it was projected that of all the current (at 1 April 2019) and future wastes expected to arise, 8% of all the UK's LLW and 2% of all VLLW would be permanently disposed of at the CLESA facility (NDA and BEIS, 2019b). This provides an alternative pathway for these wastes, diverting them away from LLWR, where limited disposal capacity exists. Indeed, the establishment of the National Waste Programme in 2011 was in response to the diminishing capacity at LLWR and as much as 95% of wastes generated per year are now diverted away from LLWR for disposal through alternative routes or for recycling or reuse (LLW Repository Ltd, 2018). As more waste is generated on site as a result of decommissioning activities, alternative disposal routes will need to be considered. The site is already considering options for alternative disposal, including the building of new landfill facilities on-site for when CLESA has reached capacity (LLW Repository Ltd and Sellafield Ltd, 2019) which must fulfil the requirements set out by the Environment Agency in the Guidance on Requirements for Authorisation for near-surface disposal facilities (GRA) document (Environment Agency et al., 2009). Furthermore, a review of options for site interim/end states are currently being developed by the site in line with the GRR regulations (LLW Repository Ltd and Sellafield Ltd, 2019). Additional considerations include options for remediation of contaminated land in situ rather than disposal through traditional 'dig and dump' methods, which would contribute to waste minimisation and potentially limit radioactivity exposure to workers (Cleary et al., 2019; Newsome et al., 2017; Vermeul et al., 2014).

In addition to the release of radioactivity on-site, since the start of its nuclear activities in 1952, Sellafield has discharged low-level radioactive effluents into the Irish Sea under authorisation. The main effluent sources at the Sellafield site comprise treated liquor from fuel reprocessing and purge water from the fuel storage ponds (Gray et al., 1995; Kershaw et al., 1992). During spent fuel reprocessing, a series of separation and extraction steps vastly reduce the radiological inventory of the effluent prior to discharge. For example, solvent extraction of the spent fuel results in the extraction of highly active fission products which are then vitrified into glass waste forms. Subsequent extraction steps to separate and purify plutonium and uranium result in active liquors that historically were discharged to the sea following a short period of delay storage, largely to allow for the decay of ^{106}Ru (Gray et al., 1995). The discharge of these untreated medium active liquors to the sea was stopped in 1980 and additional reprocessing facilities were introduced which allowed for the concentration of this liquor through evaporation which is now

processed by the Enhanced Actinide Removal Plant (EARP), commissioned in 1994 (Gray et al., 1995). EARP reduces the activity of the final effluent by inducing the precipitation of iron(oxyhydr)oxides from aqueous Fe(III) present in the acidic active liquor (Winstanley et al., 2019). Sodium hydroxide is added to the liquor to raise the pH and results in the formation of an iron(oxyhydr)oxide floc, which is gelatinous in nature and immobilises radionuclides present in solutions through adsorption, incorporation and physical entrapment processes (Weatherill, 2017). This floc is then filtered before the subsequent release of effluent to the sea. Historically, and until the late 1970s, fuel storage pond water was also discharged to the environment after decay storage and settling. These practices changed with the introduction of the site ion exchange effluent plant (SIXEP) in 1985 (Leonard et al., 1995). This plant works by using a combination of sand and clinoptilolite ion exchangers to effectively remove radionuclides from solution and have significantly reduced the concentrations of ^{90}Sr, ^{134}Cs and ^{137}Cs present in effluents since its introduction (Gray et al., 1995). The introduction of facilities such as those mentioned above have contributed to significantly reduced levels of radioactivity discharged to the sea (see Figure 2.16 for an example (Sellafield Ltd, 2020a)).
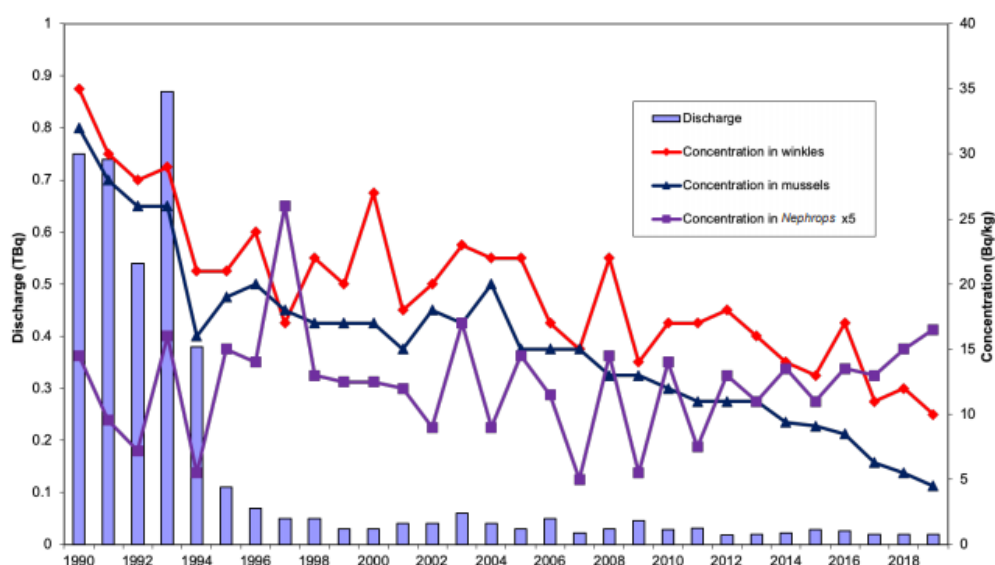
Figure 2.16: Americium-241 discharge concentrations into the sea and comparative concentration in winkles, mussels and *Nephrops*. An example highlighting the decreasing concentrations of discharges to the sea (Sellafield Ltd, 2020a).

Indeed, the most recent environmental monitoring reports show that radioactive effluent discharges to the sea have largely decreased between 2015 and 2019, and were well below the authorised limits in all cases (Sellafield Ltd, 2020a). Now, as fuel reprocessing ends and the site's focus shifts further towards site clean-up and decommissioning, effluent discharges are further projected to substantially decrease, with the release of tritium in particular set to almost completely cease (Sellafield Ltd, 2020a). Despite projected reductions in radioactive effluents, the

legacy of radioactivity released to the sea has resulted in concentrated patches around the coast of Cumbria, particularly in intertidal and estuarine sediments (Keith-Roach et al., 2003; Livens and Baxter, 1988; Morris et al., 2000) and in a mudpatch close to the site's discharge pipeline (Morris et al., 2000; Ray et al., 2020). Studies have shown that radionuclides associated with the mudpatch can be easily remobilised by sediment mixing and bioturbation at the site, resulting in the redistribution of radionuclides along tidal coastal sites (Morris et al., 2000; Ray et al., 2020).

2.5.2 Savannah River Site, USA

The US DOE site, Savannah River Site (SRS), located in Aiken, South Carolina, USA, was first constructed in the 1950s to produce and refine tritium and plutonium-239 for the fabrication of nuclear weapons in response to the Soviet Union's first weapon's test in 1949 (Savannah River Site, 2021a). The site covers an area of 310 square miles, bordering the Savannah River and Georgia to the South West (Figure 2.17). Five nuclear reactors were originally built on the site in addition to a range of support facilities including chemical separations and waste management facilities and a heavy water extraction plant (Figure 2.17).
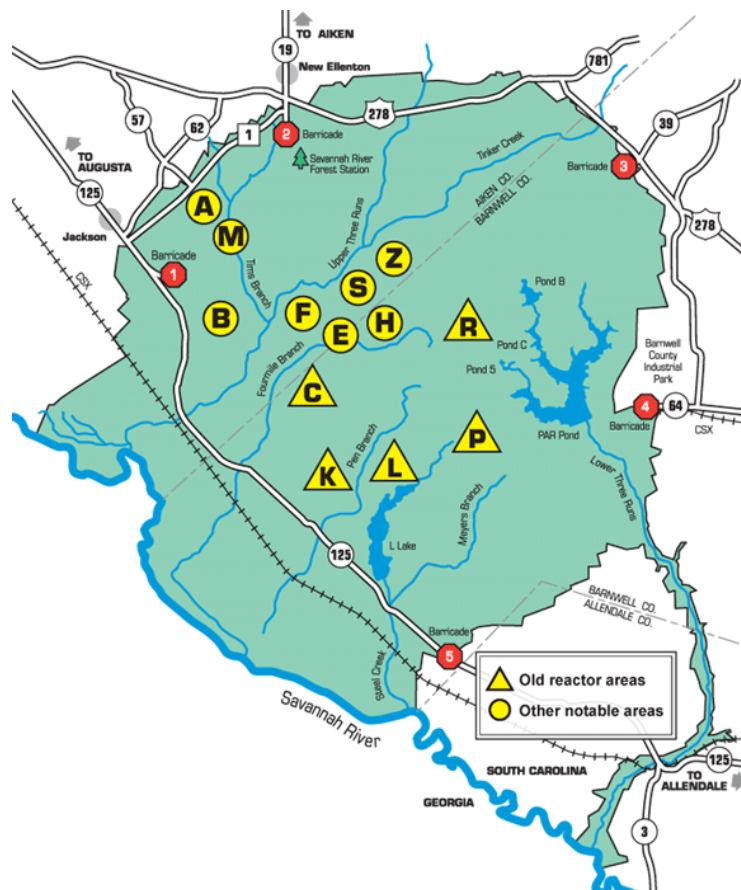
Figure 2.17: Map of the Savannah River Site showing the site area in green (Savannah River Site, 2013). The five original nuclear reactor areas are highlighted.

The five reactors have now been shut down (circa 1980s) and the site is now predominantly in a state of decommissioning and has been designated as a national environmental research park (Davis and Janecek, 1997). SRS is also home to the Savannah River National Laboratory (SRNL), which conducts a range of research in areas including environmental remediation and risk reduction and nuclear materials characterisation (Savannah River Site, 2021b).

Between 1953 and 1988, SRS produced ~36 metric tons of plutonium for weapons (Savannah River Site, 2020b). The by-products of these historical operations, accidental releases and disposal practices on the site have resulted in a legacy of contaminated land, groundwater and surface water that encompasses a range of mixed hazardous and radioactive wastes, with estimated volumes of contaminated soil and groundwater in 1999 at 8.6×10^6 and 3.1×10^8 m^3, respectively (National Research Council, 1999). In particular, the use of rudimentary burial grounds and trenches, similar to the one at the Hanford Site pictured in Figure 2.18, is one pathway to the release of radioactivity into the local environment (Flach, 1994).

Figure 2.18: Photograph of typical disposal of radioactive waste into an unlined burial trench at the Hanford US DOE site prior to 1970 (US GAO, 2007).

Similarly, waste effluents containing a range of metals, nitric acid, sodium hydroxide and radionuclides were routinely emptied into unlined seepage basins at the site's F area (Figures 2.17 and 2.19) between 1955 and 1988 (Kaplan et al., 1994a). The seepage basins were designed to contain wastewater and retard metals and radionuclides through natural attenuation to surrounding soils, however metals including Cr, Co, Cd, and Pb and radionuclides including Am, Pu, Cm, ^{129}I and U have been found in the aquifers beneath these seepage basins and up to 1 km away as the result of transport and in some cases, colloidal transport (Dong et al., 2012; Kaplan et al., 1994a, 1994b; Looney et al., 1988; Neeway et al., 2019). A groundwater management strategy involving active remediation and extensive groundwater monitoring now takes place to meet current regulatory requirements (Savannah River Site, 2020a). One area of research at SRS

that is relevant to this thesis is the study of long-term transport of radionuclides in field lysimeters using the Radionuclide Field Lysimeter Experiment (RadFLEX), housed at SRNL (Roberts et al., 2012). This facility has been utilised to study the interactions of radionuclides including radiostrontium, plutonium and neptunium in the vadose zone on a scale not typically replicated in laboratory settings (Demirkanli et al., 2008, 2007; Kaplan et al., 2014, 2006; Miller et al., 2012; Peruski et al., 2018; Powell et al., 2015). In these studies, typically radioactive source terms are emplaced into lysimeters and exposed to natural rainfall for years at a time. The lysimeters are eventually extracted and samples are analysed to determine the speciation and transport of contaminants. A study with radiostrontium saw significant transport in SRS sediments over 11 years with migration both upwards as well as downwards (Kaplan et al., 2014). Upwards transport was predicted to be as a result of dispersion, evaporation or uptake into plant roots that had grown in the lysimeters (Kaplan et al., 2014). This upwards movement was also seen in lysimeter experiments with Pu (Demirkanli et al., 2008, 2007; Kaplan et al., 2006) and Np (Peruski et al., 2018), where some contribution from plants was reported.
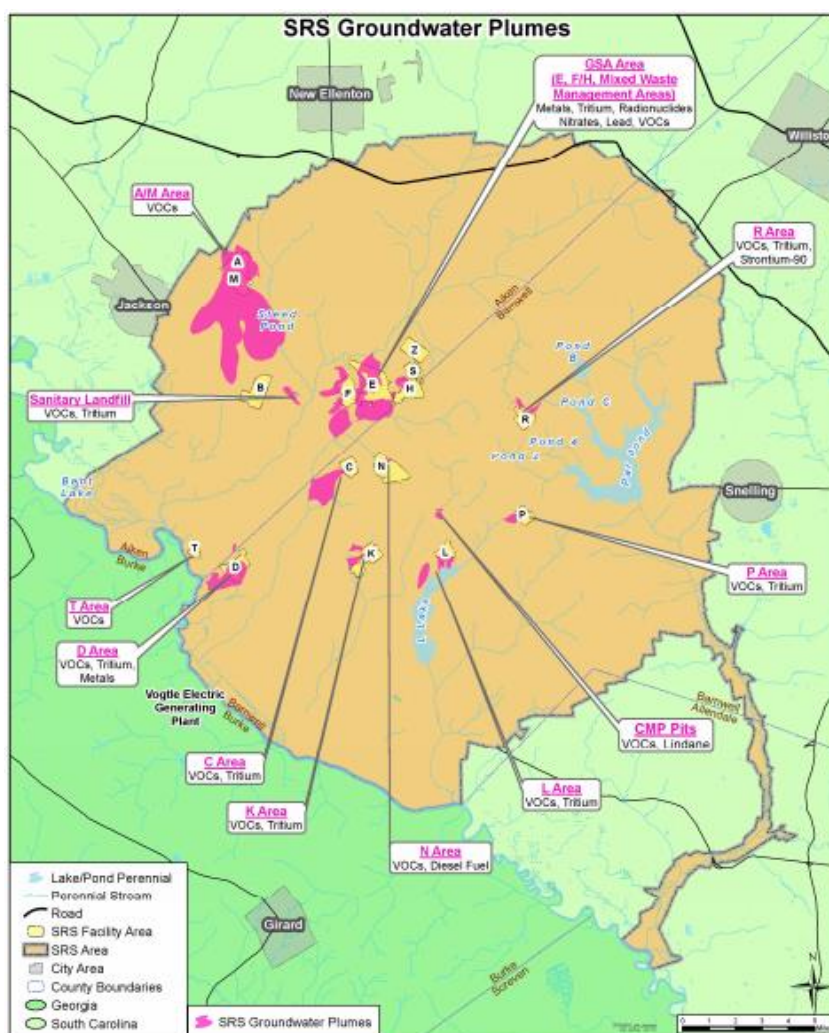
Figure 2.19: A map of the SRS site showing areas of groundwater contamination (pink). Associated area labels also list the main components of the contaminants (Savannah River Site, 2020a)

For uranium in particular, environmental releases at SRS have largely been associated with fuel fabrication or chemical processing facilities and the disposal of waste into streams and seepage basins (F, H, M and A areas, Figure 2.19) (Evans et al., 1992). Of particular note are the accidental and purposeful releases of uranium wastes generated during fuel fabrication (M area – Figure 2.19), where a reported 43.5 metric tonnes of uranium has been released to the subsurface since 1955 (Evans et al., 1992). Here, the uranium flowed from a tributary into Tims branch (pictured in Figure 2.17) and Steed Pond (pictured in Figure 2.19) over 2 km from the fabrication facility, where elevated uranium concentrations (as high as 6000 ppm) have been reported in stream waters (Evans et al., 1992). The released uranium was present as depleted uranium in particulate, colloidal and dissolved phases, with uranium bound to clay particles, waste process precipitates and metallic fines and may have present in the 0, +4, +5 or +6 oxidation states (Kaplan et al., 2020). A range of studies have explored the attenuation of these phases to the wetland areas surrounding the release sites (Kaplan et al., 2020; Kaplan and Serkiz, 2001; Li et al., 2015). These studies have shown that uranium generally binds strongly to wetland sediments (Kaplan and Serkiz, 2001; Li et al., 2015; Li and Kaplan, 2012). Here, uptake of both U(IV) and U(VI) into plant roots, forming bidentate complexes with carbon and U(VI) phosphate minerals (Li et al., 2015) were reported. Desorption studies on 'aged' SRS contaminated sediments showed uranium desorption K_d values, where K_d is the distribution coefficient and describes the ratio of the contaminant in the solid and aqueous phases, that were significantly larger than previous conservative sorption K_d values, where all uranium in the solid phase and not just the reversibly-sorbed uranium was taken into account (Kaplan and Serkiz, 2001). Similar results were seen for Hanford sediments, where desorption U(VI) K_d values were higher than sorption U(VI) K_d values (Um et al., 2007). Kaplan and Serkis found that the high K_d values measured in the aged U-contaminated samples were likely attributed to the incorporation of uranium into sediment components, or that uranium was located on the sediments buried beneath newly formed Fe-oxide precipitates and therefore significantly occluded and thus retarded. This complements recent work mapping the Tims branch and Steed Pond areas using portable gamma and X-ray spectroscopy equipment which showed that the vast majority of the 43.5 metric tonnes of uranium originally released (83%) had been retained in the wetland, with uranium soil concentrations of up to 14099 ppm U seen in one region sampled (Kaplan et al., 2020). Furthermore, the uranium was largely concentrated in the top 25 cm of soil cores collected from the area, highlighting strong retention in the sediments. Despite the reported retention of uranium in these wetland areas, elevated concentrations of uranium have been reported in streams following periods of high rainfall potentially reflecting washout events (Batson et al., 1996). X-ray absorption spectroscopy on samples from these regions were consistent with uranium present as U(VI) (Bertsch et al., 1994; Kaplan et al., 2016) and suggested some sorption

to iron (oxyhydr)oxide phases (Bertsch et al., 1994). Interestingly, Kaplan et al. (2016) provided evidence for the plant root-induced formation of Fe(III)-(oxyhydr)oxide phases that stabilised organic matter. Ultimately they found that uranium was enriched on plant root plaques and associated with phosphorus, however the formation of iron(oxyhydr)oxide phases could also have contributed to the immobilisation of uranium in the surveyed wetland sediments.

2.6 Summary

The Sellafield site in the UK has been shown to be a globally significant location for radioactively contaminated land, with a legacy of radioactively contaminated land and structures posing a series of challenges for the nuclear industry as more sites progress towards decommissioning. Waste management strategies such as in-situ disposal present an opportunity to reduce the volume of waste disposed of off-site and enable the beneficial reuse of materials to aid further decommissioning. Not only will this potentially result in cost saving, both for the site licence companies and the taxpayer, but it has the opportunity to benefit the environment with a reduction in transportation costs (and associated CO_2 burden) for the wastes and potentially a reduction in the dose received by workers. The in-situ disposal of contaminated materials is a new approach which brings with it a need to characterise and fully understand the interactions between radionuclides and the contaminated land environments on site to ensure site end states are achievable and safe. Iron (oxyhydr)oxide minerals including magnetite are likely to be present in the subsurface at nuclear sites either as a result of steel and zero-valent iron corrosion processes on in-situ pipelines or rebar and/or may be present naturally. At the same time, cements and concretes are used widely in the nuclear industry and will constitute a large proportion of the contaminated materials produced as a result of decommissioning, and indeed that could be disposed of in-situ. As uranium is typically the most abundant radionuclide by mass in contaminated land environments, and has a very long half-life, developing an understanding of its long term interactions between engineered subsurface components including steel corrosion products and cementitious materials is a first step in exploring the potential for in-situ disposal. Specifically, building a picture of uranium mobility and speciation in representative engineered subsurface systems will enable technical underpinning of waste disposal and management approaches.

Whilst there is a large body of literature surrounding the interactions of uranium with magnetite and cementitious materials, none of this literature focusses on a field approach to characterisation which can offer a different perspective on the behaviour of uranium in the vadose-zone subsurface at nuclear sites. Therefore, this thesis focusses on uranium interactions with magnetite and concrete in the subsurface using field lysimeter experiments to expose samples to natural environmental conditions such as wet and dry cycles, building on previous laboratory research to help to underpin radioactive waste management strategies such as in-situ disposal.

Blank page

Chapter 3   Research Methods

3.1 Overview

This chapter discusses the details of both field and laboratory experimental methods used to investigate the behaviour and fate of uranium during the in situ experiments performed at the Radionuclide Fate and Transport Experiment (RadFATE) facility which are described in this thesis.

3.2 Reagents and Solution Preparation

All solutions were made using Milli-Q system (18.2 MΩ) deionised (DI) water and chemical reagents used in experiments were all analytical grade. Any glassware used was washed with 5% Decon solution overnight, then 5% Nitric acid overnight and thoroughly rinsed with DI water before use. All experiments were performed under chemical and, if applicable, radiological risk assessments in accordance with The University of Manchester and Clemson University guidelines.

3.3 Lysimeter Experiments

Lysimeter experiments were a key feature of the work undertaken as part of this project. The thesis examines four lysimeter systems under natural environmental conditions (Lysimeter 1: Chapter 4; U(V) incorporated into magnetite system (deployed May 2017-May 2018); Lysimeters 2, 3 and 4: Chapter 5; U(VI) in sediment- and concrete-containing environments (deployed June 2018-August 2019). Lysimeters are used to mimic subsurface environments and provide information on the fate and transport of radionuclides in the vadose zone. Lysimeters are open at the top, meaning the natural environmental and meteorological conditions they are exposed to, help to provide an insight into radioactively contaminated land scenarios at a representative scale and heterogeneity not usually possible with laboratory work. In this work, the RadFATE experimental array at Clemson University (SC, USA) was used (Arai et al., 2018; Kilgo, 2018), which was informed in its design by the Long-term Radionuclide Field Lysimeter Experiment (RadFLEX), a larger scale array based at Savannah River National Laboratory (SRNL) (Kaplan et al., 2006; Miller et al., 2012; Peruski et al., 2018; Powell et al., 2015; Roberts et al., 2012). As a result of the scale and cost of running the lysimeter array, the experiments were performed as single lysimeters in the experimental set up. Generally, these experiments are not replicated but where post-experiment characterisation analyses of the lysimeters took place, samples were duplicated or triplicated to improve reliability of analytical results from the altered lysimeter materials.

3.3.1 Lysimeter facility set-up

The lysimeters consisted of a PVC pipe of either 78 cm or 71 cm length and 10 cm or 15 cm diameter, respectively. Both diameters were used in this project; the larger diameter pipe allows for a greater experimental volume and was used in Chapter 4, whilst the approximately 10 cm diameter pipe was selected for the experiments described in Chapter 5 as it was routinely used for experiments with additional sensors (not included in the experiment outlined in Chapter 4). The lysimeters were housed in a cement-backfilled test bed and held in place by PVC secondary containment embedded in the test bed (Figure 3.1B). To enable water drainage, a polypropylene grid covered in a nylon mesh (0.3 mm, McMaster Carr) was fitted to the bottom of the lysimeter, and held in place by a PVC reducer. Piping leading to high-density polyethylene (HDPE) bottles to collect effluent was attached to the bottom of the reducers.
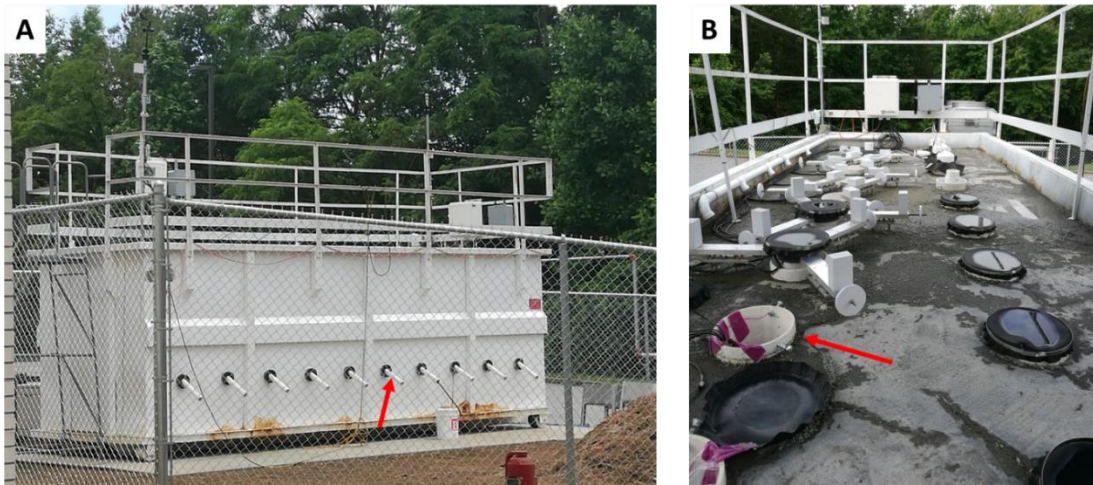
Figure 3.1: Photographs of the field lysimeter RadFATE facility at Clemson University, SC, USA, (A) Side on view of the facility with lysimeter effluent pipes highlighted; (B) View from the top of the facility with secondary containment pipes embedded into the cement-backfilled testbed visible and highlighted with the red arrow.

Lysimeters were fitted with a series of sensors to record a range of in situ geochemical measurements. Each lysimeter was fitted with two soil water potential sensors (MPS-6, METER Group Inc.) measuring water potential (kPa) and temperature (°C). Also fitted were three soil moisture sensors (5TE, METER Group, Inc.) monitoring dielectric permittivity, bulk electrical conductivity (dS m^{-1}) and temperature (°C). Volumetric water content (VWC) was determined using dielectric permittivity (d.p.) from a calibration equation derived for each media the sensors were placed in (either Savannah River Site (SRS) sediment (Chapter 4) or Ottawa sand, Sellafield representative sediment or concrete (Chapter 5)). The calibration equation for SRS sediment has been defined previously (Kilgo, 2018) and the equation is given below (Eq. 3.1). The calibration equations and curves for each of the media used are given below (Eq. 3.2-3.4).

$$\text{VWC}_{SRS\ Sediment} = 100(0.0245(d.p.) - 0.0533)\ (R^2 = 0.9832) \qquad \text{(Eq. 3.1)}$$

Where $\text{VWC}_{SRS\ Sediment}$ is the volumetric water content (expressed as a percentage) of the Savannah River Site sediment used in Chapter 4 and d.p. is the 5TE sensor dielectric permittivity measurement. The VWC of the Ottawa sand used in Chapter 5 was described by a linear fit with an R^2 value of 0.988 (Eq. 3.2).

$$\text{VWC}_{Ottawa\ sand} = 100(0.026(d.p.) - 0.065) \qquad \text{(Eq. 3.2)}$$

Where $\text{VWC}_{Ottawa\ sand}$ is the volumetric water content (expressed as a percentage) of the Ottawa sand and d.p. is the 5TE sensor dielectric permittivity measurement. The VWC of the Sellafield representative sediment used in Chapter 5 was described by a linear fit with an R^2 value of 0.986 (Eq. 3.3)

$$\text{VWC}_{Sellafield\ Sediment} = 100(0.028(d.p.) - 0.066) \qquad \text{(Eq. 3.3)}$$

Where $\text{VWC}_{Sellafield\ Sediment}$ is the volumetric water content (expressed as a percentage) of the Sellafield representative sediment and d.p. is the 5TE sensor dielectric permittivity measurement. The VWC of the Sellafield representative concrete used in Chapter 5 was described by a quadratic fit with an R^2 value of 0.968 (Eq. 3.4). As this material was not sediment/soil/sand, the accuracy of the calibration can be poor and so this needs to be taken into account when interpreting data (Cobos and Chambers, 2010).

$$\text{VWC}_{Concrete} = 100(-0.001(d.p.)^2 + 0.044(d.p.) - 0.082) \qquad \text{(Eq. 3.4)}$$

Where $\text{VWC}_{Concrete}$ is the volumetric water content (expressed as a percentage) of the Sellafield representative crushed concrete and d.p. is the 5TE sensor dielectric permittivity measurement.

Sensor measurements for both lysimeter deployments (Chapter 4: May 2017-May 2018 and Chapter 5: June 2018-August 2019) were recorded every 2 hours, with the exception of power outages at the site. The work described in Chapter 5 also included the addition of 2 x pH and 1 x Eh probes. Positioning of sensors in the lysimeters is detailed in Figure 3.2. Probes were positioned such that they could provide information on the environmentally altered zones surrounding the sources and are consistent with positioning in published work (Peruski et al., 2018). Effluent was collected periodically and analysed for cation content by ICP-MS (Thermo Scientific X-series 2) in addition to pH and dissolved O_2 measurements.
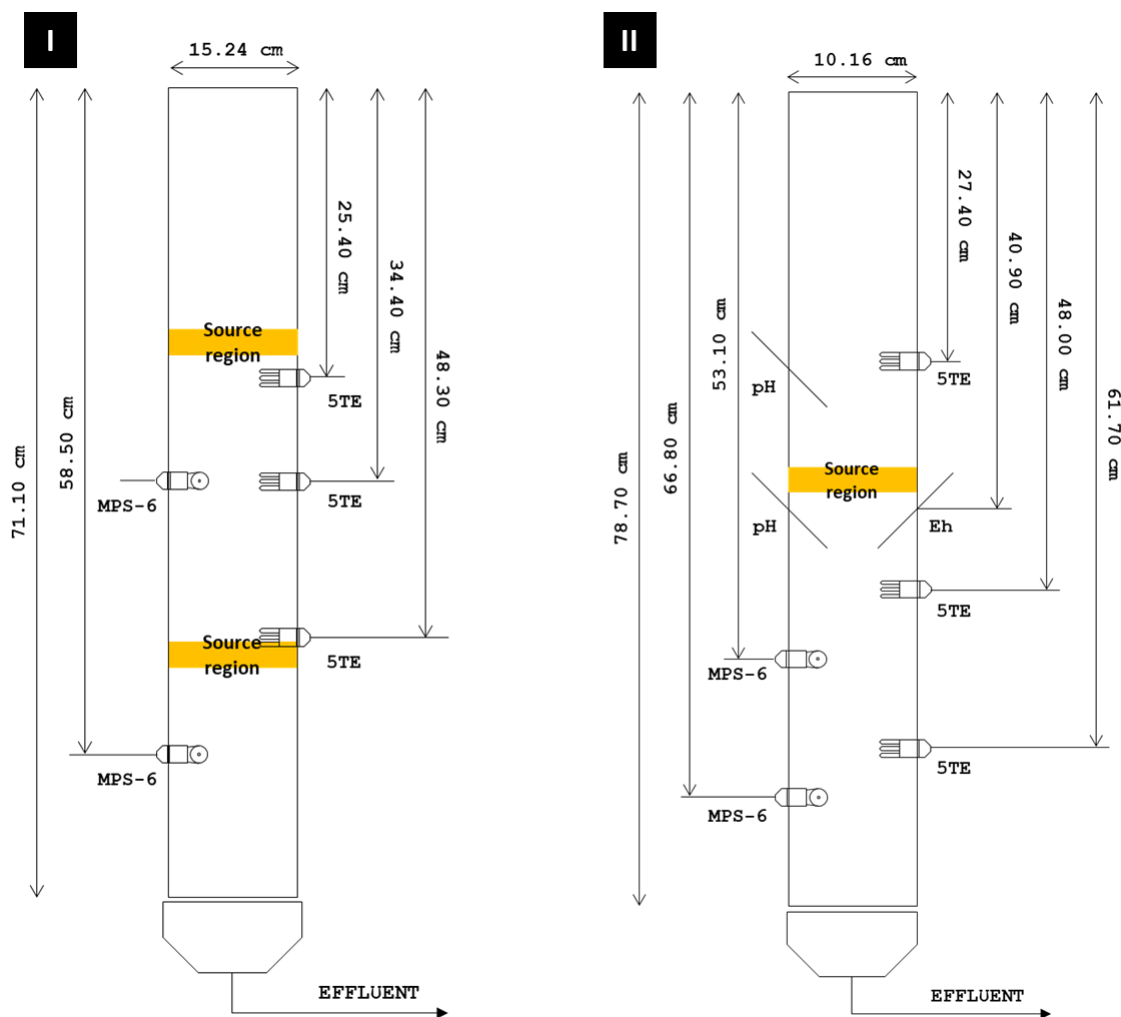
Figure 3.2: Lysimeter schematics indicating the uranium source regions relative to probe depths within the lysimeter. (I) Chapter 4 lysimeter; (II) Chapter 5 lysimeters. Indicated depths relate to the midpoint of probes.

3.3.2 Lysimeter Packing and Source Material Preparation

The lysimeter described in Chapter 4 was packed with sediment representative of the Savannah River Site (SRS), collected from the uncontaminated, well-characterised West Borrow Pit (Montgomery et al., 2017; Peruski et al., 2018; Roberts et al., 2012). Excess debris (e.g. roots, pebbles) were removed and sediment was sieved (1 mm mesh) prior to use in the lysimeter.

Two identical source horizons with U(V)-incorporated into magnetite were emplaced at two depths in the lysimeter. The U-magnetite samples were prepared in Manchester using a method adapted from Pearce *et al.* (2012) and Roberts et al. (2017) and shipped to the RadFATE facility. On site, two identical source horizons were prepared where the pre-prepared U(V)-incorporated into magnetite at a loading of 3000 ppm was mixed with SRS-representative sediment to achieve a final deployment loading of approximately 100 ppm. These horizons were pressed into cylinders (10 x 1 cm) and lowered into the centre of the lysimeter where blank sediment was then used to

pack the approximately 2.5 cm gap between the side of the lysimeter and the source horizons. Lysimeter deployment occurred in May 2017 and was carried out by Dr William Bower, Dr Connaugh Fallon, Professor Brian Powell and Dr Kathryn Peruski. Lysimeter dismantling and all experimental analyses were completed by the author with assistance from Dr William Bower and Dr Connaugh Fallon.

The lysimeters in Chapter 5 were packed with Sellafield representative sediment, collected from Peel Place, Tendley Quarries Ltd, in Holmrook, Cumbria and shipped to the RadFATE facility for May 2018. On-site, the Peel Place sediment was dry screened through a 45 mm screen to remove the larger material before being wet screened over a 6 mm grid and eventually washed and sieved to separate into concrete-grade and fine sand and a silt. Unfiltered water was used for washing and wet screening. The sediment fraction used in these experiments was the concrete grade sand, known to be similar to the subsurface at Sellafield (Dr Nick Smith (NNL), personal communication (2018); Smith et al., 2020). The sediment is largely homogenous with a sandy texture and the presence of small amounts of gravel. The sediment comprises largely of quartz (79%) with feldspars (albite, 6%; microcline, 10%) and a small fraction of mica (muscovite, 4%;) and clay (chlinochlore, 1%). Organic matter content determined by loss on ignition at 550 °C was 0.38(±0.05)% and trace XRF data indicated the presence of 4.8 (±0.4) ppm U in the sediment. Building concrete, sourced from a Nuclear Decommissioning Authority legacy site was also used in these experiments. Concrete was sourced by Dr John Shevelan from a demolished building at the Low Level Waste Repository (LLWR), Drigg, originally built in the 1970s and known to have been constructed in a similar way to buildings on site at Sellafield by using pre-cast units and transporting those to site to allow a quicker construction (John Shevelan, personal communication, 2018). The concrete was in 5-10 kg pieces. Information provided to us from LLWR shows us the concrete comprised Portland cement with no admixtures and with a range of pebble-sized aggregate. The concrete samples were first disaggregated into small clasts, before crushing using a rock crusher, and then sieved to give an aggregate size of 1 mm < 5 mm (Figure 3.3).
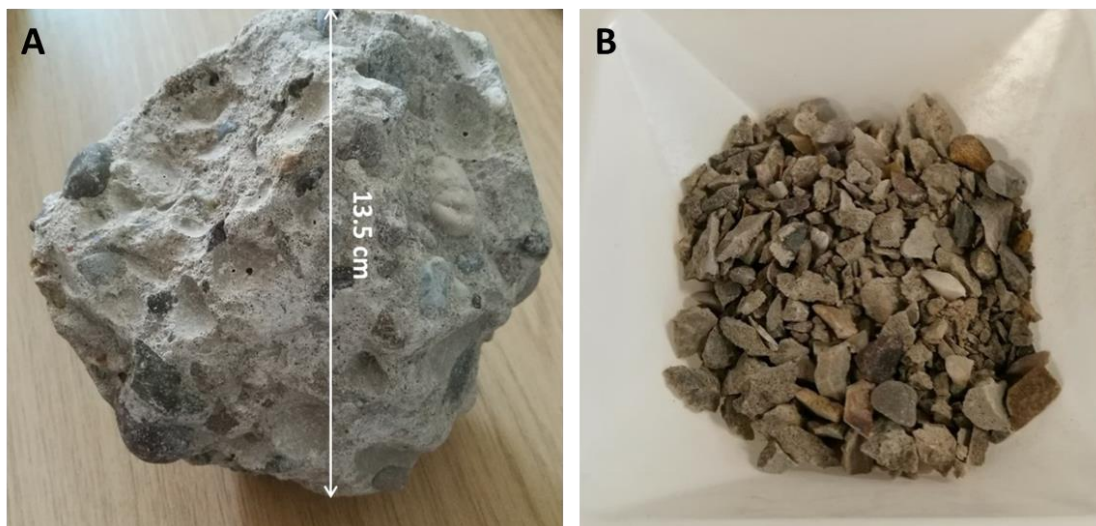
Figure 3.3: (A) Unprocessed concrete sourced from LLWR; (B) 1-5 mm chips of crushed and sieved LLWR concrete

For the uranium sources in the lysimeters described in Chapter 5, both sediment and concrete were used. The target loading for both types of sources was 6000 ppm which was informed by our analysis work using XAS as a sensible compromise between relevant U concentrations and analytically amenable levels of U for X-ray absorption spectroscopy (XAS) and electron microscope (EM) analysis. For the sediment sources, uranyl nitrate salt was mixed with the Peel Place sediment to achieve the required loading and homogenised by manual mixing in a fume hood. The doped sediment was then pressed into a cylinder of approximately 8.5 x 1.5 cm and lowered into the centre of the lysimeter. Blank sediment was added between the approximately 0.5 cm edges of the cylinder and the lysimeter wall.

To prepare the U(VI) doped concrete, uranyl nitrate was dissolved in 20 mL 1 M nitric acid which was added to 20 L deionised water in a carboy, vigorously shaken and left to equilibrate for 24 h. The resultant U(VI) solution was at pH 3 and had 110 ppm U(VI) present in solution. After 24 h, 400 g crushed concrete material (1-5 mm) was added to the U(VI) nitrate solution at pH 3 and the carboy was shaken every hour during working hours for 24 hours. A yellow precipitate was formed in the reaction vessel after 24 h. The supernatant was gently removed using a peristaltic pump and the U doped-concrete was extracted and thoroughly mixed before packaging and shipment to Clemson University. A sub-sample of U doped-concrete was retained for analysis.

At the RadFATE facility, to pack the lysimeter in order to limit preferential flow through the column, sediment and/or concrete was added a few cm depth at a time and the pipe was firmly tapped against the ground repeatedly to bed the sediment down before the addition of more sediment/source material (Peruski et al., 2018).

3.4 Lysimeter Sampling

On completion of lysimeter experiments, the lysimeters were transferred to an argon filled glovebox to provide anaerobic conditions, ensuring preservation of samples. Each lysimeter was sectioned by first cutting along the longitudinal axis. One half was preserved by wrapping in plastic film and storing in a freezer at -40 °C, whilst the other half was sectioned into approximately 1 cm samples (or 2 cm in concrete regions and sediment at the base of the lysimeters; Chapter 5). These samples were double bagged in the anaerobic environment prior to storage and transport back to the UK for analysis. In addition, the source horizons were also sampled using a rectangular steel sampling housing (Chapter 4: 10 x 7 x 2 cm; Chapter 5: 9 x 3.5 x 3 cm) which was gently pressed into the source regions (Figure 3.4). The resultant subsamples, which included the U doped layer as well as approximately 3-6 cm of pre-and post-horizon sediments and/or concrete were stored at -80 °C before shipment to Manchester and resin embedding (Section 3.4.1).

3.4.1 Resin Embedding

Rectangular sections of the source horizons in the magnetite lysimeter (Chapter 4) (Figure 3.4), were resin embedded under anaerobic conditions for preservation in Spurr™ Epoxy resin (Bower et al., 2019; Jilbert et al., 2008). Embedded samples were then used for autoradiography (Section 3.6.4), environmental scanning electron microscopy (ESEM) (Section 3.6.5) and μ-focus XAS analysis (Section 3.7.4).

Figure 3.4: Photographs of the rectangular steel sample housings used to retrieve sections of the source regions, using the magnetite lysimeter (Chapter 4) as an example, showing positioning relative to source horizons (black magnetite layer).

The cut out sediment samples were embedded in an N_2-filled polypropylene glovebox (Bower et al., 2019; Jilbert et al., 2008). The sections were covered with a fine mesh and wrapped in wire to

minimise sample disturbance during the embedding process. Each of the 10 x 7 x 2 cm sections from the experiments was placed into an aluminium foil bath and initially dehydrated with N_2 sparged acetone. The deoxygenated acetone was added to each aluminium foil bath and emptied and replaced with fresh acetone twice daily for 5 days by using a reversible pump system. The baths were then flushed with a deoxygenated Epoxy resin: acetone mix with the proportion of Epoxy resin gradually increasing from 50% to 90% over 8 days, before 2 final replacements with 100% resin. Samples were left in 100% resin for 48 hours before curing for a further 48 hours at 60 °C in a vented oven.

Spurr™ epoxy resin was used due to its durability and stability under synchrotron conditions (Bower et al., 2019). It was prepared in 2 L batches using the components listed in Table 3.1, procured from Electron Microscopy Sciences as a Low Viscosity resin kit.

Table 3.1: Components of the low viscosity Spurr™ epoxy resin kit used to resin embed source horizon samples in Chapter 4.

Component	Code	Volume (L)
Nonenyl Succinic Anhydride	NSA	1.02
Cycloaliphatic Epoxide Resin	ERL 4221	0.71
Diglycidal Ether of Polypropyleneglycol	DER 736	0.25
Dimethylaminoethanol	DMAE	0.02
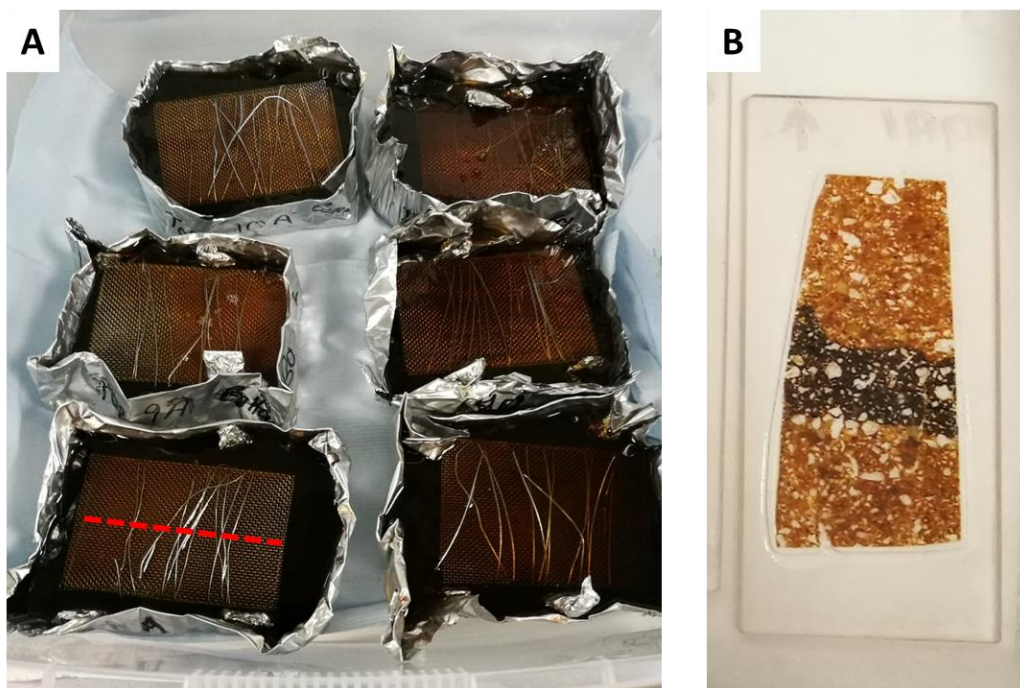
Figure 3.5: (A) Lysimeter sections after being embedded with Epoxy resin in aluminium baths, then cured; (B) Example of a thin section mounted onto a quartz slides (magnetite project, Chapter 4). Red dashed line indicates direction of cutting for thin sectioning

After curing the sediment sections, each sample was cut lengthways in the direction of water flow through the lysimeter (highlighted in Figure 3.5-A) and thin section transects of approximately 100 μm thickness were cut, mounted onto quartz slides and polished. The sectioning, mounting and polishing of the resin-embedded sections were carried out by Stephen Stockley, Department of Earth and Environmental Sciences, School of Natural Sciences, The University of Manchester.

3.5 Geochemical Analyses

The laboratory based techniques used throughout this project to characterise the behaviour and fate of uranium in subsurface contaminated scenarios are described here.

3.5.1 pH

The pH of solutions were measured using a Jenway 3520 pH meter and a Fisherbrand FB68801 electrode. The electrode was rinsed with deionised (DI) water and dried with tissue before each measurement. Before every use, the meter was calibrated using pH 4, 7 and 10 Fluka buffer solutions. For solution measurements, the pH probe was immersed in the solution and readings recorded when the probe gave a stable output. For soil pH measurements, samples were added to DI water in a 1:1 ratio and left for 1 hour to equilibrate before measurement of the solution aliquot (Thomas, 1996). Throughout, pH measurements were quoted to 1 decimal place, assuming an error of ± 0.1 pH unit.

3.5.2 Acid Digestion

The total *aqua regia* extractable uranium and other elemental concentrations (incl. Fe, Mn, Sr, Ca, K) in samples from each lysimeter were determined by digestion of samples in hot *aqua regia*. For the digestions, 0.5 g of sediment from select lysimeter horizons (1 cm in sediments and 2 cm in concrete regions) was accurately weighed out and dried (40 ^{o}C overnight) with both wet and dry weights recorded. The dry samples were then digested in 100 mL beakers with 20 mL of *aqua regia* (3 parts concentrated hydrochloric acid: 2 parts concentrated nitric acid). A watch glass was placed atop each beaker and the solution was gently heated and refluxed for up to 4 hours. The solution was then filtered to remove solids (11 μm, Whatman™ 1001-110) and the residue thoroughly washed with 3M HNO_3. The filtered solution was then heated to almost dryness. The sample was made up into 3 M nitric acid and analysed by ICP-MS after further dilution into 2 % HNO_3.

3.5.3 Acid Dissolution

To further understand the uranium distribution in magnetite-containing samples (Chapter 4), acid dissolution experiments, as a function of H^+ concentration in solution, were performed (Doornbusch et al., 2015; Roberts et al., 2017).

An accurately weighed quantity (approximately 0.1 g dry weight) of each sample was added to a centrifuge tube before the addition of 10 mL of 0.001 M, 0.01 M, 0.1 M, 1 M, 2 M, 4 M and 6 M HCl, sequentially. At each acid concentration, the sample was left on a rotator for 30 minutes at room temperature then centrifuged. The supernatant was carefully removed from the sediment pellet before sequential addition of the next acid. An aliquot of the resultant supernatants were passed through a 0.22 μm filter and acidified into 2 % HNO_3 for Fe and U concentration measurements in solution using ICP-MS. The final 6 M step was reacted for 48 hours to allow complete magnetite dissolution.

3.5.4 Sequential Extractions

Sequential extractions were carried out in Chapters 4 and 5 on sediments and source horizons to further explore the distribution of uranium in the reacted lysimeter materials. Sequential extraction, an indirect speciation technique, involves the addition of increasingly aggressive reagents to sediment samples to determine elemental distribution in the defined leachate fractions which in turn are linked to operationally defined fractions of the sample (e.g. exchangeable, residual etc) (Tessier et al., 1979). The protocol used in this study was adapted from Tessier et al, 1979 using five extraction steps; exchangeable (1 M $MgCl_2$, pH 7), carbonates (1 M NaOAc, pH 5), reducible (0.04 M $NH_2OH.HCl$), oxidisable (30% H_2O_2, pH2; 1 M NH_4OAc) and residual (*aqua regia*, 3 HCl: 2 HNO_3). Again, an accurately weighed sample of approximately 0.5 g sediment was added to a 50 mL centrifuge tube for the sequential extraction procedure. Firstly, 16 mL $MgCl_2$ was added and samples were agitated on a shaker before being centrifuged (10 minutes, 10000 rpm, 11200 g) and an aliquot of the supernatant removed for dilution into 2% HNO_3 and ICP-MS analysis of U. The rest of the supernatant was then carefully removed and the residual sample washed with 10 mL DI water, centrifuged and re-suspended in the next reagent in the procedure. The final step was with *aqua regia* where the procedure used in section 3.5.2 was used. The reagents used and reaction times in each step are described in Table 3.2 below.

Table 3.2: Experimental conditions and reagents used to determine uranium association with mineral phases over five sequential extraction steps. Based on the methods of Tessier et al (1979).

Extraction Step	Reagent	Reaction Time and Temperature
Exchangeable	1 M MgCl$_2$ (pH 7, 16 mL)	1 hour, 20 °C
Carbonates	1 M sodium acetate (pH 5, 20 mL)	5 hours, 20 °C
Reducible	0.04 M hydroxylamine hydrochloride in 25% (v/v) acetic acid (pH 3, 20 mL)	16 hours, 20 °C
Oxidisable	(i) 30% hydrogen peroxide (2 x 5 mL) (ii) 1 M ammonium acetate in 20% (v/v) nitric acid (pH 2, 20 mL)	3 hours, 20 °C 16 hours, 20 °C
Residual	Aqua regia (20 mL)	4 hours, 80 °C

3.5.5 Inductively-Coupled Plasma Mass Spectrometry (ICP-MS)

ICP-MS is widely used in the environmental sciences to determine trace concentrations of analytes in aqueous samples and was used extensively throughout the project to determine the concentration of U and Fe in solution. The technique involves nebulisation of samples, where they are passed through a nozzle at high pressure to generate an aerosol which is injected into an argon plasma, where it is ionised. These ions are passed through cones to alter the pressure from atmospheric to high vacuum for detection and then through a quadrupole mass spectrometer where different voltages are applied and ions are detected based on the mass/charge ratio. The intensity of the ions that reach the detector is proportional to the concentration of that analyte in the sample and is compared to known standards to give elemental concentration. Drawbacks of the technique include a lack of elemental sensitivity at atomic masses around 40 due to interference with Ar$^+$ ions in the plasma and intolerance towards elevated dissolved solids in aqueous samples (Schönbächler, 2016).
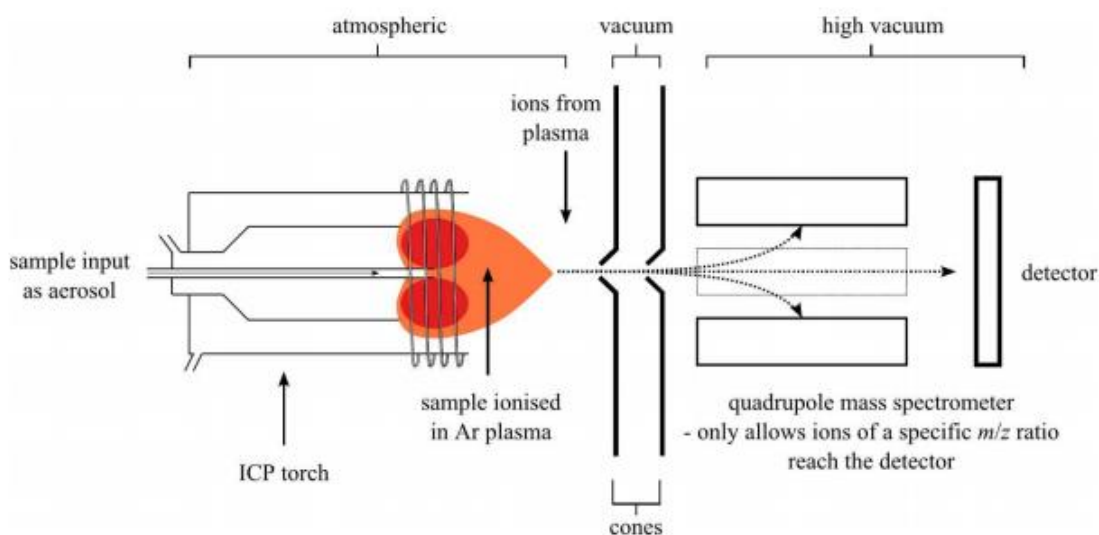
Figure 3.6: Schematic of the key components of ICP-MS (sourced from Smith, 2014).

All ICP-MS sample analyses were carried out in the Manchester Analytical Geochemistry Unit, by either Paul Lythgoe or Ilya Strahovksy, on an Agilent 7500cx ICP-MS using certified reference standards, diluted to a pre-determined threshold. Aqueous samples were diluted and acidified in 2% nitric acid, ensuring the concentration of the analytes was between 1 and 100 µg/L before measurement. Check samples were run routinely throughout the PhD to ensure reproducibility of analyses.

3.6 Solid Phase Analyses

3.6.1 X-ray Fluorescence (XRF)

X-ray fluorescence (XRF) was used to characterise bulk elemental concentrations of lysimeter sections, sediment and concrete samples. Each sample was dried at 40 °C before being ground to a fine powder using a pestle and mortar. 12 g of powder was mixed with 3 g wax and pressed into a homogenous pellet, then analysed using a PANalytical Axios.

When X-rays hit the sample, an inner shell electron is ejected from the atom leaving a vacancy which results in electronic instability. To increase stability, the vacancy is filled by an outer electron from a higher energy shell, simultaneously emitting secondary X-rays; this process is fluorescence. The individual fluorescence energies are specific to each element, producing a characteristic XRF pattern, where peaks are defined by energy and intensity and allow characterisation of samples.

3.6.2 Itrax XRF Core Scanning

An Itrax™ XRF Core Scanner (Cox Analytical Systems) (Figure 3.7) was used to scan undisturbed sectioned cores of the lysimeters in Chapter 5 to give a detailed picture of the U distribution in each system on a much smaller scale than was possible with the bulk aqua regia digestions (Section 3.5.2) and using a non-destructive technique (Löwemark et al., 2019). Approximately 30-40 cm sections of each of the longitudinally sectioned lysimeter cores were scanned at 200 μm resolution down the length of each core, with high resolution optical line scan images, X-ray radiographs and X-ray fluorescence measurements (Mo tube, 30 kV, 40 mA, dwell time 15 s) collected for each lysimeter. The beam width for the XRF elemental analysis was ~2 cm and so the recorded measurements at each 200 μm step were averaged over both space (2 cm) and time (dwell time 15 s) for increased accuracy.
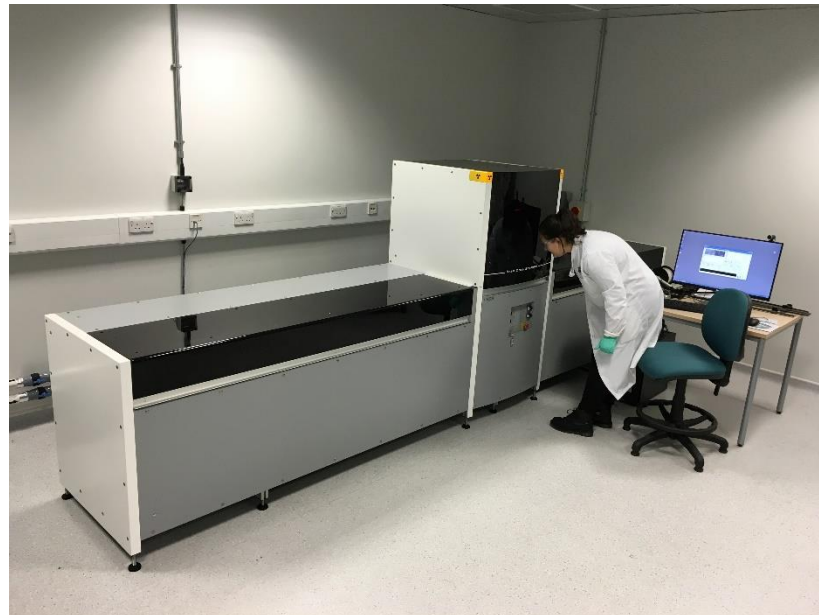
Figure 3.7: Itrax XRF core scanner, capable of 200 μm resolution XRF measurements (sourced from http://blogging2.humanities.manchester.ac.uk/geolabs/lab-equip/itrax/)

For each lysimeter, a layer of Mylar film (1.5 μm) was placed over the half-cores followed by loading onto the scanner rails which enable the samples to be passed through the machine, where the centre of each lysimeter was scanned. Post-analysis, data was processed using ReDiCore (v8.6.0, Cox Analytical Systems) and ItraxPLOT (Croudace and Rothwell, 2015). Dr Thomas Bishop provided access to the Itrax™ XRF scanner and provided assistance with data acquisition and processing.

3.6.3 Powder X-Ray Diffraction (P-XRD)

Powder X-ray diffraction (P-XRD) was used to characterise both starting materials and experimental samples in the projects described in this thesis. It is a non-destructive technique used to determine the crystalline mineral phases present within samples. All minerals have a specific unit cell and crystal lattice with specific lattice spacing (d). X-rays of a specific wavelength (λ) are directed onto a sample and rotated through angles of incidence (θ) from 5° to 70°. This enables a range of lattice spacings to be determined through various diffraction angles, creating a diffraction pattern (Cullity and Stock, 2001). The relationship between d, λ and θ is defined by Bragg's Law (Eq. 3.5).

$$n\lambda = 2d\ \sin\theta \hspace{4cm} \text{(Eq. 3.5)}$$

Where n is an integer. An XRD pattern is produced when the lattice planes are in the correct orientation to diffract (angle of reflection = angle of incidence) (Figure 3.8). Minerals present within a sample are identified by the comparison of the measured lattice spacings with standard reference materials. Here, resultant patterns were evaluated using EVA version 4 which uses standards from the International Centre for Diffraction Data (ICDD) database.
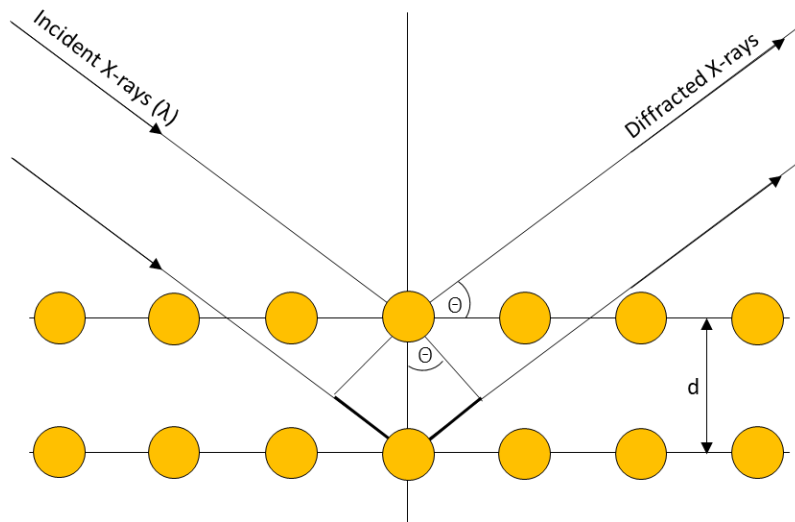
Figure 3.8: Schematic of Bragg diffraction (adapted from Waseda, Matsubara and Shinoda, 2011). The yellow circles indicate atoms present in a sample.

Aerobic samples were prepared by grinding ~0.1 g sample with amyl acetate and suspending onto a glass slide and being allowed to dry in air. As magnetite samples from Chapter 4 were air sensitive, they were ground inside an anaerobic chamber and allowed to dry in the chamber inside a silica-bead box. All uranium-containing and air sensitive samples were analysed using an anaerobic sample holder to prevent both radionuclide contamination of the XRD equipment and

oxidation of samples. Measurements were carried out on a Bruker D8 Advance (λ= 1.5406 Å; Cu K$_{\alpha1}$) diffractometer, equipped with a Göbel Mirror and Lynxeye detector. P-XRD was carried out with the assistance of Dr John Waters.

3.6.4 Autoradiography

Autoradiography was used in Chapter 4 to determine the level of radioactivity in thin section samples of the source horizons. It is a technique that has been used to detect radioactivity using storage phosphor screens, and can be applied to environmental samples (Pöllänen et al., 1999). Here, thin section samples from the source regions of the magnetite lysimeter were exposed to a phosphor storage screen (GE Healthcare) for 2 months before measurement on a Typhoon phosphorimager to determine the location of any radioactivity present within the samples.

Autoradiography is based on the phenomenon of photostimulated luminescence, where radioactivity can be used to stimulate phosphor crystals such as BaFBr: Eu^{2+} (Takahashi et al., 1985), which store energy proportional to the radioactivity present within a sample. Radioactive samples placed onto a phosphor storage screen emit ionising radiation which interacts with Eu^{2+} in the crystal and ionises it to Eu^{3+}. The electron that is emitted is excited to the conduction band of the crystal and trapped in bromine vacancies to form 'F centres' (BaF(Br$^-$): Eu^{3+}) (Upham and Englert, 2003). After a certain amount of exposure time, the phosphor screen can then be exposed to a phosphorimager which scans a red laser (~633 nm) over the surface of the screen. During this process, the electrons are released from the bromine vacancies back to the conduction band of the crystal and an excited state of Eu^{2+*} is formed. When this relaxes back to the ground state, it emits a photon in the visible light range (390 nm), which is detected by a photomultiplier tube and the signal is converted to an image, where both the location and intensity of radioactivity within a sample exposed to the phosphor screen can be analysed. One advantage of this technique is that the storage phosphor screens can be re-used, with exposure to bright light needed to 'erase' the 'image' from any previous samples, however, in the same way, any exposure of the screen to light during sample exposure can erase any accumulated signal (Upham and Englert, 2003). In this work, Image Quant and ImageJ software were used to enhance the brightness and contrast of the autoradiograph of thin section samples so the signal could be clearly seen.

3.6.5 Environmental Scanning Electron Microscope (ESEM)

An ESEM was used in Chapters 4 and 5 to acquire detailed images of sediments, concrete and altered source horizons from thin sections and bulk material. The microscope works by using an atmosphere of water vapour and directing a focused beam of electrons through this onto a

sample. An image is produced through detection of the electrons emitted back from the sample in two modes as the beam is scanned across a sample. Backscattered electron mode works through the detection of high energy electrons emitted following elastic collisions with different atomic nuclei. The higher the atomic number of the nuclei hit, the brighter the ESEM image produced as there is a greater degree of backscattering (Davis, 2005). Secondary electron emission mode produces images that are sensitive to changes in the sample topography, where peaks appear brighter than troughs. Images are resolved through the detection of low energy electrons that are emitted from the sample surface. Energy dispersive X-ray spectroscopy (EDS) which is used to determine sample chemical composition works by using the electron beam to excite electrons in the sample. When these electrons relax back to the ground state configuration they emit X-rays of characteristic energies enabling elemental identification (Brydson, 2011).

Here, an FEI XL30 ESEM-FEG equipped with an EDAX Gemini EDS system was used to obtain images in either secondary electron emission or backscattered electron modes and EDS spectra for samples. Samples were prepared by either loading a small quantity of sample onto a mount, or by directly loading a thin section onto a mount.

3.7 X-Ray Absorption Spectroscopy (XAS)

Various synchrotron-based techniques have been widely used in this project to characterise uranium interactions with mineral phases. The author prepared all samples for XAS and was trained on a number of beamlines to load samples, operate the beamline and acquire data. Beamtime support was provided by Diamond Light Source (DLS) staff (Shu Hayama, Steve Parry, Giannantonio Cibin and Fred Mosselmans), Swiss Light Source (SLS) staff (Peter Warnicke) and also staff from the Synchrotron Radiation Source at KIT (Bianca Schacherl, Jurij Galanzew).

XAS is used to determine the speciation and local coordination environment of an analyte. Only small amounts of sample are needed for these non-destructive techniques (100 mg sample is ample and the analyte can be at tens of parts per million concentration, here, extended analytical times also improved the quality of data collected) which provides an advantage when working with limited or potentially hazardous environmental samples (Schnohr and Ridgway, 2015). Furthermore, crystallinity is not required for XAFS data collection, making it a key tool for environmental scientists working with complex heterogeneous environmental samples. Data is acquired through the use of X-ray light harnessed at specific energies for individual techniques and the X-rays used in the techniques described below utilise synchrotrons. A synchrotron is used to accelerate electrons around a ring to near the speed of light, where a series of bending magnets

are used to distort the electron beam path. This change of direction generates the synchrotron light used in beamline experiments (Schnohr and Ridgway, 2015).

Briefly, electrons are fired into a linear accelerator (linac), from an electron gun, which increases the energy of the electrons up to 100 MeV by using alternating electric fields. The electrons are then further accelerated in a booster ring before injection into the storage ring, where a series of magnetic fields generated by the bending magnets keep the electrons in the ring, producing synchrotron radiation (X-rays) as result (Willmott, 2011). Experimental beamlines at a tangent to the storage ring are specifically set up for the technique being used, for example X-ray absorption spectroscopy, but they each exploit the radiation produced in the ring. At each beamline, the X-ray beam passes through an optics hutch where focusing mirrors and a monochromator can then be used to focus the beam and define the energy of the X-rays at any particular beamline.
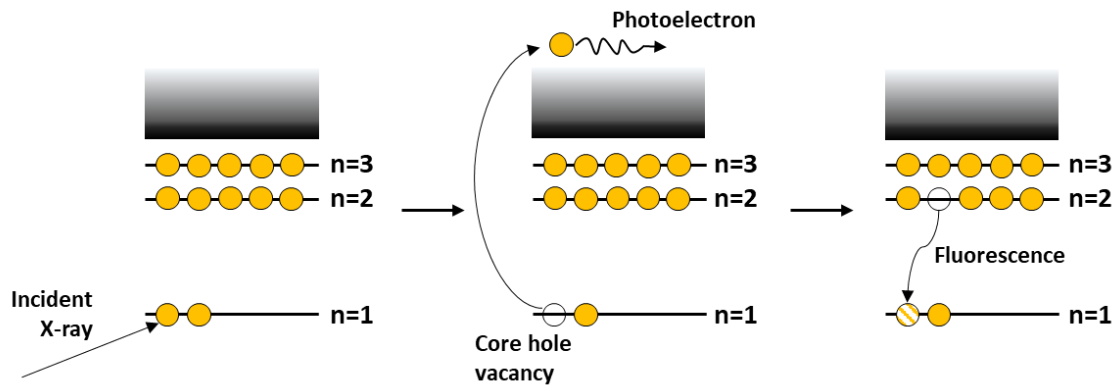
Figure 3.9: A simplified schematic of the interaction between X-rays and core electrons to produce fluorescence

When focussed onto a sample, incident X-rays interacting with the sample excite a core electron from the K, L or M shell into the continuum state, producing a photoelectron, resulting in a core hole vacancy (Figure 3.9). The core electron can only be ejected if the energy of the incident X-ray (I_0) is greater than or equal to the energy required to excite the electron, thereby obeying the Beer-Lambert Law (Newville, 2014) (Equation 3.6).

$$I = I_0 e^{-\mu t} \qquad \text{(Eq. 3.6)}$$

Where μ is the absorption coefficient and t is the sample thickness. The absorption coefficient itself strongly depends on the atomic number (Z) and X-ray energy (E) and so contrast between different materials can be easily achieved for XAS (Newville, 2014). The absorption coefficient is approximately defined by Equation 3.7, where ρ is the density of the sample and A is the atomic mass.

$$\mu \approx \frac{\rho Z^4}{A E^3} \qquad \text{(Eq. 3.7)}$$

After excitation, or absorption, a higher level core electron then fills the core hole vacancy emitting a fluorescent X-ray or Auger electron in the process (Calvin, 2013). All elements have core electrons in the K, L and M shells with defined binding energies which are dependent on the oxidation state of the absorbing atom. This defined energy is a function of the absorption coefficient, μ, and is known as the absorption edge, $\mu(E)$. By adjusting the energy of the incident X-ray, specific electronic transitions can be targeted; for example, the L_3 and M_4 edges of uranium can be targeted in this way to probe slightly different information related to the principle quantum number (n) of the electron orbital (L edge, n=2; M edge, n=3). By increasing the incident energy step-wise beyond the targeted absorption edge, the associated XAS spectrum is produced (Calvin, 2013). The absorbance of concentrated samples is measured by comparing the intensity of the transmitted beam (I_t) to that of the incident beam (transmission mode) and can be converted to $\mu(E)$ using the equation:

$$\mu(E) = \ln\left[\frac{I_0(E)}{I_t(E)}\right]$$

(Eq. 3.8)

Absorbance can also be quantified through the measurement of fluorescence (FF) registered through a fluorescence detector (fluorescence mode) placed at 90° to the sample and incident beam (Equation 3.9). In this project, dilute samples or samples with a complicated sample matrix such as iron oxides were collected in fluorescence mode. $\mu(E)$ can be determined through the following equation:

$$\mu(E) \propto \frac{FF}{I_0}$$

(Eq. 3.9)

Standard reference foils were also used to calibrate the energy of collected data and allow calibration and thus different spectra, to be compared to each other.

XAS spectra can be divided into 3 main regions (Figure 3.10). The region before the absorption edge generally does not produce any features with uranium and is where excitation of electrons to the lowest partially unoccupied level occurs. In an XAS spectrum, the absorption displays a downward trend with increasing energy. The slope of this region can be used to normalise data when compared to the data collected after the absorption edge. The X-ray absorption near-edge structure (XANES) region is characterised by a sharp increase in absorption (the absorption edge) which corresponds with the energy at which a core electron is excited to the continuum state and extends to up to ~50 eV above the absorption edge. The oscillations in the spectra after the XANES region relate to information on the bonding environment and local coordination and is known as the extended X-ray absorption fine structure (EXAFS) region, where the resultant spectra is a combination of the constructive and destructive interference of the wave emitted from the central and neighbouring atoms (Schnohr and Ridgway, 2015).
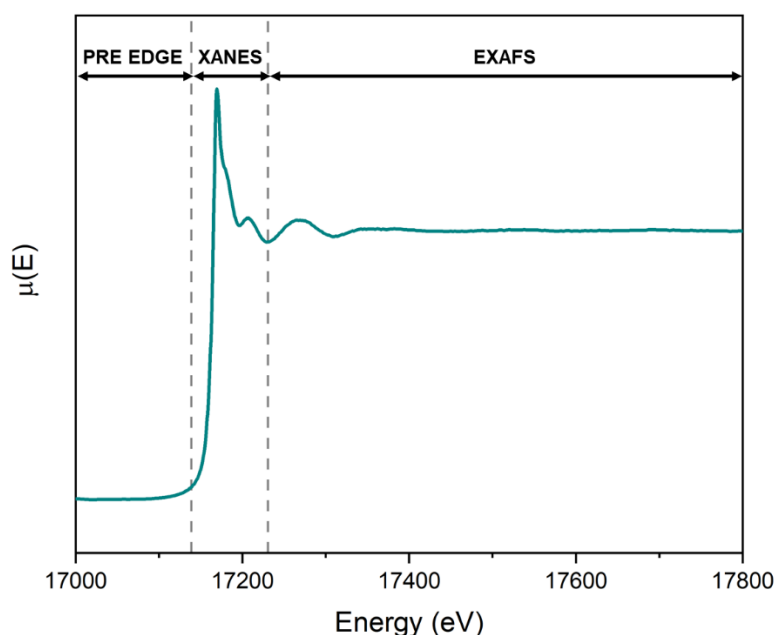
Figure 3.10: U L$_3$ edge normalised XAS spectra, with the pre-edge, XANES and EXAFS regions highlighted

Athena and Artemis software (Ravel and Newville, 2005) can then be used to process the data produced at a beamline. Here, Athena was used to normalise XAS spectra, and if required, to remove any glitches in the data, whilst Artemis was used to create a model based on the data and reference spectra.

3.7.1 L$_3$ edge Uranium XANES

The L$_3$ edge of uranium corresponds to the $2p^{3/2}$ electron excitation at ~17200 eV (Thompson et al., 2009) and can be used to gauge oxidation state and local coordination. The position of the absorption edge feature in an XAS spectrum is indicative of the oxidation state of the element of interest (Penner-Hahn, 2004) and so calibration to a known standard that does not have multiple oxidation states (eg. Y-foil) is essential when comparing samples to others and to the literature. The relationship between the position of the edge and the valence state is as a result of the Coulomb effect, whereby an atom with a greater charge density, and therefore higher binding energy of the core electrons is shifted to higher energy in the XAS spectra (Newville, 2014). Local coordination environment can also be determined through XANES; oscillations in the post-edge region arise from scattering off neighbouring atoms, for example, features *a* and *b* in the U(VI)-uranyl spectrum in Figure 3.11 correspond to the axial and equatorial oxygen atoms that are present, respectively. Through visual, qualitative analysis, it is possible to determine the species present through analysis of the edge shape (white line) coupled with the edge position. Feature *a* is typically present in uranyl species, and arises from the scattering of the neighbouring uranyl axial oxygen atoms. In contrast, this feature does not manifest in uranate species, such as the U(V)-incorporated into magnetite standard in Figure 3.11, or in U(IV) uraninite (Figure 3.11),

which do not contain any axial oxygen atoms and so do not display the shoulder-like feature (*a*) exhibited by U(VI)-uranyl.
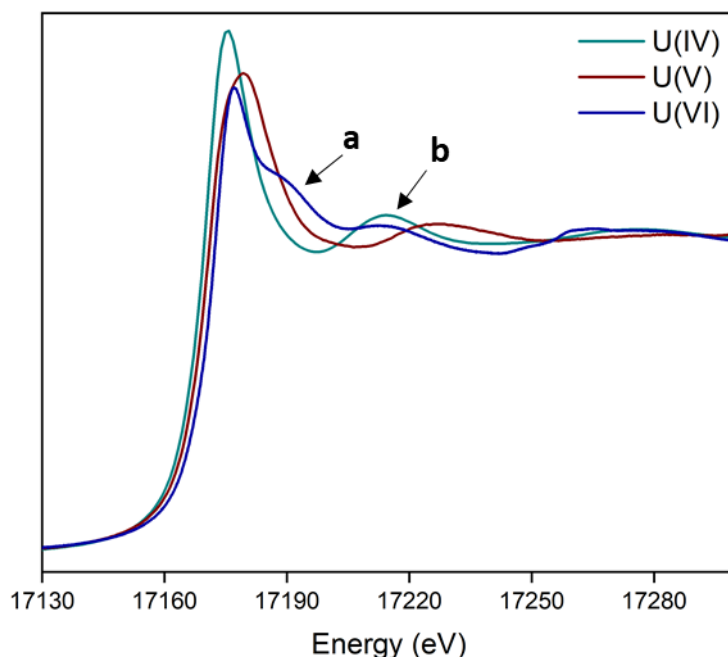
Figure 3.11: U(IV) uraninite , U(V) and U(VI) schoepite XAS spectra with typical features highlighted

For uranium at the L_3 edge, the shift in energy between U(IV) and U(VI) oxidation states is relatively clear (Figure 3.11), however identifying U(V) species using U L_3 edge XANES is more challenging due to the similar edge positions of U(VI) and U(V) (Kvashnina et al., 2013). For this reason, M_4 edge high-energy-resolution fluorescence detection-XANES (HERFD-XANES), a relatively newly explored technique for U oxidation state analyses (Bès et al., 2016; Pidchenko et al., 2017; Podkovyrina et al., 2016; Roberts et al., 2017; Zimina et al., 2016), was also used in this thesis to accurately distinguish between U(VI) and U(V) in Chapter 4 and U(VI) uranyl and uranate in Chapter 5 (Further detail in Section 3.7.2).

In this thesis, beamlines I20 (Diaz-Moreno et al., 2009) and B18 (Dent et al., 2009) at the Diamond Light Source, UK, were used to collect data for Chapters 4 and 5. Beamline I20 in scanning mode was used to collect data on samples with lower uranium concentrations in this thesis, with a cryostat used to increase the quality of data. Beamline B18 differs from I20 by collecting Quick EXAFS (QEXAFS) data, where data is collected in continuous scan mode (Dent et al., 2009).

Here, Athena (Ravel and Newville, 2005) was used to pre-process data collected at beamlines I20 and B18. In Athena, multiple scans of a sample can be merged and aligned to reference spectra, with options to deglitch or spline data if required before background subtraction. The absorption edge, E_0, can be selected, and here the peak of the first derivative was used to ensure consistency between samples. Background subtraction, which can affect the EXAFS region of the spectra,

involves linear regression by selection of two points in each of the pre- and post-edge zones. To improve the data quality, significant glitches can be truncated, and at high k can be improved by the application of spline clamps, however this process does cut down the amount of usable data. The EXAFS Fourier Transform (R-space) can also be viewed in Athena which provides insight into the approximate radial distribution (Å) of atoms.

Once aligned to reference spectra and background subtracted, linear combination fitting (LCF) of a spectrum in Athena can be used to determine approximate composition of a sample with mixed phases using end member standards. In this thesis, LCF was carried out using group uraninite (U(IV)) and schoepite (U(VI)) standards and a published U(V)-incorporated into magnetite standard (Roberts et al., 2017) used. Experimental end members in Chapter 5 were also used to provide a semi-quantitative understanding of mixed U(VI) uranyl and uranate phases. Linear combination fitting is subject to uncertainty of approximately ±10-15 % (Boyanov et al., 2007).

3.7.2 M_4 edge Uranium HERFD-XANES

The ability to distinguish between oxidation states using L_3 edge uranium XANES can often be difficult due to the small differences in edge positions of U(IV), U(V) and U(VI) (~1 eV) (Conradson et al., 2004). Recently, advances in high-energy resolution fluorescence detection XANES (HERFD-XANES), or HR-XANES, at the lower energy (3.5 - 3.7 keV) uranium M_4 edge have shown that the oxidation states, including U(V), can be more easily distinguished including in samples with environmentally relevant concentrations of U present (Figure 3.12) (Kvashnina et al., 2013; Pidchenko et al., 2017; Roberts et al., 2017; Vettese et al., 2020). Similarly, structural differences between uranyl and uranate samples can also be easily identified, with a shift of the main resonance peak to slightly higher energy seen for uranate samples, comparative to uranyl (Podkovyrina et al., 2016). The higher resolution data in comparison with L_3 edge XANES is a result of the reduced core-hole lifetime broadening effects with M edge analysis (Bès et al., 2016; Glatzel and Bergmann, 2005; Kvashnina et al., 2013).
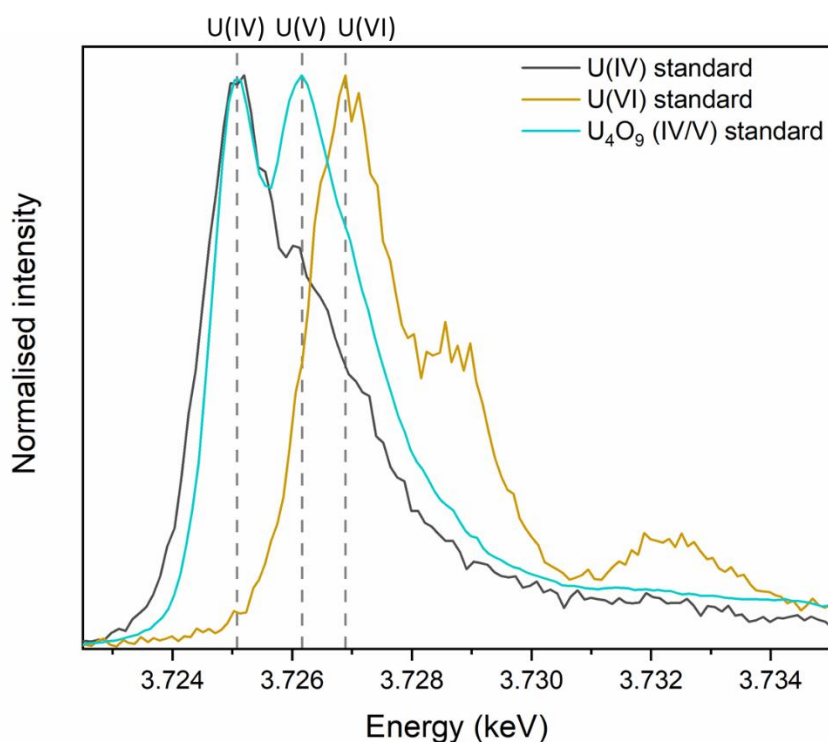
Figure 3.12: Uranium M_4 edge spectra for U(IV) uraninite, U(IV/V) U_4O_9 and U(VI) schoepite standards with dashed lines highlighting the edge position of each standard.

In this thesis, data were collected on the CAT-ACT beamline at KIT Synchrotron Radiation Source (Zimina et al., 2017, 2016), which differs slightly in set-up compared to beamlines B18 and I20 discussed previously (Section 3.7.1). The detector (KETEK silicon drift detector), sample and 5 spherically bent crystal analysers (Si(220) crystals, 75° Bragg angle) were positioned on a Rowland circle (1 m radius) (Figure 3.13) and U M_4 edge HERFD-XANES spectra were collected by recording the intensity as a function of incident energy of the U M_β emission line. As this technique used soft X-rays (~3.7 keV), to ensure significant flux for data collection and avoid loss of intensity through X-ray absorption by air, the sample stage, crystal analysers and detector were placed under a He atmosphere. Calibration of the double monochromator was achieved through the collection of U M_4 edge HERFD-XANES spectra of a known UO_2 sample and calibrating the white line maximum to 3.7252 keV.
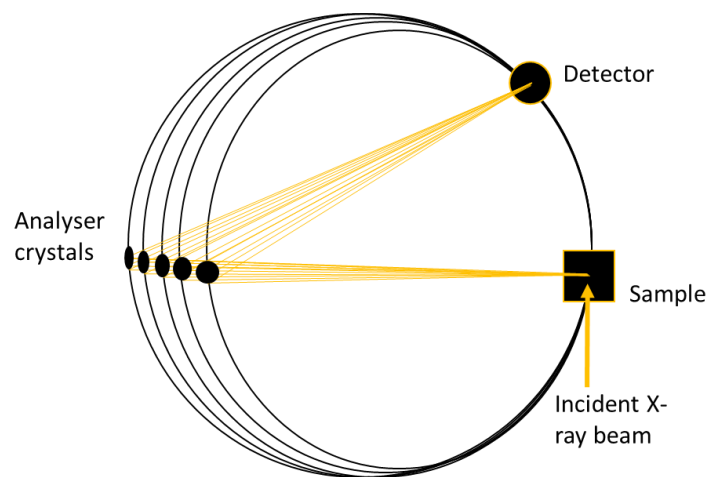
Figure 3.13: Simplified schematic of the experimental set-up used for M_4 edge HERFD-XANES adapted from Glatzel and Bergmann, (2005).

Here, data were background subtracted and normalised using PyMCA (Solé et al., 2007) and Iterative Transformation Factor Analysis (ITFA) (Rossberg et al., 2003; Solé et al., 2007) was used to quantify oxidation states within mixed valence samples using U(IV), U(V) and U(VI) standards in Chapter 4, and to quantify structural differences in samples in Chapter 5, where uranate and uranyl end member standards were used (Podkovyrina et al., 2016).

3.7.3 EXAFS

The EXAFS signal is generated through interactions of the ejected photoelectron from the central atom, which acts as a wave that radiates in all directions, interacting with neighbouring atoms, resulting in a series of single and multiple backscattering events (Newville, 2014; Willmott, 2011). The backscattered photoelectrons can have both constructive (increased oscillations) and destructive (decreased oscillations) interference with the original photoelectron. As EXAFS depends on the wave-like photoelectron ejected during absorption, it is referred to in terms of wavenumber, k, defined by:

$$ k = \sqrt{\frac{2m(E-E_0)}{\hbar^2}} \qquad\qquad \text{(Eq. 3.10)} $$

Where *m* is the mass of an electron, *E* is the incident energy, E_0 is the absorption edge energy and $\hbar = h/2\pi$, where *h* is Planck's constant (Newville, 2014). The oscillations in $\chi(k)$ are a function of the photoelectron wavenumber with amplitude decreasing with increasing k and so $\chi(k)$ is often multiplied by a power of 3 to emphasise the oscillations in the spectrum. An EXAFS spectrum is produced through the changes in absorption probability as a result of various interference patterns and corresponds to the structure between neighbouring shells and is modelled by the following equation:

$$\chi(k) = \sum_j \frac{S_0^2 N_j f_j(k)}{kR_j^2} e^{-2k^2\sigma_j^2} e^{-2R_j/\lambda_j} \sin[2kR_j + \delta_j(k)] \qquad \text{(Eq 3.11)}$$

Where S_0^2 is the amplitude reduction factor which approximates the loss in photon intensity due to relaxation, N_j is the coordination number of neighbouring atoms j in a shell; $f(k)$ is the scattering amplitude, R is the average interatomic distance between the central absorber and the scattering atoms; σ^2 is the Debye-Waller factor and represents the mean-square disorder of the interatomic distance which can be reduced in samples by lowering the temperature; $\lambda(k)$ in the mean free path length and $\delta(k)$ is the phase shift resulting from backscattering. Each ejected photoelectron has a finite lifetime with a mean free path of approximately 8 Å; the factor e^{-2R_j/λ_j} represents this mean free path. An approximate radial distribution function can be determined through applying a Fourier transform to a k^3 weighted spectra. This produces a spectrum where the peaks correspond to backscattering shells. Samples do not need to be crystallographic for EXAFS as it deals only with local coordination environment, however EXAFS spectra are as a result of averaged configurations as it is a bulk technique and so variances in atomic environment, particularly relevant to these complex environmental systems, will be averaged out in the spectrum.

3.7.3.1 EXAFS Fitting

To generate a model, Crystallographic Information Files (CIFs) that provide structural data from standards are imported into Artemis and compared to pre-processed sample data by varying certain parameters. The CIFs themselves can be altered to produce scattering paths for compounds that do not have a CIF available but will help in the production of a model. For example, in Chapter 4, the magnetite CIF file was altered to generate scattering paths for uranium incorporated into magnetite, by replacing the central Fe atom with a U atom and altering the core hole to L_3 prior to FEFF6 calculations. Similarly, in Chapter 5, the CIF for clarkeite was altered by replacing Na with Ca or K to test whether the fit could be improved by the inclusion of a different cation. Once suitable standards have been selected, the variables E_0, S_0^2, N, R and σ^2 (defined above in 3.7.3) can be parameterised and fitting involves the iterative changes to these variables to optimise the fit.

Artemis software was used to fit EXAFS data in this work, where models from relevant scientific literature were used as starting points to generate a fit and coordination numbers (N) were refined until a satisfactory fit was achieved (Chapter 4) or, where shells were added sequentially, informed by literature (Chapter 5). Fits were included only if they had realistic σ^2 values, bond lengths and coordination numbers (informed by literature) and had fewer variables than independent points. The R-factor was also reviewed for each fit and gives an assessment of the

'goodness of fit' by comparison of how closely the model fits the data (Equation 3.12) (Calvin, 2013). Generally, an R-factor of less than 0.02 is considered to be a good fit. F-tests were also performed to test the statistical significance of fits (Downward et al., 2007), and where additional shells or added parameters did not statistically improve the fit, they were not included.

$$R = \frac{\sum_{i=1}^{N}(data_i - fit_i)^2}{\sum_{i=1}^{N}(data_i)^2}$$ (Eq. 3.12)

3.7.4 µ-Focus X-Ray Fluorescence Spectroscopy (XRF)

µ-focus XRF is a technique through which elemental 'mapping' of samples can be achieved by rastering a micro-focused beam at a specific energy across samples and detecting the emission of X-rays characteristic of a certain element. This technique cannot be used to quantify elemental concentrations without a calibration standard, which were not used here, and so maps denote relative concentrations of elements only.

The X05-LA micro-focus beamline at Swiss Light Source was used for µ-focus XRF measurements of samples from Chapter 4, using a KETEK GmbH silicon drift detector. Maps were collected at ~17.6 keV with beam sizes of 1 µm for fine maps and approximately 25 µm for coarse maps. Generally, data from a range of larger sample areas were first collected and areas of interest from these were selected for analysis using a smaller beam size to collect fine maps. Beam dwell time at each sample point was 0.1 s to ensure beam damage did not occur. Spot µ-XANES using a defocused beam (25 µm) were then collected on areas with comparatively high U concentrations. Autoradiography on thin section samples, whose preparation was described earlier, in Section 3.4.1, was used to pin-point areas with higher uranium concentrations for analysis on the X05-LA beamline. Prior to shipment and analysis, the thin sections were covered in a layer of Kapton tape, acting as a containment layer. PyMCA software (Solé et al., 2007) was used to process the map data and Athena was used for µ-XANES processing.

3.7.5 X-Ray Magnetic Circular Dichroism (XMCD)

XMCD was used in Chapter 4 to obtain information on the magnetic behaviour of each source horizon to determine any change in magnetite speciation. An XMCD spectra is generated by taking the difference between two XAS spectra in opposing magnetic fields of left and right circularly polarised light, in this case at the Fe $L_{2,3}$ edges at ~700 eV (Figure 3.14) (Equation 3.13).

$$\Delta\mu = \mu^+ - \mu^-$$ (Eq. 3.13)

Where, $\Delta\mu$ is the difference in absorption between two absorption spectra in opposing magnetic fields (μ^+ is the parallel circular polarisation vector and μ^- is the antiparallel circular polarisation

vector). L edge XAS spectra for iron and other 1st row transition metal elements, which correspond to the dipole-allowed 2p-3d electronic transition, are dominated by 2 main peaks corresponding to the L_3 and L_2 edges. These two peaks are a result of spin-orbit coupling, where the intensity of the two peaks are related to the number of core holes (Kowalska et al., 2017). For magnetite, the intensities of the multiplet structure of the L_3 edge XMCD is related to the amounts of Fe present in the three different Fe octahedral and tetrahedral sites (d^6 O_h, d^5 O_h and d^5 T_d) (Figure 3.14) (Pattrick et al., 2002). This dependence on the local electronic structure means the XAS spectra are sensitive to oxidation state and local symmetry and, in this thesis, could therefore garner information relating to any Fe speciation changes in magnetite-sediment samples (Chapter 4) by comparing the intensities of these peaks to a magnetite standard.
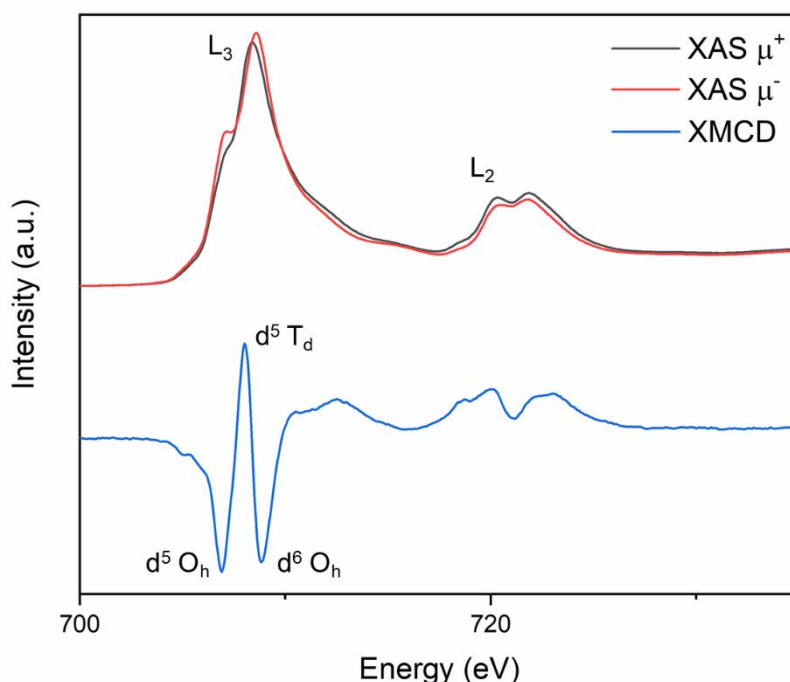
Figure 3.14: XMCD difference spectra and corresponding XAS spectra in opposing magnetic fields for a magnetite sample. The main L_3 and L_2 edge peaks are highlighted as well as the features of the L_3 edge that correspond to Fe sites.

XAS and XMCD measurements were obtained at Advanced Light Source, Berkeley, CA on beamline 6.3.1.1. XAS was measured at the Fe $L_{2,3}$ edges for two opposing magnetising directions by reversing an applied field of 0.6 Tesla. A non-linear least squares analysis using calculated spectra was used to fit the XMCD spectra to obtain the relative proportions of Fe(III) O_h, Fe(III) T_d and Fe(II) O_h (Pattrick et al., 2002; Van Der Laan and Kirkman, 1992; Van der Laan and Thole, 1991). Data was collected and processed by Dr Vicky Coker.

3.8 Geochemical Modelling

PHREEQC is a freely distributed software program from the U.S. Geological Survey that can perform a wide array of aqueous geochemical calculations based on a variety of different inputs. In this thesis, PHREEQC (v3.6.2) (Parkhurst and Appelo, 2013) was used alongside wet geochemical and XAS techniques to aid our understanding of the lysimeter systems in Chapter 5. Saturation with respect to solid phases and solution speciation modelling calculations were performed using model porewater solutions for the lysimeter systems. PHREEQC works by creating input files using keyword data blocks that are run using a database of known solubility products and stability constants for environmental reactions; here the ANDRA SIT database (ThermoChimie v10a 2018) was used for all calculations. An example PHREEQC input file to calculate U(VI) speciation and saturation in a circumneutral pH U-sediment system, using the 'SOLUTION' keyword data block, is given below in Figure 3.15.

```
SOLUTION 1
temp 25
pH 6.8
Na 1.49 mmol/kgw
K 0.13 mmol/kgw
Mg 0.23 mmol/kgw
Ca 0.68 mmol/kgw
S(+3) 0.26 mmol/kgw
N(+5) 0.27 mmol/kgw charge
Cl 1.48 mmol/kgw
C(+4) 0.96 mmol/kgw
U(+6) 2.84 mmol/kgw
```

Figure 3.15: Example PHREEQC input file using the 'SOLUTION' keyword data block to calculate the speciation and saturation of a solution containing U(VI) (25 °C, pH 6.8, 2.84 mmol U(VI)/kg water).

Blank page

Chapter 4

The behaviour and stability of U(V) incorporated into magnetite in field lysimeter experiments

Manuscript in preparation for submission to ACS Earth and Space Chemistry. Supporting information for this manuscript can be found immediately after this Chapter.

The behaviour and stability of U(V) incorporated into magnetite in field lysimeter experiments.

[1] Alana E. McNulty, [1] Sam Shaw, [2] Brian Powell, [1,3] Gareth T. W. Law, [1,3] William R. Bower, [2] Kathryn Peruski, [1] Connaugh M. Fallon, [1] Victoria Coker, [4] Peter Warnicke, [5] Liam Abrahamsen-Mills, [6] J. Frederick W. Mosselmans, [1] Hannah Roberts and [1] Katherine Morris

[1]Research Centre for Radwaste Disposal and Williamson Research Centre for Molecular Environmental Science, Department of Earth and Environmental Sciences, The University of Manchester, UK

[2]Department of Environmental Engineering and Earth Sciences, Clemson University, USA

[3]Laboratory of Radiochemistry, Department of Chemistry, University of Helsinki, Finland

[4]Swiss Light Source, Paul Scherrer Institute, Villigen, Switzerland

[5]National Nuclear Laboratory, UK

[6]Diamond Light Source Ltd, Diamond House, Harwell Science and Innovation Campus, Didcot, UK

4.1 Abstract

Understanding the interactions between iron (oxyhydr)oxides, ubiquitous in engineered and natural environments, and uranium, a priority radionuclide at many nuclear sites, is important in developing an understanding of site end states, where the two are often co-located. Here, we explored the speciation and fate of U(V)-incorporated magnetite on exposure to environmental conditions in an outdoor field lysimeter at the Radionuclide Fate and Transport Experiment (RadFATE) facility over approximately 12 months. U(V)-incorporated magnetite was emplaced in a sediment packed lysimeter in two distinct upper and lower sediment horizons and a multi-technique approach was used to examine the fate of uranium after exposure, combining geochemical characterisation with a range of X-ray absorption spectroscopy (XAS) techniques. XAS results showed significant oxidation of the U(V)-incorporated magnetite to U(VI) in both upper and lower source horizons, where incorporated U(V) was also observed. Despite significant oxidation, uranium remained largely co-located with iron in the source regions and no significant transport of uranium occurred. These experiments demonstrate the need for field scale studies to develop a thorough understanding of the transport and fate of radionuclide source terms in the environment, in addition to highlighting the environmental stability of U(V) when incorporated into iron (oxyhydr)oxides.

4.2 Introduction

Globally, both the nuclear fuel cycle and military activities have left a significant legacy of radioactively contaminated land. Nuclear sites including Hanford, US, Savannah River Site, US, Sellafield, UK, and a range of sites associated with uranium mining, have large volumes (typically in the order of millions of m^3) of radioactively contaminated land as a result of legacy operations, (Catalano et al., 2004; Gómez et al., 2006; IAEA, 1989; Mihalík et al., 2011; National Research Council, 1999; OECD, 2014; Riley and Zachara, 1992; Um et al., 2010) with significant cost associated with their clean-up. Typically, uranium is the most significant radionuclide contaminant by mass in soils, sediments and groundwaters at nuclear sites (IAEA, 1989; Riley and Zachara, 1992; Sellafield Ltd., 2016). Uranium and iron are often co-located at nuclear facilities, with metallic iron and iron oxides ubiquitous in engineered subsurface environments. The interactions of U and Fe in-situ need to be understood over extended periods to enable safe and efficient site management, decommissioning and clean up. Indeed, structural iron in buildings, pipework and made ground will be subject to corrosion processes, producing a range of iron oxides, including magnetite (Fe_3O_4) in engineered environments where uranium and other radionuclides (e.g. [137]Cs and ^{90}Sr) are significant contaminants (Dodge et al., 2002; McGill et al., 1976; Musić et al., 1993). The interaction of uranium with these iron-bearing phases has the potential to sequester and retain this radionuclide within subsurface systems e.g. soils and sediments. This retention may significantly limit uranium migration and potentially allows the contamination to be managed in situ without the need for ex situ disposal (e.g. dig and dump).

In terms of environmental chemistry, uranium behaviour is impacted by both pH and redox processes. Under oxic conditions, U(VI) dominates as the uranyl cation (UO_2^{2+}), which is soluble under circumneutral to acidic conditions (Newsome et al., 2014). At circumneutral pH and above, carbonate present in groundwater contributes to the environmental behaviour of uranium, whereby stable aqueous uranyl tris-carbonate species (eg. $UO_2(CO_3)_3^{4-}$) dominate and can increase the mobility of uranium in the subsurface (Bernhard et al., 2001; Clark et al., 1995; Kalmykov and Choppin, 2000; Krestou and Panias, 2004). The environmental mobility of U(VI) in oxic conditions is typically controlled by adsorption to minerals and subsurface components including iron (oxyhydr)oxide phases (Bargar et al., 2000; Boland et al., 2011; Hsi and Langmuir, 1985; Moyes et al., 2000; Rossberg et al., 2009; Um et al., 2008; Waite et al., 1994). In addition, sequestration of U(VI) by its incorporation into Fe(III) bearing (oxyhydr)oxides such as goethite (α-FeOOH), lepidocrocite (γ-FeOOH), magnetite (Fe_3O_4) and hematite (Fe_2O_3) has also been reported (Duff et al., 2002; Ilton et al., 2012; Kerisit et al., 2016; Marshall et al., 2014a; McBriarty et al., 2018; Mei et al., 2018; Nico et al., 2009; Stewart et al., 2009). In these studies, U(VI) is typically reported as being structurally incorporated via substitution for Fe(III), often in a uranate-

like coordination (Duff et al., 2002; Ilton et al., 2012; Marshall et al., 2014a; McBriarty et al., 2018; Nico et al., 2009).

Outside of mixed-valence U-oxide phases including U_3O_8 and U_4O_9, U(V) was traditionally thought to be transient under aqueous environmental conditions. For example, during biological U(VI) reduction, U(V) was reported as an intermediate which readily disproportionates to U(VI) and U(IV) (Jones et al., 2015; Renshaw et al., 2005; Sundararajan et al., 2008) however more recent work has shown that during biogenic U(VI) reduction, the U(V)-uranyl intermediate species is potentially stabilised by interacton with nanoparticulate UO_2 (Vettese et al., 2020). At the same time, a range of studies have identified U(V)-uranyl species across relevant environmental conditions including in solution in the presence of carbonate (Docrat et al., 1999; Ikeda et al., 2007; Madic et al., 1983), on mineral surfaces (Ilton et al., 2004; Skomurski et al., 2011; Yuan et al., 2015) and in the presence of nano zero valent iron (Tsarev et al., 2017, 2016). Furthermore, experimental and modelling work studying incorporation of U into iron oxides including hematite, goethite, green rust and magnetite highlights U(V) as a stable incorporated species (Bender and Becker, 2019; Boland et al., 2014; Dewey et al., 2020; Huber et al., 2012; Ilton et al., 2010, 2012; Kerisit et al., 2016; Marshall et al., 2015; Massey et al., 2014; McBriarty et al., 2018; Pidchenko et al., 2017; Roberts et al., 2017; Townsend et al., 2021).

U interactions with magnetite are complex with both reduction of U(VI) to U(IV) and incorporation of U(V) reported (Bots et al., 2019; Dodge et al., 2002; Huber et al., 2012; Latta et al., 2014, 2012; Marshall et al., 2015; Pan et al., 2020; Pidchenko et al., 2017, 2016; Roberts et al., 2017). Magnetite can remove aqueous U(VI) from solution by reduction to U(IV) via the coupled oxidation of Fe(II), ultimately resulting in precipitation of surface-bound UO_2 (Dodge et al., 2002; Huber et al., 2012). In addition, non-crystalline U(IV) complexes have also been reported at lower uranium to magnetite ratios (Latta et al., 2014, 2012). Later XANES and EXAFS studies have shown reduction of U(VI) to U(V) with incorporation of U(V) into magnetite / green rust during co-precipitation of U(VI) with these Fe(II)/Fe(III) bearing iron(oxyhydr)oxide phases (Pidchenko et al., 2017; Roberts et al., 2017). The U(V) is reportedly incorporated into octahedral sites of magnetite, and substitutes for Fe (Bender and Becker, 2019; Marshall et al., 2015; Pidchenko et al., 2017; Roberts et al., 2017) in a uranate-like coordination environment (Marshall et al., 2015; Pidchenko et al., 2017; Roberts et al., 2017). Some studies have explored the stability of U(V)-incorporated into magnetite when exposed to air (Marshall et al., 2015; Nico et al., 2009; Pidchenko et al., 2017). Nico *et al*. aerated samples of U(V/VI) incorporated-magnetite in air for 5 days and, despite a slight shift in the X-ray absorption near edge structure (XANES) spectra edge position (E_0) suggesting some oxidation, they did not see any change in U-O coordination pre- and post-oxidation, though a slight change in the U-Fe shell coordination was noted (Nico et al., 2009).

Similarly, Pidchenko *et al.* oxidised U(V)-incorporated magnetite samples for over 142 days with evidence that the oxidised product retained significant incorporated U(V) and that residual U(IV) oxidised to uranyl U(VI) which sorbed to the oxidised iron oxyhydroxide surface (Pidchenko et al., 2017). Minor releases of U(VI) to solution upon partial oxidation of U(V) incorporated magnetite in air have also been reported (Marshall et al., 2015). Whilst significant work at the laboratory scale has been performed, no long term studies have been undertaken to characterise the oxidation of U(V)-bearing magnetite in field conditions to determine the fate of the U in subsurface environmental systems.

In this study, and driven by the significance of both magnetite and U in radioactively contaminated land and other waste management scenarios, we used the Radionuclide Fate and Transport Experiment (RadFATE) lysimeter facility at Clemson University, USA to explore U(V) incorporated stability in the shallow subsurface environment (Roberts et al., 2012). Specifically, we explored the changes in speciation, mobility and fate of U(V)-incorporated magnetite exposed in the field. An experiment containing U(V)-incorporated magnetite in Savannah River Site (SRS) sediment was set up in a field lysimeter system and emplaced open to the environment at the RadFATE facility for 12 months. The lysimeter experiments were set up with upper and lower U(V)-incorporated nano-magnetite rich sediment horizons at 22 and 50 cm depths within a 72 cm column. After field exposure, the lysimeter was carefully extracted and sampled and the resultant post-reaction materials analysed using a range of techniques including U L$_3$-edge XANES and extended X-ray absorption fine structure (EXAFS), spatially resolved µ-focus X-ray fluorescence (XRF) and X-ray Magnetic Circular Dichroism (XMCD), in addition to autoradiography and a range of geochemical extraction and digestion techniques. Results demonstrated both limited migration of U after 357 days with partial oxidation of the starting material to form U(VI) observed within the source regions. Interestingly, the sustained incorporation of U into the reacted iron (oxyhydr)oxide phase was observed. Overall, these data suggest that U(V)-incorporated magnetite shows long term incorporation and thus immobilisation of uranium even after extensive oxidative exposure under field conditions directly relevant to contaminated land at nuclear facilities.

4.3 Methodology

Field Lysimeter Experiment. The Radionuclide Fate and Transport Experiment (RadFATE) facility at Clemson University (SC, USA) was used to perform the experimental study of U(V)-incorporated magnetite stability under field conditions (Roberts et al., 2012). The lysimeter was constructed out of PVC pipe of 15 cm diameter and 72 cm length and was emplaced vertically in the screened concrete housing in the RadFATE facility. A nylon mesh (0.3 mm) was fitted to the base of each lysimeter to keep sediment in place and allow drainage of water. A schematic of the lysimeter setup is provided in SI (Figure S4.1). A series of in-situ sensors measuring temperature, dielectric permittivity, water potential and bulk electrical conductivity were emplaced at 25, 34, 48 and 58 cm depth in the lysimeter and provided in situ measurements throughout apart from a short period due to a power outage to the facility (Figure S4.2). Two U(V)-incorporated magnetite 'source' horizons were emplaced in the lysimeter at depths of 22 cm and ~50 cm and were packed with well characterised sediments sourced from an area upstream of SRS (Montgomery et al., 2017) to a total height of 67 cm in the lysimeter. Briefly, the sediment was unconsolidated and comprised 66% sand, 14% silt and 20% clay, with less than 1% organic matter content; full details can be found in SI (S4.1.3). The U(V)-incorporated magnetite source material was prepared using an Fe(II)/Fe(III) ratio of 0.6 using a direct-coprecipitation method (Roberts et al., 2017). The U loading in the pure U(V) magnetite sample was approximately 3000 ppm and a sub sample of unaltered U(V)-bearing magnetite was retained under anaerobic conditions at -80 $^{\circ}$C for L_3 edge X-ray absorption spectroscopy (XAS) analysis. To emplace the U(V)-doped magnetite, the nanoparticulate magnetite was manually mixed with the sediment in a ratio of approximately 1:30 to yield a final concentration of U(V) incorporated magnetite through the source horizon of approximately 100 ppm U. The source horizons were shaped into disc shaped "pucks" (10 cm diameter x ~1cm depth) and lowered onto the packed sediment, with blank, gently compacted sediment filling in the gaps on the outside edges of the puck. On emplacement within the RadFATE facility, the lysimeter was then attached to an egress tube where effluent was collected in an open PTFE container for analysis. The effluent samples were collected typically after periods of heavy rainfall (6 time points), monitored for pH, and subsequently acidified in 2% HNO_3 for ICPMS analyses of U, Fe, Na, Mg, K and Ca (Agilent 7700x) (Figures S4.3, S4.4). The lysimeter was emplaced into the open air RadFATE facility on 23/05/2017 and exposed to the environment for 12 months with removal on 15/05/2018, a total of 357 days.

Lysimeter Sectioning and Sampling. After 12 months, the lysimeter was removed from the facility, cut in half vertically, and one half of the lysimeter sectioned vertically into 1 cm sediment horizons in an anaerobic glovebox. These sectioned sediment samples which included the

magnetite rich sediments and some of the blank infill sediment were then homogenised manually and stored in double sealed sample bags at room temperature prior to further analysis. In addition, prior to 1 cm sectioning, areas of the source regions were sampled for spatially resolved analyses using autoradiography and μ-focus XRF. Here, in the anaerobic glovebox, two steel sampling housings were gently pressed into the loosely aggregated sediment and capped before being carefully removed intact as a 10 x 7 x 2 cm rectangular cuboid across the two source regions (Figure S4.5). The steel-housed samples were then preserved, packed and shipped back to the UK with the sectioned material, where they were embedded under anaerobic conditions in Spurr Epoxy resin to preserve the redox integrity of the sample and enable μ-XRF analysis (Bower et al., 2019; Jilbert et al., 2008). Briefly, this involved dehydrating the samples by flushing with 100% acetone before sequentially increasing the proportion of resin to acetone added until 100% resin was applied. The sections were then cured in an oven at 60 °C for 48 h. After resin embedding, cut and polished thin sections (100 μm depth) were mounted onto quartz slides for analysis using autoradiography and μ-focus XRF.

To further define the distribution of U and Fe in the lysimeter core, 1 cm core sections in and around (up to 2 cm above and 3 cm below) the source regions were digested in *aqua regia* at 80 °C for 4 hours, filtered and diluted into 2 % HNO_3 for ICP-MS analysis of total *aqua regia* extractable U and Fe (Morris et al., 2000). To provide insight into the U distributions within the reacted lysimeter materials, the U(V) incorporated source horizons were also subjected to an increasingly acidic leaching protocol which has been used to target U associations in Fe rich sediments and in U(V)-incorporated nano-magnetite (Doornbusch et al., 2015; Roberts et al., 2017). Briefly, solutions of HCl ranging from 0.001 M to 4 M were applied successively to triplicate samples of sediment for 30 mins with samples left for 48 h in 6 M HCl. The resultant supernatants were then analysed for total U and Fe content using ICP-MS. Additional sequential extraction analyses were undertaken on select bulk source fractions to further explore the operationally defined distribution of uranium in each source region. The lixiviants were 1 M magnesium chloride ("exchangeable fraction"), 1 M sodium acetate ("carbonate fraction"), 0.04 M hydroxylamine hydrochloride in 25% HOAc ("reducible fraction"), 30% hydrogen peroxide and 1 M ammonium acetate ("oxidisable fraction") and *aqua regia* ("residual fraction") (adapted from Keith-Roach et al., (2003); Tessier et al., (1979)). Sequential extractions were performed on samples through the source regions from 2 cm above to 2 cm below. The sequential extraction leachates were prepared for analysis of U and Fe by dilution in 2% HNO_3 and analysed using ICP-MS. X-ray diffraction (XRD) measurements were collected on the starting material and altered upper and lower source horizons using a Bruker D8 Advance (λ= 1.5406 Å; Cu $K_{α1}$) in continuous scan mode in the 5-70° 2Θ range. Additional samples of the upper and lower source horizons

were sonicated and the suspended fines removed for further XRD analysis to target iron oxide phases. Patterns were analysed using EVA 4 and the ICDD database.

Autoradiography. Autoradiographs were collected to explore uranium distributions across the source horizons. Here, the resin embedded thin section samples from across the upper and lower horizons were exposed for 2 months to a GE storage phosphor screen, before being imaged on a Fujifilm FLA-3000 (Bower et al., 2019). Images were manipulated using Image Quant and ImageJ. Regions with a significant autoradiography signal and high U loading were targeted for solid phase analyses including defining target areas for µ-focus XRF.

XAS Data Acquisition and Analysis. Here, a multi-technique XAS approach was used to build a picture of the speciation of uranium after almost 12 months environmental exposure of U(V)-incorporated magnetite in a field lysimeter. We used L_3 edge XANES and EXAFS analysis, µ-focus XRF and XMCD to provide molecular scale insight into the speciation and fate of U in the lysimeters. Samples for L_3 edge XAS analyses were undertaken on selected sub-samples of the "bulk" 1cm core sections. Samples from upper and lower source horizons were mounted in anaerobic sample holders and under anaerobic conditions and stored at -80 °C prior to analysis. Samples cells were then transported to Diamond Light Source for analysis on either I20-scanning (Diaz-Moreno et al., 2009) or B18 (Dent et al., 2009), within a liquid N_2 cryostat, in fluorescence mode using solid state 64-element (I20) or 36-element (B18) Ge detectors. For µ-focus XRF, the resin embedded thin sections from upper and lower source horizons were mounted on the sample stage at Swiss Light Source on the MicroXAS beamline (X05-LA) and provided a series of µm-scale XRF maps, using a high resolution multi-modal chemical imager. To further explore magnetite speciation in lysimeter samples, semi-quantitative XAS and XMCD measurements at the Fe $L_{2,3}$ edges were obtained on beamline 6.3.1.1 at the Advanced Light Source, Berkeley, CA, USA. Here, measurements were carried out at room temperature on upper and lower source horizon samples and XAS was monitored in total electron yield (TEY) mode.

Uranium L_3 edge spectra were recorded for the unaltered U(V)-incorporated magnetite starting material, and for the altered U(V)-incorporated magnetite upper and lower source horizons after 12 months environmental exposure. Data processing was performed using Artemis and Athena software (Ravel and Newville, 2005) and analysis of the oxidation state components was performed using Iterative Transformation Factor Analysis (ITFA) (Rossberg et al., 2003). Standards for ITFA analysis included U(IV)O_2, U(VI)O_3, and the previously published U(V)-incorporated magnetite (Fe(II)/Fe(III)=0.6) (Roberts et al., 2017). For µ-focus XRF, the maps were collected at 17.6 keV with a beam size of ~25 µm for coarse maps and 1 µm for fine maps. Areas with elevated

U content were also selected for spot XANES analyses. The micro-XRF images were created using PyMCA software. For XMCD, at each photon energy of the spectrum the XAS was measured for two opposing magnetising directions by reversing an applied field of 0.6T. After normalisation to the incident beam direction the XMCD was derived as the difference between the two XAS spectra. To obtain the relative proportion of Fe^{3+} O_h, Fe^{3+} T_d and Fe^{2+} O_h within each cation site of the magnetite, the experimental XMCD spectra were fitted by means of a non-linear least-squares analysis, using calculated spectra for each site (Pattrick et al., 2002; Van Der Laan and Kirkman, 1992; Van der Laan and Thole, 1991).

4.4 Results and Discussion

A field lysimeter experiment packed with Savannah River Site sediment (Montgomery et al., 2017) with an upper source horizon of U(V)-incorporated magnetite at 22 cm and a lower source horizon at 47-50 cm from the sediment surface was prepared. This was then emplaced within the RadFATE facility and exposed to the environment for 1 year. The unaltered U-incorporated magnetite starting material was analysed before emplacement using XRD, XANES and EXAFS and showed that it was similar to the U(V)-incorporated magnetite generated by Roberts et al. (2017), using the same preparation method (Figures S4.6, S4.7).

During the lysimeter experiment, 9.7 L of rain was collected in the effluent container over the year. The resultant effluent was collected into PTFE bottles initially after 154 days, and then after periods of heavy rainfall resulting in a total of 6 time points (Table S4.1). The effluent pH was between 4.5 and 5.3, consistent with past work using lysimeters with Savannah River sediment (Peruski et al., 2018). The effluent analyses showed that only background levels (<0.1 ppb) of U were eluted from the column suggesting no significant transport of U through the column occurred over the 12 month exposure (Figure S4.3). Data from the in-situ probe measurements showed clear responses in volumetric water content and water potential during wetting/drying events (Figure S4.4). Water potential data indicated relatively free movement of water through the column and confirmed the lysimeter was not fully saturated during emplacement suggesting the lysimeter was essentially functioning as a vadose-zone experiment.

Uranium distribution in sediment core

Sectioned sediment samples taken at 1 cm intervals were analysed for total U concentration in sediments (Figure 4.1-B). These showed U was largely retained in the upper and lower source horizons with a clear increase in U concentration in the 21-22 cm fraction in the upper source and 47-50 cm fractions in the lower source (Figure 4.1-B). These corresponded to the original emplacement zones where the lysimeter sediments were notably darker (Figure 4.1-A), indicating U(V)-incorporated magnetite was emplaced. Lower concentrations (~25-30 ppm) of U in the source region samples were observed than expected from emplacement (~100 ppm) due to some homogenisation with blank sediment at the edges of the source horizons, but the concentrations observed in the source horizons were well above background U levels in this sediment (0.6 ppm). In addition to elevated U concentrations in the source horizons, there was some evidence that immediately above and below the source horizons U concentrations were slightly elevated (up to 1.9 ppm) suggesting modest, cm scale movement of U from the source horizons.
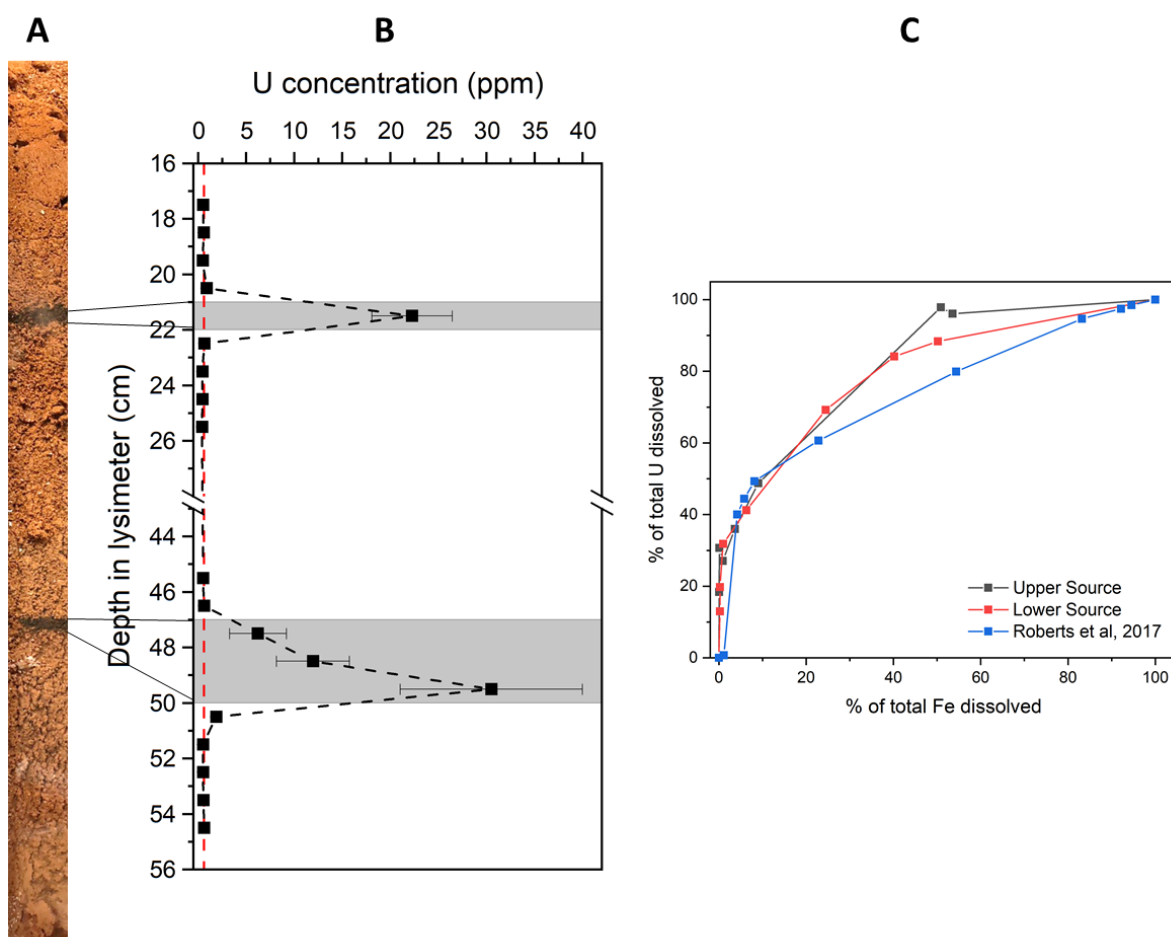
Figure 4.1: Geochemical characterisation data for bulk sediment samples from 1 cm sections in and around the upper and lower U(V)-incorporated magnetite source horizons. (A) Colour photograph of the half-sectioned lysimeter after 357 days. Note the two dark layers clearly showing the locations of the two U(V)-incorporated magnetite-SRS sediment horizons emplaced in the lysimeter. (B) Total *aqua regia* extractable U concentrations in upper (21-22 cm) and lower (47-50 cm) source horizons (grey bands indicate the original source horizon emplacement). (C) U and Fe release from solids upon progressively more aggressive acid dissolution of upper and lower source horizon samples (Doornbusch et al., 2015), compared with published data for unaltered U(V)-incorporated magnetite (Fe(II)/Fe(III) = 0.6; U = 0.3 wt%) (Roberts et al., 2017).

Using an acid leach protocol (Doornbusch et al., 2015; Roberts et al., 2017), the release of U versus Fe with increasing acidity for both upper and lower source horizons was determined (Figure 4.1-C). Interestingly, there was an initial release of U in both horizons with very little Fe dissolution (<3.5%) at acid concentrations up to 1 M HCl, consistent with up to 37% of U in the upper source and 33% in the lower source being located near the particle surface either as sorbed or near surface associated U. Furthermore, the acid leach also reflects a similar fraction of U that was near surface associated in unaltered U(V)-incorporated magnetite (0.6 Fe(II)/Fe(III)) where 40% U was leached before any significant Fe leaching (Roberts et al., 2017) (Figure 4.1-C). In both samples, following the initial near surface associated release of 33 - 37% U, the dissolution

became increasingly congruent with Fe and U leaching in a proportionate way in both upper and lower horizons. This suggested that there was a consistent distribution of U in the Fe oxide particles consistent with incorporation of U in the magnetite even after the field lysimeter deployment (Marshall et al., 2015; Roberts et al., 2017). Overall, these results indicate that little or no U is released from the magnetite, and the distribution of U associated with the iron (oxyhydr)oxide particles remains the same even after approximately 12 months of field oxidation (Figure 4.1-B).

Sequential extractions were also performed on selected 1 cm sections of the lysimeter (Figure S4.8). Overall, the sequential extraction U distribution profiles for the upper and lower horizons were similar when compared to those of the starting material (Figure S4.8). The only notable difference between the starting material and the altered source horizons was the distribution of U in the "carbonate" (1M sodium acetate) and "reducible" fractions (0.04 M hydroxylamine hydrochloride). The proportion of U in the "carbonate" fraction was significantly higher in the starting material (37%) than in the altered horizons (approximately 20%). This decrease in "carbonate" U was accompanied by an associated increase in the proportion of U in the "reducible" fraction in the altered horizons. This might suggest that a small proportion of U in the starting material may have leached/desorbed and become associated with more readily reducible iron phases as the magnetite within the sediment aged within the lysimeter. Interestingly, this indicates that some adsorbed U may become incorporated into the iron (oxyhydr)oxide as the oxidation process occurs (Henkel et al., 2016; Poulton and Canfield, 2005).

To further explore the distribution of U in the sediment samples, spatial analysis using a combination of autoradiography (Figure 4.2-B) and μ-focus X-ray fluorescence (XRF) (Figure 4.2-C, D) on sectioned samples from the upper and lower source regions were performed. Autoradiograph results were consistent with significant U retention in both upper and lower emplaced U(V)-incorporated magnetite source horizons evidenced by the elevated autoradiograph signal co-located with the dark zones of both upper and lower source horizons (Figure 4.2-A). Outside of the darker, magnetite-rich zones, background levels of radioactivity were observed. Within the source horizon zone, the autoradiograph signal was heterogeneous presumably due to sediment inhomogeneity and the resultant heterogeneity in the thin section exposure. Regardless, the black U(V)-magnetite source horizons were correlated with an elevated autoradiograph signal (Figure 4.2-B) which is consistent with the coarse section *aqua regia* digest data which showed essentially complete U retention in the source horizons (Figure 4.1-B).
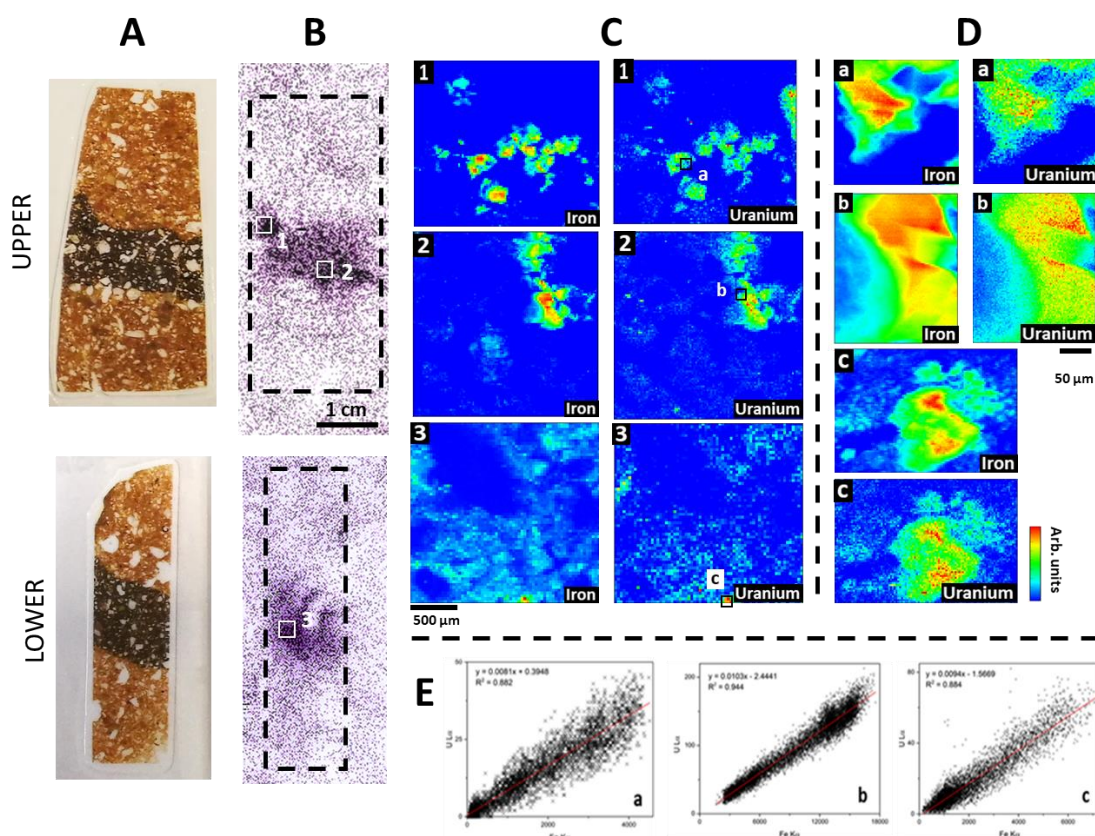
Figure 4.2: (A) Colour photographs of thin section samples from upper and lower source horizons. (B) Autoradiographs of resin embedded thin sections from each source horizon showing radioactivity distribution around the source horizons. Numbered boxes on the autoradiographs correspond to the μ-focus maps in panel C. (C) Element specific μ-focus XRF raster maps of highlighted regions. Colour intensity denotes the proportion of each element across the maps. (D) Element specific fine μ-focus XRF maps; (E) Scatter plots of correlations between Fe and U from μ-focus XRF maps in panel D, with co-location of elements evidenced by a positive correlation between Fe and U across a range of concentrations.

μ-focus XRF mapping of target U concentrated areas identified from the autoradiography (Figure 4.2-B) was used to further explore the U distribution and elemental correlations within the source regions. As observed in the autoradiographs, μ-focus XRF, across the resulting coarse 2 mm and higher resolution 200 μm maps showed U was distributed heterogeneously in the source zones. Further analysis of the μ-focus XRF maps (Figure 4.2-C, D) and elemental correlation plots of U Lα counts against Fe Kα counts (Figure 4.2-E) clearly show largely positive correlation between Fe and U concentrations in the vast majority of the higher resolution maps. Notably, some areas analysed did show areas where the U and Fe correlations were not present (Figure S4.12) and these were analysed by spot μ-XANES and are discussed later. Correlations with elements other than Fe (Ca, Mn, Ti, Zn) (Figure S4.11) were also investigated and no further statistical correlation between U and these other elements was found.

Uranium Speciation analysis via XAS

To further explore the fate of U(V) in the original source material after exposure to the environment, XAS analysis of select bulk solid phase samples was performed. Here, L_3 edge XANES/EXAFS were collected from the unaltered U(V)-incorporated magnetite, as well as from the altered bulk upper and lower source horizon samples.
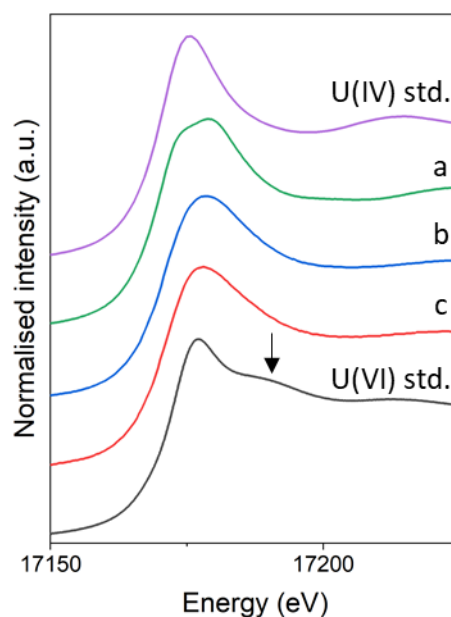
Figure 4.3: U L_3 edge XANES spectra from (a; green) starting material (unaltered U(V)-incorporated magnetite) and the altered-lower (b; blue) and -upper (c; red) source horizons with U(IV) uraninite and U(VI) schoepite standards.

The U L_3 edge XANES data suggest that even after approximately 1 year of environmental exposure, significant U(V) was present in both the upper and lower source samples with the edge positions for the upper (17171.0 eV) and lower sources (17170.9 eV) between those of the U(IV) (17170.3 eV) and U(VI) (17173.4 eV) standards (Figure 4.3). Qualitatively, the absence of a shoulder at ~17190 eV (highlighted by the black arrow in Figure 4.3) in the unaltered-, upper-, and lower U(V)-incorporated magnetite spectra, and typically indicative of uranyl species (Catalano and Brown, 2004), suggested uranate-like species dominated in the unaltered material and in both source horizons in the altered samples. Indeed, the L_3 edge XANES spectra for unaltered, upper and lower horizons were broadly consistent with reported literature for U(V) uranate incorporated in magnetite, but with upper and lower source horizons showing some evidence of oxidation as the edge position is at slightly higher energy relative to the unaltered material (Marshall et al., 2015; Pidchenko et al., 2017; Roberts et al., 2017). Iterative Transformation Factor Analysis (ITFA) (Figure S4.13, Table S4.5) of the L_3 edge XANES show that in the starting material has 27% U(IV) and 73% U(V). In contrast, the data from the upper source was fitted with 62% U(V) and 37% U(VI) with a trace of U(IV), whilst the lower source showed a fit with 72% U(V) and 28% U(VI), and no evidence for U(IV). These data suggest that some U(VI)

could be forming either as a result of oxidation of residual U(IV) associated with the U-incorporated magnetite starting material as observed in past work (Pidchenko et al., 2017), and/or due to oxidation of U(V) to U(VI) in the samples. Overall, the L_3 edge XANES suggest significant oxidation of U in the samples has occurred in the lysimeter, with the upper and lower sources dominated by U(V) and U(VI), and with some suggestion that the upper source is modestly more oxidised than the lower source.
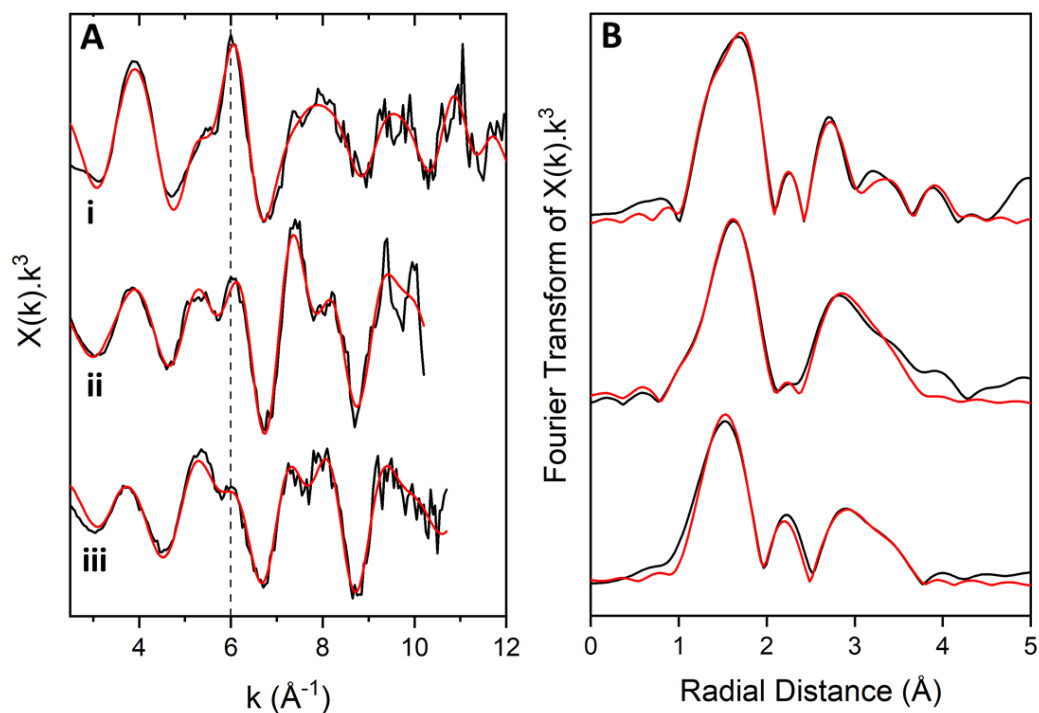
Figure 4.4: (A) U L_3 edge EXAFS spectra of (i) the starting material, (ii) lower- and (iii) upper- source horizons; (B) Fourier transform of k^3 weighted EXAFS. Black lines are data, red lines are best fit models for the data.

Table 4.1: Details of EXAFS best fit parameters from samples of unaltered U(V)-incorporated magnetite starting material and upper and lower source horizons. All coordination numbers (*N*) and S0^2 are fixed.

Sample	Pathway	*N*	(R + ΔR) Å	σ^2 (Å)	E$_0$	*R*-factor	k range	α
U(V)-incorporated magnetite starting material	U-O$_1$	0.4	1.71 ± 0.01	0.004 ± 0.002	15.07	0.010	3-12.0	100
	U-O$_2$	4	2.22 ± 0.01	0.009 ± 0.001				
	U-O$_3$	1.5	2.48 ± 0.03	0.007 ± 0.003				
	U-Fe$_1$	2	3.19 ± 0.02	0.011 ± 0.002				
	U-Fe$_2$	2	3.74 ± 0.02	0.009 ± 0.002				
	U-U	1	3.92 ± 0.03	0.006 ± 0.004				
Upper Source	U-O$_1$	1.2	1.82 ± 0.01	0.006 ± 0.001	15.42	0.012	3-10.7	100
	U-O$_2$	3.5	2.23 ± 0.02	0.012 ± 0.002				
	U-O$_3$	2	2.49 ± 0.03	0.007 ± 0.002				
	U-Fe$_1$	2	3.30 ± 0.03	0.012 ± 0.003				
	U-Fe$_2$	1	3.69 ± 0.04	0.009 ± 0.006				
Lower Source	U-O$_1$	0.9	1.81 ± 0.02	0.003 ± 0.002	7.52	0.015	3-10.2	99.8
	U-O$_2$	4	2.18 ± 0.03	0.010 ± 0.002				
	U-O$_3$	1	2.45 ± 0.08	0.010 ± 0.002				
	U-Fe$_1$	2	3.17 ± 0.04	0.010 ± 0.003				
	U-Fe$_2$	1.5	3.64 ± 0.04	0.005 ± 0.003				

N is the coordination number; *R* denotes the distance between uranium and the scatterer; σ^2 denotes Debye-Waller factor; E$_0$ describes the energy shift from the calculated Fermi level; S0^2 denotes the amplitude factor which was fixed to 1 for all samples; the *R*-factor describes the 'goodness of fit' and α is the statistical significance from F-test results (Downward et al., 2007).

The EXAFS spectra, corresponding Fourier transforms, and best fit models for the U(V)-incorporated magnetite starting material and altered upper and lower source horizons are given in Figure 4.4-A, B and Table 4.1, respectively. For the U(V)-incorporated magnetite starting material, the model described in Roberts et *al*. (2017) was used to inform the fits. Here, the U L$_3$ edge EXAFS best fit included 0.4 O backscatterers at 1.71(1) Å, two O shells with 4 and 1.5 occupancy at 2.22(1) and 2.48(3) Å, respectively, and Fe shells at 3.19(2) and 3.74(2) Å, both with an occupancy of 2 and one U backscatterer at 3.92(3) Å. Interestingly, the unaltered sample best fit included 0.4 oxygen atoms at a short U=O bond length of 1.71(1) Å suggesting the presence of up to 20 ± 10% U(VI) in uranyl coordination. This bond length is unusually short for U(VI)-O$_{ax}$ and was not reported by Roberts et *al*. (2017) in their fits for magnetite, but has been observed and discussed in past work (Conradson et al., 2004; Pidchenko et al., 2017). Here, Conradson et *al*. suggested these short bonds were attributed to U(VI) in UO$_{2+x}$ compounds, whilst Pidchenko et *al*., saw very similar short bond lengths in their EXAFS fits for U(V)-incorporated magnetite, however chose not to include it in their structural model as it can be part of a background signal. Overall, the fit was broadly consistent with the ITFA and suggested the unaltered starting U incorporated magnetite contained 80 – 90% U(V) and a small fraction of U(IV) indicated by the U-U backscatterer in the EXAFS. In addition, this is consistent with the split of the U-O$_{eq}$ shells with

U(V)-O uranate bond lengths reported between 2.1 - 2.2 Å (Huber et al., 2012; Ilton et al., 2012, 2010; Marshall et al., 2015; Pidchenko et al., 2017; Roberts et al., 2017) consistent with the U-O shell fit presented here with 4 O backscatterers at 2.21 Å. The U-O shell with 1.5 backscatterers at 2.47 Å, is consistent with U(VI)-O_{eq} backscatterers reported at 2.43-2.51 Å (Huber et al., 2012; Roberts et al., 2017). The presence of two U-Fe backscatterers at 3.19(2) and 3.72(2) Å is characteristic of reported literature values for U(V)-incorporated into magnetite, which is consistent with the starting material being dominated by U(V) incorporated into magnetite (Roberts et al., 2017). Finally, the U-U shell fitted at 3.92 Å is indicative of a small proportion of U(IV)O_2 present in the sample, as observed in past work (Pidchenko et al., 2017; Roberts et al., 2017).

After exposure to the environment for 12 months in the field lysimeter, the EXAFS of the upper, most oxidised source showed the most significant change when compared to the unaltered material (Table 4.1). Here the best fit included 1.2 O backscatterers at 1.82(1) Å, and two further U-O shells with occupancy of 3.5 O at 2.23(2) Å and 2 O at 2.49(3) Å. Two Fe shells were also fitted with an occupancy of 2 at 3.30(3) Å and 1 at 3.69(4) Å (Figure 4.4; Table 4.1). This EXAFS fit is consistent with the L$_3$ XANES data which show oxidation of either U(IV)O_2 present in the starting material or incorporated U(V), to U(VI). However, the XANES data were not reflective of uranyl coordination, which the U-O_1 bond length of 1.82 Å seems to suggest. Here, the U-O_1 shell occupancy of 1.2 suggested the presence of approximately 60% U(VI) as uranyl in the sample, a higher value than that predicted from the L$_3$ edge XANES ITFA (37% U(VI)-uranyl). Interestingly, Doornbusch et *al.*(Doornbusch et al., 2015) saw an identical bond length in their work with U(V/VI)-incorporated goethite and suggested that for U(V/VI)-incorporated goethite the inclusion of a shorter U-O bond at 1.82 Å could be required for structural reasons. This short 1.82 Å U-O bond in U(V/VI)-incorporated goethite allowed a reduction in the size of the U polyhedron, limiting the expansion of the octahedral site relative to that of Fe(III) in unsubstituted goethite, and was indicative of U(VI) incorporation to goethite, rather than indicating a significant presence of U(VI) uranyl where bond lengths are typically reported at 1.80 Å (Doornbusch et al., 2015). Due to the absence of the typical uranyl shoulder feature present at ~17190 eV in the XANES, this could also be the case here to some extent, though the presence of some adsorbed U(VI) uranyl cannot be discounted given the labile fraction of uranium seen in the acid extractions (Figure 4.1-C). It is important to note here that a U(VI) uranyl standard was used for the ITFA and as such, the apparent discrepancy between the proportion of U(VI) modelled in the EXAFS fits and ITFA could be due to the difference in coordination environment, where a U(VI) uranate would have different XANES spectra to U(VI) uranyl. The U-O_2 shell of 3.5 equatorial O backscatterers at 2.23(2) Å, a bond length typical of U(V) incorporated magnetite, suggests retention of a significant component (approximately 50%) of incorporated U(V) in the altered sample, consistent with

previous studies (Pidchenko et al., 2017; Roberts et al., 2017). Interestingly, the U-Fe_1 shell modelled for the altered lysimeter sample has a longer distance (3.30(3) Å) to the U-Fe_1 shell in the starting material (3.19(2) Å). This is presumably associated with the oxidation of the iron oxyhydroxide phases. The modelled U-Fe distance of 3.30 Å is similar to that reported for U(V/VI)-O-Fe edge sharing complexes at ~3.25-3.30 Å in goethite (Doornbusch et al., 2015; Kerisit et al., 2016; Nico et al., 2009), consistent with oxidation of magnetite to goethite and retention of U in the goethite phase. The fits show no evidence for the U-U observed in the starting material presumably due to oxidation of U(IV)O_2 to U(VI) under the oxic lysimeter conditions (Figure 4.1-C). Despite the clear evidence for oxidation of U(V), and the slight changes in the U-Fe environment compared to the starting material, the significant signal from the Fe shells observed from the EXAFS data strongly suggests that U remains incorporated in the iron (oxyhydr)oxide as both U(V) and possibly U(VI), with a proportion of the U(VI) likely to be adsorbed U(VI) uranyl.

The lower source EXAFS best fit included a U-O shell at 1.81(2) Å with an occupancy of 0.9, two U-O equatorial shells with occupancy of 4 and 1 at 2.18(3) and 2.45(8) Å, respectively. In addition, there are two Fe shells at 3.17(4) and 3.64(4) Å with occupancy of 2 and 1.5, respectively (Figure 4.4-ii, Table 4.1). This fit was closer to that of the starting material than the upper source, and suggested partial oxidation of both U(IV) and potentially some oxidation of the incorporated U(V). Here, around 45% of the U is present as U(VI) either as adsorbed U(VI)-uranyl or as U(VI)-incorporated, implied by the 0.9 occupancy for the U-O_1 backscatterer at 1.81 Å. Similar to the upper source analysis, the EXAFS suggested U(VI) oxidation at a higher level (45%) than that calculated by ITFA using a U(VI) uranyl standard (28 %). The XANES has no uranyl feature at ~17190 eV which suggests U is octahedrally coordinated in a uranate configuration, and so the greater proportion of U(VI) is likely to be as a result of a mixture of oxidised U(IV) from the starting material, now as adsorbed U(VI) uranyl, but also some oxidised U(V), retained in octahedral coordination as U(VI) and remaining incorporated into altered Fe-(oxyhydr)oxide phase, as seen in the upper source horizon. Similar to the upper source, the apparent discrepancy in the proportion of U(VI) in the samples was likely due to the use of a purely U(VI) uranyl standard in the ITFA calculation and here in the sample, a mix of U(VI) uranyl from adsorbed U(VI) and U(VI) uranate from incorporated U(VI) was likely present. The absence of a U-U shell in the fit to the lower source altered sample EXAFS data is consistent with the XANES ITFA analyses, and suggests UO_2 oxidation to U(VI)-uranyl presumably sorbed to the mineral surfaces. The two U-Fe shells modelled were comparable to the unaltered starting material, again confirming that U remains largely incorporated as U(V), and possibly U(VI), in the lysimeter sediment sample after 12 months in this lower horizon.

Spot μ-XANES analyses were performed on areas of the sectioned samples of the upper and lower source horizons to determine any heterogeneity in U speciation. In particular, spot analysis were collected on regions where the concentration of U-Fe was correlated, and where U-Fe was not correlated (Figure S4.14). The XANES spectra from the U-Fe-correlated regions were similar to the U(V)-incorporated magnetite starting material. In contrast the XANES spectra from the small number of U-Fe uncorrelated regions were more similar to those of U(IV)O_2. Overall, for the bulk samples there was no evidence in the XANES ITFA analyses to suggest that significant U(IV) was present in either the upper or lower source horizons. In particular U-U shells could not be fitted with statistical significance to either of the EXAFS spectra. It is noteworthy that the μ-focus XRF mapping showed the vast majority of the U in the samples was correlated with Fe (Figure S4.14).

Overall, for both the altered lower and upper source horizons, there was an increase in the U-O_1 component of the fits compared to the starting material modelled in the EXAFS. This suggests that both oxidation of the U(IV) identified in the starting material to U(VI) and/or oxidation of U(V)-incorporated magnetite to octahedrally coordinated U(VI) (for example in U(VI) goethite) is occurring in both upper and lower source horizons with EXAFS fitting suggesting approximately 45% U(VI) in the lower source and 60% U(VI) in the upper source. A proportion of the U(VI) observed is likely a result of the oxidation of U(IV) identified in the starting material, an observation which is supported by previous studies of U-magnetite oxidation (Pidchenko et al., 2017; Roberts et al., 2017). Indeed although acid leaching suggests 33 – 37% U(VI) is likely present as adsorbed or near-surface associated species in the upper and lower sources (Figure 4.1-C), there was little change from the fraction of U in the adsorbed phase in the U(V)-incorporated magnetite starting material (Roberts et al., 2017). Indeed, in the upper and lower source horizons, acid dissolution experiments revealed very similar distribution profiles of U dissolution as a function of Fe dissolution, to unaltered U(V)-incorporated magnetite (Figure 4.1-C). Similarly, the U/Fe ratios in the upper and lower sources were comparable to the data for the unaltered U(V)-incorporated into magnetite. This suggests that the majority of the U (both as U(V) and U(VI)) observed in our fits remains incorporated into the new Fe oxyhydroxide phases formed on reoxidation in the lysimeters and is consistent with published data for U(VI) incorporation into iron(oxyhydr)oxide phases (Boland et al., 2011; Doornbusch et al., 2015; Marshall et al., 2014a; Massey et al., 2014; McBriarty et al., 2018; Nico et al., 2009). Indeed, despite the clear oxidation to U(VI) modelled in both altered sources, the signal from the iron backscattering shells in the EXAFS data for these samples confirms that significant uranium incorporation to Fe(oxyhydr)oxide phases is occurring.

Iron (oxyhydr)oxide mineralogy in upper and lower sources.

In order to further understand the iron (oxyhydr)oxide behaviour during the environmental exposure of the sediment, a range of techniques were applied. XRD on the starting material (Figure S4.7) and on the upper and lower source horizons identified magnetite as the dominant crystalline iron phase before and after lysimeter exposure (Figures S4.15-16), with quartz and kaolinite also present in the sediment. Analysis of the fine particle fraction from the upper and lower source horizon samples that were collected showed the presence of some goethite in the XRD patterns of both upper and lower sources presumably as a result of partial oxidation of magnetite (Figures S4.17-18). Chlinochlore ($Mg_5Al(Si,Al)_4O_{10}(OH)_8$) and muscovite ($KAl_2(AlSi_3O_{10})(F,OH)_2$) were also present in the fines from both samples, presumably from the sediment.

As well as XRD analyses, Fe $L_{2,3}$ edge XAS and XMCD was used to explore the local coordination environment and relative proportions of Fe(II) and Fe(III) in tetrahedral and octahedral sites in these complex environmental samples (Coker et al., 2007; Singh et al., 2012). Here, analysis of the XMCD data showed a significant reduction in the Fe(II) in octahedral coordination associated with magnetite in both the upper and lower source horizons when compared to a magnetite standard (Figure S4.19, Table S4.6). There was also some evidence for slightly less Fe(II)-octahedral in the upper source compared to the lower source, although some Fe(II) character remained in both samples. Here there was a change in the Fe(II)/Fe(III) ratio calculated from the XMCD from the starting material (Fe(II)/Fe(III) ratio, 0.6) compared to the upper (Fe(II)/Fe(III) ratio, 0.1) and lower (Fe(II)/Fe(III) ratio, 0.3) sources (Table S4.6). The XMCD shows qualitatively that there is also approximately 50% less magnetic material in the upper and lower sources than that expected for magnetite, suggesting some phase transformation, potentially to goethite, in both sources. Analysis of the Fe $L_{2,3}$ edge XAS data shows the ingrowth of a pre-L_3 edge feature at ~707 eV in the upper and lower sources (Joshi et al., 2018) (highlighted in Figure S4.20). This feature is consistent with an increase in the ferric (e.g. maghemite or goethite) component of the sample (Brice-Profeta et al., 2005; Coker et al., 2020; Prado et al., 2015) suggesting oxidation of magnetite to Fe(III)-bearing phases. In addition, a slight shift to higher energy in the edge position in the spectra for both upper and lower sources relative to the magnetite standard (0.13 eV) also supports some limited oxidation, though retention of significant Fe(II) in both sources is clear when compared to a goethite standard (Coker et al., 2020), where the L_3 edge peak position is significantly higher in energy (~0.8 eV). Despite the observed change in Fe mineralogy, past work has highlighted that oxidation products of magnetite, including goethite and lepidocrocite, have been shown to have the capability to incorporate U as U(V) or U(VI) (Boland et al., 2011; Kerisit et al., 2016; McBriarty et al., 2017; Nico et al., 2009; Stewart et al., 2009).

In summary, XMCD confirmed there was significant oxidation of the magnetite in both upper and lower source horizons with a reduction in the Fe(II)/Fe(III) ratio relative to the starting material observed in both sources, confirming oxidation of the magnetite had occurred. Both Fe L$_{2,3}$ edge XANES and XRD supported this with goethite observed in the XRD of both upper and lower source horizons and the Fe L$_{2,3}$ edge XANES showing ingrowth of the feature typical of ferric phases in both sources. Despite this, and due to the complex nature of the samples used, the XRD and XMCD data are noisy, and although oxidation of magnetite to goethite should not be ruled out, it is not conclusive. Maghemite (γ-Fe$_2$O$_3$) could also be present, as it is a common oxidation product of magnetite (He and Traina, 2007; Swaddle and Oltmann, 1980) and displays similar features in Fe L$_{2,3}$ edge XAS and XMCD to the data presented here (Brice-Profeta et al., 2005; Prado et al., 2015). The exact distribution of iron (oxyhydr)oxide phases present in the upper and lower sources is not quantified here, but magnetite remains present in the XRD patterns of the altered source horizons and both Fe L$_3$ edge XANES and XMCD suggest some oxidation. Despite this oxidation of the magnetite, the U remains incorporated as evident from the U L$_3$ edge EXAFS data which show significant but not complete oxidation to U(VI) (up to approximately 50% U is present as U(VI) from the EXAFS data) and retention in an incorporated Fe(oxyhydr)oxide environment in the upper and lower source altered materials.

4.5 Implications

This field lysimeter study, in combination with a range of geochemical and spectroscopic techniques including L_3 and M_4 edge XAS, XMCD, acid dissolutions, XRD and μ-focus XRF has shown that U(V)-incorporated into magnetite remains largely incorporated into Fe oxyhydroxide phases over 12 months of environmental exposure*.* Application of acid digestion techniques and analysis of resin-embedded sections of the source horizons using autoradiography and μ-focus XRF spatial techniques confirmed U was retained in the emplaced source locations. This was despite the XAS analyses suggesting that significant oxidation to U(VI) had occurred in the samples, with greater oxidation to U(VI) in the upper source. Additionally, oxidation of the magnetite to goethite was observed in the altered samples. Clearly, the lack of U migration away from the original source locations despite significant oxidation coupled to the strong evidence for continued U incorporation in the oxidised iron (oxyhydr)oxide reaction products highlights the stability of these incorporated U phases in an oxic, near-subsurface setting. These data are relevant to nuclear sites where U and iron (oxyhydr)oxides are co-located in the subsurface and provide new insight into the field-scale environmental stability of U(V)-incorporated magnetite, even highlighting promising applications for U(V)-incorporated magnetite as a potential engineered wasteform.

Blank page

Supporting Information for Chapter 4

An environmental study of the behaviour and stability of U(V) incorporated into magnetite using field lysimeters.

[1] A. E. McNulty, [1] S. Shaw, [2] B. Powell, [1,3] G. T. W. Law, [1,3] W. R. Bower, [2] K. Peruski, [1] C. M. Fallon, [1] V. Coker, [4] J. Rothe, [4] T. Vitova, [5] P. Warnicke, [6] L. Abrahamsen-Mills, [7] J. F. W. Mosselmans, [1] H. Roberts and [1] K. Morris

[1]Research Centre for Radwaste Disposal and Williamson Research Centre, Department of Earth and Environmental Sciences, School of Natural Science, University of Manchester, UK

[2]Department of Environmental Engineering and Earth Sciences, Clemson University, USA

[3]Laboratory of Radiochemistry, Department of Chemistry, University of Helsinki, Finland

[4]Karlsrühe Institute of Technology (KIT), Institute for Nuclear Waste Disposal (INE), Germany

[5]Swiss Light Source, Paul Scherrer Institute, Villigen, Switzerland

[6]National Nuclear Laboratory, UK

[7]Diamond Light Source Ltd, Diamond House, Harwell Science and Innovation Campus, Didcot, UK

This document provides supporting information for the study including experimental set-up, extended methods, details of XAS set-up and data collection and additional supporting data.

Contents

S4.1: Lysimeter Experimental Set-Up and Probe Data
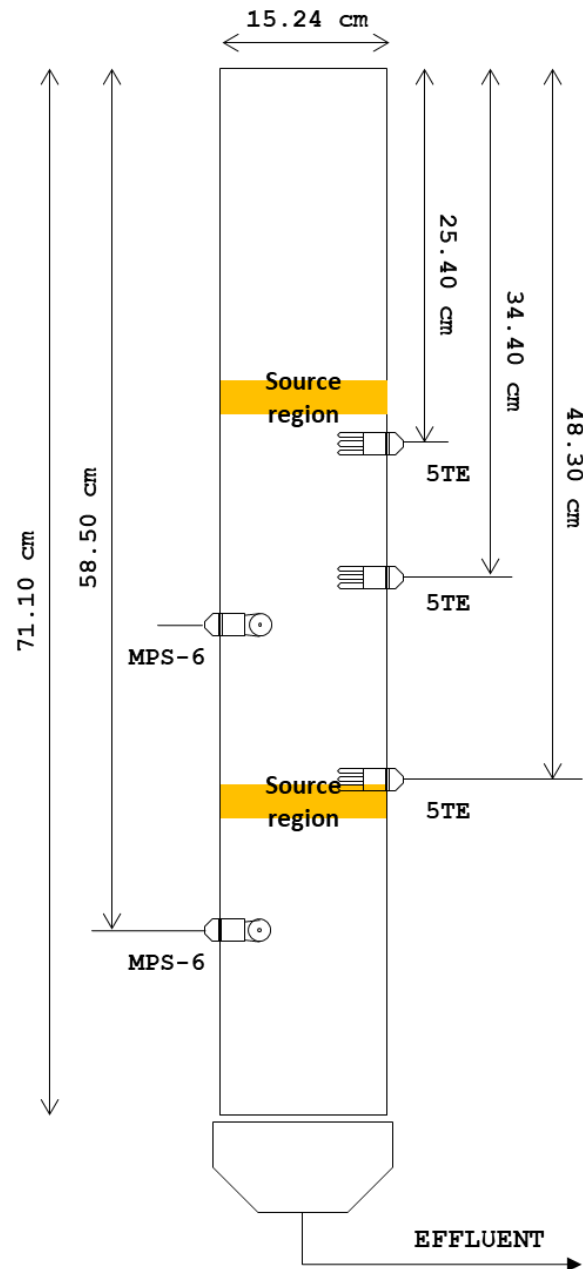
Figure S4.1: Lysimeter set-up with relative source horizon depths and probe positioning. The three 5TE soil moisture sensors monitor temperature (°C), bulk electrical conductivity (dS m^{-1}) and dielectric permittivity. MPS-6 water potential sensors measure water potential (kPa) in addition to temperature (°C). Measurements are given from the surface to the centre of each probe. Both types of probe are approximately 3.7 cm in width. Sediment was filled up to 67 cm from the base.

S4.1.1 Probe hydrology observations and interpretations
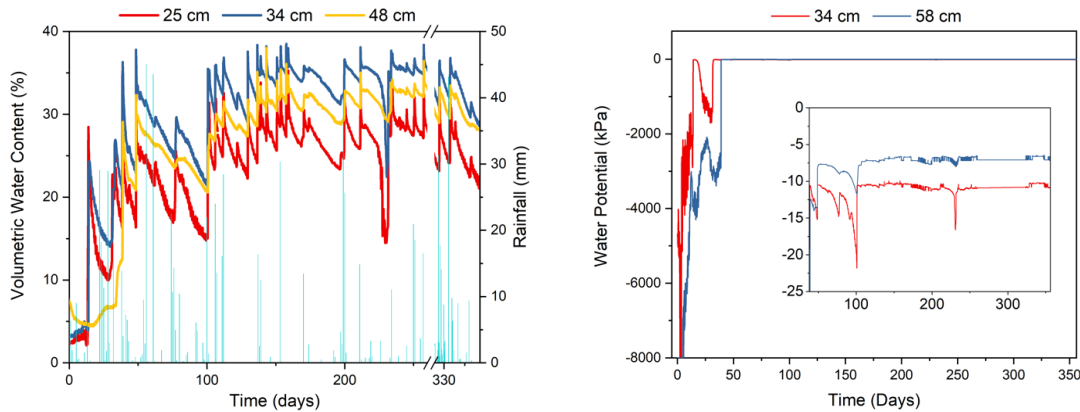
Figure S4.2: (Left) Volumetric water content for 5TE probes at 3 depths plotted against rainfall in a nearby area over 356 days; (Right) Water potential in the lysimeter at a depth of 34 cm and 58 cm measured using MPS-6 probes.

Initial water content in the lysimeter was between 2-8%. This increased initially following the first rainfall events at days 13 and 14. The top 5TE probe detected the water content increase approximately 14 hours after the rainfall whilst the middle probe detected an increase 12-14 hours after the top probe. The bottom 5TE probe detected an increase in water content 5 days later. This time lag between the top and bottom probes decreased as the lysimeter became more saturated. The decrease in time lag can be attributed to one of two things; either cracks had formed along the walls of the lysimeters after wetting and drying cycles, or there was an increase in hydraulic conductivity after several rainfall events due to water moving faster through larger pores.

On day 49, 1 L of rainwater was added manually to the lysimeter after a lack of rainfall in the area. All 5TE probes recorded a significant (5-20%) increase in water content within 2 hours of each other. The water content values started to stabilise after 110 days of deployment in the range of 23-36% after a total of 55 cm of cumulative rainfall (including the manual addition on day 49).

Upper probes recorded greater increases and steeper declines than the lower probes, indicating the magnitude of increase and the rate of decrease is dependent on the probe's position within the lysimeter. Probes at the bottom showed less variation in water content changes after a rainfall event than at the top. This is largely due to the top soil having a greater exposure to both rainfall and evaporation than the soil at the bottom of the lysimeter.

Two other lysimeters using the same sediment were run at the same time as the one described here (Fallon *et al.*, *in prep*); water content measurements by the 5TE probes in these lysimeters at the same positions differed by up to 15%.

S4.1.2 Effluent Composition

Effluent was collected and monitored at 6 time points throughout the experiment. The volume of effluent at each time point is given in Table S4.1, below.

Table S4.1: Mass of effluent at monitoring points throughout the lysimeter experiment

Time (days)	Mass of effluent (g)
154	2037.5
168	1400.0
247	1655.0
274	2013.5
330	1797.0
356	755.0
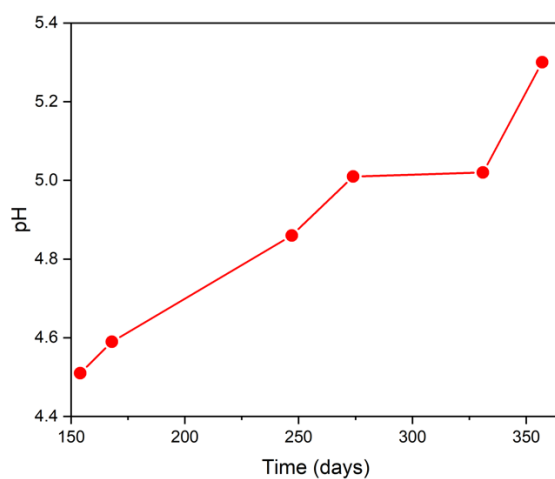
Figure S4.3: pH of the effluent collected from the lysimeter
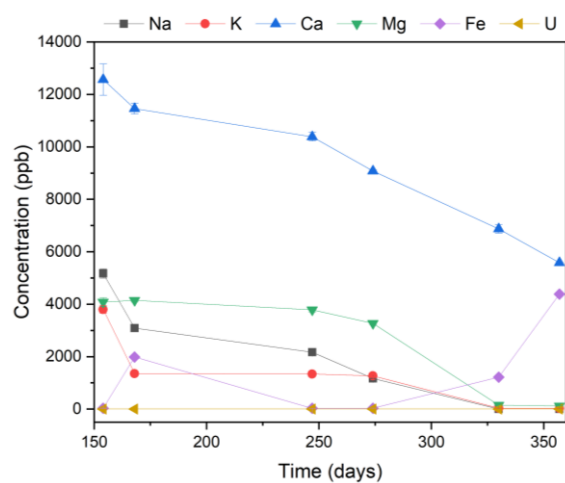
Figure S4.4: Concentration of Na, K, Ca, Mg, Fe and U in lysimeter effluent

S4.1.3 Sediment composition

The sediment used has been previously characterised (Montgomery et al., 2017). Additional XRF analyses were performed on the sediment to supplement these data.

Table S4.2: Details of XRF major and trace fractions in sediment used in the lysimeter, collected from West Borrow Pit

XRF Majors			XRF Traces		
Element	Concentration (ppm)	RSD	Element	Concentration (ppm)	RSD
Na_2O	0.028	0.004	Sc	6.4	0.141
MgO	0.251	0.012	V	63	1.273
Al_2O_3	22.217	0.468	Cr	35.8	1.131
SiO_2	68.392	0.620	Mn	27.2	0.424
P_2O_5	0.066	0.003	Co	18.2	0.283
SO_3	0.079	0.010	Ni	10.8	0.424
Cl	0.022	0.006	Cu	8.8	0.424
K_2O	0.188	0.014	Zn	16.1	0.424
CaO	0.052	0.016	Ga	13.7	0.707
TiO_2	0.608	0.023	Ge	2.1	0.000
Cr	0.007	0.000	As	6.25	1.909
MnO	0.006	0.000	Se	0.7	0.000
Fe_2O_3	3.567	0.130	Br	3.15	0.354
Co	0.007	0.001	Rb	7.9	0.283
Ni	0.004	0.001	Sr	6.75	0.354
Cu	0.004	0.000	Y	7.95	0.778
Zn	0.003	0.001	Zr	172.85	10.394
Zr	0.023	0.001	Nb	7.65	0.354
Ce	0.017	0.000	Mo	0.35	0.071
W	0.034	0.000	Sn	0.15	0.071
Pb	0.003	0.001	Te	46.6	0.707
CO_2	4.425	0.049	Cs	2.9	0.141
Ga	0.020	0.000	Ba	42.1	2.404
Hg	0.005	0.000	La	14	1.414
			Ce	18.4	2.828
			Nd	8.05	0.495
			Sm	3.25	1.485
			Yb	2.45	0.212
			Hf	7.05	0.778
			Ta	0.65	0.212
			W	233.2	5.940
			Hg	9.1	0.141
			Tl	0.3	0.141
			Pb	9	0.283
			Bi	0.5	0.566
			Th	7.1	0.566

Table S4.3: Physical and chemical properties of sediment used in the lysimeter column, previously characterised by Montgomery *et al.*, (2017)$^{\alpha}$

Pysical Properties	Measurement
Surface area	14.1 m2/g
pH (1:1 soil:water)	4.76
Point of zero charge	4.9
Sand/silt/clay (%)	66/14/20
Organic matter	0.90%
Chemical Properties	
Cation exchange capacity	3.3 meq/100 g
Acidity	2.4 meq/100 g
CBD-extractable Fe	6.01 ± 0.68 mg/g
CBD-extractable Al	1.98 ± 0.20 mg/g

$^{\alpha}$*CBD – citrate bicarbonate dithionite*

S4.2: Extended Methods and XAS (U L_3 edge, micro-focus XRF, XMCD) Set-Up

S4.2.1 Resin Embedding of Source Horizons

The resin embedding procedure took place in a N_2-filled polypropylene glove box to preserve an anaerobic atmosphere (Jilbert et al., 2008). Each source horizon section was reacted with a series of reagents in an aluminium foil bath, starting with a stepwise dehydration using acetone. Over 10 days, the reaction baths were flushed with fresh acetone daily, before being flushed with an acetone: Epoxy resin mix. The ratio of Epoxy resin added increased from 25%, 50% to 75%, before two final flushes with 100% resin. The reaction baths were then cured in an oven for 48 hours at 60 °C before sections were cut, mounted on quartz slides and polished (Figure S4.10). The sediment sections in the foil baths and resin embedded horizons can be seen in Figure S4.5, below.

Figure S4.520: (Left) Sediment sections, wrapped in mesh and placed in aluminium foil baths for resin embedding; (right) resin embedded section, halved prior to thin sectioning – black magnetite band is clearly visible here.

S4.2.2 Sequential Extraction Procedure

Approximately 0.5 g sediment was added to a 50 mL centrifuge before the sequential addition of each lixivant (Table S4.4). The samples were agitated on a shaker for the outlined period of time before being centrifuged at 3000 g for 20 mins. The leached aqueous phases were collected and acidified with 2% nitric acid for ICP-MS analysis and the solid phase retained in each step.

Table S4.4: Lixivants used in sequential extraction procedure (adapted from Tessier et al , 1979).

Fraction	Extractant Chemical	Time	Leached phases
Exchangeable	1 M magnesium chloride (pH 7)	2 hours	Sorbed
Carbonate	1 M sodium acetate (pH 5)	5 hours	Carbonate minerals / phosphate biominerals
Reducible	0.04 M hydroxylamine hydrochloride in 25% (v/v) acetic acid (pH 3)	16 hours	Fe/Mn oxides
Oxidisable	30% hydrogen peroxide (pH 2) 1 M ammonium acetate	8 hours 16 hours	Organic matter
Residual	Aqua regia	4 hours	

S4.2.3 XRF Measurements

12 g powdered sediment was mixed with wax and pressed into a homogenous pellet before analysis using a PANalytical Axios.

S4.2.4 Micro-focus X-ray fluorescence

XRF raster maps of target areas were collected on the micro-focus beamline (X05-LA) at Swiss Light Source at 17.6 keV using a horizontal beam of size ~1 μm with a dwell time of <0.1 seconds/pixel during mapping. A Y-foil standard was used for calibration and signals were collected using a Ketek GmbH silicon drift detector. A layer of Kapton tape (25 μm) was also applied to the thin sections, acting as a secondary containment layer.

S4.2.5 U L_3 edge XAS

Oxidation state determination of the XANES data were carried out using ITFA software (Rossberg et al., 2003). Schoepite and uraninite were used as standards for U(VI) uranyl and U(IV), respectively. The U(V) standard used was from previous work (Roberts et al., 2017).

The EXAFS spectra were fitted using published reference structures of schoepite, liebigite, uraninite and magnetite using Artemis from the Demeter software package (Ravel and Newville, 2005). Based on the relative proportion of the U phase, and past literature, the coordination numbers (N) were fixed for each calculation and so errors on these numbers are not provided, but are expected to be in the order of ~5% (Koningsberger et al., 2000; Li et al., 1995). This fitting routine is also applied in other complex systems in the literature (Townsend et al., 2019). Values for ΔE_0 (represents the difference between experimental data and the threshold Fermi level of the theoretical phase shift and backscattering amplitude functions), σ^2 (represents the Debye-Waller factor informing Gaussian distribution of interatomic distances), and R (interatomic distance) were allowed to refine for each sample. S_0^2, the amplitude factor, was fixed to 1. The

number of parameters used was always less than the number of degrees of freedom, defined by $N_{idp} \approx 2\Delta k\Delta r/\pi$. The fit for the unaltered material used 11 out of 16.99 independent points, whilst the upper and lower source used 11 and 10 variables for 13.45 and 12.15 independent points, respectively. The fitting of the EXAFS spectra presented here proved to be difficult given the complex, environmental samples and the presence of multiple U and Fe phases. Together with geochemical and XMCD data, we are confident that our EXAFS interpretation of U incorporated into a ferric iron phase with the retention of some magnetite material is correct.

S4.2.6 XMCD

X-ray absorption spectra (XAS) and X-ray magnetic circular dichroism (XMCD) measurements at the Fe $L_{2,3}$ edges were obtained on beamline 6.3.1.1 at the Advanced Light Source (ALS), Berkeley, CA. Samples were prepared by leaving sediment samples to dry in an anaerobic chamber before grinding to a powder. The powders were mounted on carbon tape attached to the sample manipulator within an anaerobic chamber. All measurements were carried out at room temperature and XAS was monitored in total electron yield (TEY) mode. At each photon energy of the spectrum the XAS was measured for two opposing magnetising directions by reversing an applied field of 0.6T. After normalisation to the incident beam direction the XMCD was derived as the difference between the two XAS spectra. A non-linear least squares analysis was performed to fit the experimental XMCD spectra, using calculated spectra from each site, to obtain the relative proportion of Fe^{3+} O_h, Fe^{3+} T_d and Fe^{2+} O_h in the samples (Pattrick et al., 2002; Van Der Laan and Kirkman, 1992; Van der Laan and Thole, 1991).

S4.3: Supplementary Data

This section includes any additional data that may have been referred to in the main text or supports the data presented.

S4.3.1 Starting Material Characterisation (Comparison to Literature)
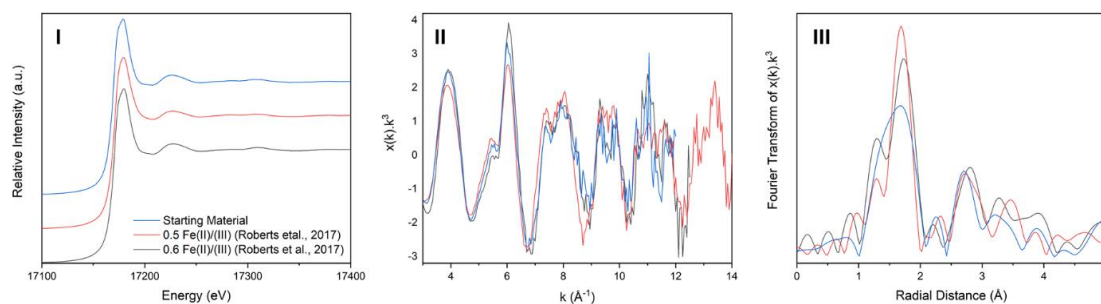
Figure S4.6: XAS comparison of the U(V)-incorporated magnetite starting material (blue) to previous research using the same Fe(II/III) ratio as used here (black; 96% U(V)) and a Fe(II)/Fe(III)=0.5 sample (red; 88% U(V)), both taken from Roberts et al. (2017). (I) U L_3 XANES; (II) k^3 weighted EXAFS; (III) Fourier transform of the k^3 weighted EXAFS.
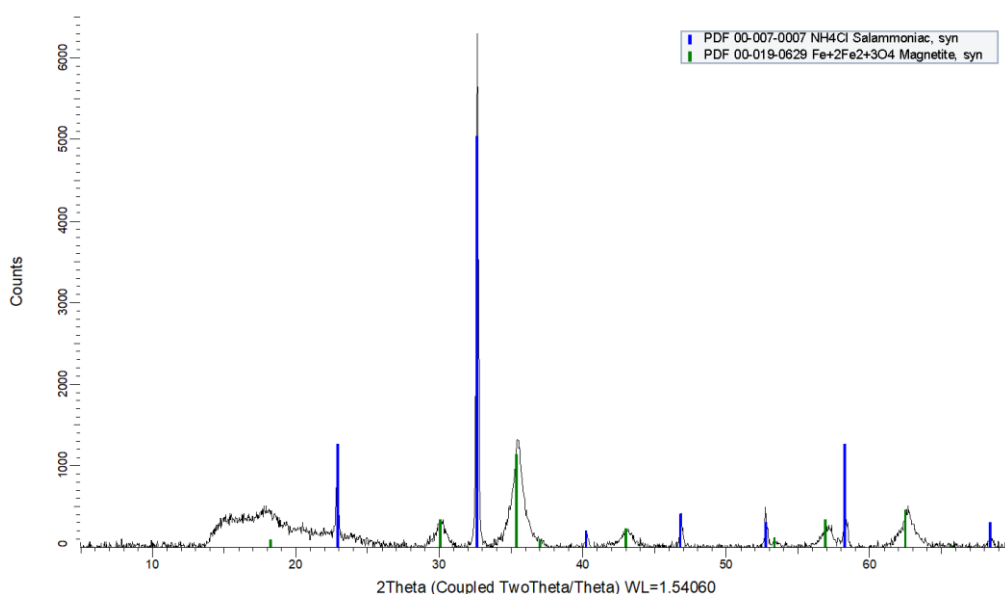
Figure S4.7: Bulk XRD pattern (Bruker D8 Advance) of the U(V)-incorporated magnetite starting material. Patterns were evaluated using EVA v4 and the ICDD database. Magnetite (Fe_3O_4) is the dominant phase here, with a contribution from NH_4Cl from the synthesis of the starting material. The magnetite diffraction peaks highlighted here match that of literature U(V)-incorporated into magnetite samples (Roberts et al., 2017).

S4.3.2 Sequential Extractions
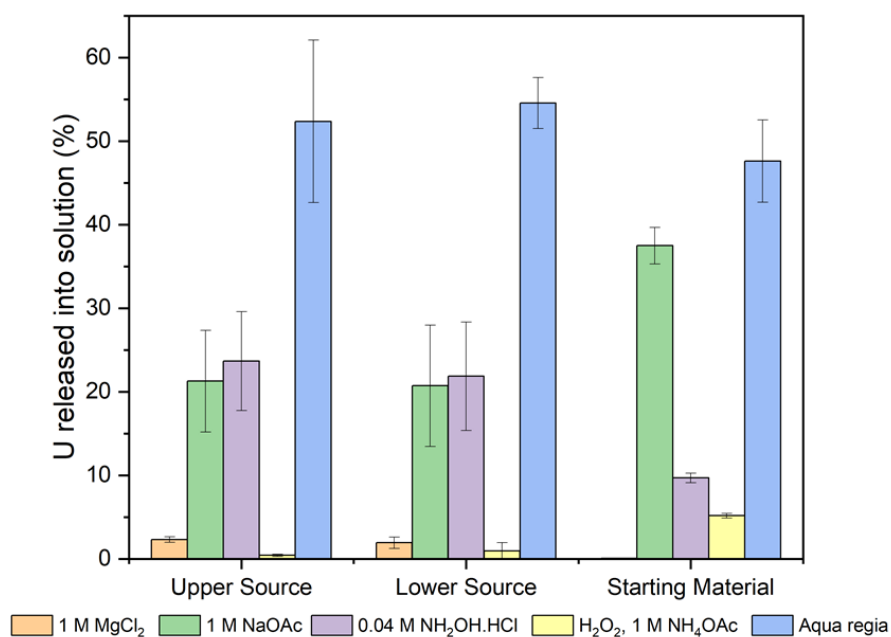
Figure S4.21: Percentage proportions of U released in different chemical fractions during sequential extractions using a method adapted from Tessier et al (1979).

S4.3.3 Autoradiography

Imaging software, ImageJ and Corel Paintshop Pro were used to enhance the brightness and contrast on the autoradiograph (original autoradiographs in Figure S4.9). This editing was done to highlight the areas where U was and was not present. Areas around the source horizons are left in the images to show the 'signal' from the slide itself, and give a comparative background. The upper and lower sources were edited separately due to a difference in signal (upper had a greater radioactivity signal) and so the contrast on the lower source needed to be increased more significantly (Figure S4.10).
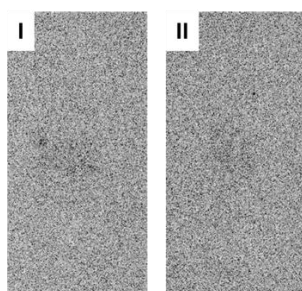
Figure S4.9: Original autoradiograph of resin-embedded thin sections of the upper (I) and lower (II) source horizons.
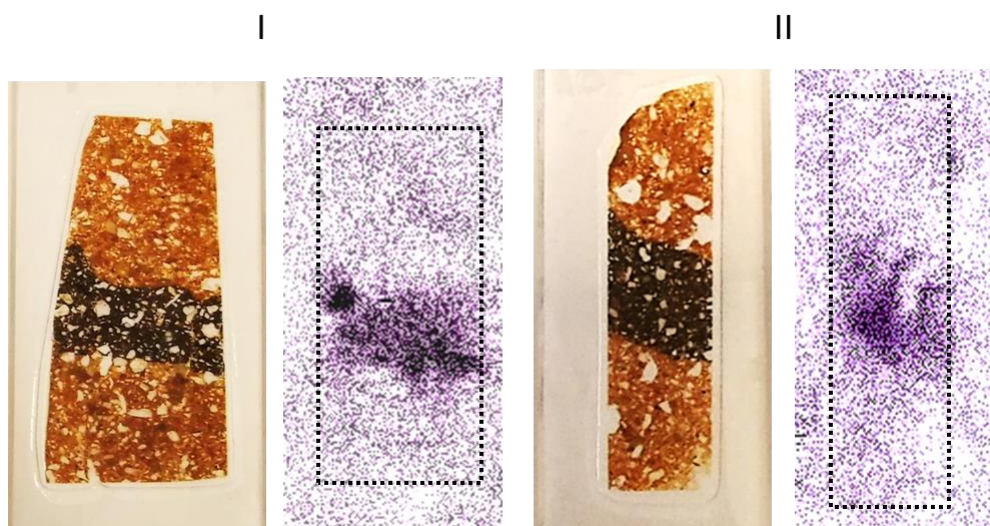
Figure S4.10: Photographs of resin embedded thin sections mounted on quartz slides next to their respective autoradiograph (with enhanced contrast). (I) Upper source; (II) Lower source

S4.3.4 Micro-focus XRF
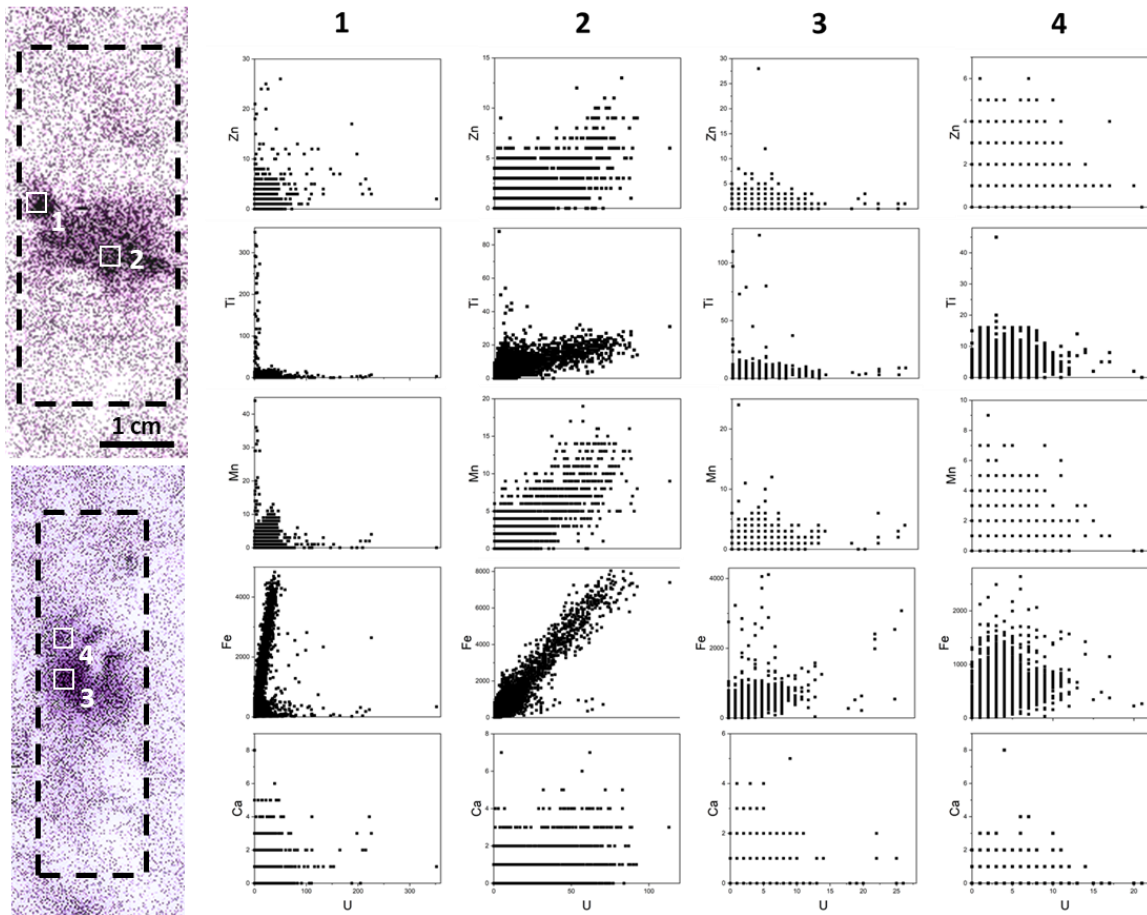
Figure S4.11: Scatter plots of U vs Ca, Fe, Mn, Ti and Zn for the areas highlighted in the autoradiographs on the right. 1&2 relate to the upper source; 3&4 relate to the lower source.

These plots show the relationships between U and other element concentrations in 2x2 mm raster scans. Regions 1-4 were selected for their higher U content based on autoradiography analyses, as such the scatter plots of these areas show any potential co-location on a larger scale. For most elements, the concentration in the samples is too low to detect and so you get a binning effect (clearly seen in all four U vs Ca scatter plots). There is some correlation in regions 1 & 2 between U and Fe, but this is not seen on the same scale in regions 3 & 4, highlighting the heterogeneity of the magnetite band. Indeed, in 3 & 4, the U concentration is much lower than in the upper source, resulting in a binning effect for U itself.

Ti was selected as it is often found with aluminosilicates in the clay fraction of sediments (Spears and Kanaris-Sotiriou, 1976). In the upper source (region 2) there seems to be a slight correlation of U with Ti.
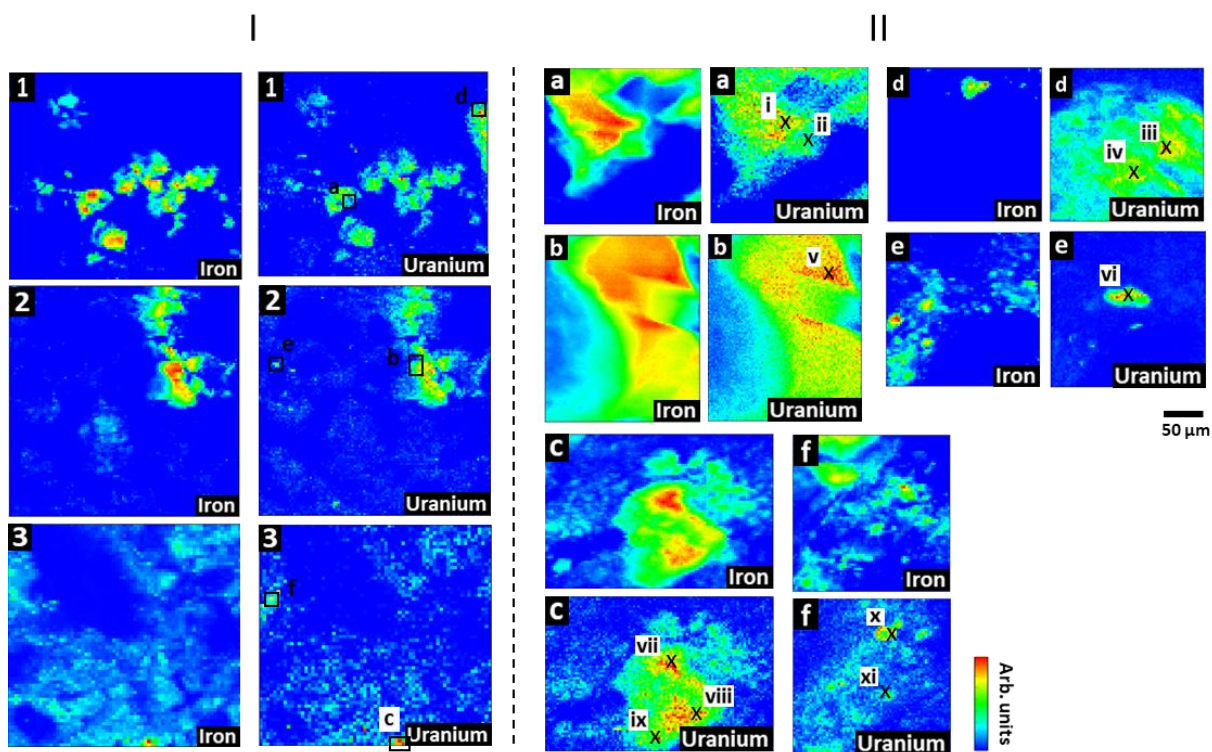
Figure S4.12: Element specific μ-focus XRF raster maps collected at 17600 eV of (I) coarse 2x2 mm areas of source horizons (areas 1, 2 and 3 are highlighted in Figure S4.11) and (II) selected regions of coarse XRF maps for 200/300 x 200 μm mapping with a ~1 μm beam size. Areas for targeted μ-focus spot XANES are highlighted (Figure S4.14).

S4.3.5 Iterative Transformation Analysis (ITFA) of U L₃ edge XANES

ITFA was used to gauge the relative fractions of U(IV), U(V) and U(VI) with the lower and upper source horizons. L_3 edge XANES spectra were compared to U(IV), U(V) and U(VI) standards and the software determined the relative concentrations of each.
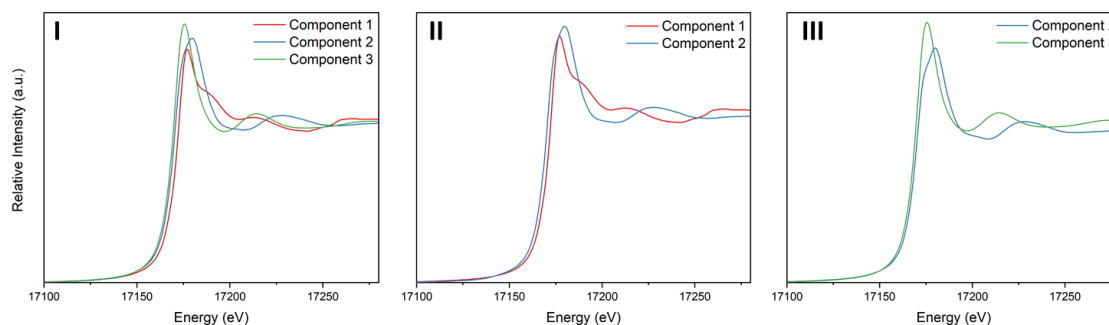
Figure S4.13: Single component spectra for upper (I) and lower (II) source horizons and the U(V)-incorporated magnetite starting material (III), calculated using ITFA from U L_3 edge XANES. In all spectra, component 1 (red) is representative of U(VI), component 2 (blue) is representative of U(V) and component 3 (green) represents U(IV).

Table S4.5: Relative concentrations of U(IV), U(V) and U(VI) in the upper and lower source horizons, calculated using ITFA from U L_3 edge XANES.

Sample	U(IV) %	U(V) %	U(VI) %
Starting Material	27	73	0
Upper Source	1	62	37
Lower Source	0	72	28

S4.3.6 Micro-focus XRF Spot XANES
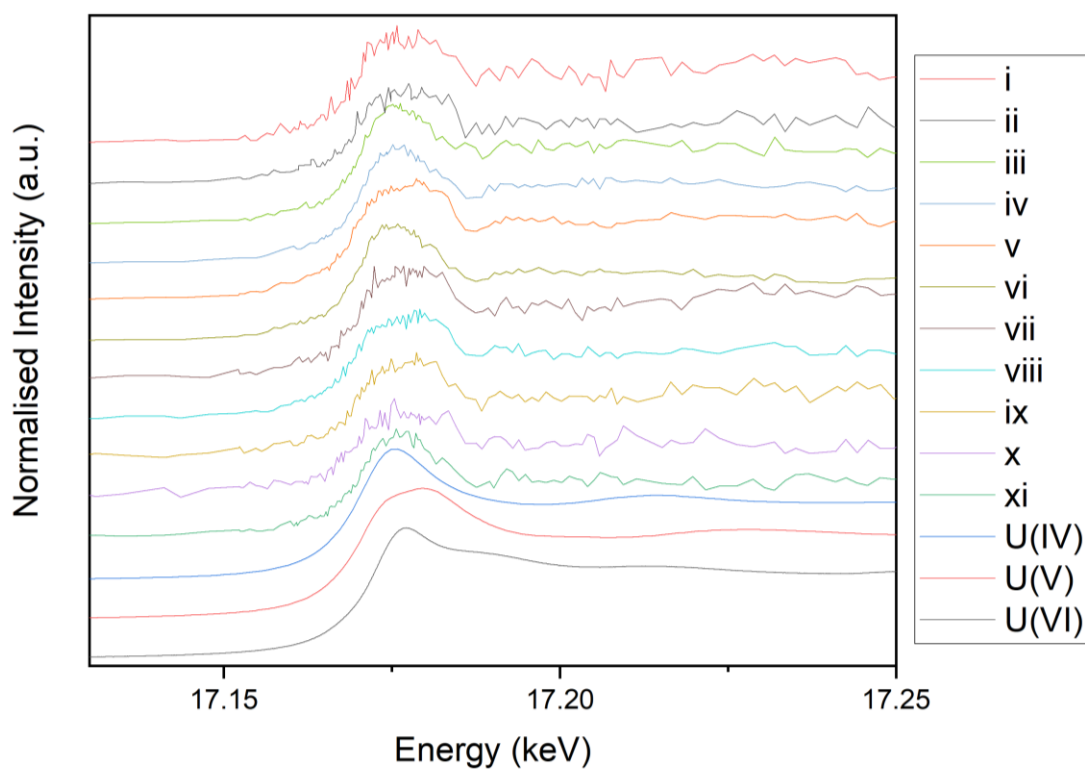
Figure S4.14: Low quality spot XANES (XANES regions highlighted in Figure S4.12 (II)) as a result of low U detection limits and the nature of the samples. These data were not included in the analysis but are included here to evidence low quality. U(IV), U(V) and U(VI) standards are included here for use as a data quality comparison.

S4.3.7 XRD
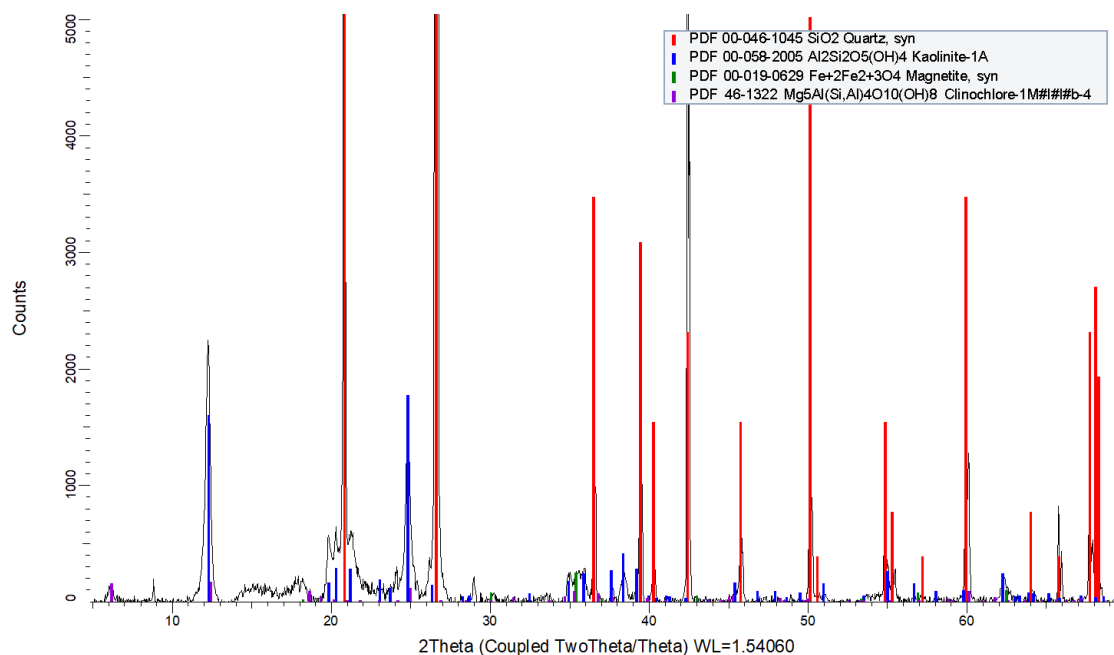
Figure S4.15: Bulk XRD pattern with altered y-axis scaling to capture minor phases of the altered upper source horizon after ~12 months environmental exposure – Quartz (SiO_2) is the dominant phase with additional contributions from kaolinite ($Al_2Si_2O_5(OH_4)$) as a result of contributions from the SRS sediment. Magnetite (Fe_3O_4) is the only identified iron phase.
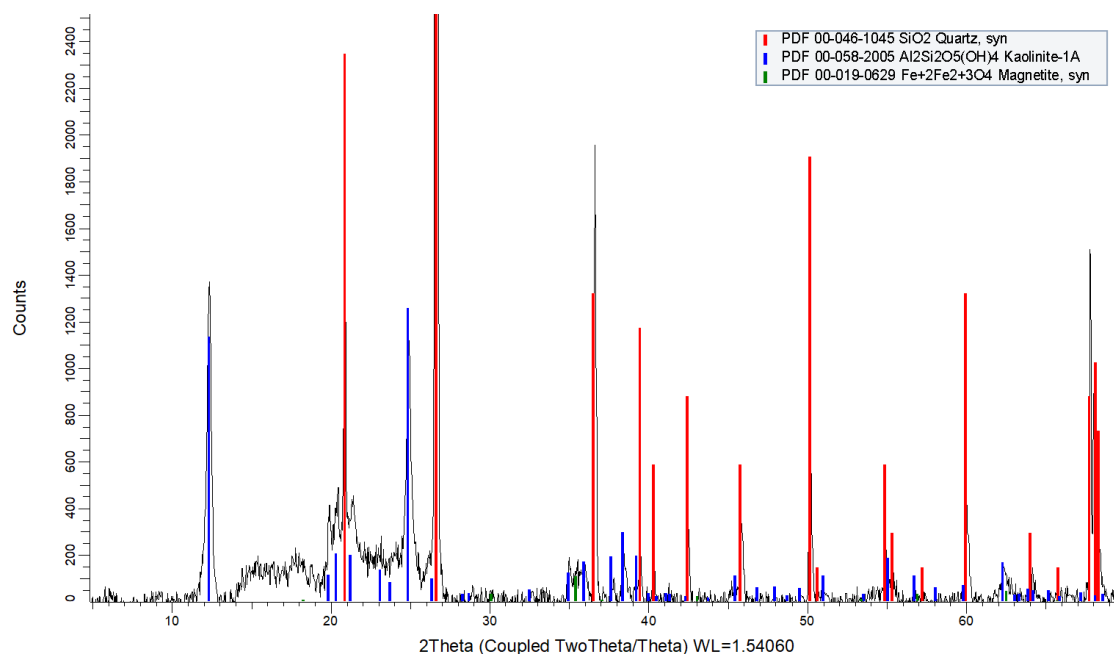
Figure S4.16: Bulk XRD pattern with altered y-axis scaling to capture minor phases of the altered lower source horizon after ~12 months environmental exposure – similar to the upper source, quartz (SiO_2) is the dominant phase and again contributions from kaolinite ($Al_2Si_2O_5(OH_4)$) are observed from SRS sediment. Magnetite (Fe_3O_4) is the only identified iron phase.
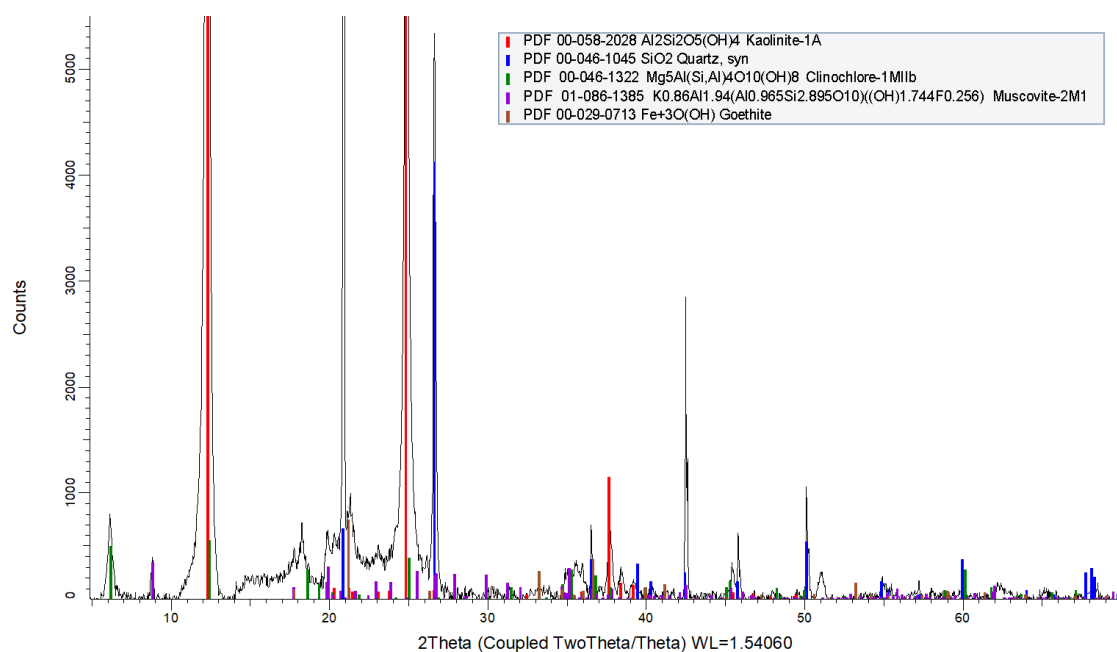
Figure S4.17: XRD pattern of collected fines with altered y-axis scaling to capture minor phases of the altered upper source horizon. Here, smaller amounts of quartz are identified with sediment phases kaolinite, chlinochlore and muscovite also present. Magnetite was not identified here due to its density, but a small proportion of goethite is identified.
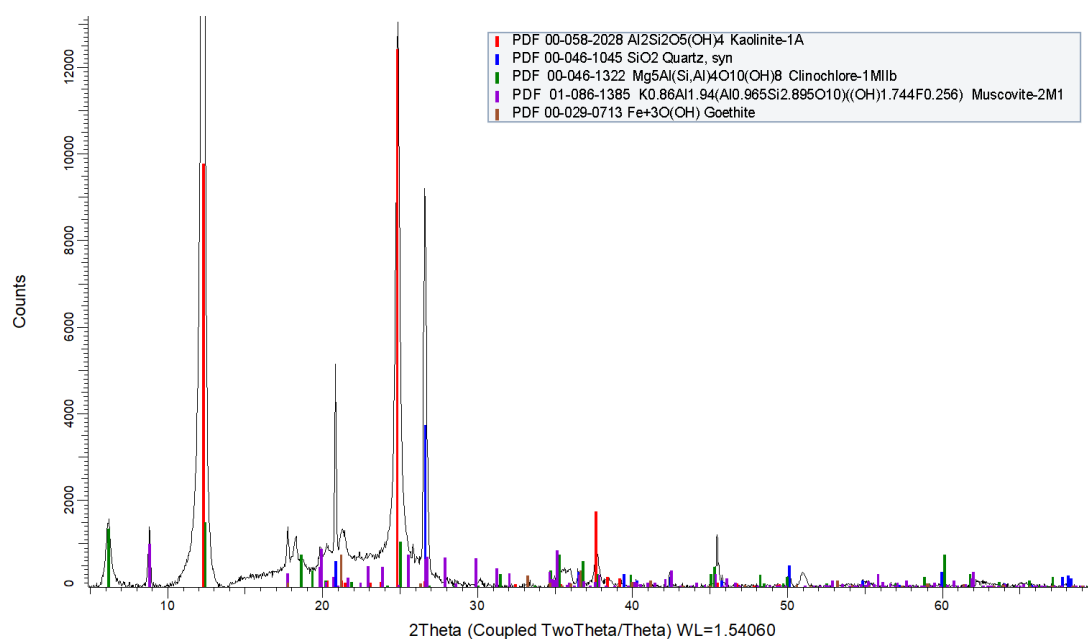
Figure S4.18: XRD pattern of collected fines with altered y-axis scaling to capture minor phases of the altered lower source horizon. Here, the pattern is similar to the upper source (Figure A1-17) with sediment phases identified in addition to minor amounts of goethite.

S4.3.8 XMCD
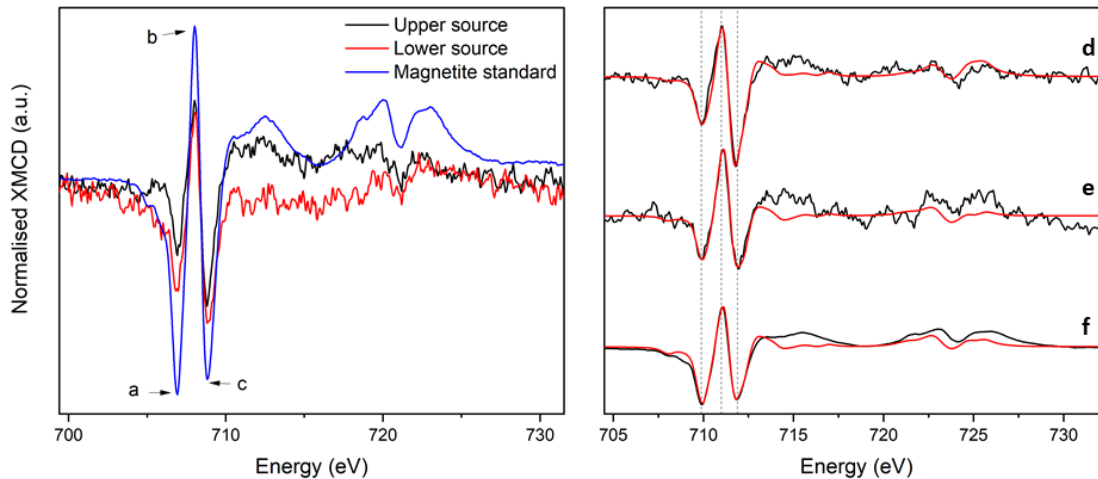
Figure S4.19: (Left) Experimental Fe $L_{2,3}$ XMCD spectra for the upper and lower source horizons plotted against a magnetite standard. (Right) Experimental Fe $L_{2,3}$ XMCD spectra and their fits for the lower (d) and upper (e) source horizons plotted against a magnetite standard (f). Here, feature 'a' represents Fe^{2+} in O_h coordination, 'b' represents Fe^{3+} in T_d coordination and 'c' represents Fe^{3+} in O_h coordination.

The relative proportions of Fe^{2+} O_h, Fe^{3+} T_d and Fe^{3+} O_h were calculated using a non-linear least-squares analysis, using calculated spectra for each of the Fe sites (Van der Laan and Thole, 1991) and are given in Table S4.6, below.

Table S4.6: Proportions of $Fe^{2+/3+}$ in Oh/Td sites and a relative ratio of Fe(II)/Fe(III) in each sample.

	$Fe^{2+} O_h$	$Fe^{3+} T_d$	$Fe^{3+} O_h$	Fe^{2+}/Fe^{3+}
Upper Source	0.45	1.2	1.85	0.1
Lower Source	0.62	1.25	1.13	0.3

The XMCD data collected for the upper and lower source horizons was noisy and so the numbers in Table S4.6 should be used as guidance only. Stoichiometric magnetite has equal proportions across all sites, with a Fe(II)/Fe(III) ratio of 0.5, though here, the starting material was prepared with an Fe(II)/Fe(III) ratio of 0.6. The data above was noisy and so it cannot be assessed reliably quantitatively, qualitatively however, there is a lower proportion of Fe(II) in the upper source compared to the lower, and both have less Fe(II) than stoichiometric magnetite. This shows there has been some change in Fe speciation, with oxidation evident from the reduction in Fe(II) present.
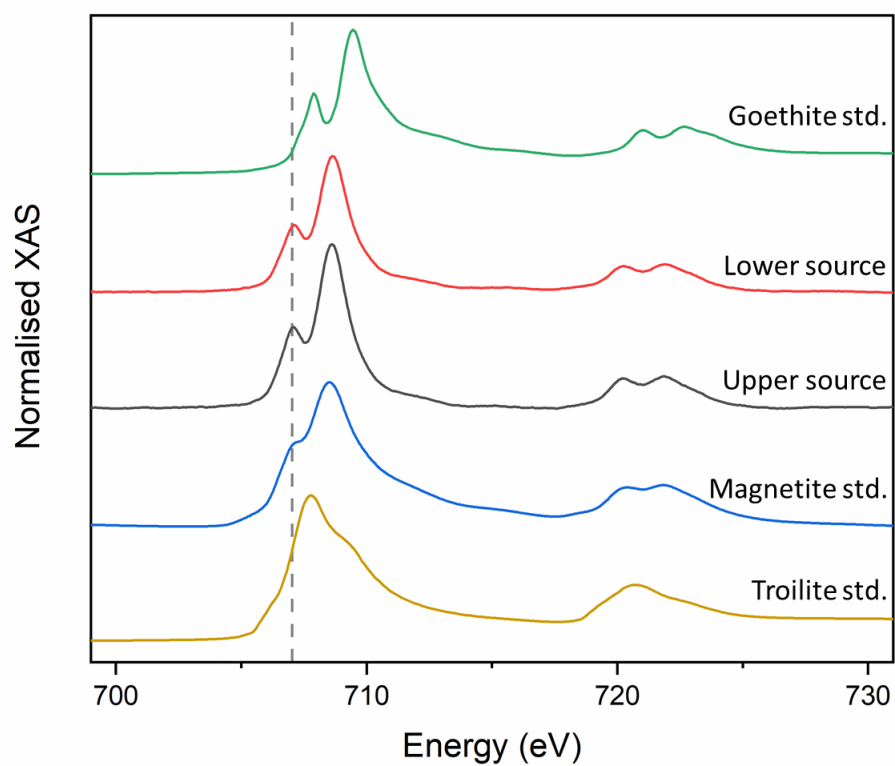
Figure S4.20: Fe $L_{2,3}$ edge XAS spectra for the upper and lower source horizons, plotted with magnetite, goethite (Fe(III)) and troilite (Fe(II)) standards for comparison. Goethite and troilite standards are taken from Coker et al. (2020). The highlighted pre-edge feature at 707.05 eV is highlighted to show the difference between the standard and altered sources.

Blank page

Chapter 5

Environmental behaviour of uranium in concrete impacted contaminated land – a field based lysimeter study

Manuscript in preparation for submission to Environmental Science and Technology. Supporting information for this manuscript can be found immediately after this chapter.

Environmental behaviour of uranium in concrete impacted contaminated land – a field based lysimeter study

[1] Alana E. McNulty, [1] Sam Shaw, [2] Brian Powell, [1,3] Gareth T. W. Law, [1,3] William R. Bower, [2] Kathryn Peruski, [4] Joerg Rothe, [4] Tonya Vitova, [5] Liam Abrahamsen-Mills and [1] Katherine Morris

[1]Research Centre for Radwaste Disposal and Williamson Research Centre for Molecular Environmental Science, Department of Earth and Environmental Sciences, School of Natural Science, The University of Manchester, UK

[2]Department of Environmental Engineering and Earth Sciences, Clemson University, USA

[3]Laboratory of Radiochemistry, Department of Chemistry, University of Helsinki, Finland

[4]Karlsrühe Institute of Technology (KIT), Institute for Nuclear Waste Disposal (INE), Germany

[5]National Nuclear Laboratory, UK

5.1 Abstract

Large volumes of radioactively contaminated land and concrete rubble are expected to be produced during the decommissioning of nuclear sites. With disposal capacity for radioactive wastes limited, alternative disposal options for the large volumes of low-level radioactively contaminated materials generated during decommissioning are being explored. One such option is in-situ disposal, where low activity wastes and/or contaminated structures will be left in-situ at nuclear sites. Uranium (U) is typically the most abundant radionuclide by mass in many contaminated land scenarios and as such, developing an understanding of U interactions with subsurface structures, including with concrete, is a priority to underpin in-situ disposal options. Here, three outdoor field lysimeters with U(VI)-emplaced within the lysimeters with and without concrete were exposed to the environment for 13 months. After exposure, the lysimeters were sampled and geochemical and X-ray absorption spectroscopy (XAS) analyses performed to explore U mobility and fate. There was significant movement of U in the system with no concrete present, U mobility was reduced in the lysimeter with a concrete cap over the U(VI)-source and, where the U(VI)-source was mixed with concrete prior to emplacement, U had the lowest mobility. XAS measurements highlighted the role of U(VI)-speciation in controlling U-mobility; in the sediment only system, U(VI) was present as relatively mobile U(VI)-uranyl on solids after 12 months; in the lysimeter with U(VI)-mixed with concrete, the U was present as poorly soluble Ca-uranate phases as a result of U-concrete interactions and, in the concrete cap experiment, the U speciation was consistent with a mix of U(VI)-uranyl and U(VI)-uranate. This work has clear implications for U-mobility at the field scale with and without concrete present and is relevant to the options for in situ disposal at nuclear facilities.

5.2 Introduction

Civil and military nuclear activities over the last 75 years have resulted in a global legacy of radioactively contaminated land and structures at many nuclear facilities and typically uranium is the most abundant radionuclide contaminant by mass at these sites (Catalano et al., 2004; Evans et al., 1992; Sellafield Ltd., 2016; Um et al., 2010; Wang et al., 2016, 2014). Uranium (U) is a long lived chemo- and radio-toxic radionuclide (U^{238} half life = 4.5 x 10^9 years) and can present a danger to human health (Taylor and Taylor, 1997).

Disposal of radioactive wastes that arise from the decommissioning of sites is a complex challenge with volumes of contaminated land (soils, sediments and made-ground) at nuclear mega-facilities such as Hanford in the USA and Sellafield in the UK estimated in the millions of m^3 (NDA and BEIS, 2019b; US DOE, 1997). Decommissioning wastes, including those arising from the demolition of contaminated buildings and structures has heterogeneous contamination, and in many cases is poorly characterised but it is clear that a significant volume of the contaminated land and building materials will have lower levels of radionuclide contamination. In recent years, in-situ disposal of radioactively contaminated land has developed as a potential strategy for management of radioactively contaminated land and materials (IAEA, 1999; SEPA et al., 2018). In-situ disposal is the permanent emplacement of radioactive waste in the shallow sub-surface at a nuclear site, with contaminated land and/or structures left in-situ. It also encompasses the re-use of low-level contaminated materials such as concrete and rubble from the decommissioning of on-site facilities as backfill or void filler (SEPA et al., 2018). Understanding optimal management pathways for radioactively contaminated land and associated structures brings a requirement to understand radionuclide speciation and fate in the complex interface environments between made-ground, buried concrete structures, and the subsurface. Clearly, developing an understanding of the interactions of uranium with subsurface material and concrete in these complex engineered environments is important in underpinning safety arguments for in-situ disposal.

U mobility in the environment is controlled by its speciation which dictates its solubility and sorption to mineral surfaces (Silva and Nitsche, 1995). The chemical speciation and fate of U is sensitive to redox and pH change. In aqueous oxic, circumneutral conditions, U is typically present either as the uranyl ion, $U(VI)O_2^{2+}$, or in a range of soluble U(VI) uranyl complexes, dependent on pH and the presence of carbonate (Newsome et al., 2014). The migration of U(VI) in oxic, organic matter-poor sediments at circumneutral pH can be limited through sorption to minerals present in natural sediments including iron- (Bargar et al., 2000; Crawford et al., 2017; Um et al., 2008) and manganese- (Wang et al., 2013) (oxyhydr)oxides and clays, (Catalano and Brown, 2004;

Maher et al., 2013) where U(VI) typically forms inner-sphere bidentate complexes. At higher pH, such as that expected in the leachates from cementitious materials (pH 10-13), often a mix of solid and solution U phases are present and speciation and solubility is highly dependent on pH and U loading. Here, various uranate phases (Bots et al., 2014; Bube et al., 2014; Felipe-Sotelo et al., 2017; Smith et al., 2015; Sutton et al., 1999; Yamamura et al., 1998), uranophane (Bube et al., 2014) and uranyl oxyhydroxides (Felipe-Sotelo et al., 2017; Philipp et al., 2019; Smith et al., 2015; Sutton et al., 2003, 1999; Yamamura et al., 1998) have been reported. Calcium silicate hydrates (C-S-H), which are a key component of cementitious materials (Hewlett and Lea, 1998), have a significant control on radionuclide sorption to cements (Macé et al., 2013; Tits and Wieland, 2018) and, as such, are an important phase in examining U interactions with cements and concrete at high pH (Gaona et al., 2012; Harfouche et al., 2006; Kremleva et al., 2020; Moroni and Glasser, 1995; Pointeau et al., 2004; Tits et al., 2015, 2011; Zhao et al., 2000). Various studies examining U(VI) and C-S-H interactions have shown that U can be immobilised through the precipitation of uranate phases (Macé et al., 2013; Tits et al., 2015, 2011), incorporation into C-S-H (Gaona et al., 2012; Tits et al., 2015, 2011) and adsorption to C-S-H mineral surfaces (Harfouche et al., 2006; Macé et al., 2013; Pointeau et al., 2004; Tits et al., 2015, 2011).

U loading in experimental systems has also been shown to affect speciation across a range of pH values. Under circumneutral pH conditions, where solutions are supersaturated with respect to U, surface precipitation of uranyl oxyhydroxide phases such as schoepite and metaschoepite can occur (Giammar and Hering, 2001). The solubility of these phases is highly pH dependent and they form stable precipitates only around near-neutral pH (Stanley and Wilkin, 2019). Additionally, the presence of carbonate has been shown to promote the formation of stable, soluble anionic uranyl carbonate complexes (eg. $UO_2(CO_3)_3^{4-}$) at circumneutral pH and above, which are mobile in the environment (Bargar et al., 2000; Bernhard et al., 2001; Kalmykov and Choppin, 2000; Krestou and Panias, 2004) and are widely reported to limit U precipitation or sorption to subsurface materials (Akçay, 1998; Duff and Amrhein, 1996; Hsi and Langmuir, 1985; Stanley and Wilkin, 2019; Tournassat et al., 2018; Um et al., 2007; Zheng et al., 2003). In contrast, at high pH, elevated U(VI) loadings typically promote the precipitation of insoluble uranate phases (Macé et al., 2013). Here, uranate phases are typically characterised by an elongation of the linear axial U-O bonds in the $[O=U=O]^{2+}$ uranyl moiety from the characteristic ~1.80 Å in uranyl phases (Thompson et al., 1997) to 1.86-1.97 Å (Bots et al., 2014; Catalano and Brown, 2004; Macé et al., 2013). This is usually coupled with a shorter U-O equatorial bond (typically around 2.15-2.30 Å (Bots et al., 2014; King, 2002; Macé et al., 2013)) than is found in uranyl phases, typical of alkali metal uranates (Allen et al., 1996). Understanding the differences in solubility of uranyl and uranate phases in complex subsurface/cement systems, with a range of pH conditions, is key to building a picture of the long term behaviour and fate of uranium at nuclear sites.

In this study, three "field-scale" lysimeter experiments (78 cm length, 10 cm diameter) were set up to replicate near-surface disposal scenarios similar to those expected at radioactively contaminated facilities. The first lysimeter, the "sediment source lysimeter" was designed as relevant to a sediment subsurface environment contaminated with elevated levels of uranium (as uranyl nitrate). The second lysimeter, the "concrete cap lysimeter" was designed to represent a layer of uranium (as uranyl nitrate) contaminated sediment with the addition of a crushed concrete cap above the uranium contaminated sediment to explore scenarios where uranium contamination in sediments was affected by cementitious materials. The third and final lysimeter, the "concrete source lysimeter" was prepared using uranyl nitrate solution which had been reacted with crushed concrete to reflect scenarios where uranium has been contacted fully with concrete at nuclear facilities. Each lysimeter was exposed to the environment (and rainfall) for 13 months at the RADFATE Facility, University of Clemson, SC, USA, before sacrificial sampling, where a multi-technique approach utilising a range of geochemical and X-ray absorption spectroscopy (XAS) characterisation methods were used to analyse uranium speciation and fate in each lysimeter. Significant retardation of uranium was observed with the formation of increasingly crystalline insoluble Ca-uranate phases in the concrete source lysimeter after 13 months. In contrast, significant transport was observed in the sediment-only system facilitated by the dominance of mobile uranyl species, however the addition of a concrete cap to contaminated sediments significantly reduced transport through the sediment and was reflected in a mixed uranyl / uranate speciation in the sediments.

Overall, these results highlight the impact of concrete in controlling uranium speciation and reducing the mobility of uranium in subsurface systems relevant to radioactively contaminated land. In addition, the lysimeter facility, which bridges between laboratory scale and field scale experiments has provided significant new insights on U reactivity in vadose zone environments relevant to the contaminated land legacy. The results have clear implications for the global decommissioning industry, where contaminated land and concrete materials are produced in large volumes during site decommissioning.

5.3 Methodology

Field Lysimeter Experiment. To explore the geochemical behaviour of U in contaminated land environments, three lysimeters were emplaced into the open air Radionuclide Fate and Transport Experiment (RadFATE) facility at Clemson University (SC, USA) and exposed to the environment for 399 days, from 12/07/2018 to 15/08/2019 (Figure S5.1). Each lysimeter was constructed out of PVC pipe of approximately 78 cm length and 10 cm diameter and was fitted with a polypropylene grid covered in nylon mesh at the base of the lysimeter to enable water drainage whilst keeping the sediment / concrete in place. A reducer attached to tubing was also fitted to the base of each lysimeter to collect effluent into open polypropylene bottles at approximately quarterly intervals. Effluent samples were monitored for pH, then acidified and analysed for elemental concentration by inductively coupled plasma-mass spectrometry (ICP-MS). In-situ probes measuring temperature, electrical conductivity and volumetric water content were placed at 27, 48 and 62 cm horizons in each lysimeter and probes measuring water potential were placed at 53 and 67 cm. Probe measurements were taken every 2 hours throughout the experiment with the exception of 14/06/2019 to 06/08/2019 when a power outage occurred at the facility.

The lysimeters were packed with sediment from Peel Place Quarry, Holmrook, Cumbria, located approximately 2 km from Sellafield, UK. This material was chosen as it is representative of the Sellafield facility sub-surface environment where radioactive contamination is known to exist (Smith et al., 2020). The sediment was characterised by powder X-ray diffraction (p-XRD), X-ray fluorescence (XRF), and scanning electron microscopy (SEM) and organic matter content was determined by loss on ignition at 550 °C. Briefly, the sediment was dominated by quartz sand, with organic matter content at <1 wt% (SI Section S5.1.2.1). Uncontaminated concrete which was contemporaneous with, and representative of concrete at the Sellafield nuclear facility was sourced from a demolished building at a Nuclear Decommissioning Authority site. This was again characterised by p-XRD, XRF and SEM (Table S5.4, Figures S5.9,10). Here, the analyses were consistent with the history of the building concrete which was originally constructed in the 1970s from pre-fabricated sections and was thought to comprise Ordinary Portland Cement and pebble aggregate and was not expected to have additives associated with the concrete (John Shevelan, Personal communication, 2017). The concrete was crushed and sieved to a size of 1-5 mm for use in the lysimeter experiments.

The lysimeter experiments (10 cm internal diameter) were packed by partially filling with Sellafield-representative sediment before adding the U-source horizons on top (Figure S5.2). In the first "sediment-only" lysimeter, the source horizon was a mixture of uranyl nitrate with Peel Place Quarry Sediment and a layer of 17 cm inert, quartz dominated Ottawa sand was placed

above this. In the second "concrete-cap" lysimeter, the source horizon was also a uranyl nitrate sediment mixture, but with a 12 cm layer of crushed concrete added above and topped with an additional 12 cm of Ottawa sand. The third lysimeter ("concrete source lysimeter") employed a uranyl nitrate solution reacted with concrete as a source layer on top of the sediment, with a further 12 cm of uncontaminated concrete placed above the source layer which was then capped with 12 cm of Ottawa sand. Each lysimeter had an approximately 12 cm gap between the top of the lysimeters and the sand interface to promote drainage and limit the formation of preferential flow pathways above the source horizons.

U source material preparation. The uranium sediment source horizons used in the "sediment-only" and "concrete cap" lysimeter experiments were prepared by thoroughly mixing uranyl nitrate salt (approximately 1.4 g, accurately weighed) into sediment to a final concentration of approximately 6000 ppm U. The source material was then lightly pressed into cylinders of 8.5 cm width and 1.3 cm depth with ~115 g of contaminated U-sediment before being placed onto the uncontaminated sediment layer that had been loaded into the lysimeter experiments. Uncontaminated Peel Place Quarry sediment (approximately 45 g) was then used to fill the edges around the uranyl nitrate / sediment layer and approximately 0.5 cm of uncontaminated Peel Place Quarry sediment was then sprinkled on top of the contaminated material. Finally, approximately 12 cm of Ottawa sand ("sediment-only" lysimeter) or 12 cm of 1 – 5mm fraction crushed building concrete ("concrete-cap" lysimeter) was used to cap the experiments. The U-concrete source material used in the concrete source lysimeter was prepared by reacting 400 g of crushed concrete with 20 L of uranyl nitrate solution at pH 3 to achieve an approximate loading of 6000 ppm U on solids. After 48 hours, the vast majority of U had partitioned to the solid phase and the yellow-orange concrete solid phase was removed for use in the lysimeter. The concrete and U precipitate were extracted and thoroughly mixed before packaging as moist solids for shipment to the RadFATE facility. A sample of the fresh U-concrete source material was retained for L_3 edge XAS analysis.

Lysimeter sampling. After 399 days emplacement in the field, the lysimeters were extracted and each was then sectioned by cutting each in half, vertically in an anaerobic chamber (Figure S5.4) (Peruski et al., 2018). One half was preserved intact for later analyses with an Itrax X-ray fluorescence (XRF) scanner (full details in SI Section S5.2.3.1), whilst in the second half of each lysimeter, steel sampling housings (9 x 3.5 x 3 cm) were gently pressed into the source horizons, before being removed intact (Figure S5.5). The remaining material in the second half was segmented into 1 or 2 cm vertical sections, in an anaerobic glovebox (sediment horizons towards the bottom of the lysimeters and crushed concrete areas were sectioned in 2 cm fractions). The sectioned sediment and concrete samples were homogenised and stored double sealed, in the

dark and at room temperature prior to packing and shipping back to the UK for analysis. In the source horizons, the removal of contaminated material in the steel sampling housings, and subsequent homogenisation of the remaining contaminated materials with the blank material around the sources resulted in dilution of U in the samples with resultant approximate loadings in the source horizons of ~3000 ppm (Figure S5.6).

Solid phase geochemical analysis. To determine the sediment U distribution along the length of each lysimeter, the 1 or 2 cm vertical sections were dried, accurately weighed and digested in *aqua regia* for 4 hours (Bower et al., 2019; Morris et al., 2000). The solution was then filtered and the resultant leachate taken to near dryness before dilution into a known volume of 3 M HNO_3 prior to dilution into 2% HNO_3 for analysis of U by ICP-MS (Agilent 7500cx ICP-MS) (Bower et al., 2019; Morris et al., 2000). In addition to *aqua regia* leaching, in the sediment-only lysimeter sequential extractions were used on selected 1 cm vertical sections using a methodology adapted from Tessier et al., (1979). The sequential extraction leachates were: 1 M magnesium chloride (pH 7, 1 h; typically targets exchangeable U), 1 M sodium acetate (pH 5, 5 h; targets U bound to carbonates), 0.04 M hydroxylamine hydrochloride in 20% HOAc (pH 2, 16 h; targeted U bound to Fe/Mn oxides), 30% hydrogen peroxide and 1 M ammonium acetate (pH 2, 16 h; targets U bound to organic matter), and finally heated *aqua* regia to extract any residual U. Sequential extractions were performed on duplicate or triplicate samples of selected 1 cm vertical sections from the sediment-only lysimeter and a sample of unaltered U-sediment source material was also run as a control. The 1 or 2 cm vertical sections from all lysimeters were also analysed for pH (1 g sediment to 1 g 18 MΩ water, 1 hour equilibration, measurement; Thomas, 1996).

For Environmental-Scanning Electron Microscopy (E-SEM) analysis, samples of sediment or concrete were mounted onto SEM stubs and left uncoated. Images were obtained using an FEI XL30 ESEM-FEG operating in low vacuum mode between 15 and 30 keV and imaged in both secondary electron and backscattered electron modes. An EDAX Gemini EDS system was used to collect energy dispersive X-ray spectroscopy (EDS) spectra at selected points of interest for the uncontaminated sediment and concrete starting materials and lysimeter-altered materials.

Powder X-ray Diffraction (XRD) measurements were performed on dried, powdered starting material and altered samples using a Bruker D8 Advance in continuous scan mode in the 5-70° 2Θ range. Patterns were analysed using EVA 4 and the ICDD database.

Modelling. All solution modelling was carried out with PHREEQC (version 3.6.2) using the ANDRA SIT database (ThermoChimie v10a 2018).

XAS Data Acquisition and Analysis. L_3-edge X-ray absorption near edge structure (XANES), extended X-ray absorption fine structure (EXAFS) analysis and M_4-edge high energy resolution

fluorescence detection (HERFD)-XANES were used to build a molecular-scale picture of U speciation in sediment/concrete samples after 399 days of environmental exposure in the different lysimeter systems. Sediment / concrete samples for both L_3-edge XAS and M_4-edge HERFD-XANES analyses were taken from sectioned sub-samples of the altered source horizons or from the U-concrete starting material. Samples were mounted in anaerobic sample holders and stored at -80 °C prior to shipment in a liquid N_2 dry shipper to Diamond Light Source for analysis on beamline B18 (Dent et al., 2009) or beamline I20 (Diaz-Moreno et al., 2009). On both beamlines, samples were analysed in fluorescence mode, inside a liquid N_2 cryostat, using solid state 36-element (B18) or 64-element (I20) Ge detectors. The ACT station of the CAT-ACT beamline at Karlsruhe Institute of Technology (Zimina et al., 2016) was used to record U M_4-edge HERFD-XANES spectra. U L_3-edge XANES and EXAFS spectra data processing and linear combination fitting were performed using Artemis and Athena from the Demeter software package (Ravel and Newville, 2005). U M_4-edge XANES were processed using PyMCA (Solé et al., 2007) and component analysis of spectra were performed using Iterative Transformation Analysis (ITFA) (Rossberg et al., 2003).

5.4 Results and Discussion

Three different uranium lysimeter systems were emplaced for approximately 1 year in the RadFATE facility at Clemson University, SC, USA (Kilgo, 2018). The first "sediment-only" lysimeter was packed with representative Sellafield sediment, and had a sediment-uranyl nitrate source emplaced at 30 cm depth. The second "concrete-cap" lysimeter had a sediment-uranyl nitrate source emplaced at 40 cm depth and had 12 cm of 1-5 mm crushed concrete emplaced above this. The third "concrete-source" lysimeter had an emplaced uranyl nitrate solution reacted with concrete source at 40 cm depth. A range of geochemical and spectroscopic techniques were used to explore the U speciation and fate in these different lysimeter experiments.

Lysimeter Effluent Geochemistry. Throughout the lysimeter emplacement, the effluent was collected at approximately quarterly intervals. The total volume of effluent that had passed through each lysimeter was approximately 7 L (Table S5.5). The sediment only lysimeter effluent pH was 6.7 - 7.2 and in the concrete cap and concrete source experiments, the pH was between 6.7 and 7.7, increasing on average over the experiment (Table S5.5). Effluent ICP-MS data indicated that U concentrations were below background in all lysimeters in the first effluent collection at 96 days (Figure S5.11-13). Thereafter, the sediment only lysimeter showed U concentrations above background with approximately 1.8 % of the originally emplaced U eluted from the column over the experiment suggesting relatively high U mobility (Table S5.6). The concrete cap lysimeter showed background levels and then a flush of U in the 201 day sample with the levels declining after that, with approximately 1 % of the originally emplaced U eluted over the experiment (Table S5.6). Finally, the concrete-source lysimeter effluents showed U concentrations below the level of detection throughout the experiment suggesting U was strongly retained in the column.

In-situ geochemical sensor data. After several rainfall events, water content values (expressed as % saturation) stabilised in the range of 3-15% in the top sensors across all lysimeters, 15-30% in the middle and 23-35% at the bottom sensors and reflecting increased saturation at the base of the lysimeters due to water retention (Figure S5.14). Water potential sensors stabilised after 15 days and data suggests the lysimeters were all close to, but just below saturation, indicative of a vadose-zone environment (Figure S5.16). Eh probes fitted just below the source horizons in all lysimeters showed an oxic environment was maintained in all lysimeters throughout their emplacement (Table S5.7).

Solid Phase Geochemistry.

Sediment pH. Sediment samples down the length of each lysimeter were analysed for pH (Figure S5.17) to inform PHREEQC and EXAFS analyses. In the sediment-only lysimeter, pH values in the sediment ranged between 6.5 and 7 consistent with the in situ pH probe measurements (pH 6.8 – 6.9; Figure S5.17-A) and the effluent samples. In the concrete cap lysimeter, the concrete above the U-sediment source was at a pH of 12.5 and typical of aged cementitious samples suggesting pore saturation with $Ca(OH)_2$ (Tits and Wieland, 2018). The pH was 10.7 immediately below (0-1 cm below) the concrete layer in the sediment source region reflecting the movement of alkaline cement leachate in the lysimeter. Thereafter, the sediment pH stabilised around pH 9 at 3-4 cm below the source to the base of the lysimeter (Figure S5.17-B). This was also reflected in the pH probe measurements at approximately 45 cm depth, where the pH increased from pH 8.8, 2 weeks after the initial emplacement, to 9.9 at 399 days. In the concrete source lysimeter, pH in the concrete source region was 12.5, stabilising around pH 9 2-3 cm below the concrete (Figure S5.17-C), similar to the concrete cap lysimeter. Additionally, in situ pH probe data for the concrete source system and taken at ~45 cm depth (Table S5.6) reflects the sediment pH values measured (Figure S5.17-C), with pH 9.4 routinely measured with time.

Uranium Distribution in the Cores. The 1-2 cm sediment sections that were sampled around the source horizons and down the length of the lysimeters were digested in *aqua regia* to investigate U distribution profiles after 399 days of environmental exposure (Figure 5.1). In the sediment-only lysimeter, the maximum U concentrations were approximately 2500 ppm in the location of the originally emplaced uranyl nitrate source (Figure 5.1A). Below the originally emplaced source, sediment U concentrations fell from approximately 215 ppm immediately (0-1 cm) below the source zone down to approximately 8 ppm at the base of the lysimeter suggesting enhanced uranium concentrations were present in sediments throughout the sediment column. Interestingly, the uranium concentration above the source was also elevated (280 ppm 0 - 1 cm above) suggesting either sediment mixing from the source during sampling or some modest upwards movement of uranium. Past lysimeter work has also identified upwards movement of plutonium (Demirkanli et al., 2008, 2007), radiostrontium (Kaplan et al., 2014) and neptunium (Peruski et al., 2018). The mechanisms for this upward migration included upwards diffusion through pore spaces (Peruski et al., 2018) as well as dispersion, evaporation, transpiration (Kaplan et al., 2014). In the concrete cap lysimeter, the maximum U concentrations in the originally emplaced source location were approximately 3100 ppm, this decreased to 16 ppm 0-1 cm below the source and fell to 0.5 ppm at the lysimeter base and suggesting modest U mobility within the column (Figure 5.1B). Again, there was some U (approximately 1200 ppm 0-1 cm above) above the source emplacement zone, which was attributed to sampling mixing during sectioning and potentially upward migration, which has been reported in past work with other radionuclides (Demirkanli et al., 2008, 2007; Kaplan et al., 2014; Peruski et al., 2018) and which may be due to

capillary action due to the reduced porosity of the crushed concrete above the source. In the concrete source lysimeter, the maximum U concentrations in the source region were approximately 2500 ppm. In the 0 – 1 cm section immediately below the concrete, the sediment concentration of U was measured as 318 ppm although, because of the large concrete clasts, some sediment/concrete mixing had likely occurred in this horizon (Figure 5.1C). Below this, the U concentration fell to 0.7 ppm and at 2-3 cm below the source, the U concentration fell below the ICP-MS detection limit, suggesting U was at background concentrations and there was very little evidence for transport of U over 399 days. To further compare transport through the column between the sediment-only and concrete cap lysimeters, U concentrations at 5, 10, 20 and 30 cm below each source horizon were compared based on interpolation of the data points. Here, at 5 cm below the source horizons, the U concentration in the sediment-only lysimeter was over 6 times that in the concrete cap lysimeter, increasing to 10 times the U concentration compared to the concrete cap experiment at 20 and 30 cm below the source regions (Figure 5.1A, inset; Table S5.8). This suggests significant transport over 1 year exposure in the sediment-only lysimeter, with lower transport in the concrete cap system. In the concrete-source lysimeter, the U concentration at 5, 10, 20 and 30 cm below the source was below the limit of detection and was essentially at background levels from 2-3 cm below the source confirming very restricted mobility of U in this system.
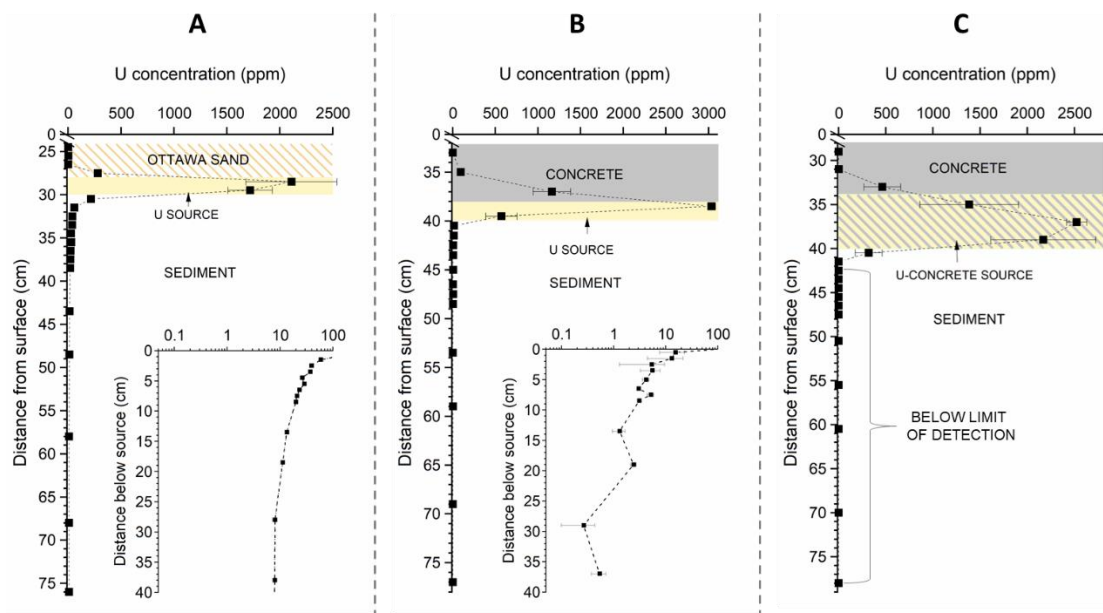
Figure 5.1: U concentration profiles from aqua regia digestions of 1 or 2 cm sections from each lysimeter. Error bars represent the standard deviation of triplicate, or range of duplicate samples and when not visible, they are within the plotted data point. Inset graphs A and B show U concentration (log$_{10}$ scale) against distance below the source horizon. (A) Sediment-only lysimeter; (B) Concrete cap lysimeter; (C) Concrete source lysimeter. Yellow areas indicate original emplacement of U in sediment; grey areas represent

uncontaminated concrete and yellow with grey stripes indicates original emplacement of U in concrete in the concrete source lysimeter.

An Itrax XRF core scanner was used to complement *aqua regia* digest measurements and provide higher resolution data on the undisturbed lysimeter halves (200 μm steps vs 1 cm steps in *aqua regia* digests) to determine the relative concentration of U and other elements in the areas surrounding the source regions of each lysimeter (Figures S5.18-20). In all systems, Fe was present in the sediment regions, with an average of 59 counts/mA Fe in sediment. In non-sediment zones (i.e. in Ottawa sand or concrete zones), the average Fe concentration fell to less than half of this value. In the sediment-only lysimeter, the Itrax data showed a spike of U in the originally emplaced source zone, with a maximum of 48 counts/mA measured, with slightly elevated levels of U also seen above, indicating modest upwards migration of U (Figure S5.18), and consistent with the *aqua regia* digest data (Figure 5.1-A). Elevated levels of U were seen to approximately 14 cm below the source region, with background U levels seen below 14 cm, suggesting the levels of U dropped below the sensitivity of the instrument beyond this point. In the concrete cap system, a spike of U in the originally emplaced zone, with a maximum of 52 counts/mA was measured, (highlighted in Figure S5.19). This was consistent with the aqua regia data and elevated levels of U counts extend to 4 cm below the source region before falling below the limit of detection. Compared to the sediment-only lysimeter, this suggests in the concrete cap system, limited uranium transport occurred over 399 days. Interestingly, elevated U counts above the sediment source in the concrete region suggest upwards mobility of U, and again consistent with the *aqua regia* digest data. In the concrete source lysimeter, Itrax XRF data were broadly consistent with the digest data, with a maximum measurement of 73 counts/mA in the source zone and with U counts/mA falling below the background level less than 1 cm below the base of the source region and highlighting the low mobility of U in this experiment (Figure S5.20). Results also highlight the U distribution was heterogeneous in the source region with some evidence for modest upwards migration of U (Figure S5.20).

A comparison of Ca counts in the concrete-containing systems also showed significant elevation of Ca, up to 8 times higher counts/mA in the sediments up to 10 cm below the concrete regions (14.9-23.2 counts/mA) compared to the average counts in the sediment-only lysimeter (3.1 counts/mA). This elevated Ca level was expected from the concrete pore waters and is consistent with pH data which suggest cement pore waters became saturated with $Ca(OH)_2$ (typically associated with a pH of 12.5 (Tits and Wieland, 2018)) and subsequent leaching of Ca^{2+} ions when the lysimeter was subjected to rainwater flow.

These data, coupled with the *aqua regia* digestion data suggest U transport through the near subsurface is greatest in the sediment-only system and is significantly limited when a concrete

'cap' is present, or where concrete is exposed to rainwater, creating a high pH leachate plume which interacts with surrounding contaminated sediments. The lack of U present above the ICP-MS limit of detection in aqua regia digests of the concrete source lysimeter beyond 2-3 cm below the source, and 1 cm in Itrax measurements, is evidence of strong retention of U on concrete, greatly reducing the migration of U through subsurface sediments. Interestingly, upwards migration of U from the sediment source region to the concrete above in the concrete cap lysimeter was observed in the experimental set up.

U solid phase speciation. Sequential extractions were performed on 6 regions (source region, and 1 cm, 5 cm, 14 cm, and 29 cm below the source region and a sample from the base of the lysimeter) of the sediment-only lysimeter and compared to the U-sediment starting material to gain insight into the operationally defined U speciation after 399 days of environmental exposure (Figure S5.21). In the uranyl nitrate-doped starting material, uranium was predominantly present in the exchangeable, $MgCl_2$ leachate (60% ± 9%), with 38% (± 3%) in the carbonate, 1 M sodium acetate, pH 5 leachate. These data suggest that prior to environmental exposure, the emplaced uranyl nitrate was largely present in the exchangeable and weak acid leachate fractions and that U was weakly bound to the sediments. In contrast, after weathering the largest proportion of U in all the altered regions (between 94 and 54 %) was leached in the carbonate (1 M sodium acetate, pH 5) phase with less than 10% of U leached in the exchangeable $MgCl_2$ leachate in all samples. This suggests a significant change in U speciation compared to the unaltered source material, with U becoming more strongly associated with the sediment on exposure. With increasing depth in the lysimeter, sequential extraction data showed a trend towards an increase in U associated with the more strongly bound reducible, oxidisable and residual fractions (Figure S5.21). This suggests that with depth from the uranyl nitrate source, mobile uranyl is becoming more strongly associated with the sediments, potentially by association with iron (oxyhydr)oxides.

ESEM backscattered electron images of samples from the sediment-only lysimeter source horizon showed there was a high Z contrast precipitated phase on the sediment grains (Figure S5.22). EDS maps of these high Z areas showed co-location of U and Fe in the sediment, consistent with U becoming associated with iron (oxyhydr)oxide phases in the sediment. In the concrete cap lysimeter, ESEM backscattered imaging of a sediment samples from the source region again showed high Z areas which EDS mapping confirmed were U rich precipitates (Figure S5.23). In this lysimeter, U rich precipitates were also identified in concrete samples from 1 cm above the source region (Figure S5.24). Backscattered electron images and EDS maps from a concrete chip sample from the concrete source lysimeter after 399 days clearly showed significant amounts of uranium precipitates at the concrete chip surface (Figure S5.25). EDS analysis confirmed that U and Ca

165

were collocated in this precipitate and this is consistent with the bright yellow U precipitate coated concrete chips seen in the sectioned lysimeter (Figure S5.4-C).

Geochemical Modelling.

PHREEQC modelling of the sediment-only lysimeter using a model Sellafield groundwater (Table S5.9) and U concentrations in the original U-sediment source material predict that, under circumneutral pH conditions, U was present in solution largely as cationic uranyl-carbonate and - hydroxide species (Table S5.10). PHREEQC also predicted oversaturation of several U phases including schoepite, metaschoepite and other solid uranyl phases (Table S5.11), which is consistent with the scanning electron microscopy, where backscattered electron images of samples from the sediment-only lysimeter source horizon showed clear evidence for U rich precipitates (Figure S5.22). These data, coupled with the high mobility of U in this system, show that U was oversaturated in the source horizon and suggest that transport of U was controlled by dissolution and re-precipitation of solubility limiting mobile U phases. At depth in the core, there was some evidence for more inner sphere sorption to iron rich sediment components (Figure S5.21). Similar behaviour was observed in oxic laboratory experiments with metaschoepite sources where mobile U became associated with Fe (oxyhydr)oxides in sediment columns (Bower et al., 2019). PHREEQC modelling of the concrete cap system source region at the final measured pH (10.7) suggested U solution phases included only anionic and neutral uranyl hydroxide and carbonate species, however saturation index calculations predicted oversaturation of several uranate phases including $CaU_2O_7.3H_2O$, $CaUO_4$ and clarkeite (Table S5.13) consistent with the high pH Ca-containing leachate impacting U solid speciation and favouring uranate precipitation and consistent with the literature (Allen et al., 1996; Mühr-Ebert et al., 2019; Uyuşur et al., 2015). In addition, the concrete layer above the contaminated sediment is likely to act as a carbonate sink in this lysimeter (Xi et al., 2016), potentially limiting the ingress of carbon dioxide into the U-contaminated zone and thus formation of typically mobile uranyl carbonate phases. This, in addition to the predicted precipitation of sparingly soluble U phases such as Ca-uranate (Wang et al., 2017), could explain the lower mobility of U in this concrete containing system compared to the sediment only experiment. For the concrete source lysimeter, PHREEQC modelling using the same Sellafield groundwater solution as above with altered Ca^{2+} ion concentration (taken from aqua regia ICP data) at pH 12.5, predicted the solution phase was dominated by anionic uranyl (oxyhydr)oxide species (Table S5.14) and also predicted the oversaturation of several U phases, including Ca-uranates (Table S5.15). Clearly, thermodynamic modelling suggests there is a complex potential mix of U species both in solution and in the solid phase in all the lysimeter systems. Uranyl phases are predicted to be oversaturated in the sediment-only system, uranate

phases typically forming in the concrete source system and a mixture of both uranyl and uranate species predicted in the concrete cap lysimeter.

U-solid phase speciation - Bulk X-Ray Absorption Spectroscopy.

Select samples of the unaltered U-sediment and U-concrete source materials and from within and around the source horizons in each lysimeter were analysed using bulk U L_3-edge XANES and EXAFS and in a restricted range of samples, U M_4-edge XANES after 399 days of environmental exposure. In all systems, the source horizon was sampled at the point where the U concentration was the highest (determined by *aqua regia* digests, Figure 5.1) with samples also taken from several additional interesting areas. These include: 5 cm below the source in the sediment-only lysimeter where the U concentration measured by aqua regia digests was 26 ppm and targeting analysis of sediment associated transported U in the sample (U L_3-edge XAS); 1 cm above the source in the concrete-cap lysimeter where the aqua regia extractable U concentration was 1162 ppm and targeting either source mixing and or upwards diffusion (U L_3-edge XAS) and 1 cm below the source in the concrete source lysimeter where the U concentration was 318 ppm and representing either source mixing or U transport (U L_3-edge XAS and M_4-edge XANES).
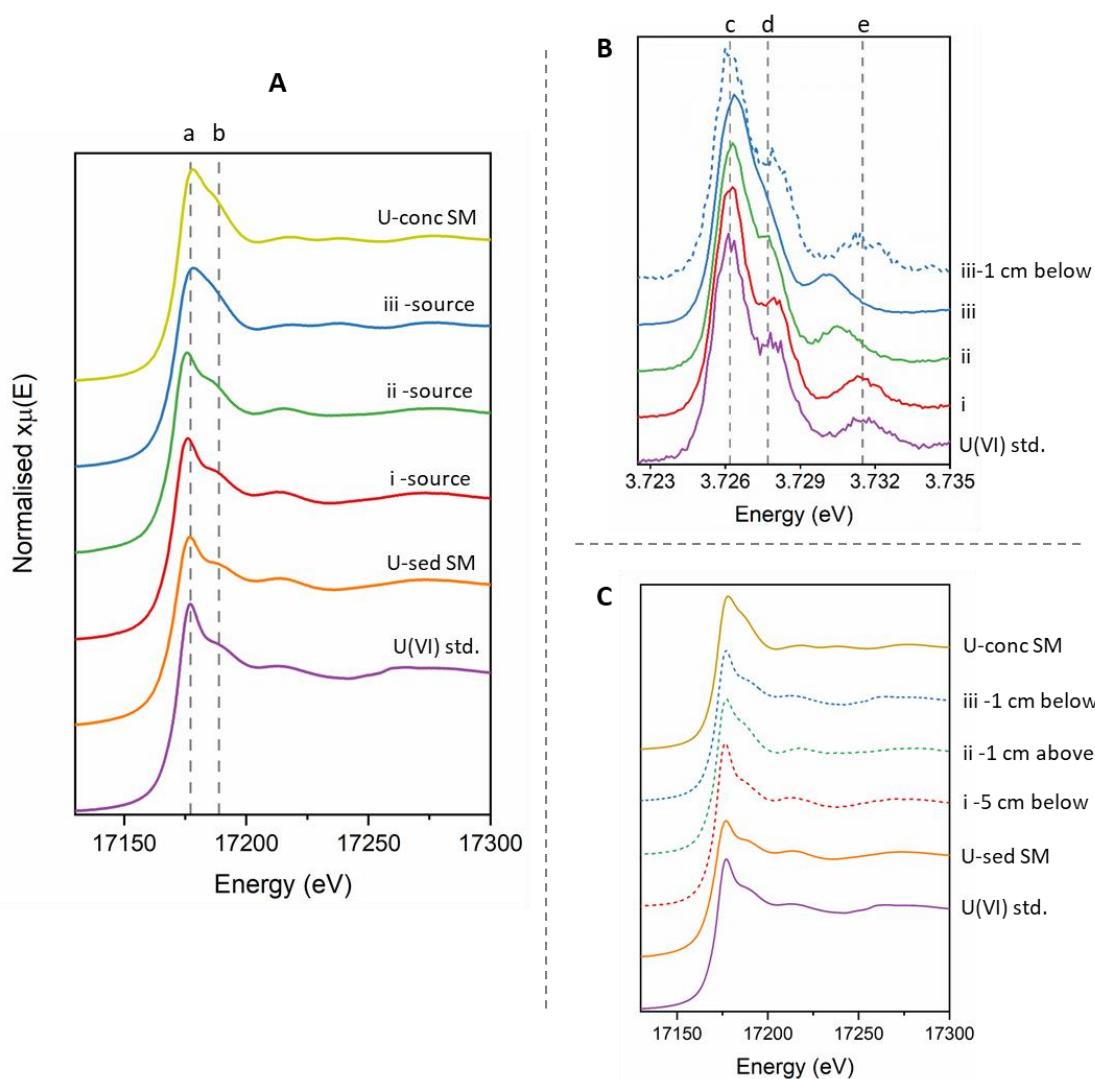
Figure 5.2: (A) U L$_3$-edge XANES spectra of samples from each lysimeter source horizon and U-sediment and U-concrete source starting materials. i – Sediment-only lysimeter, ii – Concrete cap lysimeter, iii – Concrete source lysimeter; (B) M$_4$-edge HERFD-XANES spectra of samples taken from each lysimeter source horizon and a second sample from the sediment 1 cm below the concrete source (blue dotted line). (C) L$_3$-edge XANES spectra of additional samples from i – Sediment-only lysimeter, ii – Concrete cap lysimeter, iii – Concrete source lysimeter. U(VI) white line positions (features a and c) and uranyl resonance features (features b, d and e) are also highlighted in the figure.

The U L$_3$-edge XANES spectra of altered samples from the source regions of the lysimeters and the selected additional samples are plotted in Figure 5.2. Also plotted are the unaltered U-sediment and U-concrete starting materials (Figure 5.2A and C). All samples were compared to standards and determined to be U(VI), with no evidence for reduction of U in any of the samples (U(VI) schoepite standard included in Figure 5.2A (dashed line, a)). The lysimeter samples from the U-sediment starting material and the altered samples in the U-sediment source region and 5 cm below, all exhibited a sharp white line at ~17177 eV with the shoulder feature (dashed line b, Figure 5.2A) typical of uranyl speciation also present (Catalano and Brown, 2004). By contrast, the

unaltered U-concrete starting material and lysimeter-altered concrete source horizon sample showed a broader white line at 17178 eV with an absence of any post edge shoulder confirming these high pH solid samples were uranate-like (Catalano and Brown, 2004). For the concrete cap sample where uranyl nitrate was mixed with sediment, capped with concrete and reacted in the lysimeter, the XANES were intermediate between the U(VI) uranyl in sediments and U(VI) uranate in concrete samples (Figure 5.2A). Linear combination fitting of the XANES data (Table S5.16) was applied to the altered concrete cap lysimeter source horizon sediment using the uranyl nitrate doped starting sediment and altered U-concrete source horizon samples as end members to explore the relative contributions of uranyl and uranate in the sample. This LCF analysis suggested a mix of uranate and uranyl speciation in this sample (with approximately 60% uranyl, 40% uranate; Table S5.16). This confirmed that the high pH leachate passing through the sediment from the concrete resulted in significant alteration of the U speciation from the uranyl nitrate / sediment mixture to a more complex uranyl/uranate speciation during exposure in the lysimeter.

Additionally, samples from the altered lysimeter source horizons (sediment only, concrete-cap and concrete source) and a sample from 1 cm below the source in the concrete source lysimeter were analysed using M_4-edge HERFD XANES (Figure 5.2B). Similar to the U L_3-edge XANES data, all the samples here had a similar white line position to that of the U(VI) uranyl standard, with a slight shift to higher energy seen for the sample from the source zone of the concrete source lysimeter. Here, the sediment-only lysimeter altered source sample was a good match to the U(VI) uranyl standard, with the post-edge shoulder feature (dashed line d, Figure 5.2B) clearly evident. Similar to the L_3-edge XANES spectrum, the concrete-source lysimeter altered source horizon sample displayed a broader white line with the absence of a shoulder feature, indicating uranate-like coordination, similar to published work where a CaU_2O_7 uranate sample was analysed using M_4-edge HERFD XANES (Podkovyrina et al., 2016). Podkovyrina et al. also observed the slight shift of the main peak to higher energy in uranate samples relative to uranyl samples, consistent with our data, due to reduced screening of the core-hole as a result of elongation of the U-O_{axial} bond, thus less electronic density around U. Indeed, the resonance feature identified by the dashed lines (e) in Figure 5.2B moved to lower energy from the uranyl dominated sediment-only lysimeter source to the uranate dominated concrete source lysimeter source samples. Interestingly, the same resonance feature from the source region of the concrete cap lysimeter is positioned in between the two end members again suggesting a mix of uranate and uranyl phases are present in the solids. Iterative transformation factor analysis (ITFA) (Rossberg et al., 2003) using the sediment only and U-concrete source regions as end members for uranyl and uranate species respectively was performed on the concrete cap lysimeter source region sample. Results suggested a mix of approximately 60% uranate and 40% uranyl (Table S5.16) broadly consistent with the L_3-edge XANES. In the concrete source lysimeter, a sample from 1 cm below

the concrete source was also analysed using L_3- and M_4-edge XANES and here there was a distinct shift in the XANES in both spectra towards a more uranyl like spectrum, with an increase in the prominence of post-edge shoulder features in both the L_3- and M_4-edge XANES spectra (Figure 5.2B and C; feature d). This suggests that a small fraction of uranyl like uranium was mobile over sub-cm distances in this system.
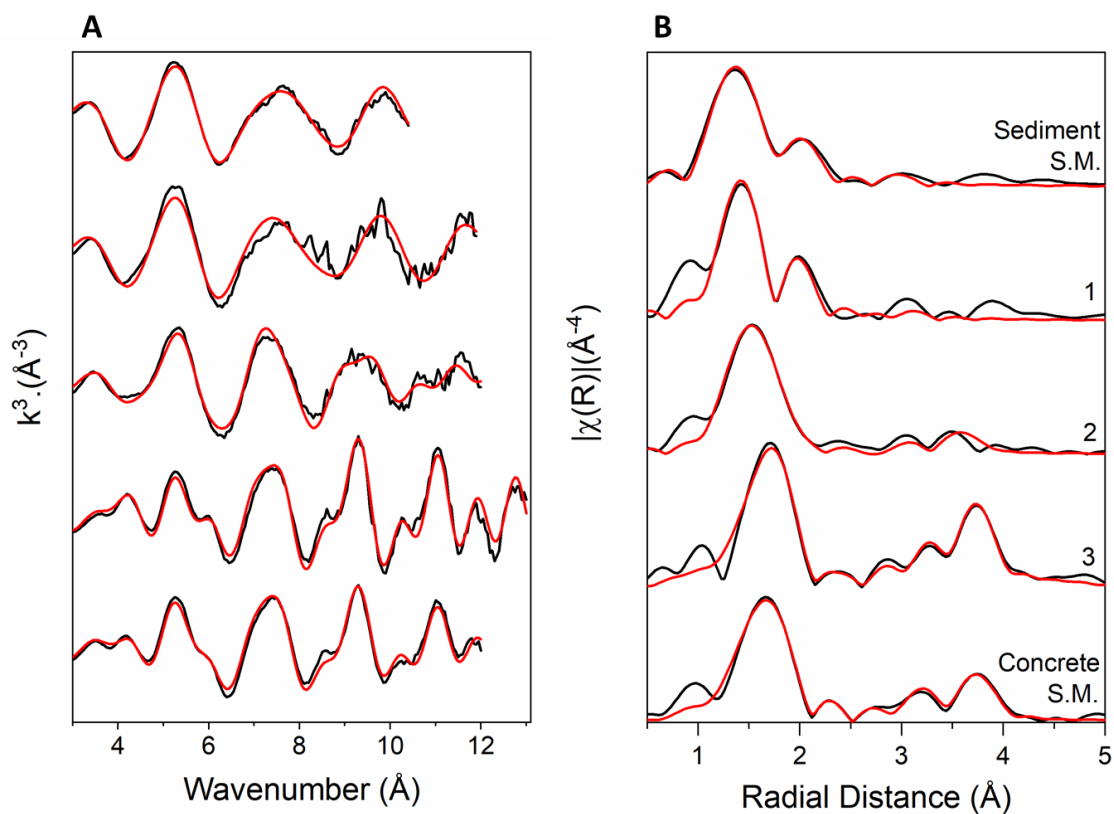
Figure 5.3: (A) U L_3 edge k^3-weighted EXAFS spectra; (B) Fourier transform of k^3 weighted EXAFS. Black lines are data, red lines are best fit models for the data. (a) Sediment-only lysimeter source; (b) Concrete cap lysimeter source; (c) Concrete source lysimeter source

Table 5.1: EXAFS fitting parameters for sample of the U-bearing starting materials and source regions from each of the lysimeters. 2 U-O axial forward through absorber multiple scatterers were also included in the fits for the sediment-only- and concrete cap lysimeter source region samples (Catalano and Brown, 2004).

Sample	Pathway	N	$(R + \Delta R)$ Å	σ^2 (Å)	ΔE_0	R-factor	k range	α
U-Sediment Starting Material	U-O$_{ax}$	2	1.79 ± 0.01	0.004 ± 0.001	6.181	0.009	3-10.4	
	U-O$_{eq}$	4	2.40 ± 0.02	0.007 ± 0.003				97.9
	U-O$_{eq}$	2	2.20 ± 0.02	0.007 ± 0.003				
U-Concrete Starting Material	U-O$_{ax}$	2	1.87 ± 0.004	0.005 ± 0.001	4.023	0.006	3-12.0	
	U-O$_{eq}$	4.5	2.24 ± 0.01	0.006 ± 0.0005				
	U-O$_{eq}$	1	2.47 ± 0.02	0.006 ± 0.003				
	U-Ca	2	3.69 ± 0.02	0.010 ± 0.002				100
	U-U	3	3.84 ± 0.01	0.006 ± 0.001				100
Sediment-only lysimeter source region	U-O$_{ax}$	2	1.81 ± 0.01	0.003 ± 0.001	6.144	0.018	3-11.9	
	U-O$_{eq}$	1.5	2.17 ± 0.02	0.004 ± 0.005				
	U-O$_{eq}$	4	2.38 ± 0.03	0.007 ± 0.003				
	MS - O$_{ax}$	2	3.61	0.007				
Concrete cap lysimeter source region	U-O$_{ax}$	2	1.83 ± 0.01	0.004 ± 0.001	3.938	0.012	3-12.0	
	U-O$_{eq}$	3.5	2.24 ± 0.03	0.006 ± 0.002				
	U-O$_{eq}$	1.5	2.37 ± 0.05	0.007 ± 0.008				
	U-U	1.5	3.71 ± 0.04	0.005 ± 0.003				
	MS - O$_{ax}$	2	3.67	0.008				
Concrete source lysimeter source region	U-O$_{ax}$	2	1.88 ± 0.005	0.004 ± 0.001	3.929	0.012	3-13.0	
	U-O$_{eq}$	4.5	2.23 ± 0.01	0.005 ± 0.0005				
	U-O$_{eq}$	1	2.52 ± 0.03	0.006 ± 0.003				
	U-Ca	3	3.70 ± 0.02	0.011 ± 0.002				100
	U-U	3	3.84 ± 0.01	0.004 ± 0.001				100

N denotes the coordination number; R is the interatomic distance between uranium and the scatterer; σ^2 denotes the Debye-Waller disorder factor; E_0 describes the energy shift from the calculated Fermi level; S_0^2, which is not shown here was fixed to 1 for all samples and is the amplitude factor; the R-factor describes the 'goodness of fit' and α is the statistical significance from F-test results (Downward et al., 2007).

The U k^3-weighted L$_3$-edge EXAFS and corresponding Fourier Transform for samples of the U-sediment and U-concrete starting materials and samples from the source horizons of each lysimeter can been seen in Figure 5.3A and B, and details of fits can be found in Table 5.1.

The EXAFS best fit for the unaltered U-sediment starting material included 2 O backscatterers at 1.79(1) Å, 2 equatorial O at 2.20(2) Å and 4 O backscatterers at 2.40(2) Å consistent with the expected uranyl speciation from the XANES data and PHREEQC modelling results which predicted a range of uranyl species to be present including the uranyl (oxyhydr)oxides schoepite, metaschoepite and becquerelite (Table S5.8) (Allen et al., 1996; Catalano and Brown, 2004). The best fit contained split equatorial oxygen shell at 2.20(2) and 2.40(2) Å which may suggest some evidence for U(VI) adsorption to sediment components (Bower et al., 2019).

For the unaltered U-concrete starting material which was prepared by exposing the concrete to a uranyl nitrate solution at pH 3, the best fit included 2 axial O backscatterers at 1.87(0) Å, 4.5 equatorial O at 2.24(1) Å, a further O backscatterer at 2.47(2) Å, 2 Ca backscatterers at 3.69(2) Å

and 3 U backscatterers at 3.84(1) Å. This was consistent with published fits for Ca-uranate-like species (Bots et al., 2014; Macé et al., 2013). The U-O$_{ax}$ shell fit here had a bond length of 1.87(0) Å which is similar to published U-O$_{ax}$ bond lengths seen in metal uranate phases (Allen et al., 1996; Bots et al., 2014; Catalano and Brown, 2004; Macé et al., 2013).

For the altered sediment-only lysimeter source region, the best fit included two U-O axial scatterers at 1.81(1) Å, 1.5 O backscatterers at 2.17(2) Å and 4 O backscatterers at 2.38(3) Å (Table 5.1). The U-O axial bond length is similar to the U-sediment starting material (1.79 Å), consistent with the formation of a uranyl species (Catalano and Brown, 2004). The split U-O equatorial shell indicated some disorder within the structure and suggested some surface bound U(VI) consistent with the sequential extraction data (Figure S5.20). The feature at ~3 Å in the Fourier Transform could be fitted with the addition of a shell of 0.5 Fe backscatterers, typical of U sorption to iron phases present in the sediment (Bower et al., 2019) but this was not significant using the F-test methodology. PHREEQC modelling and ESEM images of this altered sample, both suggest oversaturation of U and discrete precipitation of uranyl-bearing phases including becquerelite, schoepite and/or metaschoepite, however U-U backscatterers were not able to be fitted here with any certainty. Determining the exact uranyl species present proved difficult given EXAFS is an averaged technique and the sample likely contained a mix of precipitated and adsorbed phases leading to complexity. A further breakdown of the different fits we applied to the data can be seen in the SI (Section S5.3.4.2) and these demonstrate the complexity of fitting for this environmental sample.

The best fit for the concrete source lysimeter source region included 2 axial O backscatterers at 1.88(0) Å, 4.5 equatorial O at 2.23(1) Å, 1 O backscatterer at 2.53(3) Å, 3 Ca backscatterers at 3.69(2) Å and 3 U backscatterers at 3.84(1) Å (Table 5.1). Here, consistent with the unaltered starting material, we fit split U-O equatorial shells, which have been attributed to the formation of hydrated clarkeite phases, distorting the hexagonal structure and are consistent with literature fits for clarkeite, (Bots et al., 2014; Catalano and Brown, 2004). Clearly, this fit is similar to the unaltered concrete starting material suggesting that Ca uranate precipitate dominates after alteration. Interestingly, the sample showed an increase in the amplitude of the U-Ca feature (approximately 3.2 Å) and U-U feature (approximately 3.8 Å) in the Fourier Transform (Figure 5.3) compared to the unaltered starting material, suggesting that the precipitate was becoming more crystalline after weathering. This observation was also supported by the decrease in the Debye-Waller parameters, consistent with a decrease in disorder, hence more crystallinity in the concrete source region fit after exposure in the environment (Table 5.1).

Finally, the best fit for the concrete cap lysimeter source region included 2 axial O backscatterers at 1.83(1) Å, 3.5 equatorial O backscatterers at 2.24(3) Å, 1.5 O backscatterers at 2.37(5) Å, and

1.5 U backscatterers at 3.71(4) Å. Here, the EXAFS fits suggest a mix of uranate and uranyl phases were present, consistent with the XANES analyses. In the EXAFS model, the U-O axial bond length (1.83(1) Å) is midway between the equivalent shells in the sediment starting material (1.79(1) Å) and the concrete starting material (1.87(0) Å), consistent with an approximately 50 : 50 contribution from uranyl and uranate species. The U-O equatorial occupancies are also suggestive of a mix of uranyl and uranate species, with a greater occupancy of the 1st U-O equatorial shell at approximately 2.24 Å seen in this sample compared to the sediment-only lysimeter source region. Indeed, qualitatively, the position of the U-O shells in the Fourier Transform is equidistant between that of the source material in the sediment only and concrete source lysimeters (Figure 5.3B). Interestingly, the U-U bond length here is a good match to the pH 9 sample analysed by Allen et al (1996). Here Allen et al. precipitated a series of U(VI) oxides in aqueous solution as a function of pH; one at pH 7, one at pH 9 and a final sample at pH 11. For the pH 9 sample, they also fit a U-U at 3.71 Å and described it as an intermediary between samples prepared in the same way at pH 7 (described as schoepite-like) and pH 11 (described as a uranate). Here, further fitting of additional shells in the 2.5-3.7 Å region of the Fourier transform was not justified due to the complex nature of the sample.

The EXAFS results presented here suggest that the mobility of U in these subsurface systems is controlled by the speciation of U solid phases formed under different pH conditions. In the sediment-only lysimeter, formation of mobile uranyl phases at circumneutral pH contributed to the increased transport of U through the lysimeter. In contrast, precipitation of a Ca-uranate phase that apparently increased in crystallinity over 399 days, limited the transport of U in the concrete source lysimeter. Here, the system was modelled to be oversaturated with respect to calcium uranate phases, consistent with the EXAFS fits presented here. Interestingly, in the concrete cap lysimeter source, where the pH was measured to be ~10.7, intermediate phases formed, with a mixture of uranate and uranyl species present in the source horizon, consistent with PHREEQC modelling.

5.5 Implications

Under oxic, circumneutral subsurface conditions, where U was predicted to be oversaturated with respect to uranyl (oxyhydr)oxide phases, significant transport of U(VI) was observed over 1 year. Here, in the sediment-only lysimeter, both aqua regia digestions and ITRAX XRF scanning suggested significant transport of U in the system, with sequential extractions also suggesting some sorption to sediments was occurring over 399 days of field exposure. In this system, XAS confirmed the presence of uranyl species. In contrast, during environmental exposure of U-contaminated concrete, U transport was limited and U was strongly retarded on the concrete with EXAFS confirming precipitation of calcium uranate phases, which are typically highly insoluble. Here, evidence for the increased crystallinity of the Ca-uranate phase was observed over 12 months. Furthermore, the addition of a concrete cap to U-contaminated sediments revealed that U transport was significantly reduced compared with the sediment-only system as evidenced in both the ICP-MS and ITRAX XRF analyses. PHREEQC modelling predicted supersaturation of a mix of uranyl (oxyhydr)oxide and calcium uranate phases in this system, whilst EXAFS modelling also supported the formation of a mixture of uranyl and uranate phases, likely as a result of the high pH leachate from the concrete above inducing precipitation of uranate phases. These findings are significant and underpin the exploration of in-situ disposal for management of low-level contaminated concrete and contaminated land.

Supporting Information for Chapter 5

Environmental behaviour of uranium in concrete impacted contaminated land – a field based lysimeter study

[1] A. E. McNulty, [1] S. Shaw, [2] B. Powell, [1,3] G. T. W. Law, [1,3] W. R. Bower, [2] K. Peruski, [4] J. Rothe, [4] T. Vitova, [5] L. Abrahamsen-Mills and [1] K. Morris

[1]Research Centre for Radwaste Disposal and Williamson Research Centre, Department of Earth and Environmental Sciences, School of Natural Science, University of Manchester, UK

[2]Department of Environmental Engineering and Earth Sciences, Clemson University, USA

[3]Laboratory of Radiochemistry, Department of Chemistry, University of Helsinki, Finland

[4]Karlsrühe Institute of Technology (KIT), Institute for Nuclear Waste Disposal (INE), Germany

[5]National Nuclear Laboratory, UK

This document provides additional supplementary information including lysimeter experiment set-up, extended methodology and details of XAS set-up, data collection and processing. Additional supporting data are also included.

Contents

S5.1: Lysimeter Experimental Set-Up, Materials Characterisation and Probe Data

S5.2: Supplementary Data

S5.1: Lysimeter Experimental Set-Up, Materials Characterisation and Sensor/Probe Data

S5.1.1 Lysimeter Schematics and Layout
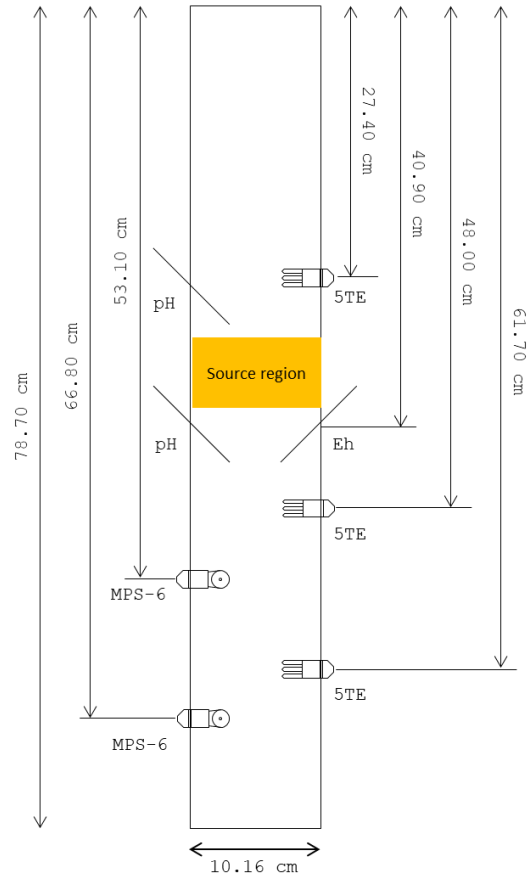
Figure S5.1: Lysimeter schematic showing probe positioning and relative source horizon depth within each of the lysimeters. MPS-6 and 5TE probe measurements were taken in situ, with measurements recorded approximately every 2 hours for the duration of the experiment, with the exception of a ~2 month period due to a power outage at the facility. pH and Eh probe measurements were taken at specific points during the experiment. MPS-6 water potential sensors measured water potential (kPa) and temperature (°C) and 5TE soil moisture sensors monitored dielectric permittivity, bulk electrical conductivity (dS m-1) and temperature (°C). Both sensors were ~3.7 cm in depth and 1 cm in width and measurements here are given from the surface to the centre of the sensor (depth-wise). All probes and sensors were inserted after lysimeter packing into pre-cut holes and were glued in place.
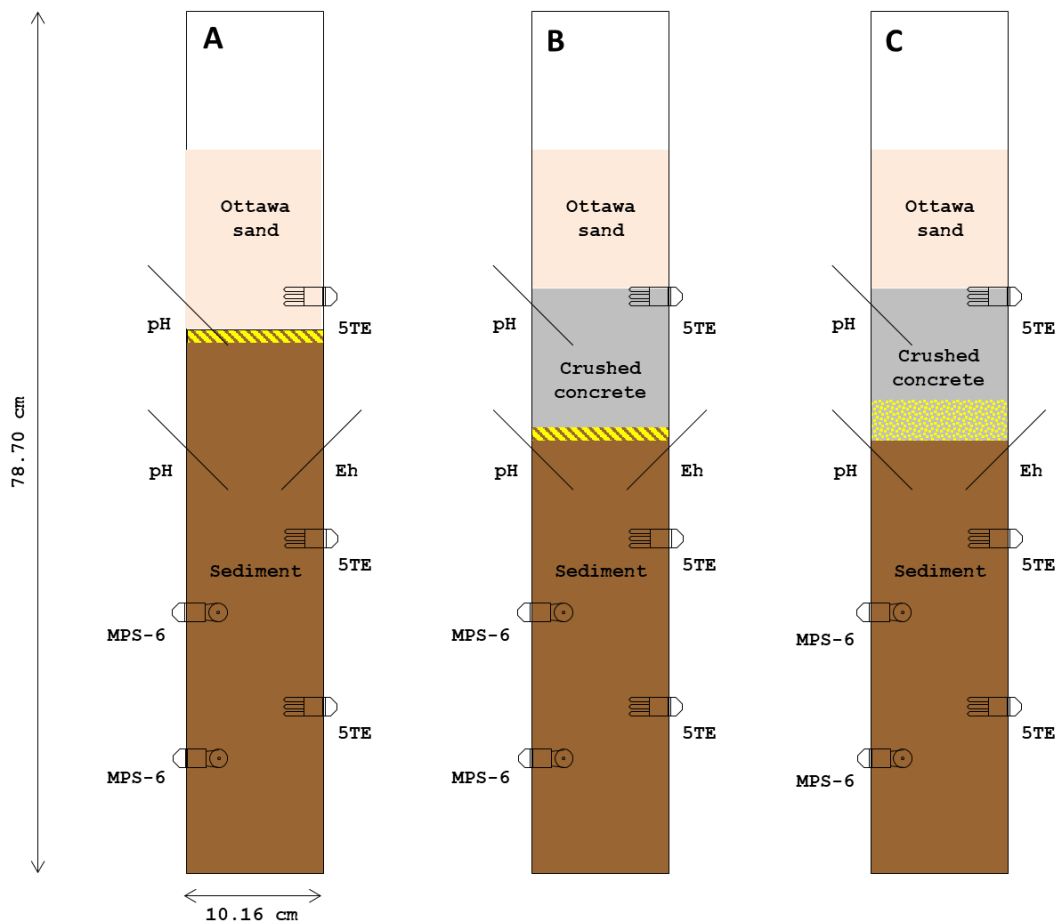
Figure S5.2: To-scale lysimeter schematics for each experiment with the positioning of sediment, concrete, source horizons and Ottawa sand shown. (A) Sediment source lysimeter with U-sediment source horizon depicted as yellow band with brown stripes. (B) Concrete cap lysimeter with U-sediment source below layer of crushed concrete (grey). (C) Concrete source lysimeter with concrete source horizon depicted here as grey background with yellow spots. Relative sensor positions also shown.

Figure S5.3: The three lysimeters pre-deployment with sensors glued in place.

To pack the sediment in each lysimeter, approximately 10 cm depth was added to the lysimeter pipe at a time and the lysimeters were tapped against the ground between additions to limit preferential flow pathways as a result of layered, compacted sediment.

Figure S5.4: Longitudinally sectioned lysimeters (A) Sediment-only lysimeter; (B) Concrete-cap lysimeter; (C) Concrete source lysimeter.

S5.1.2 Lysimeter Sampling

Figure S5.5: Photograph highlighting the placement of rectangular steel sampling housings that were placed into the source region of each lysimeter and removed intact for future spatial analyses on the materials.
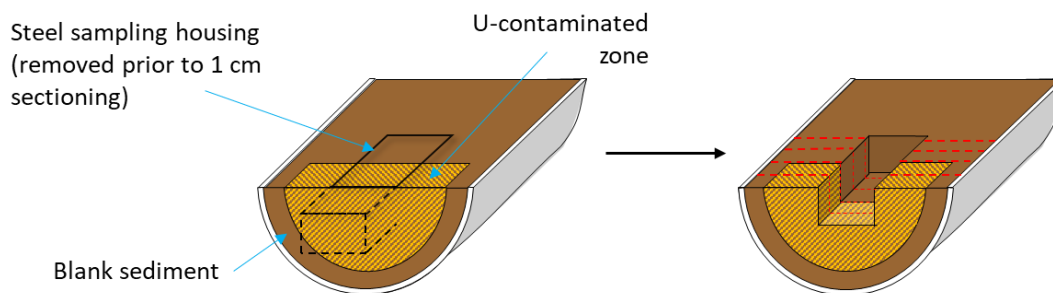
Figure S5.6: Diagram highlighting the removal of the steel sampling housing and remaining material available for sectioning (not to scale).

By removing the intact samples across each lysimeters' source region using the steel sampling housings, approximately 30% of the contaminated sediment was removed prior to sectioning into 1 cm vertical fractions. Once sectioned into 1 cm fractions, the sediment was placed into bags and homogenised by hand. As a result, the contaminated sediment was diluted by the blank sediment at the edges (approximate 50% dilution). Consequently, aqua regia digestions on the source materials reveal a lower concentration than the emplaced 6000 ppm due to this removal of contaminated sediment and later homogenisation with blank material. In the concrete source lysimeter, the same trend is seen but was attributed to an unequal levelling of the contaminated material in the lysimeter when emplaced (Figure S5.4-C shows this in the longitudinally sectioned view) and so mixing in each 2 cm horizon with uncontaminated concrete in the layers above resulted in some dilution of the overall concentration of U within each source horizon layer.

S5.1.3 Materials Characterisation

The sediment and concrete used here were sourced for these lysimeter experiments to be as representative as possible to the Sellafield site, UK. Sediment, was sourced from Peel Place Quarry (managed by Tendeley Quarries), Holmrook, UK which is based ~2 km from the Sellafield site. Concrete was sourced from a recently demolished building, originally built in the 1950s, at the Low Level Waste Repository site, Drigg, UK, from pre-fabricated concrete sections. Here, X-ray diffraction (XRD), X-ray fluorescence (XRF) and environmental scanning electron microscope (E-SEM) with energy dispersive X-ray spectroscopy (EDS) characterisation data for both the sediment and concrete are presented.

S5.1.3.1 Sediment Characterisation

Table S5.3: Major and trace elements/phases of the sediment measured by XRF.

XRF Majors			XRF Traces		
Element	Average wt%	RSD	Element	Concentration (ppm)	RSD
SiO_2	81.516	0.554	W	552.33	24.15
Al_2O_3	8.545	0.245	Mn	385.00	8.22
K_2O	3.229	0.087	Ba	315.90	14.03
Fe_2O_3	2.520	0.110	Zr	243.87	1.10
LOI @ 1000 °C	1.010	0.089	Cr	98.67	53.86
CaO	0.647	0.045	Sr	71.93	0.15
MgO	0.638	0.155	Rb	55.43	0.32
LOI @ 110 °C	0.560	0.044	Te	48.33	1.36
Na_2O	0.544	0.083	Co	35.83	3.33
TiO_2	0.345	0.012	As	27.97	1.25
P_2O_5	0.109	0.034	Ni	25.70	12.30
W	0.097	0.007	V	24.07	1.36
MnO	0.081	0.004	Ce	19.87	1.03
Zr	0.040	0.001	Zn	17.60	0.17
Ce	0.027	0.001	Y	10.47	0.21
SO_3	0.023	0.007	Nd	10.10	1.18
Cr	0.021	0.011	La	9.87	1.45
Sr	0.012	0.001	Hg	9.77	8.35
Cl	0.012	0.003	Hf	6.13	0.15
Rb	0.010	0.001	Cu	5.93	0.40
Co	0.009	0.001	Ga	5.27	0.06
Ni	0.008	0.002	U	4.83	0.38
Cu	0.004	0.001	Pb	4.47	0.31
Zn	0.004	0.001	Nb	4.20	0.10
			Sc	3.50	0.69
			Ge	2.77	0.23
			Cs	2.40	1.93
			Sm	2.30	1.57
			Th	2.27	0.12
			Sn	1.83	0.67
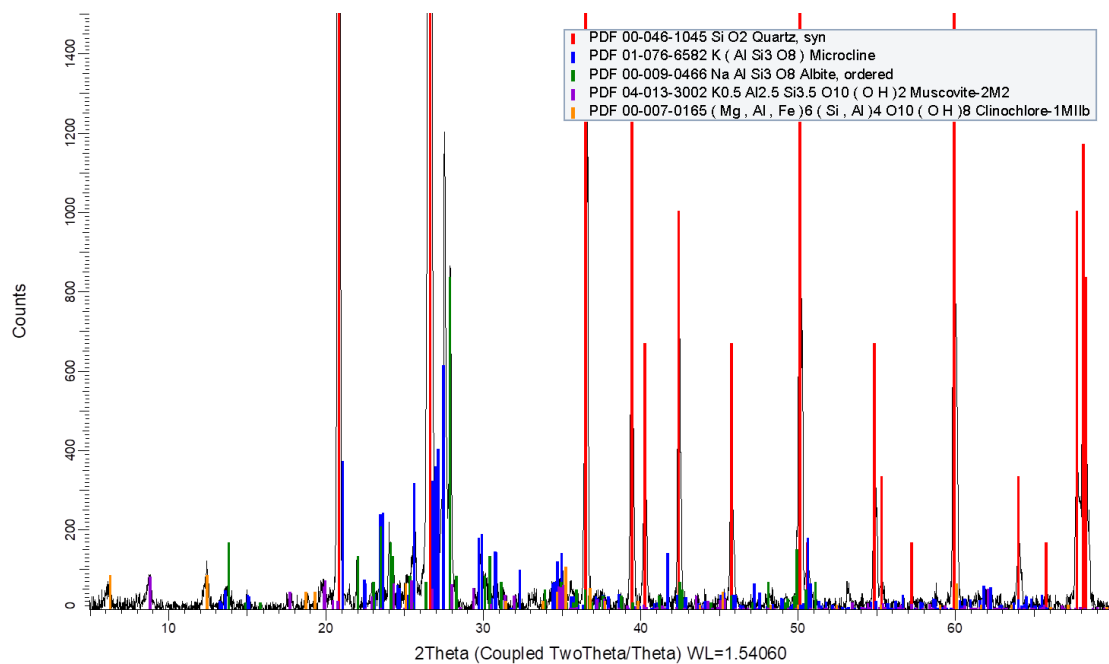
Figure S5.7: Y-axis scaled p-XRD pattern of the unaltered sediment used in each lysimeter.

The sediment was dominated by quartz (SiO_2), with the feldspars microcline ($K(AlSi_3O_8)$) and albite ($NaAlSi_3O_8$) also present. The mica muscovite ($K_{0.5}Al_{2.5}Si_{3.5}O_{10}(OH)_2$) and chlorite mineral chlinochlore (($(Mg,Al,Fe)_6(Si,Al)_4O_{10}(OH)_8$) were also present in smaller quantities.

Table S5.2: XRD quantification of phases present in the sediment.

Phase Name	Weight %	Error %
Quartz	78.629	0.991
Microcline	9.821	0.646
Clinochlore IIb-2	0.887	0.368
Muscovite 2M1	4.521	0.735
Albite	6.142	0.413

Table S5.3: Additional characterisation and properties of the unreacted Peel Place Quarry sediment, representative of the Sellafield site.

Parameter	Detail
pH	6.93
B-E-T Surface Area	2.14 ± 0.01 m^2/g
Organic matter content*	0.38 ± 0.05 wt. %

*Organic matter content was determined by loss on ignition at 550 °C.
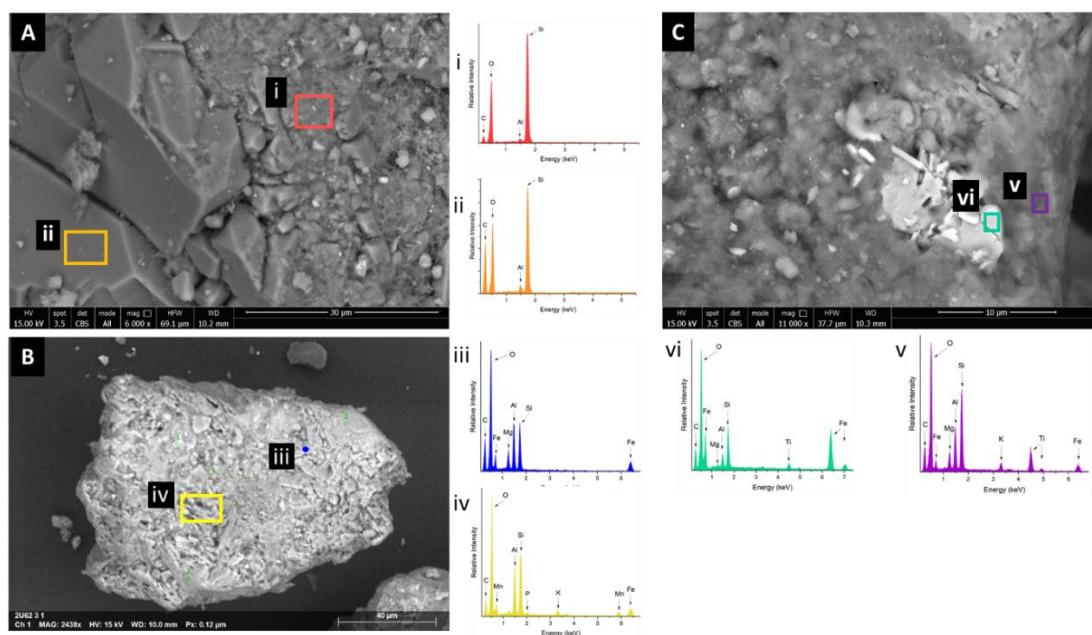
Figure S5.8: SEM images of sediment used in the lysimeter experiments. EDS spectra from each image are also presented (i-vi). The sediment is typically dominated by Si and O peaks, with Al, Mg also detected. Areas of Ti and Fe enrichment were also detected.

S5.1.3.2 Concrete Characterisation

Table S5.4: XRF major and trace elements/phases

XRF Majors			XRF Traces		
Element	Average wt%	RSD	Element	Concentration (ppm)	RSD
SiO_2	56.905	0.589	W	318.00	41.45
CaO	24.562	0.114	Mn	193.00	26.13
LOI @ 1000 °C	5.920	0.044	Sr	172.57	2.08
Al_2O_3	4.695	0.302	Ba	112.87	42.47
LOI @ 110 °C	2.657	0.070	Zr	104.10	4.39
Fe_2O_3	1.966	0.034	Te	48.77	2.87
K_2O	1.266	0.017	Rb	29.77	0.32
SO_3	1.016	0.202	Co	29.67	2.73
MgO	0.383	0.047	Hg	23.77	15.21
TiO_2	0.249	0.007	Zn	22.00	0.40
P_2O_5	0.085	0.015	Cr	21.17	9.28
W	0.077	0.002	V	16.17	3.46
MnO	0.054	0.003	As	15.40	2.17
Na_2O	0.049	0.007	Ni	10.60	2.33
Cl	0.036	0.009	Ce	9.33	7.01
Sr	0.035	0.001	La	8.67	5.87
Cr	0.008	0.002	Y	8.40	0.20
Co	0.008	0.001	U	6.13	1.10
Ni	0.006	0.001	Hf	4.00	0.35
Rb	0.006	0.001	Ga	3.70	0.20
Zn	0.005	0.001	Nd	3.50	2.14
Cu	0.004	0.001	Sn	3.43	1.17
			Nb	3.13	0.21
			Cu	2.83	2.68
			Pb	2.50	1.08
			Ge	2.43	0.38
			Th	2.33	0.93
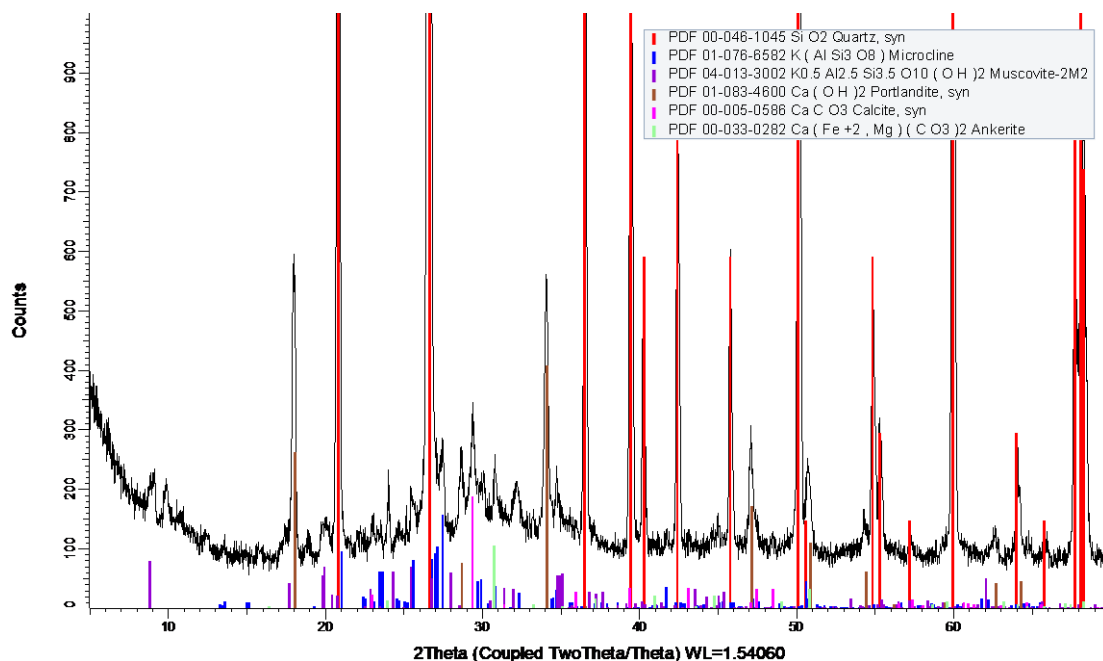
Figure S5.9: Y-axis scaled p-XRD pattern of the unaltered concrete used in the lysimeters.
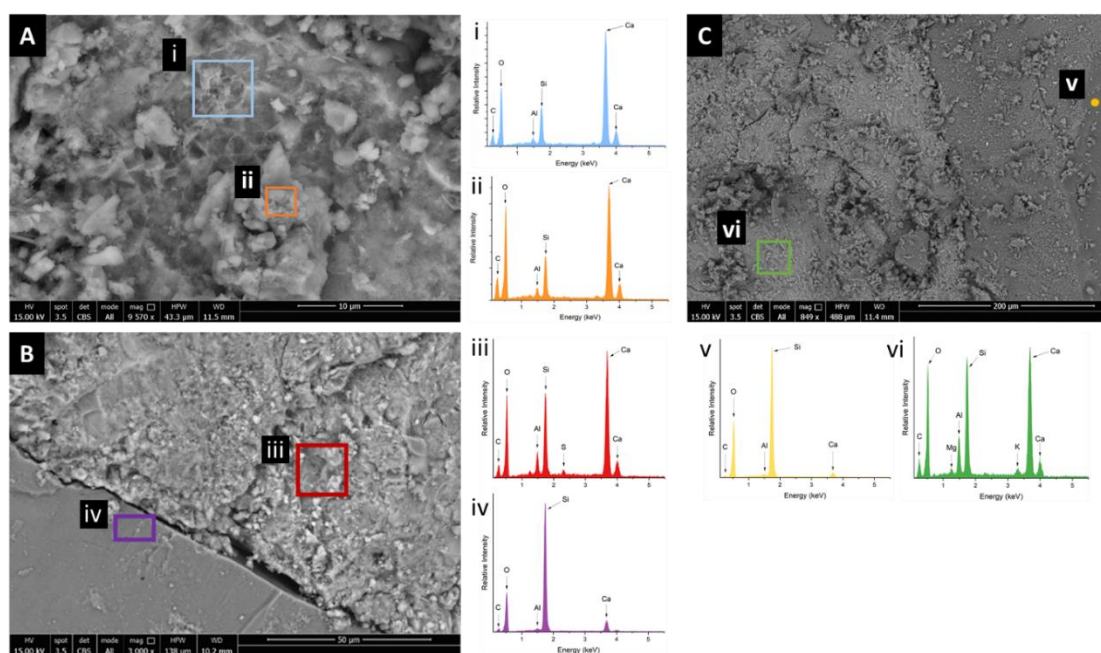
Figure S5.10: E-SEM images of concrete samples. (A) Highlights an area of amorphous material, typical of calcium silicate hydrates; (B) and (C) are both images of cement/aggregate boundaries. EDS spectra from each image are also presented (i-vi). Cement is typically dominated by Ca, Si and O peaks, with small amounts of Al and S also observed. Aggregate areas are comprised mostly of Si and O, with Al and Ca also detected in small quantities.

The concrete was dominated by quartz (SiO_2), with minor contributions from microcline, muscovite and ankerite also attributed to pebble aggregate present in the concrete. Portlandite ($Ca(OH)_2$) and calcite ($CaCO_3$) are also present and derived from the cement phase. Although calcium-silicate hydrate phases were not captured by p-XRD, SEM images of the concrete did

capture areas of amorphous material, where EDX captured Ca, Si and Al present. Additionally, the broad nature of some of the peaks captured in the XRD are indicative of amorphous material present in the sample.

S5.2: Supplementary Data

S5.2.1 Lysimeter Effluent Geochemistry

The effluent was monitored for volume, pH and Na, Mg, K, Ca, Fe and U concentrations at 4 time points during the experiment. The data for each lysimeter are presented below.

S5.2.1.1 Effluent volumes and pH

Table S5.5: Effluent volumes and pH for each lysimeter taken at 4 sampling points during the experiment Total effluent volume for each lysimeter is also given.

Sampling Day	Sediment-only lysimeter		Concrete cap lysimeter		Concrete source lysimeter	
	Effluent Volume / mL	Effluent pH	Effluent Volume / mL	Effluent pH	Effluent Volume / mL	Effluent pH
96	2021.7	6.73	2002.23	6.67	2054.10	6.95
201	1994.21	7.19	2015.46	6.99	1986.95	6.92
286	1925.97	6.81	1941.65	6.79	1779.12	6.75
370	1278.73	7.04	910.79	7.65	1225.46	7.65
TOTAL	7220.61		6870.13		7045.63	

NB: Final effluent collection was at 370 days, no data was collected at 399 days (conclusion of lysimeter experiment).

S5.2.1.2 Effluent cation composition
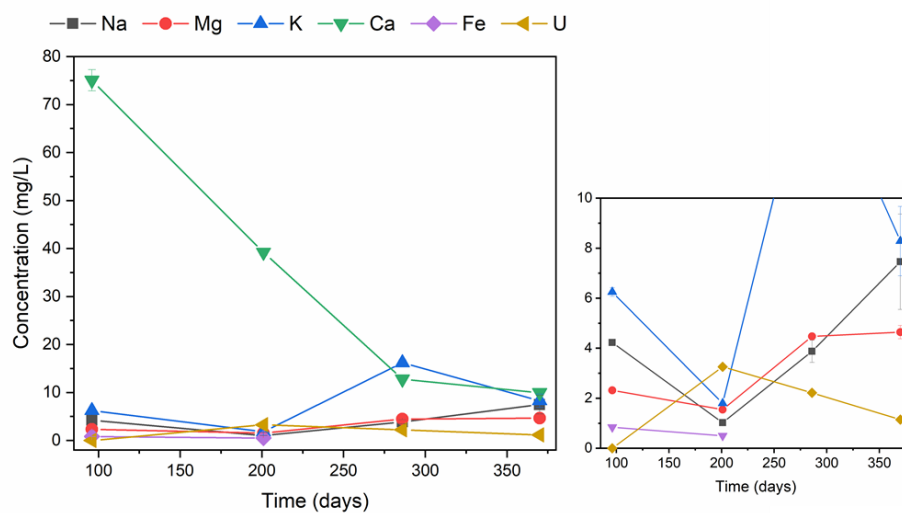
Figure S5.11: Na, Mg, K, Ca, Fe and U concentration in effluents collected from the sediment-only lysimeter.
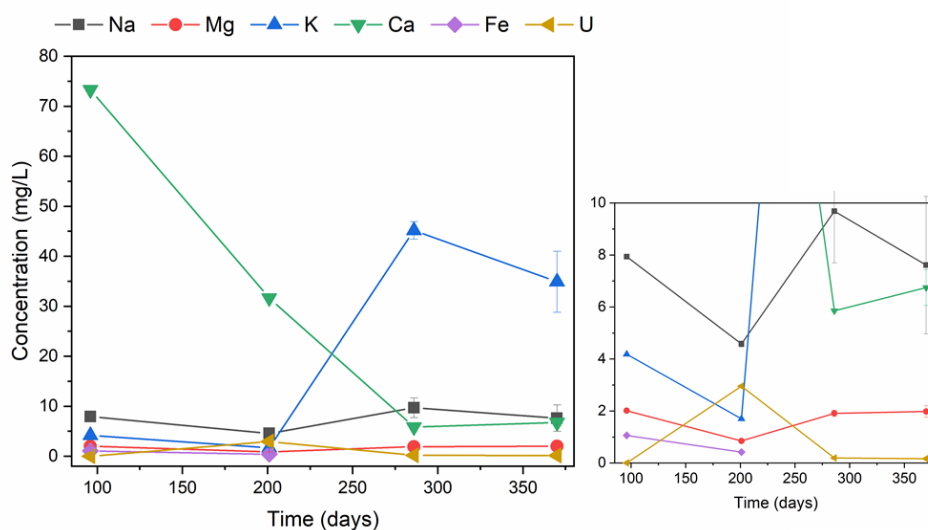
Figure S5.12: Na, Mg, K, Ca, Fe and U concentration in effluents collected from the concrete cap lysimeter.
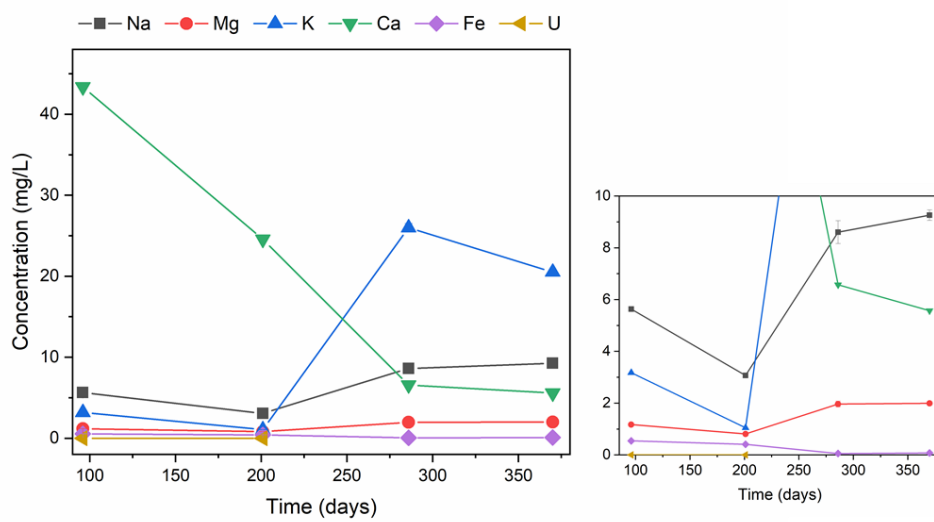
Figure S5.13: Na, Mg, K, Ca, Fe and U concentration in effluents collected from the concrete source lysimeter.

Table S5.6: Comparison of the total U eluted from each lysimeter with the originally emplaced total U (mg).

Lysimeter	Emplaced U (mg)	Eluted U (mg)	Eluted U (%)
Sediment-only	677	12.2	1.8
Concrete cap	668	6.5	1
Concrete source	2348	0.001	4.3E-05

S5.2.2 In-situ geochemical sensor data

In all lysimeters (Figure S5.1), the 5TE sensors inserted at 48.0 and 61.7 cm were placed in the sediment. In the sediment only lysimeter, the sensor at 27.4 cm is in Ottawa sand; in the concrete cap and concrete source lysimeters, the 5TE sensors at 27.4 cm were placed in the concrete layer. After multiple rainfall events, the sensors in all lysimeters recorded a significant increase in the water content. Values in the sediment in the lowest probe (61.7 cm) were highest across all lysimeters and this is seen consistently in previous lysimeter work (Fallon, 2019), where water is retained at the base.

The difference in VWC seen in the 5TE probes at 27.4 cm in B and C (Figure S5.14) can be attributed to the sensors perhaps not being in full contact with the concrete chips.
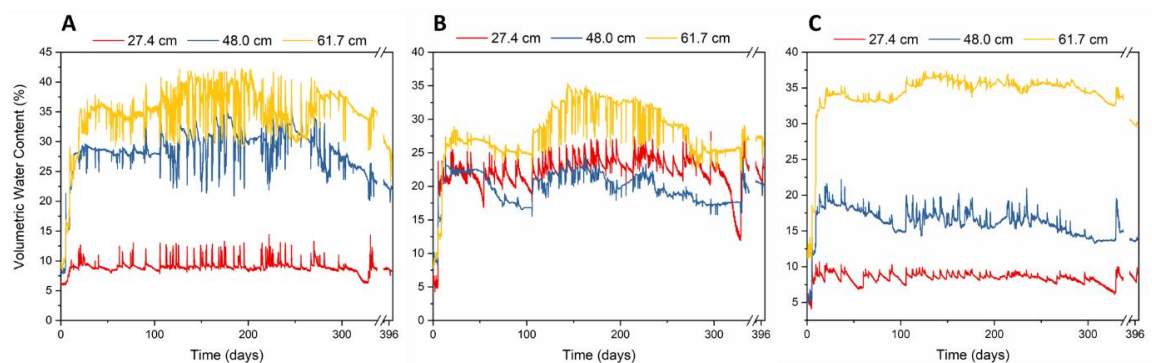
Figure S5.14: In situ 5TE sensor volumetric water content (%) for the duration of the experiment. (A) Sediment-only lysimeter; (B) Concrete cap lysimeter; (C) Concrete source lysimeter. Volumetric water content (%) was derived from sensor dielectric permittivity measurements (unitless) and calibrated using each of the media the sensors were placed in (either Ottawa sand, concrete or sediment). All R^2 values for the calibrations were >0.95.
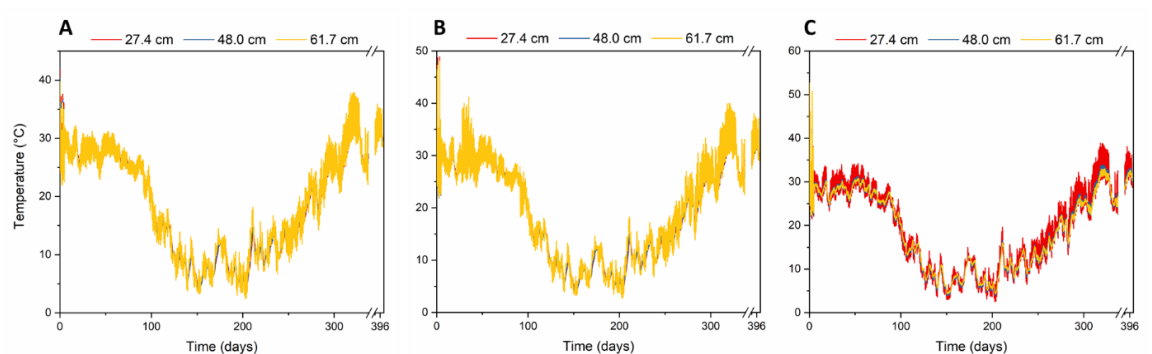
Figure S5.15: In situ 5TE sensor temperature data for the duration of the experiment. (A) Sediment-only lysimeter; (B) Concrete cap lysimeter; (C) Concrete source lysimeter.
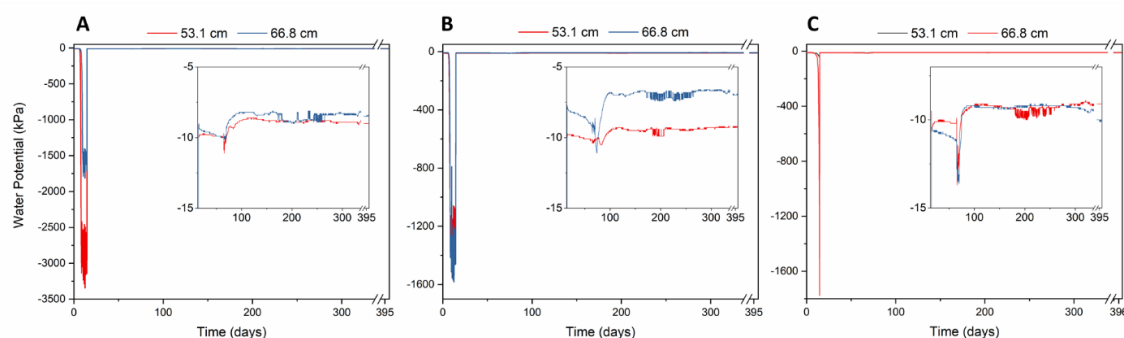
Figure S5.16: In situ MPS-6 sensor water potential data for the duration of the experiment. (A) Sediment-only lysimeter; (B) Concrete cap lysimeter; (C) Concrete source lysimeter.

S5.2.3 Eh/pH probe data

Table S5.7: pH and Eh probe data collected during the experiment from probes inserted at 40.9 cm depth in all lysimeters.

Date	Day of experiment	Sediment-only lysimeter		Concrete cap lysimeter		Concrete source lysimeter	
		pH	Eh (mV)	pH	Eh (mV)	pH	Eh (mV)
01/08/2018	20	6.79	408.7	8.78	288.0	11.61	369.8
06/08/2018	25	6.80	436.0	8.80	287.2	11.68	349.5
22/08/2018	41	6.83	473.0	8.89	284.0	11.98	338.8
12/03/2019	243	6.90	539.0	9.57	462.0	11.69	215.8
15/08/2019	399	6.94	363.7	9.86	300.3	9.42	376.3

Data from top pH probes inserted at 27.4 cm depth in each lysimeter were discounted in this study due to pH values greatly outside the expected range for the materials they were placed in. This was likely due to the materials used around that depth (Ottawa sand in the sediment-only lysimeter and crushed concrete in the concrete-cap and concrete source lysimeters) as the probes were likely not in full contact with these materials and so accurate measurements could not be taken.

S5.2.3 Solid Phase Geochemistry

S5.2.3.1 U Concentration Profile

Table S5.8: Interpolated U concentrations at select points below the source horizon in the sediment-only and concrete cap lysimeters.

Distance below source	U concentration / ppm	
	Sediment-only lysimeter	Concrete cap lysimeter
5 cm	27.1	4.21
10 cm	17.6	2.01
20 cm	11.5	1.11
30 cm	8.93	0.78

S5.2.3.1 pH
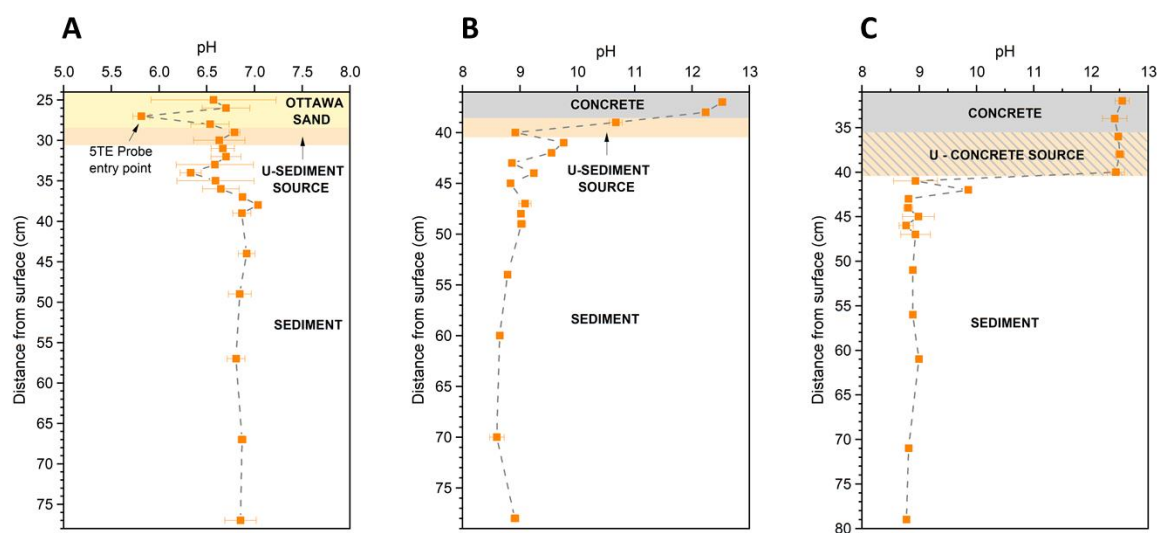
Figure S5.17: pH values for select horizons of each lysimeter experiment. (A) Sediment-only lysimeter; (B) Concrete cap lysimeter; (C) Concrete source lysimeter.

S5.2.3.2 ITRAX XRF

An ITRAX XRF core scanner was used to analyse ~30 cm length sections of each lysimeter core around the source horizons. XRF elemental data was collected for each core using a Mo tube source (30 kV, 40 mA) with a dwell time of 15 s at 200 μm resolution. The beam width was ~2 cm so XRF count data are averaged over both time and space for each 200 μm vertical step. In addition, high resolution optical line scan images and X-radiograph line scans at 200 μm resolution

were also collected. In some areas, where the core surfaces were not reasonably flat as a result of coarse grain size, measurements were not taken.
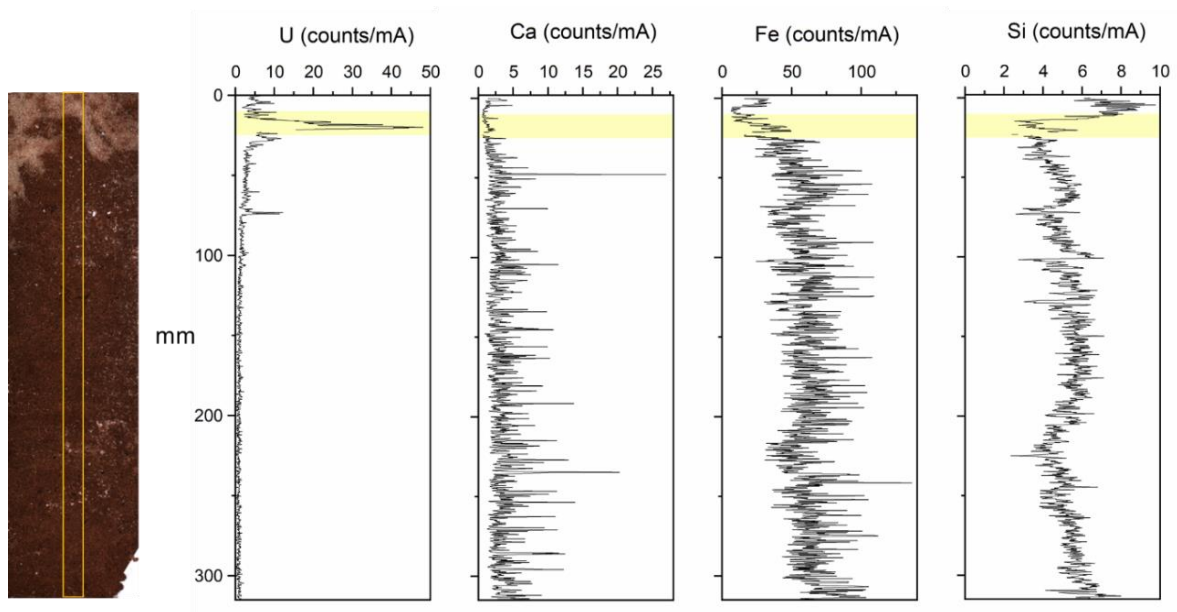
Figure S5.18: ITRAX XRF scan of sediment-only lysimeter with a high-resolution line scan image of the sectioned core and the XRF scan region highlighted. Elemental counts/mA (U, Ca, Fe and Si) plotted against the core position (total core section length = 315 mm), with the position of the emplaced source region highlighted in yellow.
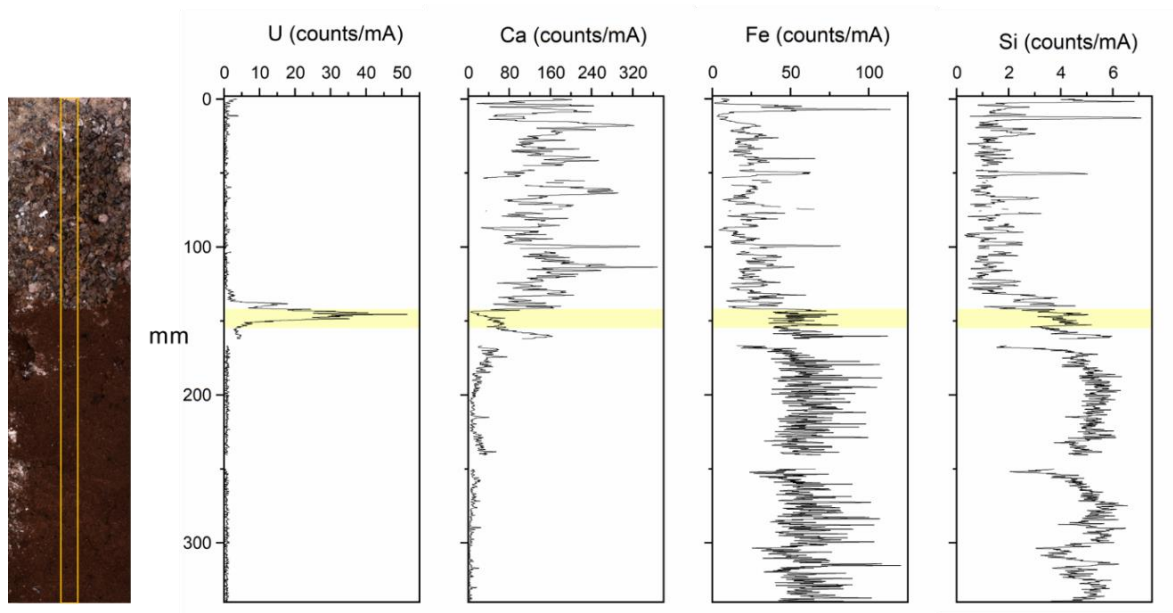
Figure S5.19: ITRAX XRF scan of the concrete cap lysimeter with a high-resolution line scan image of the sectioned core and the XRF scan region highlighted. Elemental counts/mA (U, Ca, Fe and Si) plotted against the core position (total core section length = 340 mm), with the position of the emplaced source region highlighted in yellow.
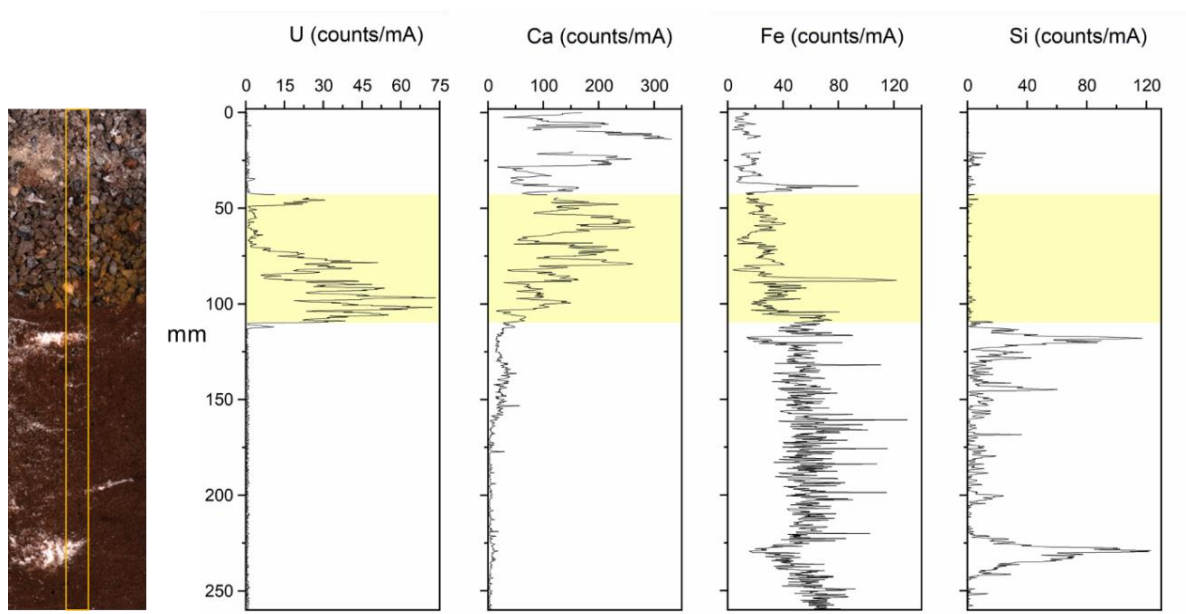
Figure S5.20: ITRAX XRF scan of the concrete source lysimeter with a high-resolution line scan image of the sectioned core and the XRF scan region highlighted. Elemental counts/mA (U, Ca, Fe and Si) plotted against the core position (total core section length = 260 mm), with the position of the emplaced source region highlighted in yellow.

S5.2.3.3 Sequential Extractions

Sequential extractions were performed on select samples from the sediment-only lysimeter and the U-sediment starting material as a standard.
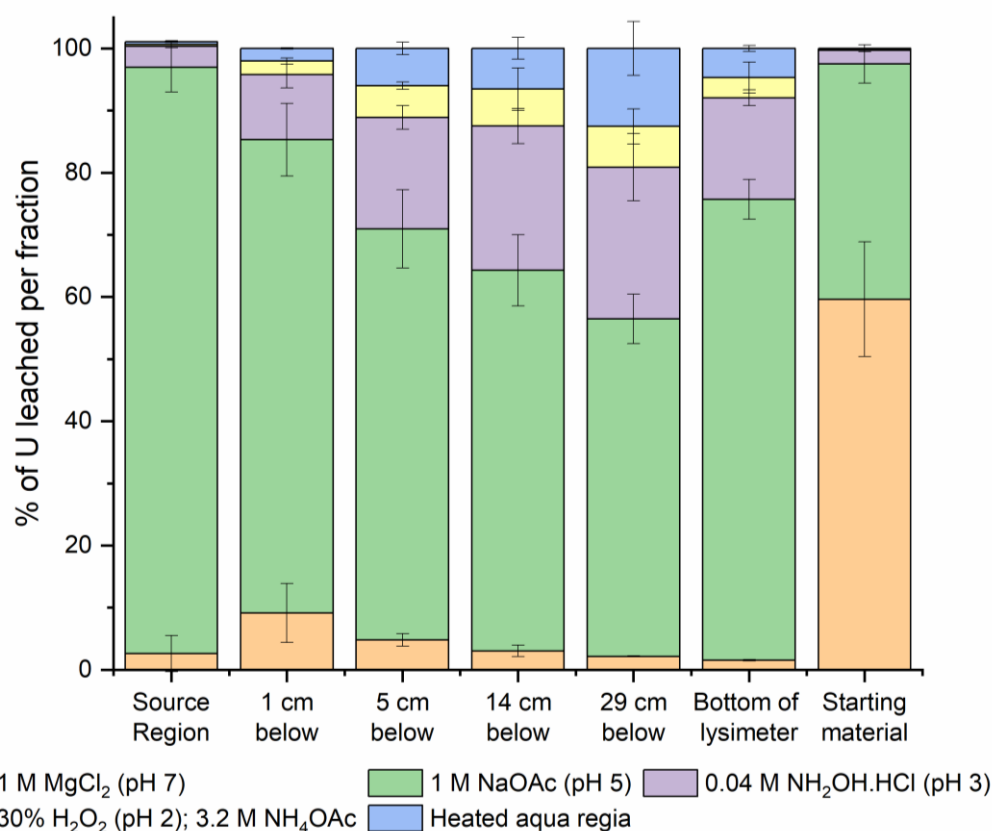
Figure S5.21: Operationally defined sequential extraction results from samples from the sediment-only lysimeter.

S5.2.3.4 Environmental scanning electron microscopy (ESEM)

ESEM was used to examine the sediment and concrete used in this study on samples both pre- and post-lysimeter experiment. Images were collected in both backscattered electron mode, where U phases could be easily identified, and also in secondary electron mode, where sample topography could be explored. Crucially, energy dispersive x-ray spectroscopy (EDS) was used to determine the elements present in the samples in addition to the elements associated with U in the altered post-lysimeter samples. EDS spot and map analyses were used and U and Ca ratios were explored in further detail.
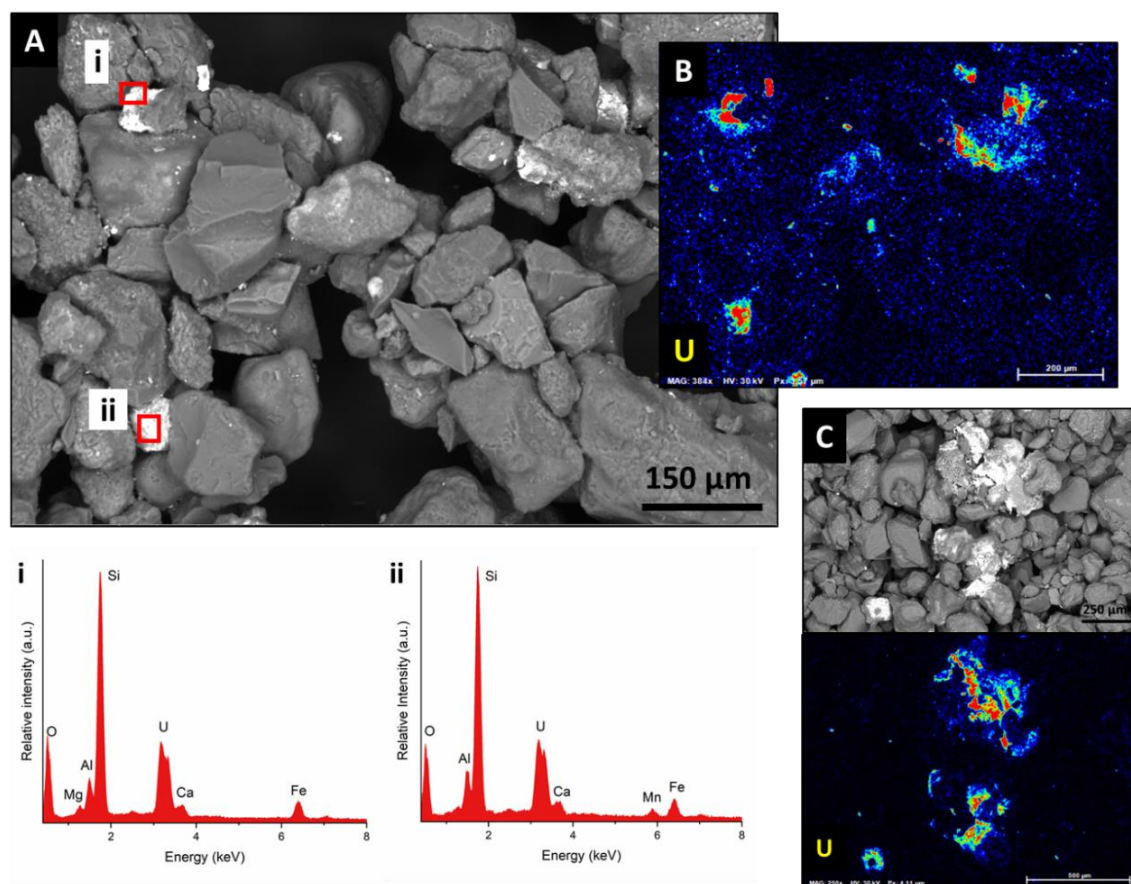
Figure S5.22: ESEM data from a sediment sample taken from the source region of the sediment-only lysimeter. (A) Backscattered electron image; (i-ii) EDS spectra for highlighted areas. (B) EDS map of U where 'warmer colours' are indicative of areas of higher concentration. (C) Backscattered SEM image of a second sediment sample with U EDS map.
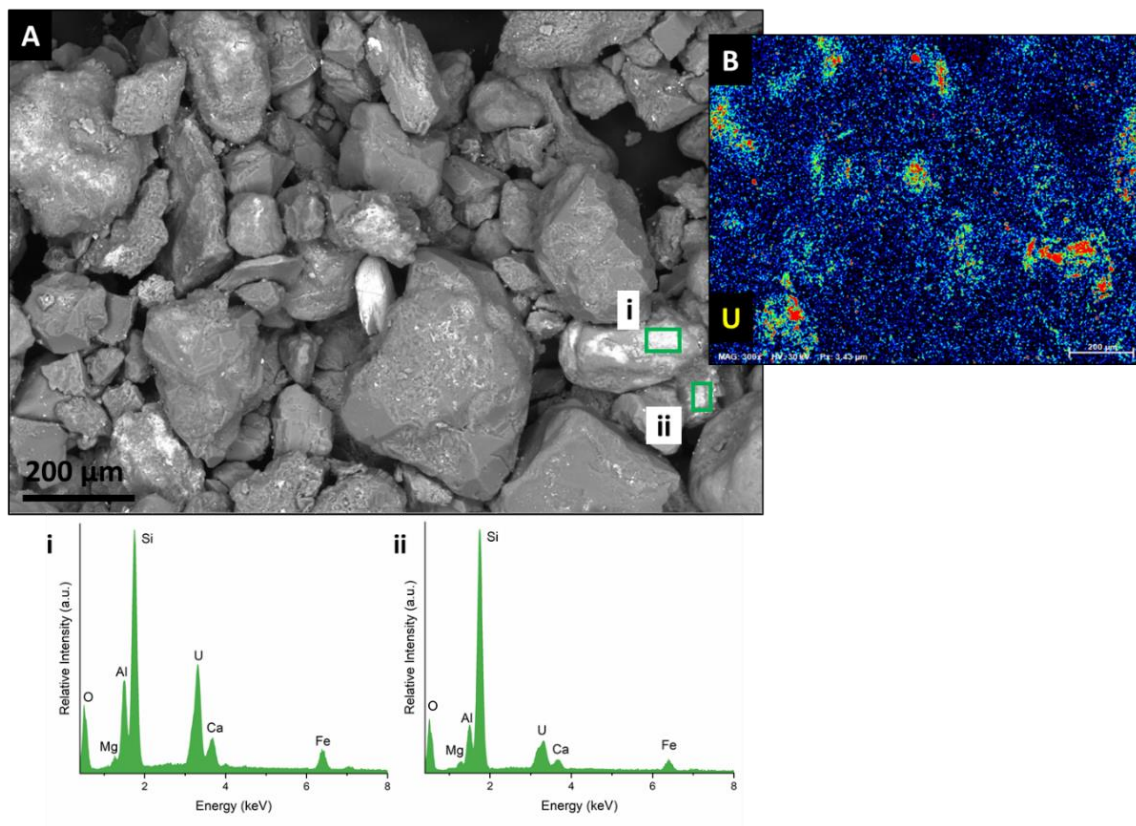
Figure S5.23: ESEM data from a sediment sample taken from the source region of the concrete-cap lysimeter. (A) Backscattered electron image. (B) EDS map of U where 'warmer colours' are indicative of areas of higher concentration. (i-ii) EDS spectra for highlighted areas
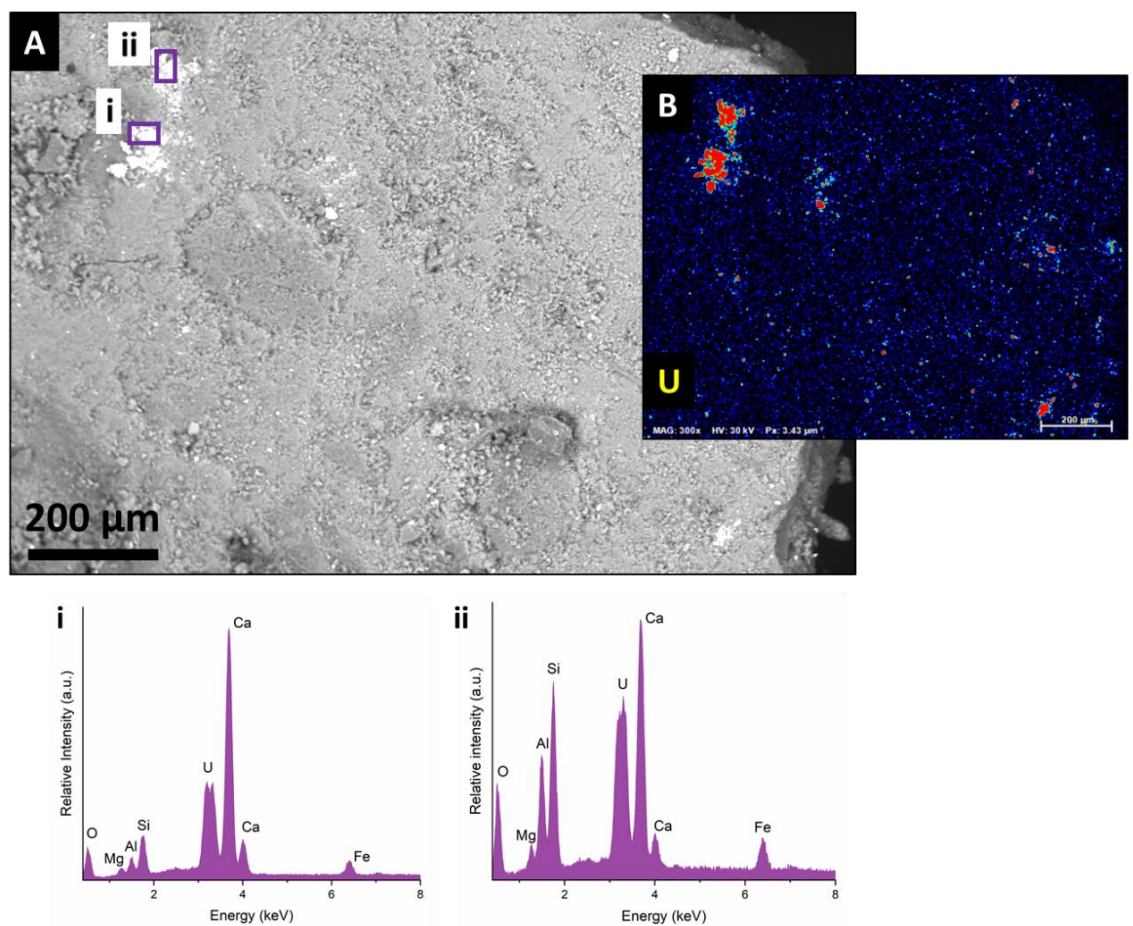
Figure S5.24: ESEM data from a concrete sample taken from 1 cm above the sediment source in the concrete cap lysimeter. (A) Backscattered electron image. (B) EDS map of U where 'warmer colours' are indicative of areas of higher concentration. (i-ii) EDS spectra for highlighted areas.
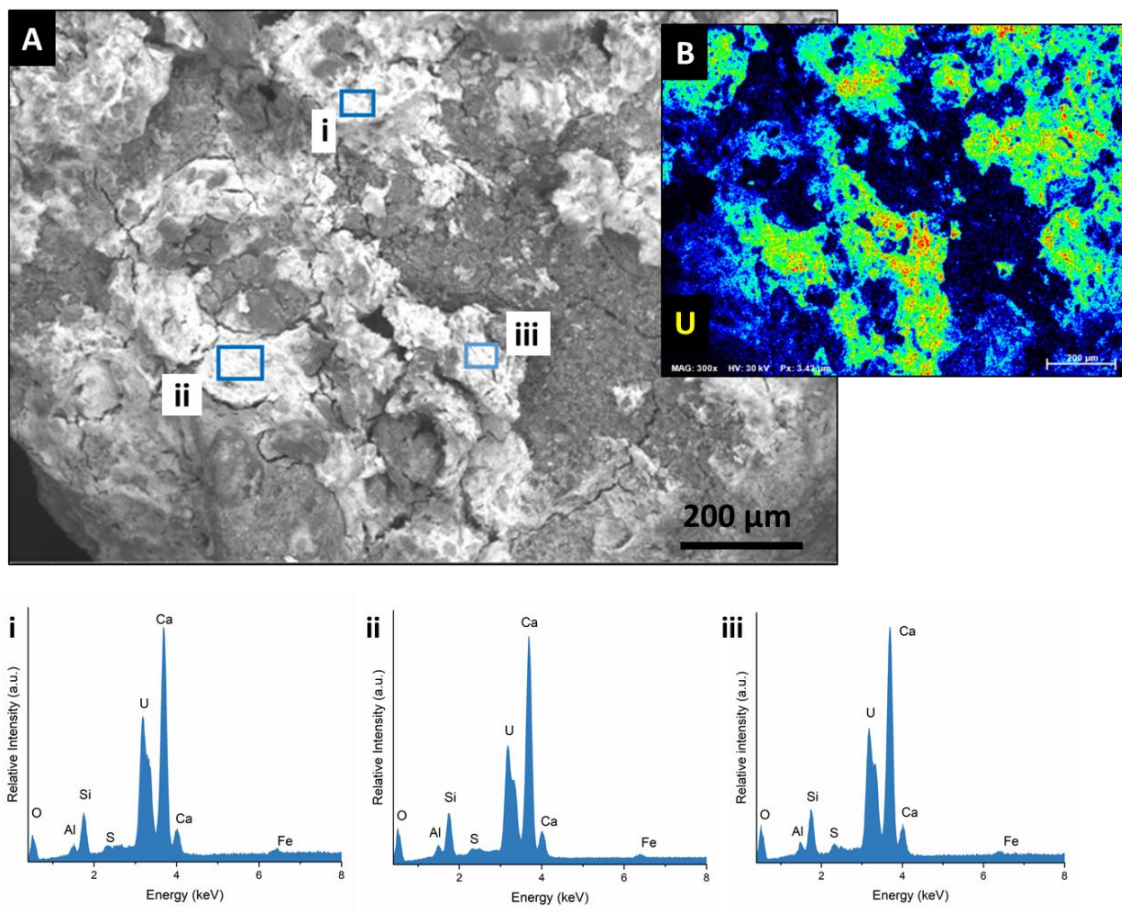
Figure S5.25: ESEM data of an altered concrete sample from the source region of the concrete source lysimeter. (A) Backscattered electron image where areas containing U can clearly be seen; (B) EDS map of U - areas with higher U concentration appear in 'warmer' colours. EDS spectra from select areas in A are also shown to highlight U and Ca ratio (I – iii).
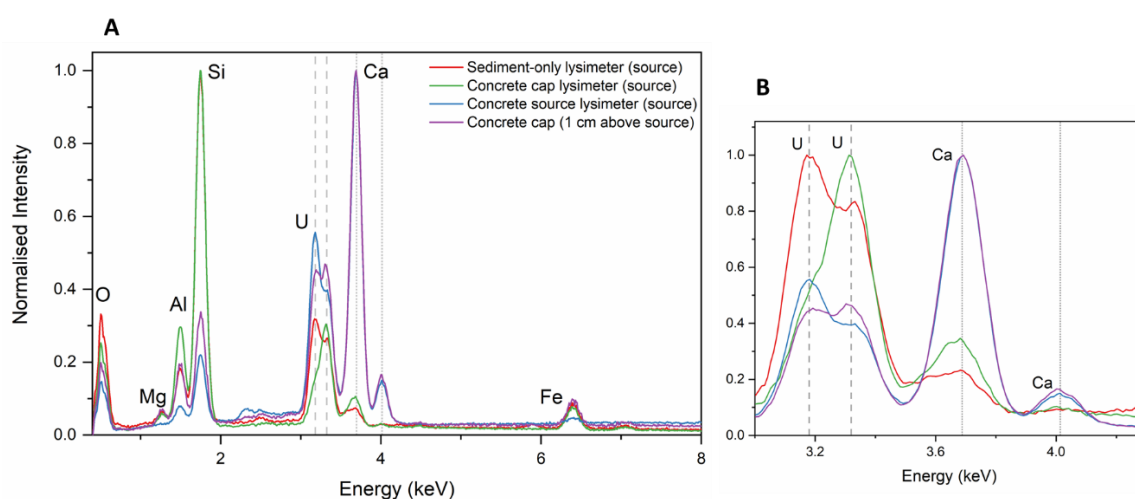
Figure S5.26: Averaged normalised EDS spectra from the highlighted regions from each lysimeter sample (Figures S5.18-21) plotted against each other to highlight the differences in U and Ca ratio across each sample. (A) Normalised EDS spectra (0.4 – 8 keV); (B) EDS spectra (3.0 – 4.3 keV) normalised to U and Ca.

Figure S5.26, (above) shows overlaid averaged EDS spectra from maps of each source horizon sample from the three lysimeters. Figure S5.26-A clearly shows the Si component is much higher in the samples from the sediment-only and concrete cap lysimeters as a result of the quartz-based sediment and so the relative U/Ca peaks in the concrete source lysimeter appear much larger. Similarly, it is clear than there is significantly more Ca present in the concrete source lysimeter and in the concrete zone above the sediment source in the concrete cap lysimeter (as expected). In Figure S5.26-B, the spectra have been normalised to highlight the relative proportions of Ca and U in each sample. There is a slight increase in the proportion of Ca, relative to U in the concrete cap lysimeter source, compared with the sediment-only lysimeter likely as a result of the leachate from the concrete.

S5.2.3.5 PHREEQC modelling

PHREEQC was used in this study to model the solution and solid phases expected to form in each lysimeter to aid our understanding of the phases present in each system and provide a basis for EXAFS fitting.

Table S5.9: Model Sellafield pore water composition used in PHREEQC calculations. Ca concentration was varied for the concrete cap and concrete source lysimeter source horizon calculations based on the aqua regia digestion ICP-MS concentrations.

Species	mmol/kgw
Na	1.49
K	0.13
Mg	0.23
Ca	0.68
S(+3)	0.26
Cl	1.48
C(+4)	0.96

Here, the model Sellafield pore water composition was generated by Callum Robinson from the compilation of borehole data.

Table S5.10: Major solution species predicted to form in the sediment-only lysimeter PHREEQC calculations presented as fractional composition. U and N concentrations were added to the input file using the solution composition in Table S5.9 (above) and these were based on the quantity of uranyl nitrate added to the sediment-only lysimeter. pH was set at 6.8.

Species	Composition
$(UO2)_4(OH)_7^+$	0.54
$(UO2)_3(OH)_5^+$	0.33

$(UO_2)_2(CO_3)(OH)_3^-$	0.13
$UO_2(OH)^+$	5.0×10^{-4}
$UO_2(OH)_2$	3.5×10^{-4}
$(UO_2)_3(OH)_4^{2+}$	3.2×10^{-4}
$UO_2(CO_3)$	3.2×10^{-4}
$(UO_2)_3(OH)_7^-$	3.0×10^{-4}
$(UO_2)_2(OH)_2^{2+}$	1.7×10^{-4}

Table S5.11: Saturation indices for U phases that were predicted to be oversaturated when the U-sediment starting material and sediment-only lysimeter source regions were modelled.

Phase	SI
Becquerelite (nat)	20.61
Becquerelite (syn)	9.11
Clarkeite	1.09
Compreignacite	9.30
Schoepite	0.60
Metaschoepite	1.56
Na-compreignacite	7.82
$\beta\text{-}UO_2(OH)_2$	1.63
UO_4Ca (cr)	0.87

Table S5.4: Fractional composition of major ions (representing 99.99%) in solution in the source region of the concrete-cap lysimeter.

Species	Fractional composition
$(UO_2)_3(OH)_7^-$	0.84
$UO_2(OH)_3^-$	0.10
$(UO_2)_2(CO_3)(OH)_3^-$	0.03
$Ca_2UO_2(CO_3)_3$	0.02
$UO_2(OH)_4^{2-}$	5.8×10^{-3}
$CaUO_2(CO_3)_3^{2-}$	2.2×10^{-3}
$UO_2(OH)_2$	2.1×10^{-4}

Table S5.13: Saturation indices for phases predicted to precipitate in the concrete cap lysimeter source region.

Phase	SI
Becquerelite (nat)	28.72
Becquerelite (syn)	17.22
$CaU_2O_7 \cdot 3H_2O$ (cr)	8.57
Clarkeite	4.84
Compreignacite	14.22

Schoepite	0.48
Metaschoepite	1.44
Na-compreignacite	14.83
$Na_2U_2O_7$	5.88
β-$UO_2(OH)_2$	1.51
UO_4Ca (cr)	9.60
UO_4Mg (cr)	0.65

Table S5.14: Fractional composition of major ions (representing 99.99%) in solution in the source region of the concrete source lysimeter.

Species	Fractional composition
$UO_2(OH)_4^{2-}$	0.85
$UO_2(OH)_3^-$	0.15
$(UO_2)_3(OH)_7^-$	3.9×10^{-3}
$Ca_2UO_2(CO_3)_3$	1.7×10^{-5}

Table S5.15: Saturation indices for phases predicted to precipitate in the concrete source lysimeter source region.

Phase	SI
Becquerelite (nat)	25.66
Becquerelite (syn)	14.16
$CaU_2O_7.3H_2O$ (cr)	10.53
Clarkeite	5.30
Compreignacite	12.18
Metaschoepite	0.19
Na-compreignacite	10.73
$Na_2U_2O_7$	6.81
β-$UO_2(OH)_2$	0.26
UO_4Ca (cr)	12.83
UO_4Mg (cr)	2.22

S5.2.3.6 X-ray Absorption Spectroscopy (XAS)

S5.2.3.6.1 Linear Combination Fitting

Linear combination fitting was performed in Athena(Ravel and Newville, 2005) in normalised $\mu(E)$ space on the concrete cap lysimeter source horizon sample. The U-sediment starting material sample (uranyl) and the concrete source lysimeter source horizon sample (uranate) were used as end member standards. The standard weights were forced to sum to 1. Though linear combination fitting is subject to uncertainty (Boyanov et al., 2007), the results from both LCF on the L_3-edge and ITFA of the M_4-edge XANES data (below) were roughly within error of each other,

providing confidence in the fits, but also highlighting the heterogeneity between samples. The results of the linear combination fit is given in Table S5.16 and plotted in Figure S5.27.

Table S5.16: Linear combination fitting results for concrete cap lysimeter source horizon sample using U-sediment starting material and concrete source lysimeter source horizon samples as end members.

Sample	Concrete cap lysimeter source horizon	
Fitting space	normalised $\mu(E)$	
Fit range	-50 to 100 eV	
R	0.00571	
χ^2	0.365	
χ_v^2	0.00116	
Standard	U-sediment starting material	Concrete source lysimeter source
Weighting (%)	59.2 ± 4	40.8 ± 4
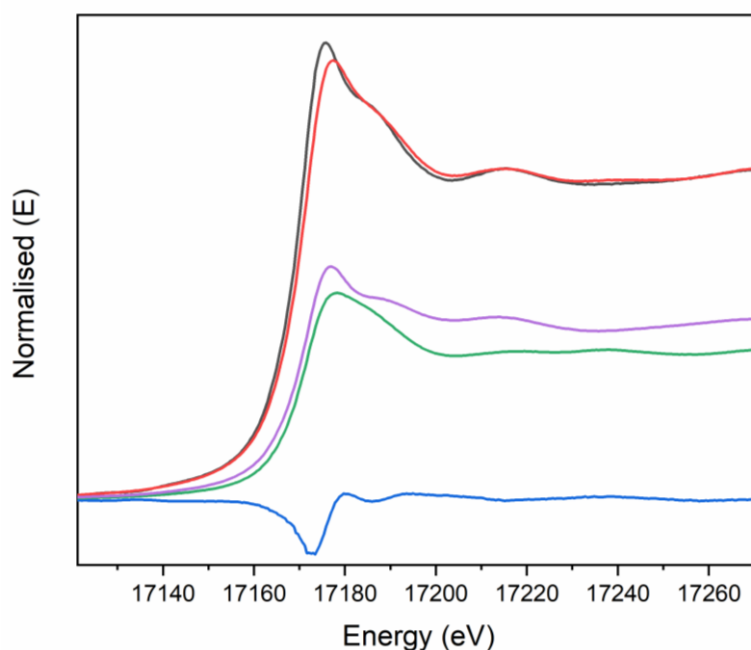
Figure S5.27: Linear combination fit to 'concrete cap' lysimeter source horizon data in normalised $\mu(E)$ space. Black line is the data. Red line is the fit. Green and purple lines are the scaled contributions from the concrete source lysimeter source horizon and U-sediment starting material 'standards', respectively. Blue line is the residual.

S5.2.3.6.2 Iterative Transformation Factor Analysis (ITFA)

ITFA on M_4-edge XANES data of the concrete-cap lysimeter source horizon was performed to obtain an indication of the uranyl and uranate content of the sample. M_4-edge XANES of the

sediment-only and concrete source lysimeters source horizons were used here as end member standards.

Table S5.17: Relative concentrations of uranyl (component 1) and uranate (component 2) in the concrete cap source horizon M_4-edge XANES sample, calculated using ITFA.

	Component 1	Component 2
Standard	Sediment only lysimeter source	Concrete source lysimeter source
Normalised weighting (%)	37.2	62.8

S5.2.3.6.3 U L_3 edge EXAFS

EXAFS Fitting Approach. EXAFS fitting of all spectra were fitted using published reference structures of schoepite, clarkeite, (which was adjusted to include Ca) and uraninite, UO_2 using Artemis from the Demeter suite (Ravel and Newville, 2005). Based on analysis of similar work in the literature, in all fits here, the coordination numbers (N) were manually varied, refined and finally fixed and so errors are not provided for these but are expected to be in the order of 5-20% (Koningsberger et al., 2000). The amplitude reduction factor (S_0^2) was fixed to 1. All other variables were allowed to refine. The number of fitting parameters used were always less than the number of independent points.

EXAFS Fitting of the sediment-only lysimeter source sample. Iterative fitting results to the sediment-only lysimeter source horizon data are presented below. Shell coordination is given in Table S5.18, k^3-weighted EXAFS and resulting Fourier Transforms are presented in Figure S5.28. EXAFS fitting parameters for each of the iterative fits are provided in Table S5.19.

The Fourier transform of the sediment-only lysimeter source horizon sample yielded 4 main peaks, with an additional peak below 1 Å, which is typically associated with the background (Calvin, 2013) and was not taken into account in the fits presented here.

Here, in the final structural model for the sediment-only lysimeter source horizon sample (Table 5.1), we chose to be conservative with the fitting window and determined the fitting of additional paths to be unjustified due to the potential for destructive interference where multiple phases are present. Here, destructive interference between shells at similar distances from U contributed to the difficulty in fitting and dampening of certain features in the Fourier Transform that may have been diagnostic of the phases present. Regardless, the fit we present is indicative of uranyl speciation, and is consistent with PHREEQC modelling and both L_3-edge and M_4-edge XANES data.

Table S5.18: Coordination numbers for different fits applied to the sediment-only lysimeter source horizon data.

Fit	(a)	(b)	(c)	(d)	(e)	(f)	(g)	(h)	(i)	(j)	(k)
O_{ax}	2	2	2	2	2	2	2	2	2	2	2
O_{eq1}		1	1.5	1.5	1.5	1.5	1.5	1.5	1.5	1.5	1.5
O_{eq2}	5	4	4	4	4	4	4	4	4	4	4
C					3	1.5	1.5	1.5	1.5	1.5	
Fe								0.5		0.5	
U									1	1	1
O_{dist}							3				
O_{ax} MS			2	2	2	2	2	2	2	2	2
C-O_{dist} MS							6				
C-O_{dist}-C MS							3				
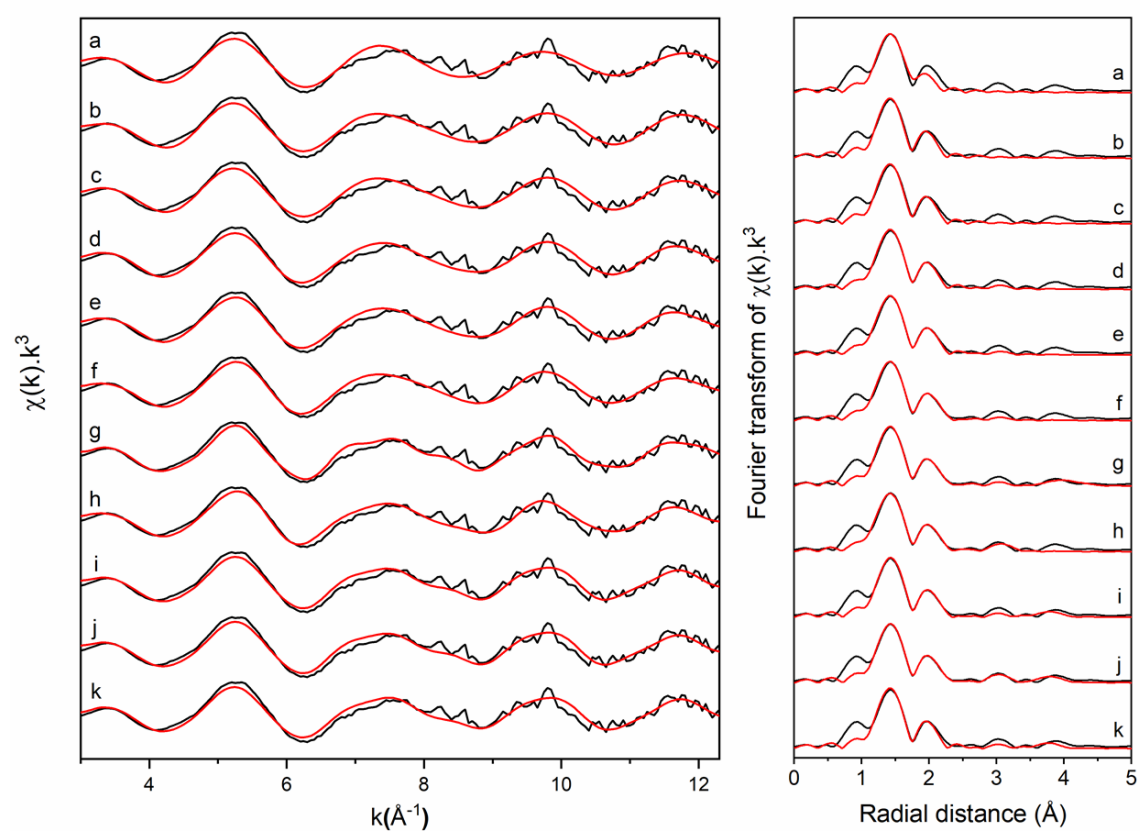
Figure S5.28: k^3-weighted EXAFS data (black) with fits (red). Fit parameters and details are given in Table S5.19. All Fourier transforms are non-phase shift corrected.

Table S5.19: EXAFS fitting parameters for iterative fits (a-k) to the altered sediment-only lysimeter source horizon sample.

Fit	Path	CN	R(Å)	σ^2 (Å^2)	ΔE_0(eV)	S_0^2	χ_v^2	R	NIDP	Var
(a)	O$_{ax}$	2	1.82 (2)	0.003 (1)	9.2 ± 4.1	1	345.9	0.032	9.58	5
	O$_{eq2}$	5	2.36 (5)	0.018 (5)						
(b)	O$_{ax}$	2	1.82 (2)	0.002(1)	12.4 ± 5.6	1	206.7	0.014	9.58	6
	O$_{eq1}$	1	2.11 (11)	0.011(4)						
	O$_{eq2}$	4	2.40 (3)	0.011(4)*						
(c)	O$_{ax}$	2	1.81 (1)	0.003(1)	8.4 ± 2.5	1	204.4	0.014	9.58	6
	O$_{eq1}$	1.5	2.17 (3)	0.008(2)						
	O$_{eq2}$	4	2.39 (2)	0.008(2)*						
(d)	O$_{ax}$	2	1.81 (1)	0.003(1)	6.1 ± 2.8	1	141.4	0.018	14.45	7
	O$_{eq1}$	1.5	2.17 (2)	0.004(4)						
	O$_{eq2}$	4	2.37 (2)	0.007(2)						
	O$_{ax}$ MS	2	3.61	0.006						
(e)	O$_{ax}$	2	1.80 (3)	0.003(1)	5.8 ± 7.3	1	188.7	0.017	14.45	9
	O$_{eq1}$	1.5	2.18 (4)	0.004(6)						
	O$_{eq2}$	4	2.38 (5)	0.006(3)						
	C	3	2.92 (27)	0.042(47)						
	O$_{ax}$ MS	2	3.61	0.007						
(f)	O$_{ax}$	2	1.80(2)	0.003(1)	6.5 ± 6.0	1	170.8	0.013	14.45	9
	O$_{eq1}$	1.5	2.19(4)	0.004(6)						
	O$_{eq2}$	4	2.39(5)	0.007(3)						
	C	1.5	2.88(6)	0.009(10)						
	O$_{ax}$ MS	2	3.61	0.007						
(g)	O$_{ax}$	2	1.81(1)	0.003(1)	8.7 ± 1.5	1	86.6	0.011	17.89	10
	O$_{eq1}$	1.5	2.20(2)	0.008(2)						
	O$_{eq2}$	4	2.40(1)	0.008(2)*						
	C	1.5	2.88(4)	0.008(6)						
	O$_{dist}$	3	4.54(4)	0.008(4)						
	O$_{ax}$ MS	2	3.63	0.006*						
	C-O$_{dist}$ MS	6	4.55	0.008*						
	C-O$_{dist}$-C MS	3	4.55	0.008*						
(h)	O$_{ax}$	2	1.80(2)	0.004(1)	5.6 ± 6.1	1	211.7	0.009	14.45	11
	O$_{eq1}$	1.5	2.18(4)	0.003(6)						
	O$_{eq2}$	4	2.38(5)	0.006(3)						
	C	1.5	2.89(7)	0.009(11)						
	Fe	0.5	3.47(8)	0.006(7)						
	O$_{ax}$ MS	2	3.6	0.007						

Fit	Path	CN	R(Å)	σ^2 (Å^2)	ΔE_0(eV)	S_0^2	χ_v^2	R	NIDP	Var
(i)	O_{ax}	2	1.82(1)	0.003(1)	9.9 ± 2.1	1	149.7	0.018	17.89	10
	O_{eq1}	1.5	2.20(3)	0.008(2)						
	O_{eq2}	4	2.41(2)	0.008(2)*						
	C	1.5	2.85(7)	0.013(13)						
	U	1	3.89(5)	0.007(5)						
	O_{ax} MS	2	3.64	0.006						
(j)	O_{ax}	2	1.82(1)	0.003(1)	9.4 ± 2.0	1	157.2	0.012	17.89	12
	O_{eq1}	1.5	2.20(2)	0.008(2)						
	O_{eq2}	4	2.41(2)	0.008(2)*						
	C	1	2.87(6)	0.005(8)						
	Fe	0.5	3.49(6)	0.006(7)						
	U	1	3.9(5)	0.006(5)						
	O_{ax} MS	2	3.63	0.006						
(k)	O_{ax}	2	1.81(1)	0.003(1)	8.7 ± 1.6	1	128.6	0.022	17.89	8
	O_{eq1}	1.5	2.18(2)	0.008(2)						
	O_{eq2}	4	2.39(2)	0.008(2)*						
	U	1	3.88(5)	0.008(6)						
	O_{ax} MS	2	3.63	0.006						

CN is the coordination number; R is the atomic distance; σ^2 denotes the Debye-Waller disorder factor; ΔE_0 is the energy shift from the calculated Fermi level; S_0^2 is the amplitude factor which was constrained to 1 for all fits here; χ_v^2 denotes the value for reduced Chi square; R is the 'goodness of fit'; NIDP is the number of independent points; Var denotes the number of variables used within the limits of NIDP. *indicate where σ^2 parameters have been fixed. Numbers in parentheses are the errors on the last significant figure.

Chapter 6   Conclusions and Future Work

6.1 Conclusions

The key aim for this thesis was to investigate the interactions between uranium and engineered, subsurface components under environmentally relevant conditions. Specifically, interactions between uranium and magnetite, an environmentally relevant iron (oxyhydr)oxide, and concrete, which is widely used in the nuclear industry in construction and encapsulation of radioactive waste, were explored in two separate deployments of field lysimeter experiments. Prior to this work, studies examining the mechanism of U(V) incorporation into magnetite had taken place and U(V), previously thought to be transient, had been observed to be stable under anoxic conditions for up to 480 days (Pidchenko et al., 2017; Roberts et al., 2017). Furthermore, limited oxidation studies of U(V)-incorporated magnetite had also been carried out, where U(V) was seen to persist for up to 226 days (Marshall et al., 2015; Pidchenko et al., 2017). These studies significantly furthered the scientific knowledge in this area, however there was a gap in understanding the longer-term behaviour of U(V)-incorporated magnetite in subsurface field conditions relevant to nuclear sites. Similarly, though a wide range of previous research has focussed on uranium interactions with concrete and cement phases, no research thus far has explored the environmental behaviour of uranium with concrete in field conditions relevant to the in-situ disposal of radioactive waste. Here, by using outdoor field lysimeter experiments deployed for ~12 months at the RadFATE facility at Clemson University, USA, in combination with a series of geochemical techniques and X-ray absorption spectroscopies, a unique picture of the environmental behaviour and stability of these source terms was explored in order to underpin future safety cases for disposal of radioactive waste, particularly through optimised routes such as in-situ disposal.

The research questions proposed at the start of this thesis were as follows:

- How does environmental exposure alter the speciation of U(V) when incorporated into magnetite?
- What is the impact of environmental alteration at the cement/subsurface interface on uranium mobility and speciation?

In **Chapter 4**, U(V)-incorporated magnetite was emplaced at two depths in a field lysimeter and deployed for ~12 months, exposed to rainfall and natural environmental conditions. After 12 months, aqua regia digestions of 1 cm vertical sections around both source horizons revealed very limited transport (up to 1 cm) of uranium away from the magnetite zones, consistent with autoradiography of thin section samples, where all radioactivity above background was

207

associated with magnetite. μ-focus XRF analysis of source horizon thin section samples revealed strong correlations between iron and uranium location, suggestive of uranium remaining incorporated into- or associated with iron after environmental exposure, however there was also some evidence to suggest minor areas of dissociation. Acid dissolution experiments determined that ~40% of the uranium was leachable without any iron dissolution suggestive of some surface bound or near-surface associated uranium. Despite this, the U/Fe dissolution profiles in both upper and lower source horizons remained similar to a sample of unaltered U(V)-incorporated magnetite (Roberts et al., 2017). Uranium speciation in the altered source horizons was determined using U L_3-edge XANES and EXAFS analysis and here, ITFA determined from the L_3-edge data suggested significant retention of U(V) in both upper and lower source horizons compared with the starting material. Oxidation of U(IV) in the starting material to U(VI) in the altered source horizons was observed with marginally more U(VI) identified in the upper source, possibly due to a slightly more oxic environment. Qualitative analysis of the L_3-edge XANES suggested the uranium in both upper and lower sources was present in uranate-like coordination given the absence of the post-edge shoulder typical of uranyl species (Catalano and Brown, 2004), and this is consistent with previous studies investigating U(V)-incorporated into magnetite (Pidchenko et al., 2017; Roberts et al., 2017). Analyses of the EXAFS spectra however, revealed increasing contributions from a U-O backscatterer at ~1.82 Å from lower to upper sources, suggesting some contribution from U(VI) uranyl in both sources. Despite this, previous work investigating U incorporated into goethite suggested that these short U-O bonds were attributed to U in a uranate-like coordination, where a shorter U-O bond was required to enable facile substitution of U for Fe(III) in the octahedral site (Doornbusch et al., 2015). Due to the lack of a uranyl shoulder feature in the XANES, we propose this is the case here, though some contribution from U(VI)-uranyl sorbed to the surface of magnetite cannot be discounted. Iron $L_{2,3}$-edge XAS and XMCD were used in conjunction with XRD and showed that some oxidation of the magnetite itself had occurred, likely to goethite as identified by XRD. XMCD revealed greater oxidation of the upper source, with a final Fe(II)/Fe(III) ratio of 0.1, compared to 0.3 in the lower source and 0.6 in the starting material. A change in the U-Fe$_1$ distance in the upper source from the starting material in the EXAFS also seemed to suggest iron speciation change. Despite the evidenced oxidation to U(VI) and oxidation of the magnetite, strong signals from the iron shells in the EXAFS of both upper and lower sources are indicative of persistent incorporation, and, coupled with the lack of uranium movement away from the original source horizons, is a positive prospect for the environmental stability of uranium in magnetite over extended periods.

In **Chapter 5**, a series of three lysimeter experiments were set up to replicate in-situ disposal scenarios where uranium and concrete were emplaced in the subsurface for ~13 months. In the first column, containing no concrete and a uranyl nitrate mixed with sediment source, transport

of uranium through the column was significant, with uranium seen in elevated levels in the effluent and at concentrations up to ~ 10 ppm at the base of the lysimeter. Sequential extractions on several sections throughout the column revealed a change in uranium association with depth, with an increasing proportion of uranium becoming more strongly bound and requiring increasingly aggressive reagents to remove at greater depth and with lower uranium concentrations, suggesting that although migration over 13 months was significant, natural attenuation over time is likely to retard movement. A sample of unaltered source material showed uranium was largely outer sphere sorbed when emplaced, whilst after aging, the source region, which was modelled to be oversaturated with respect to a number of uranyl (oxyhydr)oxide phases including schoepite and metaschoepite, was altered with a significant proportion bound to carbonates present in the sediment. Precipitated uranium phases coating the sediment grains were observed in SEM images from the source region, with XAS analysis of the source horizon from this lysimeter revealing uranyl speciation with some evidence for a sorbed component, though multiple uranium phases were likely present here which made fitting difficult due to destructive interference in the EXAFS.

The source material in the U-concrete source, which was identified to be a calcium uranate precipitated phase prior to emplacement was seen to be relatively immobile. A small proportion of dissolution and movement was observed with spatially resolved analysis using an Itrax XRF scanner suggesting modest movement (up to 1 cm) of uranium away from the source region. In this region, the XANES data suggested a change in speciation from a calcium uranate phase to a uranyl phase, highlighting potential limited capability for remobilisation in the long term. Over the course of the 13 months however, the calcium uranate phase in the concrete region became more crystalline as observed in the EXAFS, suggesting an increasing recalcitrance towards mobilisation. The structural parameters for the calcium uranate phase identified here were comparable with a previous study identifying the formation of a calcium uranate precipitate at high U(VI) loading in a cementitious environment (Macé et al., 2013). Interestingly, in the lysimeter system with a uranyl nitrate sediment source and a concrete 'cap' above it, M_4-edge HERFD-XANES data showed a mix of uranyl and uranate phases were present in the source region, with EXAFS analysis supporting this through the elongation of the U-O axial component relative to sole uranyl speciation (Catalano and Brown, 2004). The formation of the insoluble uranate phase here is likely to have contributed to the reduction in uranium movement below the source, where migration through the lysimeter was limited, relative to the sediment-only system. Overall here, we observed significant transport mediated by the movement of uranyl phases through the system containing no concrete. With the addition of a concrete cap to contaminated sediment retardation of uranium was observed to some extent, with XAS analyses revealing a mixture of uranyl and uranate phases. Where uranium was precipitated onto concrete, transport through

the subsurface was negligible and the increased crystallinity of the calcium uranate-like phase over the duration of the experiment suggests these phases may become more insoluble over time. These results further our understanding of uranium behaviour in subsurface cementitious systems typical of a nuclear site.

Ultimately, this research has highlighted a range of processes whereby uranium may be sequestered in engineered, subsurface environments. Through the use of field lysimeter experiments, which bridge the gap between small-scale laboratory column experiments and nuclear sites themselves, the transport and speciation of uranium in various systems has been explored. Uranium incorporated into magnetite has been shown to be stable for up to 12 months in oxic, subsurface systems, which provides new awareness into the long-term fate of uranium in environments where corroding iron is present. Additionally, calcium uranate phases, precipitated onto the surface of concrete, have been shown to be immobile in dynamic subsurface systems. Precipitation of these uranate phases in sediments impacted by high pH concrete leachate were also shown to limit the migration of uranium, relative to systems without concrete, where mobile uranyl phases dominated. In the context of in-situ disposal of radioactive waste, these results provide new insight into the behaviour of uranium in engineered subsurface systems, including the potential long-term immobilisation of uranium phases. Moving forward, particularly as sites in the UK start to develop environmental safety cases for optimised disposal routes, underpinning research such as this is pivotal to enhancing our understanding of radionuclide fate in the environment.

6.2 Future Work

Results from Chapter 4 indicate that uranium remains stable and immobilised in oxic environmental conditions when incorporated into magnetite, despite oxidation of the magnetite to goethite. To further work performed here, other radionuclides could also be investigated in field lysimeter conditions, both incorporated into magnetite, and its oxidation products including maghemite and goethite. By investigating the incorporation of radionuclides in this way, using representative subsurface and 'aged' iron (oxyhydr)oxide source terms, it could provide a perspective on the long term immobilisation of radionuclides in the subsurface. For example, Marshall et al. successfully incorporated Tc as Tc(IV) into the structure of magnetite in batch experiments, where Tc(IV) was seen to be largely recalcitrant to remobilisation on oxidation (Marshall et al., 2014b). Similarly, Um et al. incorporated Tc(IV) into goethite and subsequent diffusion coefficients in a Hanford pore water solution were observed to be very low suggesting significant Tc immobilisation (Um et al., 2012). Despite these extensive studies, the behaviour of Tc(IV) (and indeed other radionuclides) could be significantly different when exposed to the environment in a dynamic flow-through system such as a field lysimeter, where samples are exposed to wetting and drying cycles. Over longer timescales, these experiments could provide key information on the evolution of incorporated species that will underpin the safety cases at nuclear sites, and potentially inform the use of iron (oxyhydr)oxides as waste forms if multiple key radionuclides, relevant to radioactive waste, are found to remain stable.

Marshall et al. conducted their experiments with Tc(IV) at high pH and that opens an interesting area for research around the behaviour of radionuclides in contact with corroding rebar within concrete. Here, there is the potential for both iron (oxyhydr)oxide and concrete interactions with uranium and other radionuclides to be studied simultaneously. Site samples of concrete containing steel rebar could be utilised for sorption or flow-through experiments, whereby thin section samples encompassing a cross section of concrete with rebar running through could be exposed to uranium- (or other radionuclide) containing solution. Here, the preferential partitioning of uranium to either the iron (oxyhydr)oxide phases and/or concrete could be explored over time, with techniques including SEM-EDX and μ-focus XRF utilised to determine phase association.

For the concrete work, there is potential for a wide range of additional follow-up work to take place, including using existing samples from the lysimeter experiments performed in this thesis to further explore the long-term stability of these systems. For instance, because of the multiple uranyl phases present in the source region of the 'sediment-only' lysimeter, phase identification using the averaged bulk EXAFS technique was difficult. Techniques such as luminescence

spectroscopy however, could be employed to differentiate between species and will infer the likely long-term fate of uranium in these systems. Additionally, intact samples were taken from each of the source horizons and were preserved at -80 °C. If those samples were to be resin embed, thin sections of the source horizons could be created to analyse the source regions using spatially-resolved techniques such as SEM-EDX and μ-focus XRF, used in Chapter 4. μ-focus XAS could be used to determine uranium speciation on a finer scale to build on the bulk XAS work performed as part of this thesis. It would also be helpful to conduct remobilisation and desorption experiments on bulk 1 or 2 cm fraction samples collected here to determine the extent of uranium sorption to sediments and concrete.

Furthermore, though the concentrations of uranium used in these experiments were relatively high compared to what may be expected in some areas at nuclear sites, ever improving detection limits with XAS techniques could allow the exploration of similar systems at lower concentrations. In particular, the speciation of uranium in concrete-containing systems using lower U(VI) concentrations are typically different to the speciation observed in this work, where sorption to the concrete may be favoured over precipitation of calcium uranate phases in undersaturated solutions (Macé et al., 2013). Further exploration of the fate of U(VI)-sorbed to concrete in field lysimeter systems could ultimately provide a wider picture of the potential for uranium to be immobilised or remobilised in the subsurface. With regards to the use of lysimeter experiments in particular, an inexhaustible body of work could take place. From using site-specific samples to look at remobilisation of contaminants present in a range of waste forms, to the application of in-situ remediation treatments to sediments on a larger scale than is typical in a laboratory, field lysimeters present a unique capability to study radionuclide behaviour in complex, environmental subsurface systems.

Finally, there are significant avenues to be explored with regards to the future stability of U-incorporated into iron (oxyhydr)oxides and the stability of uranate phases in cementitious environments that would provide significant value to the nuclear industry. In particular, with sea-levels set to rise over the coming years, the impacts of seawater intrusion at nuclear sites may well be significant. Setting up desorption experiments in seawater and other media for reacted, oxic samples, such as those produced during the course of this work, could shed light on the future potential for uranate phases and/or uranium-incorporated iron (oxyhydr)oxide phases to remobilise. In addition, a combination of speciation and transport modelling over longer timescales to assess the behaviour of uranium and other key radionuclides in scenarios such as those described above will provide the nuclear industry with vital insight regarding the long-term stability and fate of these radioactive species.

The results produced in this work in conjunction with areas for further work discussed here, have shown the use of field lysimeters in radionuclide subsurface research can provide a unique picture of the fate of many contaminants in the subsurface, at scales not typically achievable in a laboratory setting. As nuclear sites continue to look at optimised end states following the release of the GRR guidance in 2018, comprehensively understanding a range of different subsurface scenarios in which radioactively contaminated engineered environments are left in situ is pivotal.

Blank page

References

AECOM, 2017. CLESA PCRSA Review Report, 60493376/MARP003. Manchester.

Akçay, H., 1998. Aqueous speciation and pH effect on the sorption behavior of uranium by montmorillonite. J. Radioanal. Nucl. Chem. 237, 133–137.

Allen, P.G., Shuh, D.K., Bucher, J.J., Edelstein, N.M., Palmer, C.E.A., Silva, R.J., Nguyen, S.N., Marquez, L.N., Hudson, E.A., 1996. Determinations of Uranium Structures by EXAFS: Schoepite and Other U(VI) Oxide Precipitates. Radiochim. Acta 75, 47–53.

Altmaier, M., Yalçıntaş, E., Gaona, X., Neck, V., Müller, R., Schlieker, M., Fanghänel, T., 2017. Solubility of U(VI) in chloride solutions. I. The stable oxides/hydroxides in NaCl systems, solubility products, hydrolysis constants and SIT coefficients. J. Chem. Thermodyn. 114, 2–13.

Anderson, R.T., Vrionis, H.A., Ortiz-Bernad, I., Resch, C.T., Long, P.E., Dayvault, R., Karp, K., Marutzky, S., Metzler, D.R., Peacock, A., White, D.C., Lowe, M., Lovley, D.R., 2003. Stimulating the In Situ Activity of Geobacter Species to Remove Uranium from the Groundwater of a Uranium-Contaminated Aquifer. Appl. Environ. Microbiol. 69, 5884–5891.

Arai, Y., Powell, B.A., Kaplan, D.I., 2018. Residence time effects on technetium reduction in slag-based cementitious materials. J. Hazard. Mater. 342, 510–518.

Atkins, M., Glasser, F.P., 1992. Application of portland cement-based materials to radioactive waste immobilization. Waste Manag. 12, 105–131.

Ayora, C., Salas, J., Made, B., Ledoux, E., 1998. Reactive Transport Around Bangombé Uranium Deposit, Gabon. Mineral. Mag. 62A, 87–88.

Bargar, J.R., Reitmeyer, R., Lenhart, J.J., Davis, J.A., 2000. Characterization of U(VI)-carbonato ternary complexes on hematite: EXAFS and electrophoretic mobility measurements. Geochim. Cosmochim. Acta 64, 2737–2749.

Baston, G.M.N., Cowper, M.M., Marshall, T.A., 2012. Sorption properties of aged cements. Mineral. Mag. 76, 3411–3423.

Batson, V.L., Bertsch, P.M., Herbert, B.E., 1996. Transport of Anthropogenic Uranium from Sediments to Surface Waters During Episodic Storm Events. J. Environ. Qual. 25, 1129–1137.

BEIS, 2021. Notice: Decommissioning EDF Advanced Gas Cooled Reactor (AGR) Stations [Website]. URL https://www.gov.uk/government/publications/decommissioning-edf-advanced-gas-cooled-reactor-agr-stations/advanced-gas-cooled-reactor-agr-decommissioning-factsheet

Bender, W.M., Becker, U., 2019. Quantum-Mechanical Investigation of the Structures and Energetics of Uranium and Plutonium Incorporated into the Magnetite (Fe3O4) Lattice. ACS Earth Sp. Chem. 3, 637–651.

Berner, U.R., 1992. Evolution of pore water chemistry during degradation of cement in a radioactive waste repository environment. Waste Manag. 12, 201–219.

Bernhard, G., Geipel, G., Reich, T., Brendler, V., Amayri, S., Nitsche, H., Nitsche, H., 2001. Uranyl(VI) carbonate complex formation: Validation of the $Ca_2UO_2(CO_3)_{3(aq.)}$ species. Radiochim. Acta 89, 511.

Bertsch, P.M., Hunter, D.B., Sutton, S.R., Bajt, S., Rivers, M.L., 1994. In Situ Chemical Speciation of Uranium in Soils and Sediments by Micro X-ray Absorption Spectroscopy. Environ. Sci. Technol. 28, 980–984.

Bès, R., Rivenet, M., Solari, P.L., Kvashnina, K.O., Scheinost, A.C., Martin, P.M., 2016. Use of

HERFD-XANES at the U L_3- and M_4-Edges to Determine the Uranium Valence State on $[Ni(H_2O)_4]_3[U(OH,H_2O)(UO_2)8O_{12}(OH)_3]$. Inorg. Chem. 55, 4260–4270.

Bigham, J.M., Fitzpatrick, R.W., Schulze, D.G., 2002. Chapter 10: Iron Oxides, Soil Mineralogy with Environmental Applications.

Blesa, M.A., Matijević, E., 1989. Phase transformations of iron oxides, oxohydroxides, and hydrous oxides in aqueous media. Adv. Colloid Interface Sci. 29, 173–221.

Bliem, R., Pavelec, J., Gamba, O., McDermott, E., Wang, Z., Gerhold, S., Wagner, M., Osiecki, J., Schulte, K., Schmid, M., Blaha, P., Diebold, U., Parkinson, G.S., 2015. Adsorption and incorporation of transition metals at the magnetite Fe_3O_4 (001) surface. Phys. Rev. B - Condens. Matter Mater. Phys. 92, 1–9.

Boglaienko, D., Soltis, J.A., Kukkadapu, R.K., Du, Y., Holfeltz, V.E., Hall, G.B., Buck, E.C., Segre, C.U., Katsenovich, Y., Levitskaia, T.G., Sweet, L.E., Emerson, H.P., 2020. Spontaneous redox continuum reveals sequestered technetium clusters and retarded mineral transformation of iron. Commun. Chem. 1–11.

Boland, D.D., Collins, R.N., Glover, C.J., Payne, T.E., Waite, T.D., 2014. Reduction of U(VI) by Fe(II) during the Fe(II)-accelerated transformation of ferrihydrite. Environ. Sci. Technol. 48, 9086–9093.

Boland, D.D., Collins, R.N., Payne, T.E., Waite, T.D., 2011. Effect of amorphous Fe(III) oxide transformation on the Fe(II)-mediated reduction of U(VI). Environ. Sci. Technol. 45, 1327–1333.

Bots, P., Morris, K., Hibberd, R., Law, G.T.W., Mosselmans, J.F.W., Brown, A.P., Doutch, J., Smith, A.J., Shaw, S., 2014. Formation of stable uranium(VI) colloidal nanoparticles in conditions relevant to radioactive waste disposal. Langmuir 30, 14396–14405.

Bots, P., Shaw, S., Law, G.T.W.W., Marshall, T.A., Mosselmans, J.F.W., Morris, K., 2016. Controls on the Fate and Speciation of Np(V) during Iron (Oxyhydr)oxide Crystallization. Environ. Sci. Technol. 50, 3382–3390.

Bots, P., van Veelen, A., Mosselmans, J.F.W., Muryn, C., Wogelius, R.A., Morris, K., 2019. Neptunium(V) and Uranium(VI) Reactions at the Magnetite (111) Surface. Geosciences 9, 81.

Bower, W.R., Morris, K., Livens, F.R., Mosselmans, J.F.W., Fallon, C.M., Fuller, A.J., Natrajan, L., Boothman, C., Lloyd, J.R., Utsunomiya, S., Grolimund, D., Ferreira Sanchez, D., Jilbert, T., Parker, J., Neill, T.S., Law, G.T.W., 2019. Metaschoepite Dissolution in Sediment Column Systems - Implications for Uranium Speciation and Transport. Environ. Sci. Technol. 53, 9915–9925.

Bower, W.R., Morris, K., Mosselmans, J.F.W., Thompson, O.R., Banford, A.W., Law, K., Pattrick, R.A.D., 2016. Characterising legacy spent nuclear fuel pond materials using microfocus X-ray absorption spectroscopy. J. Hazard. Mater. 317, 97–107.

Boyanov, M.I., O'Loughlin, E.J., Roden, E.E., Fein, J.B., Kemner, K.M., 2007. Adsorption of Fe(II) and U(VI) to carboxyl-functionalized microspheres: The influence of speciation on uranyl reduction studied by titration and XAFS. Geochim. Cosmochim. Acta 71, 1898–1912.

Brice-Profeta, S., Arrio, M.A., Tronc, E., Menguy, N., Letard, I., Cartier Dit Moulin, C., Noguès, M., Chanéac, C., Jolivet, J.P., Sainctavit, P., 2005. Magnetic order in γ-Fe_2O_3 nanoparticles: A XMCD study. J. Magn. Magn. Mater. 288, 354–365.

Brownsword, M., Buchan, A.B., Ewart, F.T., McCrohon, R., Ormerod, G.J., Smith-Briggs, J.L., Thomason, H.P., 1990. The Solubility and Sorption of Uranium (VI) in a Cementitious Repository. MRS Proc. 176, 577.

Brydson, R., 2011. Aberration-corrected analytical transmission electron microscopy. Wiley,

Oxford.

Bube, C., Metz, V., Schild, D., Rothe, J., Dardenne, K., Lagos, M., Plaschke, M., Kienzler, B., 2014. Combining thermodynamic simulations, element and surface analytics to study U(VI) retention in corroded cement monoliths upon >20years of leaching. Phys. Chem. Earth 70–71, 53–59.

Calvin, S., 2013. XAFS for Everyone, 1st Editio. ed. CRC Press, Boca Raton.

Catalano, J.G., Brown, G.E., 2004. Analysis of uranyl-bearing phases by EXAFS spectroscopy: Interferences, multiple scattering, accuracy of structural parameters, and spectral differences. Am. Mineral. 89, 1004–1021.

Catalano, J.G., Brown, G.E., 2005. Uranyl adsorption onto montmorillonite: Evaluation of binding sites and carbonate complexation. Geochim. Cosmochim. Acta 69, 2995–3005.

Catalano, J.G., Heald, S.M., Zachara, J.M., Brown, G.E., 2004. Spectroscopic and diffraction study of uranium speciation in contaminated vadose zone sediments from the Hanford site, Washington State. Environ. Sci. Technol. 38, 2822–2828.

Catalano, J.G., McKinley, J.P., Zachara, J.M., Heald, S.M., Smith, S.C., Brown, G.E., 2006. Changes in uranium speciation through a depth sequence of contaminated Hanford sediments. Environ. Sci. Technol. 40, 2517–2524.

Choppin, G., Liljenzin, J.-O., Rydberg, J., Ekberg, C., 2002. Behavior of Radionuclides in the Environment. In: Radiochemistry and Nuclear Chemistry. Elsevier, pp. 753–788.

Clark, D.L., Hobart, D.E., Neu, M.P., 1995. Actinide Carbonate Complexes and Their Importance in Actinide Environmental Chemistry. Chem. Rev. 95, 25–48.

Cleary, A., Lloyd, J.R., Newsome, L., Shaw, S., Boothman, C., Boshoff, G., Atherton, N., Morris, K., 2019. Bioremediation of strontium and technetium contaminated groundwater using glycerol phosphate. Chem. Geol. 509, 213–222.

Cobos, D., Chambers, C., 2010. Calibrating ECH2O Soil Moisture Sensors.

Coker, V.S., Pearce, C.I., Lang, C., van der Laan, G., Pattrick, R.A.D., Telling, N.D., Schüler, D., Arenholz, E., Lloyd, J.R., 2007. Cation site occupancy of biogenic magnetite compared to polygenic ferrite spinels determined by X-ray magnetic circular dichroism. Eur. J. Mineral. 19, 707–716.

Coker, V.S., van der Laan, G., Telling, N.D., Lloyd, J.R., Byrne, J.M., Arenholz, E., Pattrick, R.A., 2020. Bacterial production of vanadium ferrite spinel $(Fe,V)_3O_4$ nanoparticles . Mineral. Mag. 84, 554–562.

Collins, R.N., Rosso, K.M., 2017. Mechanisms and Rates of U(VI) Reduction by Fe(II) in Homogeneous Aqueous Solution and the Role of U(V) Disproportionation. J. Phys. Chem. A 121, 6603–6613.

Conradson, S.D., Manara, D., Wastin, F., Clark, D.L., Lander, G.H., Morales, L.A., Rebizant, J., Rondinella, V. V., 2004. Local structure and charge distribution in the UO_2-U_4O_9 system. Inorg. Chem. 43, 6922–6935.

Corkhill, C., Hyatt, N., 2018. Nuclear Waste Management. IOP Publishing.

Cornell, R.M., Schwertmann, U., 2003a. Chapter 1: Introduction to the Iron Oxides. In: The Iron Oxides: Structure, Properties, Reactions, Occurences and Uses. Wiley, pp. 1–7.

Cornell, R.M., Schwertmann, U., 2003b. The Iron Oxides, The Iron Oxides: Structure, Properties, Reactions, Occurences and Uses. Wiley.

Cornell, R.M., Schwertmann, U., 2003c. Chapter 13: Formation. In: The Iron Oxides: Structure, Properties, Reactions, Occurences and Uses. Wiley, pp. 345–364.

Cornell, R.M., Schwertmann, U., 2003d. Chapter 2: Crystal Structure. In: The Iron Oxides: Structure, Properties, Reactions, Occurences and Uses. Wiley, pp. 9–38.

Cornell, R.M., Schwertmann, U., 2003e. Chapter 10: Surface Chemistry and Colloidal Stability. In: The Iron Oxides: Structure, Properties, Reactions, Occurences and Uses. Wiley, pp. 221–252.

Cornell, R.M., Schwertmann, U., 2003f. Chapter 11: Adsorption of Ions and Molecules. In: The Iron Oxides: Structure, Properties, Reactions, Occurences and Uses. Wiley, pp. 253–296.

Cowie, B.E., Purkis, J.M., Austin, J., Love, J.B., Arnold, P.L., 2019. Thermal and Photochemical Reduction and Functionalization Chemistry of the Uranyl Dication, $[U(VI)O_2]^{2+}$. Chem. Rev. 119, 10595–10637.

Craft, E.S., Abu-Qare, A.W., Flaherty, M.M., Garofolo, M.C., Rincavage, H.L., Abou-Donia, M.B., 2004. Depleted and natural uranium: Chemistry and toxicological effects. J. Toxicol. Environ. Heal. - Part B Crit. Rev. 7, 297–317.

Crawford, S.E., Lofts, S., Liber, K., 2017. The role of sediment properties and solution pH in the adsorption of uranium(VI) to freshwater sediments. Environ. Pollut. 220, 873–881.

Crossland, I.G., 2011. Development and use of metal containers for the disposal of radioactive wastes. In: Ojovan, M.I. (Ed.), Handbook of Advanced Radioactive Waste Conditioning Technologies. Woodhead Publishing Limited, pp. 363–394.

Croudace, I.W., Rothwell, R.G., 2015. ItraxPlot: An Intuitive flexible program for rapidly visualising Itrax data. In: Croudace, I.W., Rothwell, R.G. (Eds.), Micro-XRF Studies of Sediment Cores (Developments in Paleoenvironmental Research). Springer, Dordrecht.

Cruickshank, J., 2012. The Sellafield Contaminated Land and Groundwater Management Project: Characterisation of a Complex Nuclear Facility. In: Workshop on 'Radiological Characterisation for Decommissioning'. p. 37.

Cullity, B.D., Stock, S.R., 2001. Elements of X-Ray Diffraction, Third Edit. ed. Prentice-Hall, New York.

Cumberland, S.A., Douglas, G., Grice, K., Moreau, J.W., 2016. Uranium mobility in organic matter-rich sediments: A review of geological and geochemical processes. Earth-Science Rev. 159, 160–185.

Davis, C.E., Janecek, L.L., 1997. DOE Research Set-Aside Areas of the Savannah River Site: SRO-NERP-25. Aiken, SC.

Davis, S., 2005. Electron Microscopy. In: Colloid Science. John Wiley & Sons, Ltd, pp. 266–282.

De Sanctis, E., Monti, S., Ripani, M., 2016a. Chapter 3: Nuclear Reactions and Fission. In: Energy from Nuclear Fission. Springer, Switzerland, pp. 89–143.

De Sanctis, E., Monti, S., Ripani, M., 2016b. Chapter 4: Nuclear Reactors. In: Energy from Nuclear Fission. Springer, Switzerland, pp. 147–187.

Deacon, D., Hudson, R., 2012. Chapter 36: Corrosion and Corrosion Prevention. In: Steel Designers' Manual: The Steel Construction Institute. John Wiley & Sons, pp. 1088–1109.

DECC, 2014. Implementing Geological Disposal.

DECC, 2015. Lead Document setting out the United Kingdom's National Programme for the Responsible and Safe Management of Spent Fuel and Radioactive Waste, URN 15D/389.

DECC, 2016. UK Strategy for the Management of Solid Low Level Radioactive Waste from the Nuclear Industry.

Demirkanli, D.I., Molz, F.J., Kaplan, D.I., Fjeld, R.A., 2008. A Fully Transient Model for Long-Term Plutonium Transport in the Savannah River Site Vadose Zone: Root Water Uptake. Vadose Zo. J. 7, 1099–1109.

Demirkanli, D.I., Molz, F.J., Kaplan, D.I., Fjeld, R.A., Serkiz, S.M., 2007. Modeling Long-Term Plutonium Transport in the Savannah River Site Vadose Zone. Vadose Zo. J. 6, 344–353.

Dent, A.J., Cibin, G., Ramos, S., Smith, A.D., Scott, S.M., Varandas, L., Pearson, M.R., Krumpa, N.A., Jones, C.P., Robbins, P.E., 2009. B18: A core XAS spectroscopy beamline for Diamond. J. Phys. Conf. Ser. 190.

Dewey, C., Sokaras, D., Kroll, T., Bargar, J.R., Fendorf, S., 2020. Calcium-Uranyl-Carbonato Species Kinetically Limit U(VI) Reduction by Fe(II) and Lead to U(V)-Bearing Ferrihydrite. Environ. Sci. Technol. 54, 6021–6030.

Diaz-Moreno, S., Hayama, S., Amboage, M., Freeman, A., Sutter, J., Duller, G., 2009. I20; The Versatile X-ray Absorption spectroscopy beamline at Diamond Light Source. J. Phys. Conf. Ser. 190.

Ding, W., Botha, J.A., Hanson, B.C., Burke, I.T., 2016. Aqueous hydroxylation mediated synthesis of crystalline calcium uranate particles. J. Alloys Compd. 688, 260–269.

Docrat, T.I., Mosselmans, J.F.W., Charnock, J.M., Whiteley, M.W., Collison, D., Livens, F.R., Jones, C., Edmiston, M.J., 1999. X-ray absorption spectroscopy of tricarbonatodioxouranate(V), [UO2(CO3)3]5-, in aqueous solution. Inorg. Chem. 38, 1879–1882.

Dodge, C.J., Francis, A.J., Gillow, J.B., Halada, G.P., Eng, C., Clayton, C.R., 2002. Association of uranium with iron oxides typically formed on corroding steel surfaces. Environ. Sci. Technol. 36, 3504–3511.

Dong, W., Tokunaga, T.K., Davis, J.A., Wan, J., 2012. Uranium(VI) Adsorption and Surface Complexation Modeling onto Background Sediments from the F-Area Savannah River Site. Environ. Sci. Technol. 46, 1565–1571.

Doornbusch, B., Bunney, K., Gan, B.K., Jones, F., Gräfe, M., 2015. Iron oxide formation from FeCl2 solutions in the presence of uranyl (UO_2^{2+}) cations and carbonate rich media. Geochim. Cosmochim. Acta 158, 22–47.

Dounreay, 2021. Dounreay 2021: A guide to Scotland's centre of excellence in nuclear decommissioning.

Downward, L., Booth, C.H., Lukens, W.W., Bridges, F., 2007. A variation of the F-test for determining statistical relevance of particular parameters in EXAFS fits. AIP Conf. Proc. 882, 129–131.

Duff, M.C., Amrhein, C., 1996. Uranium(VI) Adsorption on Goethite and Soil in Carbonate Solutions. Soil Sci. Soc. Am. J. 60, 1393–1400.

Duff, M.C., Coughlin, J.U., Hunter, D.B., 2002. Uranium co-precipitation with iron oxide minerals. Geochim. Cosmochim. Acta 66, 3533–3547.

Duro, L., Domènech, C., Grivé, M., Roman-Ross, G., Bruno, J., Källström, K., 2014. Assessment of the evolution of the redox conditions in a low and intermediate level nuclear waste repository (SFR1, Sweden). Appl. Geochemistry 49, 192–205.

Dzombak, D.A., Morel, F.M., 1990. Surface complexation modelling: hydrous ferric oxide. Wiley, New York.

El Aamrani, F., Casas, I., de Pablo, J., 1999. Experimental and modeling study of the interaction between Uranium (VI) and magnetite. SKB Tech. Rep. TR-99-21.

Environment Agency, 2002. Proposed decision for the future regulation of disposals of radioactive waste from British Nuclear Fuels plc Sellafield. Warrington.

Environment Agency, 2020. Draft decision document: Sellafield Ltd and Sellafield site. Environmental Permitting: radioactive substances activities.

Environment Agency, Natural Resources Wales, 2010. The decommissioning of nuclear facilities.

Environment Agency, Northern Ireland Environment Agency, SEPA, 2009. Near-surface Disposal Facilities on Land for Solid Radioactive Wastes: Guidance on Requirements for Authorisation.

Evans, A.G., Bauer, L.R., Haselow, J.S., Hayes, D.W., Martin, H.L., McDowell, W.L., Pickett, J.B., 1992. Uranium in the Savannah River Site environment. Aiken, SC.

Evans, N.D.M., 2008. Binding mechanisms of radionuclides to cement. Cem. Concr. Res. 38, 543–553.

Evrard, O., Laceby, J.P., Nakao, A., 2019. Effectiveness of landscape decontamination following the Fukushima nuclear accident: a review. SOIL 5, 333–350.

Felipe-Sotelo, M., Hinchliff, J., Field, L.P., Milodowski, A.E., Preedy, O., Read, D., 2017. Retardation of uranium and thorium by a cementitious backfill developed for radioactive waste disposal. Chemosphere 179, 127–138.

Finch, R.J., Ewing, R.C., 1992. The corrosion of uraninite under oxidizing conditions. J. Nucl. Mater. 190, 133–156.

Flach, G.P., 1994. Mixed waste management facility (MWMF) old burial ground (OBG) source control technology and inventory study, Q-ESR-E-00001.

Fleet, M.E., 1981. The structure of magnetite. Acta Crystallogr. Sect. B Struct. Crystallogr. Cryst. Chem. 37, 917–920.

Gaona, X., Dähn, R., Tits, J., Scheinost, A.C., Wieland, E., 2011. Uptake of Np(IV) by C-S-H phases and cement paste: An EXAFS study. Environ. Sci. Technol. 45, 8765–8771.

Gaona, X., Kulik, D.A., Macé, N., Wieland, E., 2012. Aqueous-solid solution thermodynamic model of U(VI) uptake in C-S-H phases. Appl. Geochemistry 27, 81–95.

Giammar, D.E., Hering, J.G., 2001. Time scales for sorption - Desorption and surface precipitation of uranyl on goethite. Environ. Sci. Technol. 35, 3332–3337.

Glatzel, P., Bergmann, U., 2005. High resolution 1s core hole X-ray spectroscopy in 3d transition metal complexes - Electronic and structural information. Coord. Chem. Rev. 249, 65–95.

Golovich, E.C., Wellman, D.M., Serne, R.J., Bovaird, C.C., 2011. Summary of Uranium Solubility Studies in Concrete Waste Forms and Vadose Zone Environments. Richland, WA.

Gómez, P., Garralón, A., Buil, B., Turrero, M.J., Sánchez, L., de la Cruz, B., 2006. Modeling of geochemical processes related to uranium mobilization in the groundwater of a uranium mine. Sci. Total Environ. 366, 295–309.

Gorman-Lewis, D., Burns, P.C., Fein, J.B., 2008. Review of uranyl mineral solubility measurements. J. Chem. Thermodyn. 40, 335–352.

Gorski, C.A., Scherer, M.M., 2010. Determination of nanoparticulate magnetite stoichiometry by Mossbauer spectroscopy, acidic dissolution, and powder X-ray diffraction: A critical review. Am. Mineral. 95, 1017–1026.

Gray, J., Jones, S.R., Smith, A.D., 1995. Discharges to the environment from the Sellafield site, 1951-1992. J. Radiol. Prot. 15, 99–131.

Gurban, I., Laaksoharju, M., Madé, B., Ledoux, E., 2003. Uranium transport around the reactor zone at Bangombé and Okélobondo (Oklo): Examples of hydrogeological and geochemical model integration and data evaluation. J. Contam. Hydrol. 61, 247–264.

Harfouche, M., Wieland, E., Dähn, R., Fujita, T., Tits, J., Kunz, D., Tsukamoto, M., 2006. EXAFS study of U(VI) uptake by calcium silicate hydrates. J. Colloid Interface Sci. 303, 195–204.

He, Y.T., Traina, S.J., 2007. Transformation of magnetite to goethite under alkaline pH conditions. Clay Miner. 42, 13–19.

Heal, H.G., Thomas, J.G.N., 1949. Unstable ions of quinquavalent uranium. Trans. Faraday Soc. 45, 11–20.

Henkel, S., Kasten, S., Poulton, S.W., Staubwasser, M., 2016. Determination of the stable iron isotopic composition of sequentially leached iron phases in marine sediments. Chem. Geol. 421, 93–102.

Hewlett, P.C., Lea, F., 1998. Lea's Chemistry of Cement and Concrete, 4th ed. Arnold, London.

Hsi, C.D., Langmuir, D., 1985. Adsorption of uranyl onto ferric oxyhydroxides: Application of the surface complexation site-binding model. Geochim. Cosmochim. Acta 49, 1931–1941.

Huber, F., Schild, D., Vitova, T., Rothe, J., Kirsch, R., Schäfer, T., 2012. U(VI) removal kinetics in presence of synthetic magnetite nanoparticles. Geochim. Cosmochim. Acta 96, 154–173.

IAEA, 1989. Cleanup of Large Areas Contaminated as a Result of a Nuclear Accident, TECHNICAL REPORTS SERIES No. 300.

IAEA, 1996. Significant Incidents in Nuclear Fuel Cycle Facilities, IAEA-TECDOC-867. Vienna.

IAEA, 1997. Technologies for in situ immobilization and isolation of radioactive wastes at disposal and contaminated sites, IAEA-TECDOC-972. Vienna.

IAEA, 1999. On-site disposal as a decommissioning strategy, IAEA-TECDOC-1124. Vienna.

IAEA, 2004. The long term stabilization of uranium mill tailings, IAEA-TECDOC-1403. Vienna.

IAEA, 2008. Spent Fuel Reprocessing Options, IAEA-TECDOC-1587. Vienna.

IAEA, 2009. IAEA Safety Standards: Classification of Radioactive Waste - No. GSG-1, General Safety Guide IAEA. Vienna.

IAEA, 2017. Nuclear Power Reactors in the World. Reference Data Series No. 2. Vienna.

IAEA, 2019. Events and highlights on the progress related to recovery operations at Fukushima Daiichi Nuclear Power Station.

Ikeda, A., Hennig, C., Tsushima, S., Takao, K., Ikeda, Y., Scheinost, A.C., Bernhard, G., 2007. Comparative study of uranyl(VI) and -(V) carbonato complexes in an aqueous solution. Inorg. Chem. 46, 4212–4219.

Ilton, E.S., Boily, J.-F., Buck, E.C., Skomurski, F.N., Rosso, K.M., Cahill, C.L., Bargar, J.R., Felmy, A.R., 2010. Influence of Dynamical Conditions on the Reduction of UVI at the Magnetite - Solution Interface. Environ. Sci. Technol. 44, 170–176.

Ilton, E.S., Haiduc, A., Moses, C.O., Heald, S.M., Elbert, D.C., Veblen, D.R., 2004. Heterogeneous reduction of uranyl by micas: Crystal chemical and solution controls. Geochim. Cosmochim. Acta 68, 2417–2435.

Ilton, E.S., Pacheco, J.S.L., Bargar, J.R., Shi, Z., Liu, J., Kovarik, L., Engelhard, M.H., Felmy, A.R., 2012. Reduction of U(VI) incorporated in the structure of hematite. Environ. Sci. Technol. 46, 9428–9436.

Jilbert, T., de Lange, G., Reichart, G.J., 2008. Fluid displacive resin embedding of laminated sediments: Preserving trace metals for high-resolution paleoclimate investigations. Limnol. Oceanogr. Methods 6, 16–22.

Jones, D.L., Andrews, M.B., Swinburne, A.N., Botchway, S.W., Ward, A.D., Lloyd, J.R., Natrajan, L.S., 2015. Fluorescence spectroscopy and microscopy as tools for monitoring redox transformations of uranium in biological systems. Chem. Sci. 6, 5133–5138.

Joshi, N., Filip, J., Coker, V.S., Sadhukhan, J., Safarik, I., Bagshaw, H., Lloyd, J.R., 2018. Microbial reduction of Natural Fe(III) minerals; Toward the sustainable production of functional magnetic nanoparticles. Front. Environ. Sci. 6, 1–11.

Jove Colon, C.F., Brady, P. V., Siegel, M.D., Lindgren, E.R., 2001. Historical Case Analysis of Uranium Plume Attenuation. Soil Sediment Contam. An Int. J. 10, 71–115.

Kalmykov, S.N., Choppin, G.R., 2000. Mixed $Ca^{2+}/UO_2^{2+}/CO_3^{2-}$ complex formation at different ionic strengths. Radiochim. Acta 88, 603–606.

Kaminski, M.D., Dimitrijevic, N.M., Mertz, C.J., Goldberg, M.M., 2005. Colloids from the aqueous corrosion of uranium nuclear fuel. J. Nucl. Mater. 347, 77–87.

Kaplan, D.I., Bertsch, P.M., Adriano, D.C., Orlandini, K.A., 1994a. Actinide Association with Groundwater Colloids in a Coastal Plain Aquifer. Radiochim. Acta 66–67, 181–188.

Kaplan, D.I., Demirkanli, D.I., Gumapas, L., Powell, B.A., Fjeld, R.A., Molz, F.J., Serkiz, S.M., 2006. Eleven-year field study of Pu migration from Pu III, IV, and VI sources. Environ. Sci. Technol. 40, 443–448.

Kaplan, D.I., Gervais, T.L., Krupka, K.M., 1998. Uranium(VI) Sorption to Sediments under High pH and Ionic Strength Conditions. Radiochim. Acta 80, 201–211.

Kaplan, D.I., Hunter, D.B., Bertsch, P.M., Bajt, S., Adriano, D.C., 1994b. Application of Synchrotron X-ray Fluorescence Spectroscopy and Energy Dispersive X-ray Analysis To Identify Contaminant Metals on Groundwater Colloids. Environ. Sci. Technol. 28, 1186–1189.

Kaplan, D.I., Kukkadapu, R., Seaman, J.C., Arey, B.W., Dohnalkova, A.C., Buettner, S., Li, D., Varga, T., Scheckel, K.G., Jaffé, P.R., 2016. Iron mineralogy and uranium-binding environment in the rhizosphere of a wetland soil. Sci. Total Environ. 569–570, 53–64.

Kaplan, D.I., Miller, T.J., Diprete, D., Powell, B.A., 2014. Long-term radiostrontium interactions and transport through sediment. Environ. Sci. Technol. 48, 8919–8925.

Kaplan, D.I., Serkiz, S.M., 2001. Quantification of thorium and uranium sorption to contaminated sediments. J. Radioanal. Nucl. Chem. 248, 529–535.

Kaplan, D.I., Smith, R., Parker, C.J., Baker, M., Cabrera, T., Ferguson, B.O., Kemner, K.M., Laird, M., Logan, C., Lott, J., Manglass, L., Martinez, N.E., Montgomery, D., Seaman, J.C., Shapiro, M., Powell, B.A., 2020. Uranium Attenuated by a Wetland 50 Years after Release into a Stream. ACS Earth Sp. Chem. 4, 1360–1366.

Keith-Roach, M.J., Morris, K., Dahlgaard, H., 2003. An investigation into technetium binding in sediments. Mar. Chem. 81, 149–162.

Kerisit, S., Bylaska, E.J., Massey, M.S., McBriarty, M.E., Ilton, E.S., 2016. Ab initio molecular dynamics of uranium incorporated in goethite (α-FeOOH): Interpretation of X-ray absorption spectroscopy of trace polyvalent metals. Inorg. Chem. 55, 11736–11746.

Kerisit, S., Felmy, A.R., Ilton, E.S., 2011. Atomistic Simulations of Uranium Incorporation into Iron (Hydr)Oxides. Environ. Sci. Technol. 45, 2770–2776.

Kershaw, P.J., Pentreath, R.J., Woodhead, D.S., Hunt, G.J., 1992. A review of radioactivity in the Irish Sea, Aquatic Environment Monitoring Report, MAFF Directorate of Fisheries Research. Lowestoft.

Kilgo, M.K., 2018. Environmental Impact Predictions for Disposal of Emerging Energy Technologies in Solid Waste Landfills: Application to Lithium Ion Batteries and Photovoltaic Modules 1–2409.

King, R.B., 2002. Some aspects of structure and bonding in binary and ternary uranium(VI) oxides. Chem. Mater. 14, 3628–3635.

Kiyama, M., 1974. Conditions for the Formation of Fe_3O_4 by the Air Oxidation of $Fe(OH)_2$ Suspensions. Bull. Chem. Soc. Jpn. 47, 1646–1650.

Koningsberger, D.C., Mojet, B.L., Van Dorssen, G.E., Ramaker, D.E., 2000. XAFS spectroscopy; fundamental principles and data analysis. Top. Catal. 10, 143–155.

Koťátková, J., Zatloukal, J., Reiterman, P., Kolář, K., 2017. Concrete and cement composites used for radioactive waste deposition. J. Environ. Radioact. 178–179, 147–155.

Kowalska, J.K., Nayyar, B., Rees, J.A., Schiewer, C.E., Lee, S.C., Kovacs, J.A., Meyer, F., Weyhermüller, T., Otero, E., Debeer, S., 2017. Iron $L_{2,3}$-Edge X-ray Absorption and X-ray Magnetic Circular Dichroism Studies of Molecular Iron Complexes with Relevance to the FeMoco and FeVco Active Sites of Nitrogenase. Inorg. Chem. 56, 8147–8158.

Kremleva, A., Krüger, S., Rösch, N., 2020. Uranyl(VI) sorption in calcium silicate hydrate phases. A quantum chemical study of tobermorite models. Appl. Geochemistry 113.

Krestou, C.A., Panias, D., 2004. Uranium (VI) speciation diagrams in the $UO_2^{2+}/CO_3^{2-}/H_2O$ system at 25. Eur. J. Miner. Process. Environ. Prot. 4, 1303–868.

Kuras, O., Wilkinson, P.B., Meldrum, P.I., Oxby, L.S., Uhlemann, S., Chambers, J.E., Binley, A., Graham, J., Smith, N.T., Atherton, N., 2016. Geoelectrical monitoring of simulated subsurface leakage to support high-hazard nuclear decommissioning at the Sellafield Site, UK. Sci. Total Environ. 566–567, 350–359.

Kurdowski, W., 2014. Cement and concrete chemistry, Cement and Concrete Chemistry.

Kvashnina, K.O., Butorin, S.M., Martin, P., Glatzel, P., 2013. Chemical state of complex uranium oxides. Phys. Rev. Lett. 111.

Lagha, S. Ben, Crusset, D., Mabille, I., Tran, M., Bernard, M.C., Sutter, E., 2007. Corrosion of iron: A study for radioactive waste canisters. J. Nucl. Mater. 362, 485–492.

Langmuir, D., 1997. Aqueous Environmental Geochemistry. Prentice Hall.

Latta, D.E., Gorski, C.A., Boyanov, M.I., O'Loughlin, E.J., Kemner, K.M., Scherer, M.M., 2012. Influence of magnetite stoichiometry on U VI reduction. Environ. Sci. Technol. 46, 778–786.

Latta, D.E., Mishra, B., Cook, R.E., Kemner, K.M., Boyanov, M.I., 2014. Stable U(IV) complexes form at high-affinity mineral surface sites. Environ. Sci. Technol. 48, 1683–1691.

Law, G.T.W., Geissler, A., Burke, I.T., Livens, F.R., Lloyd, J.R., McBeth, J.M., Morris, K., 2011. Uranium redox cycling in sediment and biomineral systems. Geomicrobiol. J. 28, 497–506.

Leonard, K.S., McCubbin, D., Lovett, M.B., 1995. Physico-chemical characterisation of radionuclides discharged from a nuclear establishment. Sci. Total Environ. 175, 9–24.

Li, D., Kaplan, D., 2012. Literature Review on the Sorption of Plutonium, Uranium, Neptunium, Americium and Technetium To Corrosion Products on Waste Tank Liners. SRNL-STI-2012-00040.

Li, D., Kaplan, D.I., Chang, H., Seaman, J.C., Jaffé, P.R., Koster van Groos, P., Scheckel, K.G., Segre, C.U., Chen, N., Jiang, D., Newville, M., Lanzirotti, A., 2015. Spectroscopic Evidence of Uranium Immobilization in Acidic Wetlands by Natural Organic Matter and Plant Roots. Environ. Sci. Technol. 49, 2823–2832.

Li, G.G., Bridges, F., Booth, C.H., 1995. X-ray-absorption fine-structure standards: A comparison of experiment and theory. Phys. Rev. B 52.

Linsley, G., 2012. 2 - Radiological protection and the nuclear fuel cycle. In: Nuclear Fuel Cycle Science and Engineering. Woodhead Publishing Limited, Oxford, pp. 24–51.

Livens, F.R., Baxter, M.S., 1988. Chemical associations of artificial radionuclides in Cumbrian soils. J. Environ. Radioact. 7, 75–86.

LLW Repository Ltd, 2018. LLWR Plan 2018-2023. Seascale.

LLW Repository Ltd, Sellafield Ltd, 2019. Sellafield Ltd and LLW Repository Ltd Joint Waste Management Plan, LLWSSG(11)12.

Looney, B.B., Cantrell, J.E., Cook, J.R., 1988. Sampling and analysis of surface water in the vicinity

if the F- and H- area seepage basins, DPST-88-229. Aiken, SC.

Lovley, D.R., Phillips, E.J.P., Gorby, Y.A., Landa, E.R., 1991. Microbial reduction of uranium. Nature 350, 413–416.

Löwemark, L., Bloemsma, M., Croudace, I., Daly, J.S., Edwards, R.J., Francus, P., Galloway, J.M., Gregory, B.R.B., Huang, J.S., Jones, A.F., Kylander, M., Löwemark, L., Luo, Y., Maclachlan, S., Ohlendorf, C., Patterson, R.T., Pearce, C., Profe, J., Reinhardt, E.G., Stranne, C., Tjallingii, R., Turner, J.N., 2019. Practical guidelines and recent advances in the Itrax XRF core-scanning procedure. Quat. Int. 514, 16–29.

Macé, N., Wieland, E., Dähn, R., Tits, J., Scheinost, A.C., 2013. EXAFS investigation on U(VI) immobilization in hardened cement paste: Influence of experimental conditions on speciation. Radiochim. Acta 101, 379–389.

Madic, C., Hobart, D.E., Begun, G.M., 1983. Raman Spectrometric Studies of Actinide(V) and (VI) Complexes in Aqueous Sodium Carbonate Solution and of Solid Sodium Actinide(V) Carbonate Compounds. Inorg. Chem. 22, 1494–1503.

Magnox Ltd, Sellafield Ltd, NDA, 2019. News story: Last nuclear fuel flask leaves Wylfa [Website]. URL https://www.gov.uk/government/news/last-nuclear-fuel-flask-leaves-wylfa (accessed 6.30.21).

Maher, K., Bargar, J.R., Brown, G.E., 2013. Environmental speciation of actinides. Inorg. Chem. 52, 3510–3532.

Mandaliev, P., Dähn, R., Wehrli, B., Wieland, E., 2009. Macro- and microspectroscopic study of Nd (III) uptake mechanisms in hardened cement paste. Environ. Sci. Technol. 43, 8462–8468.

Marshall, A., Coughlin, D., Laws, F., McKenzie, H., Cruickshank, J., 2015. Groundwater monitoring at Sellafield annual data review 2014.

Marshall, T.A., Morris, K., Law, G.T.W., Livens, F.R., Mosselmans, J.F.W., Bots, P., Shaw, S., 2014a. Incorporation of uranium into hematite during crystallization from ferrihydrite. Environ. Sci. Technol. 48, 3724–3731.

Marshall, T.A., Morris, K., Law, G.T.W., Mosselmans, J.F.W., Bots, P., Parry, S.A., Shaw, S., 2014b. Incorporation and retention of 99-Tc(IV) in magnetite under high pH conditions. Environ. Sci. Technol. 48, 11853–11862.

Marshall, T.A., Morris, K., Law, G.T.W., W. Mosselmans, J.F., Bots, P., Roberts, H., Shaw, S., 2015. Uranium fate during crystallization of magnetite from ferrihydrite in conditions relevant to the disposal of radioactive waste. Mineral. Mag. 79, 1265–1274.

Massey, M.S., Lezama-pacheco, J.S., Jones, M.E., Cerrato, M., Bargar, J.R., Fendorf, S., Ilton, E.S., 2014. Competing retention pathways of uranium upon reaction with Fe(II). Geochim. Cosmochim. Acta 142, 166–185.

McBriarty, M.E., Kerisit, S., Bylaska, E.J., Shaw, S., Morris, K., Ilton, E.S., 2018. Iron Vacancies Accommodate Uranyl Incorporation into Hematite. Environ. Sci. Technol. 52, 6282–6290.

McBriarty, M.E., Soltis, J.A., Kerisit, S., Qafoku, O., Bowden, M.E., Bylaska, E.J., De Yoreo, J.J., Ilton, E.S., 2017. Trace Uranium Partitioning in a Multiphase Nano-FeOOH System. Environ. Sci. Technol. 51, 4970–4977.

McGill, I.R., McEnaney, B., Smith, D.C., 1976. Crystal structure of green rust formed by corrosion of cast iron. Nature 13, 258–283.

Mei, H., Tan, X., Tan, L., Meng, Y., Chen, C., Fang, M., Wang, X., 2018. Retention of U(VI) by the Formation of Fe Precipitates from Oxidation of Fe(II). ACS Earth Sp. Chem. 2, 968–976.

Mihalík, J., Tlustoš, P., Szaková, J., 2011. The impact of an abandoned uranium mining area on the contamination of agricultural land in its surroundings. Water. Air. Soil Pollut. 215, 693–700.

Miller, T.J., Kaplan, D.I., Powell, B.A., 2012. Laboratory and lysimeter experimentation and transport modeling of neptunium and strontium in Savannah River Site sediments, SRNL-STI-2012-00052. Aiken, SC.

Missana, T., García-Gutiérrez, M., Fernńdez, V., 2003a. Uranium (VI) sorption on colloidal magnetite under anoxic environment: Experimental study and surface complexation modelling. Geochim. Cosmochim. Acta 67, 2543–2550.

Missana, T., García-Gutiérrez, M., Maffiotte, C., 2003b. Experimental and modeling study of the uranium (VI) sorption on goethite. J. Colloid Interface Sci. 260, 291–301.

Missana, T., Maffiotte, C., García-Gutiérrez, M., 2003c. Surface reactions kinetics between nanocrystalline magnetite and uranyl. J. Colloid Interface Sci. 261, 154–160.

MoD, 2013. UK depleted uranium (DU) munitions policy and development.

Montgomery, D., Barber, K., Edayilam, N., Oqujiuba, K., Young, S., Biotidara, T., Gathers, A., Danjaji, M., Tharayil, N., Martinez, N., Powell, B., 2017. The influence of citrate and oxalate on 99TcVII, Cs, NpV and UVI sorption to a Savannah River Site soil. J. Environ. Radioact. 172, 130–142.

Moroni, L.P., Glasser, F.P., 1995. Reactions between cement components and U(VI) oxide. Waste Manag. 15, 243–254.

Morris, K., Butterworth, J.C., Livens, F.R., 2000. Evidence for the remobilization of Sellafield waste radionuclides in an intertidal salt marsh, West Cumbria, U.K. Estuar. Coast. Shelf Sci. 51, 613–625.

Moyes, L.N., Parkman, R.H., Charnock, J.M., Vaughan, D.J., Livens, F.R., Hughes, C.R., Braithwaite, A., 2000. Uranium uptake from aqueous solution by interaction with goethite, lepidocrocite, muscovite, and Mackinawite: An x-ray absorption spectroscopy study. Environ. Sci. Technol. 34, 1062–1068.

Mühr-Ebert, E.L., Wagner, F., Walther, C., 2019. Speciation of uranium: Compilation of a thermodynamic database and its experimental evaluation using different analytical techniques. Appl. Geochemistry 100, 213–222.

Murray, R.L., 2000. Nuclear Reactor Types. In: Kirk-Othmer Encyclopedia of Chemical Technology. John Wiley & Sons, Inc., Hoboken, NJ, USA.

Musić, S., Gotić, M., Popović, S., 1993. X-ray diffraction and Fourier transform-infrared analysis of the rust formed by corrosion of steel in aqueous solutions. J. Mater. Sci. 28, 5744–5752.

Musić, S., Ristić, M., 1988. Adsorption of trace elements or radionuclides on hydrous iron oxides. J. Radioanal. Nucl. Chem. Artic.

National Research Council, 1999. Groundwater and Soil Cleanup: Improving Management of Persistent Contaminants. The National Academies Press, Washington, D.C.

NDA, 2013. Geological Disposal: Overview of international siting processes.

NDA, 2014a. Geological Disposal: A review of the Development of Bentonite Barriers in the KBS-3V Disposal Concept. Didcot.

NDA, 2014b. FACTSHEET : Decommissioning of nuclear power facilities [Website]. URL http://ukinventory.nda.gov.uk/wp-content/uploads/sites/2/2014/01/Fact-sheet-decommissioning-of-nuclear-power-facilities.pdf (accessed 6.29.21).

NDA, 2016a. Review of NDA's Technology Baseline and Underpinning Research and Development Process.

NDA, 2016b. Strategy - effective from April 2016.

NDA, 2019. Integrated Waste Management Radioactive Waste Strategy.

NDA, 2021. Strategy Effective from March 2021.

NDA, BEIS, 2019a. 2019 UK Radioactive Waste Detailed Data.

NDA, BEIS, 2019b. 2019 UK Radioactive Waste Inventory.

NDA, BEIS, 2019c. 2019 UK Radioactive Material Inventory.

NEA/IAEA, 2021. Uranium 2020: Resources, Production and Demand, Uranium. OECD Publishing, Paris.

Neeway, J.J., Kaplan, D.I., Bagwell, C.E., Rockhold, M.L., Szecsody, J.E., Truex, M.J., Qafoku, N.P., 2019. Science of the Total Environment A review of the behavior of radioiodine in the subsurface at two DOE sites. Sci. Total Environ. 691, 466–475.

Neill, T.S., Morris, K., Pearce, C.I., Abrahamsen-Mills, L., Kovarik, L., Kellet, S., Rigby, B., Vitova, T., Schacherl, B., Shaw, S., 2019. Silicate stabilisation of colloidal UO2 produced by uranium metal corrosion. J. Nucl. Mater. 526, 151751.

Newsome, L., Cleary, A., Morris, K., Lloyd, J.R., 2017. Long-Term Immobilization of Technetium via Bioremediation with Slow-Release Substrates. Environ. Sci. Technol. 51, 1595–1604.

Newsome, L., Morris, K., Lloyd, J.R., 2014. The biogeochemistry and bioremediation of uranium and other priority radionuclides. Chem. Geol. 363, 164–184.

Newville, M., 2014. Fundamentals of XAFS. Rev. Mineral. Geochemistry 78, 33–74.

Nexia Solutions, 2007. Review of the Development of UK High Level Waste Vitrified Product. Didcot.

Nico, P.S., Stewart, B.D., Fendorf, S., 2009. Incorporation of oxidized uranium into Fe (Hydr)oxides during Fe(II) catalyzed remineralization. Environ. Sci. Technol. 43, 7391–7396.

OECD, 2014. Site Remediation and Restoration during Decommissioning of Nuclear Installations. NEA No. 7192.

Office for Nuclear Regulation, Environment Agency, Scottish Environment Protection Agency, Natural Resources Wales, 2016. Disposal of radioactive waste on nuclear sites by deposit or burial 1–9.

Ojovan, M.I., Lee, W.E., Kalmykov, S.N., 2019. Immobilisation of Radioactive Waste in Cement. In: An Introduction to Nuclear Waste Immobilisation. Elsevier, pp. 271–303.

ONR, Environment Agency, 2017. Geological disposal of radioactive waste: Pre-application advice and scrutiny of Radioactive Waste Management Limited Annual Report.

Pan, Z., Bártová, B., LaGrange, T., Butorin, S.M., Hyatt, N.C., Stennett, M.C., Kvashnina, K.O., Bernier-Latmani, R., 2020. Nanoscale mechanism of UO_2 formation through uranium reduction by magnetite. Nat. Commun. 11, 1–12.

Parkhurst, D.L., Appelo, C.A.J., 2013. Description of input and examples for PHREEQC version 3: a computer program for speciation, batch-reaction, one-dimensional transport, and inverse geochemical calculations. In: U.S. Geological Survey Techniques and Methods, Book 6. p. 497.

Pattrick, R.A.D., Van Der Laan, G., Henderson, C.M.B., Kuiper, P., Dudzik, E., Vaughan, D.J., 2002. Cation site occupancy in spinel ferrites studied by X-ray magnetic circular dichroism: developing a method for mineralogists. Eur. J. Mineral. 14, 1095–1102.

Pearce, C.I., Henderson, C.M.B., Pattrick, R.A.D., van der Laan, G., Vaughan, D.J., 2006. Direct determination of cation site occupancies in natural ferrite spinels by $L_{2,3}$ X-ray absorption spectroscopy and X-ray magnetic circular dichroism. Am. Mineral. 91, 880–893.

Pearce, C.I., Qafoku, O., Liu, J., Arenholz, E., Heald, S.M., Kukkadapu, R.K., Gorski, C.A., Henderson, C.M.B., Rosso, K.M., 2012. Synthesis and properties of titanomagnetite (Fe_3-xTixO$_4$)

nanoparticles: A tunable solid-state Fe(II/III) redox system. J. Colloid Interface Sci. 387, 24–38.

Peruski, K.M., Maloubier, M., Kaplan, D.I., Almond, P.M., Powell, B.A., 2018. Mobility of Aqueous and Colloidal Neptunium Species in Field Lysimeter Experiments. Environ. Sci. Technol. 52, 1963–1970.

Petcharoen, K., Sirivat, A., 2012. Synthesis and characterization of magnetite nanoparticles via the chemical co-precipitation method. Mater. Sci. Eng. B Solid-State Mater. Adv. Technol. 177, 421–427.

Peterson, R.E., Rockhold, M.L., Serne, R.J., Thorne, P.D., Williams, M.D., 2008. Uranium Contamination in the Subsurface Beneath the 300 Area. Tech. Rep. 1–18.

Philipp, T., Shams Aldin Azzam, S., Rossberg, A., Huittinen, N., Schmeide, K., Stumpf, T., 2019. U(VI)sorption on Ca-bentonite at (hyper)alkaline conditions – Spectroscopic investigations of retention mechanisms. Sci. Total Environ. 676, 469–481.

Pidchenko, I., Heberling, F., Kvashnina, K.O., Finck, N., Schild, D., Bohnert, E., Schäfer, T., Rothe, J., Geckeis, H., Vitova, T., 2016. Aqueous U(VI) interaction with magnetite nanoparticles in a mixed flow reactor system: HR-XANES study. J. Phys. Conf. Ser. 712.

Pidchenko, I., Kvashnina, K.O., Yokosawa, T., Finck, N., Bahl, S., Schild, D., Polly, R., Bohnert, E., Rossberg, A., Göttlicher, J., Dardenne, K., Rothe, J., Schäfer, T., Geckeis, H., Vitova, T., 2017. Uranium Redox Transformations after U(VI) Coprecipitation with Magnetite Nanoparticles. Environ. Sci. Technol. 51, 2217–2225.

Podkovyrina, Y., Pidchenko, I., Prüßmann, T., Bahl, S., Göttlicher, J., Soldatov, A., Vitova, T., 2016. Probing Covalency in the UO_3 Polymorphs by U M4 edge HR- XANES. In: Journal of Physics: Conference Series. pp. 1–6.

Pointeau, I., Landesman, C., Giffaut, E., Reiller, P.E., Pointeau, I., Landesman, C., Giffaut, E., Reiller, P.E., 2004. Reproducibility of the uptake of U(VI) onto degraded cement pastes and calcium silicate hydrate phases. Radiochim. Acta 92, 645–650.

Pointeau, I., Piriou, B., Fedoroff, M., Barthes, M.G., Marmier, N., Fromage, F., 2001. Sorption mechanisms of Eu3+ on CSH phases of hydrated cements. J. Colloid Interface Sci. 236, 252–259.

Pöllänen, R., Ikäheimonen, T.K., Klemola, S., Juhanoja, J., 1999. Identification and analysis of a radioactive particle in a marine sediment sample. J. Environ. Radioact. 45, 149–160.

Portland Cement Association, 2017. How Cement Is Made [Website]. URL http://www.cement.org/cement-concrete-applications/how-cement-is-made (accessed 11.03.17).

Poulton, S.W., Canfield, D.E., 2005. Development of a sequential extraction procedure for iron: Implications for iron partitioning in continentally derived particulates. Chem. Geol. 214, 209–221.

Powell, B.A., Kaplan, D.I., Bagwell, L., Emerson, H.P., Roberts, K., Witmer, M., 2015. Actinide transport in the vadose zone: Observations from old and new lysimeter studies. In: The International Chemical Congress of Pacific Basin Studies.

Prado, Y., Daffé, N., Michel, A., Georgelin, T., Yaacoub, N., Grenèche, J.M., Choueikani, F., Otero, E., Ohresser, P., Arrio, M.A., Cartier-Dit-Moulin, C., Sainctavit, P., Fleury, B., Dupuis, V., Lisnard, L., Fresnais, J., 2015. Enhancing the magnetic anisotropy of maghemite nanoparticles via the surface coordination of molecular complexes. Nat. Commun. 6.

Prăvălie, R., 2014. Nuclear Weapons Tests and Environmental Consequences: A Global Perspective. Ambio 43, 729–744.

Ravel, B., Newville, M., 2005. ATHENA, ARTEMIS, HEPHAESTUS: Data analysis for X-ray absorption

spectroscopy using IFEFFIT. J. Synchrotron Radiat. 12, 537–541

Ray, D., Leary, P., Livens, F., Gray, N., Morris, K., Law, K.A., Fuller, A.J., Abrahamsen-Mills, L., Howe, J., Tierney, K., Muir, G., Law, G.T.W., 2020. Controls on anthropogenic radionuclide distribution in the Sellafield-impacted Eastern Irish Sea. Sci. Total Environ. 743, 140765.

Renshaw, J.C., Butchins, L.J.C., Livens, F.R., May, I., Charnock, J.M., Lloyd, J.R., 2005. Bioreduction of uranium: Environmental implications of a pentavalent intermediate. Environ. Sci. Technol. 39, 5657–5660.

Riley, R.G., Zachara, J.M., 1992. Chemical contaminants on DOE lands and selection of contaminant mixtures for subsurface science research. DOE/ER--0547T. Richland, WA.

Roberts, H.E., 2017. Fate of Uranium and Neptunium during Fe(II)/Fe(III) (oxyhydr)oxide formation.

Roberts, H.E., Morris, K., Law, G.T.W., Mosselmans, J.F.W., Bots, P., Kvashnina, K., Shaw, S., 2017. Uranium(V) Incorporation Mechanisms and Stability in Fe(II)/Fe(III) (oxyhydr)Oxides. Environ. Sci. Technol. Lett. 4, 421–426.

Roberts, H.E., Morris, K., Mosselmans, J.F.W., Law, G.T.W., Shaw, S., 2019. Neptunium reactivity during co-precipitation and oxidation of Fe(II)/Fe(III) (oxyhydr)oxides. Geosci. 9, 1–10.

Roberts, K.A., Kaplan, D.I., Bagwell, L., 2012. SRNL Radionuclide Field Lysimeter Experiment : Baseline Construction and Implementation. Aiken, SC.

Rossberg, A., Reich, T., Bernhard, G., 2003. Complexation of uranium(VI) with protocatechuic acid-application of iterative transformation factor analysis to EXAFS spectroscopy. Anal. Bioanal. Chem. 376, 631–638.

Rossberg, A., Ulrich, K.U., Weiss, S., Tsushima, S., Hiemstra, T., Scheinost, A.C., 2009. Identification of uranyl surface complexes on ferrihydrite: Advanced EXAFS data analysis and CD-music modeling. Environ. Sci. Technol. 43, 1400–1406.

RWM, 2016. Geological Disposal Generic Environmental Safety Case - Main Report. NDA Report DSSC/203/01.

RWM, 2021. RWM welcomes launch of second GDF 'Working Group' [Website]. URL https://www.gov.uk/government/news/rwm-welcomes-launch-of-second-gdf-working-group (accessed 12.05.21).

Savannah River Site, 2013. Virtual Tour [Website]. URL https://www.srs.gov/general/tour/online.htm (accessed 08.07.21).

Savannah River Site, 2020a. Savannah River Site Groundwater Management Strategy and Implementation Plan (U). Aiken, SC.

Savannah River Site, 2020b. An Overview of the Savannah River Site.

Savannah River Site, 2021a. SRS History Highlights [Website]. URL https://www.srs.gov/general/about/history1.htm (accessed 08.07.21).

Savannah River Site, 2021b. Factsheet: SRNL at a glance [Website]. URL https://www.srs.gov/general/news/facts.htm (accessed 08.07.21).

Schlegel, M.L., Pointeau, I., Coreau, N., Reiller, P., 2004. Mechanism of europium retention by calcium silicate hydrates: An EXAFS study. Environ. Sci. Technol. 38, 4423–4431.

Schnohr, C.S., Ridgway, M.C., 2015. X-Ray Absorption Spectroscopy of Semiconductors, Springer Series in Optical Sciences. Springer, Berlin, Heidelberg.

Schönbächler, M., 2016. Inductively Coupled Plasma Mass Spectrometry (ICP-MS). In: White, W.M. (Ed.), Encyclopedia of Geochemistry: A Comprehensive Reference Source on the Chemistry of the Earth. Springer International Publishing, Cham, pp. 1–6.

Schwertmann, U., 1991. Solubility and dissolution of iron oxides. Plant Soil 130, 1–25.

Schwertmann, U., Taylor, R.M., 1989. Chapter 8. Iron Oxides. Miner. Soil Environ. 379–438.

Scott, T.B., Allen, G.C., Heard, P.J., Randell, M.G., 2005. Reduction of U(VI) to U(IV) on the surface of magnetite. Geochim. Cosmochim. Acta 69, 5639–5646.

Sellafield Ltd., 2016. Groundwater monitoring at Sellafield: Annual Data review 2016, LQTD000758.

Sellafield Ltd, 2020a. Discharges and Environmental Monitoring Annual Report 2019.

Sellafield Ltd, 2020b. Corporate Strategy.

SEPA, Environment Agency, Natural Resources Wales, 2018. Guidance on Requirements for Release of Nuclear Sites from Radioactive Substances Regulation.

Shannon, R.D., 1976. Revised effective ionic radii and systematic studies of interatomic distances in halides and chalcogenides. Acta Crystallogr. Sect. A 32, 751–767.

Sherman, D.M., Peacock, C.L., Hubbard, C.G., 2008. Surface complexation of U(VI) on goethite (α-FeOOH). Geochim. Cosmochim. Acta 72, 298–310.

Sidhu, P.S., Gilkes, R.J., Posner, A.M., 1977. Mechanism of the low temperature oxidation of synthetic magnetites. J. Inorg. Nucl. Chem. 39, 1953–1958.

Silva, R.J., Nitsche, H., 1995. Actinide Environmental Chemistry. Radiochim. Acta 70–71, 377–396.

Simnad, M.T., 2003. Nuclear Reactor Materials and Fuels. In: Meyers, R.A. (Ed.), Encyclopedia of Physical Science and Technology (Third Edition). Academic Press, New York, pp. 775–815.

Singh, V.R., Ishigami, K., Verma, V.K., Shibata, G., Yamazaki, Y., Kataoka, T., Fujimori, A., Chang, F.H., Huang, D.J., Lin, H.J., Chen, C.T., Yamada, Y., Fukumura, T., Kawasaki, M., 2012. Ferromagnetism of cobalt-doped anatase TiO 2 studied by bulk- and surface-sensitive soft x-ray magnetic circular dichroism. Appl. Phys. Lett. 100, 1–5.

Skomurski, F.N., Ilton, E.S., Engelhard, M.H., Arey, B.W., Rosso, K.M., 2011. Heterogeneous reduction of U^{6+} by structural Fe^{2+} from theory and experiment. Geochim. Cosmochim. Acta 75, 7277–7290.

Smith, K., 2014. Radionuclide behaviour in hyperalkaline systems relevant to geological disposal of radioactive waste.

Smith, K.F., Bryan, N.D., Swinburne, A.N., Bots, P., Shaw, S., Natrajan, L.S., Mosselmans, J.F.W., Livens, F.R., Morris, K., 2015. U(VI) behaviour in hyperalkaline calcite systems. Geochim. Cosmochim. Acta 148, 343–359.

Smith, N.T., Shreeve, J., Kuras, O., 2020. Multi-sensor core logging (MSCL) and X-ray computed tomography imaging of borehole core to aid 3D geological modelling of poorly exposed unconsolidated superficial sediments underlying complex industrial sites: An example from Sellafield nuclear site, UK. J. Appl. Geophys. 178.

Solé, V.A., Papillon, E., Cotte, M., Walter, P., Susini, J., 2007. A multiplatform code for the analysis of energy-dispersive X-ray fluorescence spectra. Spectrochim. Acta - Part B At. Spectrosc. 62, 63–68.

Sowder, A.G., Clark, S.B., Fjeld, R.A., 2001. The impact of mineralogy in the U (VI)–Ca–PO_4 system on the environmental availability of uranium. J. Radioanal. Nucl. Chem. 248, 517–524.

Spears, D.A., Kanaris-Sotiriou, R., 1976. Titanium in some Carboniferous sediments from Great Britain. Geochim. Cosmochim. Acta 40, 345–351.

Stanley, D.M., Wilkin, R.T., 2019. Solution equilibria of uranyl minerals: Role of the common groundwater ions calcium and carbonate. J. Hazard. Mater. 377, 315–320.

Stewart, B.D., Nico, P.S., Fendorf, S., 2009. Stability of uranium incorporated into Fe (hydr)oxides under fluctuating redox conditions. Environ. Sci. Technol. 43, 4922–4927.

Stumm, W., Morgan, J.J., 1995. Aquatic Chemistry : Chemical Equilibria and Rates in Natural Waters. John Wiley & Sons, Somerset.

Stumpf, T., Tits, J., Walther, C., Wieland, E., Fanghänel, T., 2004. Uptake of trivalent actinides (curium(III)) by hardened cement paste: A time-resolved laser fluorescence spectroscopy study. J. Colloid Interface Sci. 276, 118–124.

Sundararajan, M., Campbell, A.J., Hillier, I.H., 2008. Catalytic cycles for the reduction of $[UO_2]^{2+}$ by cytochrome c7 proteins proposed from DFT calculations. J. Phys. Chem. A 112, 4451–4457.

Sutton, M., Warwick, P., Hall, A., 2003. Uranium(VI) interactions with OPC/PFA grout. J. Environ. Monit. 5, 922–928.

Sutton, M., Warwick, P., Hall, A., Jones, C., 1999. Carbonate induced dissolution of uranium containing precipitates under cement leachate conditions. J. Environ. Monit. 1, 177–182.

Swaddle, T.W., Oltmann, P., 1980. Kinetics of the magnetite–maghemite–hematite transformation, with special reference to hydrothermal systems. Can. J. Chem. 58, 1763–1772.

Sylwester, E.R., Allen, P.G., Zhao, P., Viani, B.E., 1999. Interactions of uranium and neptunium with cementitious materials studied by XAFS. In: MRS Proceedings. Boston, MA, pp. 1–7.

Takahashi, K., Miyahara, J., Shibahara, Y., 1985. Photostimulated Luminescence (PSL) and Color Centers in BaFX : Eu^{2+} (X = Cl , Br , I) Phosphors. J. Electrochem. Soc. 132, 1492–1494.

Taylor, D.M., Taylor, S.K., 1997. Environmental Uranium and Human Health. Rev. Environ. Health 12.

Taylor, R.M., Schwertmann, U., 1974. Maghemite in soils and its origin: II. Maghemite syntheses at ambient temperature and pH 7. Clay Miner. 10, 299–310.

Tessier, A., Campbell, P.G.C., Bisson, M., 1979. Sequential Extraction Procedure for the Speciation of Particulate Trace Metals. Anal. Chem. 51, 844–851.

Thomas, G.W., 1996. Soil pH and Soil Acidity. In: Methods of Soil Analysis, Part 3 - Chemical Methods. Soil Science Society of America, Madison, WI.

Thomas, J.J., Jennings, H.M., Allen, A.J., 1999. The surface area of hardened cement paste as measured by various techniques. Concr. Sci. Eng. 1, 45–64.

Thompson, A.C., Attwood, D.T., Eric, M., Howells, M.R., Kortright, J.B., Robinson, A.L., Underwood, J.H., Kim, K., Kirz, J., Williams, G.P., Scofield, J.H., Thompson, A.C., Vaughan, D., 2009. X-ray Data Booklet. Berkeley, CA, USA.

Thompson, H.A., Brown, G.E., Parks, G.A., 1997. XAFS spectroscopic study of uranyl coordination in solids and aqueous solution. Am. Mineral. 82, 483–496.

Tits, J., Geipel, G., Macé, N., Eilzer, M., Wieland, E., 2011. Determination of uranium(VI) sorbed species in calcium silicate hydrate phases: A laser-induced luminescence spectroscopy and batch sorption study. J. Colloid Interface Sci. 359, 248–256.

Tits, J., Macé, N., Eilzer, M., Wieland, E., Geipel, G., 2008. Uranium(VI) uptake by synthetic calcium silicate hydrates. In: Mater. Res. Soc. Symp. Proc., 1107. pp. 467–474.

Tits, J., Stumpf, T., Rabung, T., Wieland, E., Fanghänels, T., 2003. Uptake of Cm(III) and Eu(III) by calcium silicate hydrates: A solution chemistry and time-resolved laser fluorescence spectroscopy study. Environ. Sci. Technol. 37, 3568–3573.

Tits, J., Walther, C., Stumpf, T., Macé, N., Wieland, E., 2015. A luminescence line-narrowing spectroscopic study of the uranium(vi) interaction with cementitious materials and titanium

dioxide. Dalt. Trans. 44, 966–976.

Tits, J., Wieland, E., 2018. Actinide Sorption by Cementitious Materials, PSI Bericht 18-02.

Tits, J., Wieland, E., Müller, C.J., Landesman, C., Bradbury, M.H., 2006. Strontium binding by calcium silicate hydrates. J. Colloid Interface Sci. 300, 78–87.

Tochiyama, O., Endo, S., Inoue, Y., 1995. Sorption of Neptunium(V) on Various Iron Oxides and Hydrous Iron Oxides. Radiochim. Acta 68, 105–112.

Tournassat, C., Tinnacher, R.M., Grangeon, S., Davis, J.A., 2018. Modeling uranium(VI) adsorption onto montmorillonite under varying carbonate concentrations: A surface complexation model accounting for the spillover effect on surface potential. Geochim. Cosmochim. Acta 220, 291–308.

Townsend, L.T., Morris, K., Harrison, R., Schacherl, B., Vitova, T., Kovarik, L., Pearce, C.I., Mosselmans, J.F.W., Shaw, S., 2021. Sulfidation of magnetite with incorporated uranium. Chemosphere 130117.

Townsend, L.T., Shaw, S., Ofili, N.E.R., Kaltsoyannis, N., Walton, A.S., Mosselmans, J.F.W., Neill, T.S., Lloyd, J.R., Heath, S., Hibberd, R., Morris, K., 2019. Formation of a U(VI)–Persulfide Complex during Environmentally Relevant Sulfidation of Iron (Oxyhydr)oxides. Environ. Sci. Technol. 54, 129–136.

Triplett, M.B., Watson, D.J., Wellman, D.M., 2013. Risks from Past, Current, and Potential Hanford Single Shell Tank Leaks: PNNL-22483.

Tsarev, S., Collins, R.N., Fahy, A., Waite, T.D., 2016. Reduced Uranium Phases Produced from Anaerobic Reaction with Nanoscale Zerovalent Iron. Environ. Sci. Technol. 50, 2595–2601.

Tsarev, S., Collins, R.N., Ilton, E.S., Fahy, A., Waite, T.D., 2017. The short-term reduction of uranium by nanoscale zero-valent iron (nZVI): Role of oxide shell, reduction mechanism and the formation of U(v)-carbonate phases. Environ. Sci. Nano 4, 1304–1313.

Um, W., Chang, H., Icenhower, J.P., Lukens, W.W., Jeffrey Serne, R., Qafoku, N., Kukkadapu, R.K., Westsik, J.H., 2012. Iron oxide waste form for stabilizing 99Tc. J. Nucl. Mater. 429, 201–209.

Um, W., Icenhower, J.P., Brown, C.F., Serne, R.J., Wang, Z., Dodge, C.J., Francis, A.J., 2010. Characterization of uranium-contaminated sediments from beneath a nuclear waste storage tank from Hanford, Washington: Implications for contaminant transport and fate. Geochim. Cosmochim. Acta 74, 1363–1380.

Um, W., Serne, R.J., Brown, C.F., Last, G. V., 2007. U(VI) adsorption on aquifer sediments at the Hanford Site. J. Contam. Hydrol. 93, 255–269.

Um, W., Serne, R.J., Brown, C.F., Rod, K.A., 2008. Uranium(VI) sorption on iron oxides in Hanford Site sediment: Application of a surface complexation model. Appl. Geochemistry 23, 2649–2657.

UNSCEAR, 1988. Report to the General Assembly (Annex D - Exposures from the Chernobyl Accident).

UNSCEAR, 1993. Report to the General Assembly (Annex B - Exposures from Man-Made Sources of Radiation).

UNSCEAR, 2020. Report to the General Assembly (Annex B - Levels and effects of radiation exposure due to the accident at the Fukushima Daiichi Nuclear Power Station: Implications of information published since the UNSCEAR 2013 report).

Upham, L. V., Englert, D.F., 2003. Radionuclide Imaging. In: L'Annunziata, M.F. (Ed.), Handbook of Radioactivity Analysis. Academic Press, pp. 1063–1127.

US DOE, 1997. Linking Legacies: Connecting the Cold War Nuclear Weapons Production Process to their Environmental Consequences, DOE/EM-0319. Washington, DC.

US GAO, 2007. DOE Disposition of Transuranic wastes, GEO-07-761.

US NRC, 2018. List of leaks and spills at U.S. commercial nuclear power plants.

Uyuşur, B., Li, C., Baveye, P.C., Darnault, C.J.G., 2015. pH-dependent reactive transport of uranium(VI) in unsaturated sand. J. Soils Sediments 15, 634–647.

Valverde, J.M., Medina, S., 2015. Crystallographic transformation of limestone during calcination under CO_2. Phys. Chem. Chem. Phys. 17, 21912–21926.

Van Der Laan, G., Kirkman, I.W., 1992. The 2p absorption spectra of 3d transition metal compounds in tetrahedral and octahedral symmetry. J. Phys. Condens. Matter 4, 4189–4204.

Van der Laan, G., Thole, B.T., 1991. Strong magnetic x-ray dichroism in 2 p absorption spectra of 3 d transition-metal ions. Phys. Rev. B 43, 13401–13411.

Vermeul, V.R., Szecsody, J.E., Fritz, B.G., Williams, M.D., Moore, R.C., Fruchter, J.S., 2014. An Injectable Apatite Permeable Reactive Barrier for In Situ 90Sr Immobilization. Groundw. Monit. Remediat. 34, 28–41.

Vettese, G.F., Morris, K., Natrajan, L.S., Shaw, S., Vitova, T., Galanzew, J., Jones, D.L., Lloyd, J.R., 2020. Multiple Lines of Evidence Identify U(V) as a Key Intermediate during U(VI) Reduction by Shewanella oneidensis MR1. Environ. Sci. Technol. 54, 2268–2276.

Waite, T.D., Davis, J.A., Payne, T.E., Waychunas, G.A., Xu, N., 1994. Uranium(VI) adsorption to ferrihydrite: Application of a surface complexation model. Geochim. Cosmochim. Acta 58, 5465–5478.

Wang, G., Um, W., Cantrell, K.J., Snyder, M.M.V., Bowden, M.E., Triplett, M.B., Buck, E.C., 2017. Effects of hydrated lime on radionuclides stabilization of Hanford tank residual waste. Chemosphere 185, 171–177.

Wang, Y., Bagnoud, A., Suvorova, E., McGivney, E., Chesaux, L., Phrommavanh, V., Descostes, M., Bernier-Latmani, R., 2014. Geochemical control on uranium(IV) mobility in a mining-impacted wetland. Environ. Sci. Technol. 48, 10062–10070.

Wang, Y., Frutschi, M., Suvorova, E., Phrommavanh, V., Descostes, M., Osman, A.A.A., Geipel, G., Bernier-Latmani, R., 2013. Mobile uranium(IV)-bearing colloids in a mining-impacted wetland. Nat. Commun. 4, 2942.

Wang, Y., Von Gunten, K., Bartova, B., Meisser, N., Astner, M., Burger, M., Bernier-Latmani, R., 2016. Products of in Situ Corrosion of Depleted Uranium Ammunition in Bosnia and Herzegovina Soils. Environ. Sci. Technol. 50, 12266–12274.

Wang, Z., Lee, S.W., Catalano, J.G., Lezama-Pacheco, J.S., Bargar, J.R., Tebo, B.M., Giammar, D.E., 2013. Adsorption of uranium(VI) to manganese oxides: X-ray absorption spectroscopy and surface complexation modeling. Environ. Sci. Technol. 47, 850–858.

Waseda, Y., Matsubara, E., Shinoda, K., 2011. Scattering and Diffraction. In: X-Ray Diffraction Crystallography: Introduction, Examples and Solved Problems. Springer Berlin Heidelberg, Berlin, Heidelberg, pp. 67–106.

Wazne, M., Korfiatis, G.P., Meng, X., 2003. Carbonate effects on hexavalent uranium adsorption by iron oxyhydroxide. Environ. Sci. Technol. 37, 3619–3624.

Wealer, B., Seidel, J.P., von Hirschhausen, C., 2019. Decommissioning of Nuclear Power Plants and Storage of Nuclear Waste. In: Haas, R., Mez, L., Ajanovic, A. (Eds.), The Technological and Economic Future of Nuclear Power. Springer VS, Wiesbaden, pp. 261–286.

Weatherill, J., 2017. Iron Oxyhydroxide Formation in the Enhanced Actinide Removal Plant. The University of Manchester.

Wieland, E., Bonhoure, T., Fujita, T., Tits, J., Scheidegger, A.M., 2003. Combined wet chemistry

and EXAFS studies on the radionuclide immobilisation by cement and calcium silicate hydrates. In: Goldschmidt Conference.

Wieland, E., Mace, N., Dähn, R., Kunz, D., Tits, J., 2010. Macro- and micro-scale studies on U(VI) immobilization in hardened cement paste. J. Radioanal. Nucl. Chem. 286, 793–800.

Wieland, E., Tits, J.A.N., Kunz, D., Dähn, R., 2008. Strontium Uptake by Cementitious Materials. Environ. Sci. Technol. 42, 403–409.

Wilkins, M.J., Livens, F.R., Vaughan, D.J., Lloyd, J.R., 2006. The impact of Fe(III)-reducing bacteria on uranium mobility. Biogeochemistry 78, 125–150.

Willmott, P., 2011. An Introduction to Synchrotron Radiation. Wiley.

Wilson, P.D., 1996. The Nuclear Fuel Cycle: From Ore to Waste, 1st ed. Oxford University Press.

Winstanley, E.H., Morris, K., Abrahamsen-Mills, L.G., Blackham, R., Shaw, S., 2019. U(VI) sorption during ferrihydrite formation: Underpinning radioactive effluent treatment. J. Hazard. Mater. 366, 98–104.

World Nuclear Association, 2020. Uranium Enrichment [Website]. URL https://world-nuclear.org/information-library/nuclear-fuel-cycle/conversion-enrichment-and-fabrication/uranium-enrichment.aspx

Wronkiewicz, D.J., Bates, J.K., Wolf, S.F., Buck, E.C., 1996. Ten-year results from unsaturated drip tests with UO_2 at 90°C: implications for the corrosion of spent nuclear fuel. J. Nucl. Mater. 238, 78–95.

Wu, B., Ye, G., 2016. Carbonation mechanism of different kind of C-S-H : rate and products. In: Jensen, O.M., Kovler, K., de Belie, N. (Eds.), Concrete with Supplementary Cementitious Materials. Paris, pp. 163–272.

Xi, F., Davis, S.J., Ciais, P., Crawford-Brown, D., Guan, D., Pade, C., Shi, T., Syddall, M., Lv, J., Ji, L., Bing, L., Wang, J., Wei, W., Yang, K.H., Lagerblad, B., Galan, I., Andrade, C., Zhang, Y., Liu, Z., 2016. Substantial global carbon uptake by cement carbonation. Nat. Geosci. 9, 880–883.

Yamamura, T., Kitamura, A., Fukui, A., Nishikawa, S., Yamamoto, T., Moriyama, H., 1998. Solubility of U(VI) in Highly Basic Solutions. Radiochim. Acta 83, 139–146.

Yorkshire, A.S., Provis, J.L., Stennett, M.C., Hyatt, N.C., Corkhill, C.L., 2018. Understanding Radionuclide Interactions with Cementitious Materials for Radioactive Waste Management. In: Waste Management 2018. Phoenix, Arizona, pp. 1–9.

Yoshida, N., Takahashi, Y., 2012. Land-surface contamination by radionuclides from the Fukushima Daiichi nuclear power plant accident. Elements 8, 201–206.

Yuan, K., Ilton, E.S., Antonio, M.R., Li, Z., Cook, P.J., Becker, U., 2015. Electrochemical and spectroscopic evidence on the one-electron reduction of U(VI) to U(V) on magnetite. Environ. Sci. Technol. 49, 6206–6213.

Zänker, H., Hennig, C., 2014. Colloid-borne forms of tetravalent actinides : A brief review. J. Contam. Hydrol. 157, 87–105.

Zhang, W., Wang, J., 2017. Leaching performance of uranium from the cement solidified matrices containing spent radioactive organic solvent. Ann. Nucl. Energy 101, 31–35.

Zhao, P., Allen, P.G., Sylwester, E.R., Viani, B.E., 2000. The partitioning of uranium and neptunium onto hydrothermally altered concrete. Radiochim. Acta 88, 729–736.

Zheng, Z., Tokunaga, T.K., Wan, J., 2003. Influence of Calcium Carbonate on U(VI) Sorption to Soils. Environ. Sci. Technol. 37, 5603–5608.

Zhou, P., Gu, B., 2005. Extraction of Oxidized and Reduced Forms of Uranium from Contaminated Soils: Effects of Carbonate Concentration and pH. Environ. Sci. Technol. 39, 4435–4440.

Zimina, A., Dardenne, K., Denecke, M.A., Doronkin, D.E., Huttel, E., Lichtenberg, H., Mangold, S., Pruessmann, T., Rothe, J., Spangenberg, T., Steininger, R., Vitova, T., Geckeis, H., Grunwaldt, J.-D., 2017. CAT-ACT—A new highly versatile x-ray spectroscopy beamline for catalysis and radionuclide science at the KIT synchrotron light facility ANKA. Rev. Sci. Instrum. 88, 113113.

Zimina, A., Dardenne, K., Denecke, M.A., Grunwaldt, J.D., Huttel, E., Lichtenberg, H., Mangold, S., Pruessmann, T., Rothe, J., Steininger, R., Vitova, T., 2016. The CAT-ACT Beamline at ANKA: A new high energy X-ray spectroscopy facility for CATalysis and ACTinide research. J. Phys. Conf. Ser. 712.

Appendix 3   Bursaries, Awards & Presentations

The following is a list of travel bursaries, funding awards and first author oral and poster presentations given at conferences throughout the course of the PhD. A list of outreach activities and community engagement work are also provided.

A3.1 Travel Bursaries

- Travel bursary covering travel, accommodation and subsistence for the *TERRITORIES Workshop on Assessing risks from radioactive legacy sites and how to better present uncertain information*, March 2019.

A3.2 Funding Awards

- A request for an additional £11,000 funding from the NDA was awarded on the successful application by the author for additional funding to cover the lysimeter experiments detailed in Chapter 5.

A3.3 Oral Presentations

- Radionuclide alteration behaviour in engineered, subsurface environments. A. E. McNulty, S. Shaw, G. T. W. Law, B. Powell, W.R. Bower, K. Peruski, J. Rothe, T. Vitova, L. Abrahamsen-Mills, K. Morris, *Dalton Nuclear Institute Seminar*, 25th May 2021, virtual.
- Radionuclide alteration behaviour in engineered, subsurface environments. A. E. McNulty, S. Shaw, G. T. W. Law, B. Powell, W.R. Bower, K. Peruski, J. Rothe, T. Vitova, L. Abrahamsen-Mills, K. Morris, *NDA PhD Research Seminar*, 29th-30th April 2021, virtual.
- Using field lysimeters to characterise uranium behaviour in contaminated land. A. E. McNulty, S. Shaw, G. T. W. Law, B. Powell, L. Abrahamsen-Mills, K. Morris, *TRANSCEND Virtual Conference*, 2nd-3rd December 2020, virtual.
- The use of field lysimeter experiments in characterising radioactively contaminated land. A. E. McNulty, S. Shaw, G. T. W. Law, B. Powell, W. R. Bower, L. Abrahamsen-Mills, K. Morris. *Yorkshire Contaminated Land Forum*, 27th February 2020, Sheffield, UK.
- Long-term behaviour and stability of U(V) incorporated into magnetite in contaminated land environments. A. E. McNulty, S. Shaw, G. T. W. Law, B. Powell, W.R. Bower, C. Fallon, J. Rothe, T. Vitova, L. Abrahamsen-Mills, H. Roberts, K. Morris. *NDA PhD Seminar*, 29th January 2020, Manchester, UK.

- Radionuclide alteration behaviour in the subsurface in the context of in-situ disposal. A. E. McNulty, S. Shaw, K. Morris, *TERRITORIES Workshop on Assessing risks from radioactive legacy sites and how to better present uncertain information*, March 2019, Oxford, UK

- Radionuclide alteration behaviour at the cement/subsurface interface: key controls on mobility. A. E. McNulty, S. Shaw, L. Abrahamsen-Mills, G. T. W. Law, K. Morris. *NDA PhD Land Quality Group Meeting*, 14th November 2019, Winfrith, UK.

- Radionuclide alteration behaviour at the cement/subsurface interface: key controls on mobility. A. E. McNulty, S. Shaw, L. Abrahamsen-Mills, G. T. W. Law, K. Morris. *NDA PhD Land Quality Group Meeting*, November 2018, Springfields, UK.

A3.4 Poster Presentations

- Long-term behaviour and stability of U(V) incorporated into magnetite in contaminated land environments. A. E. McNulty, S. Shaw, G. T. W. Law, B. Powell, W.R. Bower, C. Fallon, J. Rothe, T. Vitova, L. Abrahamsen-Mills, H. Roberts, K. Morris. *NDA PhD Seminar*, 29th January 2020, Manchester, UK.

- Long-term behaviour and stability of U(V)-incorporated into magnetite in contaminated land environments. A. E. McNulty, S. Shaw, G. T. W. Law, B. Powell, W.R. Bower, C. Fallon, J. Rothe, T. Vitova, L. Abrahamsen-Mills, H. Roberts, K. Morris, *17th International Conference on the Chemistry and Migration Behaviour of Actinides and Fission Products in the Geosphere*, 15th-20th September 2019, Kyoto, Japan.

- Understanding the long-term behaviour and stability of U(V) in magnetite under conditions relevant to in-situ disposal of contaminated land. A. E. McNulty, S. Shaw, G. T. W. Law, B. Powell, J. Rothe, T. Vitova, L. Abrahamsen-Mills, K. Morris, *NDA PhD Seminar,* January 2019, Manchester, UK